UNIVERSITY OF SOUTHAMPTON

An Investigation Of Phase-Mask Diffraction Patterns And Fibre Bragg Gratings With Scanning Near-Field Optical Microscopy

by John David Mills

A thesis submitted for the qualification of
Doctor of Philosophy

Department of Physics and Astronomy

July 2001

UNIVERSITY OF SOUTHAMPTON

ABSTRACT

FACULTY OF SCIENCE

PHYSICS AND ASTRONOMY

Doctor of Philosophy

AN INVESTIGATION OF PHASE-MASK DIFFRACTION PATTERNS AND FIBRE BRAGG GRATINGS WITH SCANNING NEAR-FIELD OPTICAL MICROSCOPY

By John David Mills

In recent years, near-field microscopy has been utilized for assessing the properties of optical wave-guides at an increasing rate. Here, a Scanning Near-field Optical Microscope (SNOM) has been designed and constructed in order to expand this work into an analysis of the optical and structural properties of fibre Bragg gratings, which are used throughout the optical fibre telecommunications network. By imaging the evanescent fields of Bragg gratings, a characterization technique has been developed which has enabled the acquisition of sub-wavelength information about the optical field distribution within a fibre grating and its refractive index structure. Six separate fibre grating samples have been examined, demonstrating the feasibility of the developed scanning technique to become a useful characterization tool. In particular, the study has enabled grating standing wave fringes to be imaged relative to corresponding refractive index fringes, for the first time.

The SNOM has also been utilized to map free-space diffraction patterns close to a phase-mask (transmission diffraction grating). The patterns are normally used to create fibre gratings via UV photosensitivity mechanisms. The field distributions have been imaged under various experimental conditions and have revealed some of the technical problems that might occur during the writing of gratings. The measured patterns have also served to confirm existing diffraction grating theory, which has been expanded during the course of this work to produce a new expression for the ‘Talbot length’, originally formulated by Rayleigh in 1881.

CONTENTS

1. Introduction

2. Theory

3. Construction Of The Scanning Near-Field Optical Microscope (SNOM)

4. Imaging of Phase-Mask Diffraction Patterns Used To Manufacture Fibre Bragg Gratings.

5. Evanescent Field Imaging Of A Phase-mask Irradiated Fibre Bragg Grating: *The Development Of A Scanning Procedure*

6. Comparative Study Of The Evanescent Fields Of Two Holographically Side-Written Multi-Mode Fibre Bragg Gratings

7. Comparative Study Of The Evanescent Fields Of Three Holographically Side-Written Single-Mode Fibre Bragg Gratings

8. Conclusions

Appendices

Acknowledgements

Warm thanks go to Bill, Barry, Chris and Ping, who have all helped to make this project possible. Also to my family, Laura, Ben and Doms, who have lived the whole experience every step of the way!

1. Introduction

1.1 General Introduction

In 1928, the British scientist E.H. Synge suggested a method of performing optical microscopy beyond the diffraction limit [1.1]. His idea consisted of raster scanning a sub-wavelength aperture in close proximity to a sample. Unfortunately, there was no way at that time to verify the technique experimentally due to the requirements of fine positioning, and it was soon forgotten. However in 1972, Ash and Nichols did manage to demonstrate two-dimensional, sub-wavelength imaging to a resolution of $\lambda/20$, by using microwave radiation [1.2]. It was not until the invention of the Scanning Tunneling Microscope (STM) by Binnig and Rohrer in 1982 [1.3], that the positioning techniques became available to enable sub-wavelength imaging at visible wavelengths. The Scanning Near-field Optical Microscope (SNOM) was subsequently born following its development by two groups [1.4, 1.5].

By around the end of the 1980's, the use of a tapered optical fibre, coated in an opaque metal film except for at its apex, became the standard way of producing the required sub-wavelength aperture [1.6, 1.7]. However, a particular mode of SNOM operation that has come to be known as Photon Scanning Tunneling Microscopy (PSTM) in analogy with STM, utilizes an uncoated optical fibre probe in order to measure evanescent fields external to a sample, generated by total internal reflection (TIR) within the sample [1.8]. The method has already been successfully employed to investigate the evanescent field properties of several types of optical wave-guide [1.9, 1.10, 1.11]. This thesis will expand on the work by presenting a comprehensive PSTM examination of the external evanescent fields of six separate optical fibre Bragg gratings [1.12].

A well-established method of producing a fibre Bragg grating is to expose a photosensitive optical fibre to periodic interference fringes of UV light [1.13]. This introduces a periodic modulation into the refractive index along a length of its core. Recently, the use of a transmission phase diffraction grating, otherwise known as a phase-mask, has become a widely used technique for achieving this [1.14]. This thesis will describe how the diffraction patterns induced by a phase-mask can also be measured with a SNOM probe, by use of a coated tip.

1.2 The Motivation For The Research:

1.2.1 SNOM Imaging Of Fibre Bragg Gratings

The fibre Bragg grating is currently used extensively throughout the telecommunications industry [1.16, 1.17]. The device can be manufactured with well controlled reflection and transmission characteristics, which are presently examined in several ways. The most general of these is a measurement of the grating's reflection and transmission spectra, to gain information about such things as the Bragg wavelength, bandwidth and scattering from the grating region [1.18]. The use of simulation is an excellent way of gaining more information from these spectra, for example it is possible to identify phase-mask stitching errors from a spectrum's bandwidth and associated noise [1.19]. Alternative techniques exist for assessing the refractive index profile of a grating, such as the 'side scatter' method [1.20], or the application of a 'heat scan' for probing the chirp of a grating [1.21, 1.22]. Diffraction limited photographic imaging of the grating fringes of fibre gratings has also been achieved [1.23]. However, none of the above methods can give localized, sub-wavelength information about either the actual electric field distribution within a fibre grating, or its refractive index profile, and therefore this valuable information can be lost. Indeed, Transmission Electron Microscopy (TEM) has been utilized in order to identify regions of densification caused by UV irradiation [1.24]. This too has its limitations in the respect that it does not give any information about the way that the light is propagating through the grating. Clearly, the electric field intensity and the physical structure of a fibre grating are intimately linked, and therefore high-resolution information on both could be extremely useful.

In 1993, D. P. Tsai et al achieved the sub-wavelength imaging of the intensity modulated by a fibre grating at the interface between its core and cladding by utilizing Aperture Photon Scanning Tunneling Microscopy (APSTM) [1.25]. In carrying out this brief experiment as part of a wider study, they speculated that local anomalies in both the variations of the refractive index and grating spacing could be detected, although not conclusively. In building on this work, this PhD project has sought to confirm this speculation and to develop a useful sub-wavelength scanning technique, not only to examine the refractive index variation of fibre gratings via their evanescent field, but also their internal, propagating field. It is hoped that the new technique will be complementary to existing fibre grating characterization procedures, in addition to offering new insight into the structure of gratings.

1.2.2 SNOM Imaging Of Phase-Mask Diffraction Patterns

The pattern formed close to a phase diffraction grating was first observed by Talbot [1.26] in 1836. The Talbot diffraction pattern is interesting because under certain conditions, it replicates the pattern of the original grating at periodic distances from its surface, subject to diffraction limits. Rayleigh first deduced the repeat length of the pattern, known as the Talbot length, in 1881 [1.27]. The actual electric field distribution in the pattern can be calculated using finite-element models [1.28], scalar Fresnel-Kirchoff diffraction theory [1.29] or with analytical functions [1.30] to provide extremely detailed information about its amplitude and phase. Techniques involving exposure of photoresists [1.30] have been used to try to characterize the field distributions experimentally but up to now, comprehensive experimental measurements of these patterns have not been carried out. As mentioned above, the phase grating diffraction patterns are utilized to fabricate fibre Bragg gratings, and therefore a thorough analysis of these free-space patterns under real experimental conditions, is useful to engineers working in the industry. The measurements would also serve as a confirmation of theory, which up to now has been the only reliable method of visualizing these sometimes complex patterns.

By positioning the coated probe of a SNOM near to the surface of a sample but not in direct contact [1.31, 1.32], propagating components of light associated with the sample can be measured. By this method, the variation of electric field intensity in the Fresnel region close to a phase-mask has been determined during the course of this project, in order to achieve the above aims. The measurements have been made under a variety of experimental conditions, and many of the patterns acquired have been matched to simulations in order to confirm theoretical predictions. It is however important to note that these experiments will not have been performed in the typical 'near-field' region of operation of a SNOM, which requires a tip-sample distance of just a few nanometres. Here, evanescent components of the electric field will not be measured in these diffraction limited patterns, and therefore the presented images contain no detail smaller than ~$\lambda/2$ [1.15].

1.3 Introduction To The Main Sections Of The Thesis:

1.3.1 *Chapter 2*: Theory

This chapter contains background theoretical issues not covered elsewhere in the thesis. It discusses matters pertaining to the mechanical operation of the SNOM, and its ability to measure optical fields. Considerations are also made relating to fibre Bragg gratings.

1.3.2 *Chapter 3*: Construction Of The Scanning Near-field Optical Microscope

To enable the acquisition of the data for this thesis, a Scanning Near-field Optical Microscope was designed and constructed, as part of the overall project. This chapter describes the operation of the complete SNOM system and introduces some data acquired early on in the project, in order to demonstrate its performance. The chapter goes on to explain how the SNOM's fibre probes were produced, and how the electronics were implemented in order to control the position of each probe, enabling the acquisition of the topographical and optical data.

1.3.3 *Chapter 4*: Free-Space Imaging Of Phase-Mask Diffraction Patterns

During this chapter, the measured free-space phase-mask diffraction patterns along with many associated simulations, both analytical and numerical are shown. A variety of experimental situations are given against the background of a discussion relating to fibre Bragg grating manufacture by phase-mask. In addition, an original mathematical expression, derived during the course of this project will be introduced. It relates to the Talbot Length of repeating diffraction patterns, and is most useful where few diffracting orders are present, as in the case of fibre grating manufacture at telecommunication wavelengths. The new expression is confirmed by experiment in every instance.

1.3.4 *Chapters 5-7*: Evanescent Field Imaging Of Fibre Bragg Gratings

Chapters 5-7 contain the largest section of original material for this thesis. They constitute a comprehensive study of the evanescent fields of six fibre Bragg gratings. Firstly, there is a discussion relating to all of the parameters associated with an evanescent field measurement of this device, including some mathematical formulation. Following this, the presentation and analysis of data acquired early in the project from a single fibre grating is expanded into a comparative study of other gratings. Finally, a wider discussion ensues in order to coalesce all of the results in this thesis, including some of those from *Chapter 4*.

1.3.5 *Chapter 8*: Conclusions

This chapter presents the conclusions of the thesis, and offers suggestions for future work.

1.4 Chapter Summary

After a brief historical perspective on Scanning Near-field Optical Microscopy, the motivation behind the research presented in this thesis was explained. Finally, an outline has been given relating to the contents of the remainder of this thesis.

1.5 References

[1.1] E.H. Synge, Phil. Mag., **6**, 356 (1928)

[1.2] E.A. Ash, G. Nichols, Nature, **237**, 510 (1972)

[1.3] G.Binnig, H. Rohrer, Helv. Phys. Acta, **55**, 726 (1982)

[1.4] D.W. Pohl, W. Denk, M. Lanz, Applied Physics Letters, **44**, 651 (1984)

[1.5] A. Harootunian, E. Betzig, M. Isaacson, A. Lewis, E. Kratschmer, Applied Physics Letters, **49**, 674 (1986)

[1.6] H. Heinzelmann, D.W. Pohl, Appl. Phys. A, **59**, 89 (1994)

[1.7] E. Betzig, J. Trautman, Science, **257**, 189 (1992)

[1.8] R.C. Reddick, R.J. Warmack, D.W. Chilcott, S.L. Sharp, T.L. Ferrell, Rev. Sci. Instrum., **61** (12), 3669 (1990)

[1.9] A.G. Choo, M.H. Chudgar, H.E. Jackson, G.N. De Brabander, M. Kumar, J.T. Boyd, Ultramicroscopy, **57**, 124 (1995)

[1.10] S. Bourzeix, J.M. Moison, F. Mignard, F. Barthe, Applied Physics Letters, **73** (8), 1035 (1998)

[1.11] D.P. Tsai, H.E. Jackson, R.C. Reddick, S.H. Sharp, R.J. Warmack, Applied Physics Letters, **56** (16), 1515 (1990)

[1.12] D. Weidman, *Laser Focus World*, 99, March (1999)

[1.13] G. Meltz, W.W. Morey, W.H. Glenn, Optics Letters, **14**, 823 (1989)

[1.14] K.O. Hill, B.Malo, F. Bilodeau, D.C. Johnson, J. Albert, Applied Physics Letters **62**, 1035 (1993)

[1.15] E. Wolf, J.T. Foley, Optics Letters, **23** (1), 16 (1998)

[1.16] K.O. Hill, Y. Fujii, D.C. Johnson, B.S. Kawasaki, Applied Physics Letters, **32** (10), 647 (1978)

[1.17] P.E. Dyer, R.J. Farley, R. Giedl, K.C. Byron, D.Reid, Electronics Letters, **30** (11), 860 (1994)

[1.18] R. Kashyap, *Fiber Bragg Gratings*, Academic Press, London, 409 (1999)

[1.19] F. Ouellette, P.A. Krug, R. Pasman, Optical Fiber Technol., **2**, 281 (1996)

[1.20] P. Krug, R. Stolte, R. Ulrich, Opt. Lett., **20** (17), 1767 (1995)

[1.21] W. Margulis, I.C.S. Carvalho, P.M.P. Govea, Opt. Lett., **18** (12), 1016 (1998)

[1.22] S. Sandgren, B. Sahlgren, A. Asseh, W. Margulis, F. Laurell, R. Stubbe, A. Lidgard, Electron. Lett., **31**, 665 (1995)

[1.23] B. Malo, D.C. Johnson, F. Bilodeau, J. Albert, K.O. Hill, Optics Letters, **18** (15), 1277 (1993)

[1.24] P.Cordier, S. Dupont, M. Douay, G. Martinelli, P. Bernage, P. Niay, J.F. Bayon, L. Dong, Appl. Phys. Lett., **70** (10), 1204 (1997)

[1.25] D. P. Tsai, J. Kovacs, M. Moskovits, Ultramicroscopy, **57**, 130 (1995)

[1.26] H. Talbot, Phil. Mag. **9**, 401 (1836)

[1.27] Lord Rayleigh, Phil. Mag. **11**, 196 (1881)

[1.28] G. Wojcik, J. Mould, Jr., R. Ferguson, R. Martino, K. K. Low, SPIE Proceedings **2197**: Optical/Laser Microlithography VII, 455 (1994)

[1.29] J.D. Prohaska, E. Snitzer, J. Winthrop, Applied Optics, **33** (18), 3896 (1994)

[1.30] P.E. Dyer, R.J. Farley, R. Giedl, Optics Communications **115**, 327 (1995)

[1.31] B. Hecht, H. Bielefeldt, Y.Inouye, D.W.Pohl, L.Novotny, J. Appl. Phys, **81** (6), 2492 (1997)

[1.32] R. Toledo-Crow, J.K. Rogers, F. Seiferth, M. Vaez-Iravani, Ultramicroscopy, **57**, 293 (1995)

2. Theory

2.1 Chapter Introduction

The background theory associated with the research carried out for this PhD project, is given in this chapter. Firstly, a discussion relating to SNOM optical measurements is followed by a description of the mechanisms that allow SNOM probes to be held close to a sample surface, enabling both evanescent components of light to be detected, and topographical measurements to be performed. Uniform fibre Bragg grating theory is also introduced, along with some details associated with the UV-photosensitivity of doped silica.

Additional theory that was developed actually during the course of this project will not be shown in this chapter, but will appear later in the thesis within the context of associated data. This consists of a new expression for the ‘Talbot length’, which will be introduced in *Chapter 4*, and some aspects relating to Photon Scanning Tunneling Microscopy (PSTM) measurements of fibre Bragg gratings, which will be detailed in *Chapter 5*.

2.2 SNOM Acquisition Of Optical Data

2.2.1 Imaging Beyond The Diffraction Limit

The difficulty associated with achieving sub-wavelength resolution with conventional optics has been known for well over a century. It was expressed in terms of diffraction theory by Abbe in 1873 [2.1], and was later reformulated by Lord Rayleigh [2.2] in the following concise form

$$r \geq \frac{1.22 l}{2n \sin(q)} . \tag{2.1}$$

The expression known as the Rayleigh criterion, states that two point objects will be seen separately only when the distance r between them is greater than a quantity that depends upon the wavelength l of the illuminating light, the refractive index n of the medium and the semi-angle q of the aperture of the objective used to collect and focus the light onto a detector. The consequence of the above expression is that there are practical limits placed on the resolution of imaging under normal experimental conditions. However, the criterion was established assuming propagating waves. By utilizing SNOM, the detection of non-radiating (evanescent) fields can be realised, allowing this diffraction limit to be circumvented.

2.2.2 The Angular Spectrum Of The Object Field

In order to demonstrate that the evanescent field contains information about the highest spatial frequencies of an object, therefore holding the key to increased resolution, an angular spectrum analysis offers a lucid description [2.3]:

A two-dimensional limited object, described by its transmittance or reflectance $f(x,y,0)$, may be expressed in the form of a two-dimensional Fourier integral

$$F_0(u,v) = \int\int_{-\infty}^{+\infty} f(x,y,0)\exp[-i2\pi(ux+vy)]dxdy \qquad (2.2)$$

where u,v are the spatial frequencies of the object. The object bounding means that $F_0(u,v)$ contains all possible frequencies, from zero to infinity. If a plane wave with uniform amplitude impinges on the limited object, to a first approximation, the field immediately beyond the object can be written

$$U(x,y,0) = f(x,y,0). \qquad (2.3)$$

The two-dimensional Fourier transform

$$U(x,y,0) = \int\int_{-\infty}^{+\infty} F_0(u,v)\exp[i2\pi(ux+vy)]dudv \qquad (2.4)$$

therefore allows the object field to be regarded as the superposition of a collection of exponential functions where the terms $\exp[i2\pi(ux+vy)]$ correspond to elementary plane waves with direction cosines

$$\alpha = \lambda u \qquad \beta = \lambda v \qquad \gamma = [1-\lambda^2(u^2+v^2)]^{1/2} \qquad (2.5)$$

where λ is the wavelength of the illuminating light. Equation (2.2) can therefore be regarded as the angular spectrum of the object field $U(x,y,0)$. Substituting Equations (2.3) and (2.5) into (2.2), and using $k = 2\pi/\lambda$ gives

$$F_0(\alpha k/2\pi, \beta k/2\pi) = \int\int_{-\infty}^{+\infty} U(x,y,0)\exp[-ik(\alpha x+\beta y)]dxdy. \qquad (2.6)$$

Since no restrictions have been put on the location of the observation plane, the distance from the object z can be chosen to be much smaller than the wavelength. Equation (2.4) then gives

$$U(x,y,z)=\frac{k^2}{4p^2}\int\int_{-\infty}^{+\infty}F(ak/2p,bk/2p,z)\exp[ik(ax+by)]dadb\ . \tag{2.7}$$

Finally, by utilizing Equations (2.6) and (2.7) in conjunction with the Helmholtz equation [2.4], the angular spectrum at a distance z from the object plane can be expressed as [2.2]

$$F(ak/2p,bk/2p,z)=F_0(ak/2p,bk/2p)\exp[ik(1-a^2-b^2)^{1/2}z] \tag{2.8}$$

where $F_0(ak/2p,bk/2p)$ is the angular spectrum of the field in the object plane (*z=0*). Equation (2.8) shows that the ability for plane wave components to propagate, depends on their direction cosines. For example, if

$$a^2+b^2<1 \tag{2.9}$$

then the plane waves are able to propagate from the object to the detector, but if

$$a^2+b^2>1 \tag{2.10}$$

then the waves are strongly attenuated in the *z*-direction. The plane waves in the latter case correspond to evanescent waves, which can be expressed in the following manner

$$F(ak/2p,bk/2p,z)=F_0(ak/2p,bk/2p)\exp[-k(a^2+b^2-1)^{1/2}z] \tag{2.11}$$

where the direction cosines depend on object structure from Equations (2.2) and (2.5). The Rayleigh criterion can be deduced from Equations (2.5) and (2.9) by introducing a one-dimensional object where v = 0 [2.3]. From this, the largest propagating spatial frequency would be given by

$$u=k/2p \tag{2.12}$$

and therefore the highest spatial frequency in the detected far-field equates to

$$u'=2u=k/p \tag{2.13}$$

which is a result that is comparable to that given in Equation (2.1).

Equation (2.11) is formally analogous to

$$F(ak/2p,bk/2p,z)=F_0(ak/2p,bk/2p)\exp\{-k[(an)^2+(bn)^2-1]^{1/2}z\} \tag{2.14}$$

which describes the generation of evanescent waves at a total internal reflection (TIR) interface, where a and b are the two direction cosines of the incident wave and n is the refractive index of the denser medium. A variation of Equation (2.14) is shown later in this thesis as Equation (5.2), where the generation of TIR evanescent fields is discussed within the context of PSTM.

The relationship between high spatial frequencies and the generation of non-propagating evanescent fields could also have been arrived at by solving Maxwell’s equations [2.5, 2.6], or by utilizing the Heisenberg uncertainty principle [2.7]. However, the angular spectrum model is a particularly useful description, because it makes clear the role of the evanescent components. It also gives an insight into how the evanescent fields relate to detection by a SNOM probe, situated at a particular distance z from a sample.

2.2.3 SNOM Detection Of Components Of The Object Field

The SNOM probes used during this project are described in *Chapter 3* of this thesis. However, they basically take two forms: an optical fibre tapered at one end down to a ~50nm diameter [2.8], and a tapered optical fibre coated in aluminium to leave a tiny aperture at its apex [2.9]. The detection of non-radiating fields by the former probe, has been described in various ways. A simple method assumes that the tip of the probe behaves like a dipole [2.10] which, when placed within the proximity of a non-radiating field, is excited and generates an electromagnetic field consisting of both propagating and non-propagating components [2.11]. The propagating components are subsequently guided along the probe’s fibre to be recorded by a remote detector. In this case, each evanescent field component $\vec{E}(x,y,z)$ induces on the tip an electric dipole $A\vec{E}(x,y,z)$, and the subsequent detected intensity is given by [2.12]

$$\begin{aligned} I_d(x,y,z) = \frac{w^4}{96c^3}|A|^2 \{[|E_x(x,y,z)|^2 + |E_y(x,y,z)|^2][16-15\cos d - \cos 3d] \\ + |E_z(x,y,z)|^2[16-18\cos d + 2\cos 3d]\} \end{aligned} \tag{2.15}$$

where w is the frequency of the incident light, c is the speed of light in a vacuum, d is the collection angle of the tip, i.e. the half angle of its taper and A is the polarizability of the tip. If the apex of the optical fibre probe is considered to be a small sphere of radius R and dielectric constant e_{tip}, then the polarizability can be written [2.13]

$$A = \frac{e_{tip}-1}{e_{tip}+2}R^3. \tag{2.16}$$

Many other theoretical approaches have been taken to model the detection of light by SNOM probes. In a similar manner to the above description, some have assumed that the detected signal is proportional to the square modulus of the electric field at the tip position [2.14, 2.15]. Another point of view has been to describe the tip as a point-like scatterer, which scatters the evanescent near-field towards a far-field detector [2.16, 2.17].

The discussion above has been principally based upon the detection of non-radiating fields with an uncoated SNOM probe. This can be related to the data shown in *Chapters 5-7* of this thesis, which carries out this function. However, in *Chapter 4*, an aluminized SNOM tip positioned some distance away from an illuminated sample is used. The measurements include only radiating components because the tip is out of the range of the quickly decaying evanescent fields. However, by the reciprocity theorem [2.18, 2.19], both evanescent and radiating fields incident on a SNOM tip will be converted partly into propagating components that can be measured by a detector [2.20]. The reason for aluminizing the tip here, was in order to prevent light incident on the probe from passing into the cladding of the fibre along its tapered region. This would have resulted in an increase in the sampled area of measurement, and consequently a reduction in resolution.

The transmission coefficient of a sub-wavelength hole in an infinitely thin, perfectly conducting screen, was first determined rigorously by Bethe [2.5]. However, there were errors in these calculations, which were subsequently corrected by Bouwkamp [2.21]. Within the Bethe-Bouwkamp model, the transmission coefficient of a sub-wavelength hole scales as d^4 where d is the diameter of the aperture [2.22, 2.23]. However, as in the dielectric case, the taper angle of an aluminized SNOM probe is also a contributing factor to throughput [2.22, 2.24]. A typical value of 100nm aperture, with a full taper angle of 30 degrees results in a transmission of between 10^{-6} and 10^{-5} [2.22]. The transmission coefficient reduces dramatically for much smaller apertures, for example, working with apertures <40-50nm is often impossible [2.22]. In the case of the data collected for *Chapter 4*, it is expected that the aperture size of the SNOM probe was in the region of ~100nm and therefore there was no difficulty in achieving a measurable signal from the incident propagating light.

2.3 SNOM Probe Oscillation And Interaction With Sample

The positioning of a SNOM tip close to a sample is necessary in order to detect the bound evanescent fields. It was achieved during this project by attaching the probe to an oscillating quartz tuning-fork, allowing for a slight tip overhang. A monitoring of the damping effect on the tip by surface shear forces enabled the probe’s height to be fixed relative to the sample [2.25]. The exact nature of the shear force is still unclear but is thought to be a combination of various forces such as electrostatic, capillary and van der Waals [2.26, 2.27]. What is clear however, is that the sample surface water layer can contribute to damping, and therefore the overall effect of the shear force can vary over time [2.28]. This effect was confirmed during the course of this PhD project.

The vibrating probe can be modeled as a classical driven harmonic oscillator [2.29] with an equation of motion given by [2.30]

$$m\frac{d^2x}{dt^2} + g\,\frac{dx}{dt} + kx = F_a \sin(wt) \qquad (2.17)$$

where the terms on the left are the inertial, damping and restoring forces respectively, and the term on the right is the driving force. The quantity m represents the effective mass, g is the damping coefficient, k is the spring constant, F_a is the driving force amplitude applied to the tuning-fork, w is the driving frequency and the vibration amplitude at the tip of the probe is given by

$$x = X\sin(wt + j) \qquad (2.18)$$

where j is the phase shift between the drive and the tip’s response. The response amplitude is calculated by substitution of derivatives of Equation (2.18) into Equation (2.17), to give [2.29]

$$X(w) = \frac{F_a / k}{\sqrt{\left(1 - \frac{w^2}{w_0^2}\right)^2 + \left(\frac{w}{Qw_0}\right)^2}} \qquad (2.19)$$

where w_0 is the undamped natural frequency, the quality factor is given by

$$Q = \frac{w_0}{\Delta w}\,, \qquad (2.20)$$

and Δw is the FWHM of the resonance. Examination of Equation (2.19) shows that a decrease in tip amplitude X, as a result of its interaction with sample shear forces, can be either due to a decrease in the quality factor Q corresponding to an increase in g, or a shift in resonant frequency w_0, resulting from a force in the direction of the probe dither motion [2.29].

As will be demonstrated in *Chapter 3* of this thesis, the theoretical consequences of tip damping as discussed above, will be confirmed by experiment.

2.4 Uniform Fibre Bragg Gratings

A PSTM investigation of the evanescent fields of several fibre Bragg gratings is shown throughout *Chapters 5-7* of this thesis. All of the fibre gratings used were created to have a uniform period of refractive index variation along their length, and are therefore known as ‘uniform gratings’. This section will give an introduction to uniform fibre grating theory in order to support some of the discussion and analysis that follows later in this thesis. However, it will not cover aspects relating to a grating’s evanescent field, as this topic will be evaluated in *Chapter 5*.

Fibre Bragg gratings are formed by exposing an optical fibre with a photosensitive core to periodic fringes of UV light [2.42]. The consequence of this is that a perturbation in the effective refractive index n_e ensues, along the affected length of the core. With the z-direction along the core’s axis, the induced perturbation can be described by [2.33]

$$dn_e(z) = \overline{dn_e}(z)\left[1 + n\cos\left(\frac{2p}{\Lambda}z\right)\right] \tag{2.21}$$

where $\overline{dn_e}$ is the average index change along the length of the grating, n is the fringe visibility of the index variation and Λ is the period of the grating. The fibre grating performs like a simple optical diffraction grating and therefore light traveling along its fibre and becoming incident on the grating at angle q_1, will be diffracted at angle q_2 according to the grating equation [2.43]

$$n\sin q_2 = n\sin q_1 + m\frac{l}{\Lambda} \tag{2.22}$$

where m defines the diffraction order. The mode propagation constant, or axial component of the wave vector, is given by [2.33]

$$\beta = nk\sin\theta = n_e k \tag{2.23}$$

where n_e is the average effective refractive index and

$$k = \frac{2\pi}{\lambda}. \tag{2.24}$$

Combining Equations (2.22) and (2.23) gives

$$\beta_2 = \beta_1 + m\frac{2\pi}{\Lambda}. \tag{2.25}$$

For first order diffraction, which dominates in fibre Bragg gratings, $m = -1$ describes a reflection condition [2.33]. Additionally, negative β values describe modes that propagate in the reflection direction. Given that this is the case, Equations (2.23) and (2.25) can be utilized to give

$$-kn_{e,2} = kn_{e,1} - \frac{2\pi}{\Lambda} \tag{2.26}$$

which, when combined with Equation (2.24) gives

$$\lambda = (n_{e,1} + n_{e,2})\Lambda. \tag{2.27}$$

The resonant wavelength for coupling of a forward propagating mode to a backward propagating mode is given when $n_{e,1} = n_{e,2}$ leading finally to the condition for Bragg reflection

$$\lambda_B = 2n_e\Lambda \tag{2.28}$$

where λ_B is the Bragg wavelength.

The periodically varying refractive index along the length of a fibre grating provides multiple reflections to incident light. The total macroscopic response of the grating can therefore be illustrated more formally by coupled-mode theory, which describes the coupling of counter-propagating guided waves [2.31, 2.44]. Given that $A(z)$ and $B(z)$ are the amplitudes of the forward and backward propagating waves respectively, the total device response can be described by

$$E(z) = A(z)e^{-i\beta_0 z} + B(z)e^{i\beta_0 z} \tag{2.29}$$

where $b_0 = p / \Lambda$, and is equivalent to the propagation constant given in Equation (2.23), at the Bragg wavelength. Significantly, the use of coupled-mode theory to describe single-mode, uniform fibre Bragg gratings has enabled the derivation of an expression for the reflection bandwidth, which is given by [2.31, 2.33]

$$\frac{\Delta l}{l} = \frac{\overline{dn_e}}{n_e}\sqrt{1+\left(\frac{l}{\overline{dn_e}L}\right)^2} \qquad (2.30)$$

where L is the overall length of the fibre grating and Δl is the width between the first two zero reflection regions, either side of the maximum reflectivity. The expression is utilized in this thesis to estimate values of induced refractive index.

2.5 UV Photosensitivity Mechanisms In Doped Silica Optical Fibres

Photosensitivity utilized for grating writing in optical fibres is predominantly associated with oxygen deficiencies in the chemical structure of a fibre [2.34]. For example, in a germanium-doped silica fibre core, the photosensitivity has been correlated with the concentration of GeO defects [2.35, 2.36]. It is a consequence of the atom immediately adjacent to a germanium atom being either silicon or another germanium, resulting in a bond with a characteristic 240nm absorption peak [2.37]. When illuminated with UV light, the bond breaks creating a GeE’ centre. The breaking of the bond, and thus the liberation of an electron causes a reconfiguration of the shape of the molecule, possibly also changing the density of the material [2.38]. The addition of boron to this type of fibre core has the effect of reducing the background refractive index. This allows a higher concentration of the index-increasing germania, resulting in greater photosensitivity, without significantly affecting the fibre’s refractive index profile. All of the Bragg grating samples examined in this thesis were germania-boron co-doped silica fibres.

One method of enhancing the photosensitivity of optical fibres is hydrogen loading. This involves placing the fibre in a high-pressure hydrogen chamber for several days in order to allow molecular hydrogen to diffuse into the fibre core, through its cladding [2.39]. Once the fibre is loaded, incident UV light leads to a dissociation of the molecule resulting in the formation of Si-OH and Ge-OH bonds, which enhance the index change [2.40]. Immersion at

~200 bar for about two weeks at room temperature, is adequate to load a fibre with 125μm diameter [2.41].

2.6 Chapter Summary

This chapter has introduced some of the background theory associated with the acquisition of data for this thesis, by explaining the main concepts of Scanning Near-field Optical Microscopy (SNOM). The chapter has also discussed theoretical issues associated with fibre Bragg gratings, which are devices associated with the majority of the work carried out during this project.

2.7 References

[2.1] E. Abbe, Archiv f. Miroskop. Anat., **9**, 413 (1873)

[2.2] D. Courjon, C. Bainier, Rep. Prog. Phys. **57**, 989 (1994)

[2.3] D. Courjon, J.-M. Vigoureax, M. Spajer, K. Sarayeddine, S. Leblanc, Applied Optics, **29** (26), 3734 (1990)

[2.4] J.W. Goodman, *Introduction to Fourier Optics*, Mcgraw-Hill, London, 48-55 (1968)

[2.5] H.A. Bethe, Phys. Rev., **66**, 163 (1944)

[2.6] C.J. Bouwkamp, Philips Res. Rep., **5**, 401 (1950)

[2.7] J.M. Vigoureux, D. Courjon, Applied Optics, **31** (16), 3170 (1992)

[2.8] G.A. Valaskovic, M. Holton, G.H. Morrison, Applied Optics, **34** (7), 1215 (1995)

[2.9] C.W. Hollars, R.C. Dunn, Review of Scientific Instruments, **69** (4), 1747 (1998)

[2.10] D. Van Labeke, D. Barchiesi, J. Opt. Soc. Am. A, **9**, 732 (1992)

[2.11] E. Wolf, M. Nieto-Vesperinas, J. Opt. Soc. Am., **2**, 886 (1985)

[2.12] D. Van Labeke, D.Barchiesi, *Near Field Optics*, Kluwer Academic, 157-178 (1993)

[2.13] B. Labani, C. Girard, D. Courjon, D. Van Lebeke, J. Opt. Soc. Amer. A, **7**, 936 (1990)

[2.14] C. Girard, A. Dereux, Rep. Prog. Phys., **59**, 657 (1996)

[2.15] J.J. Greffet, R. Carminati, Prog. Surf. Sci., **56**, 133 (1997)

[2.16] C. Girard, D. Courjon, Phys. Rev. B, **42**, 9340 (1990)

[2.17] D. Van Labeke, D. Barchiesi, J. Opt. Soc. Am. A, **10**, 2193 (1993)

[2.18] L. Landau, E. Lifshitz, L. Pitaevskii, *Electrodynamics of Continuous Media*, Pergamon, Oxford (1984)

[2.19] R. Carminati, M. Nieto-Vesperinas, J.-J. Greffet, J. Opt. Soc. Am. A, **15**, 706 (1998)

[2.20] A. Dereux, Ch. Girard, J-C. Weeber, J. Chem. Phys., **112**, 7775 (2000)

[2.21] C.J. Bouwkamp, Philips Res. Rep., **5**, 321 (1950)

[2.22] B. Hecht, B. Sick, U.P. Wild, V. Deckert, R. Zenobi, O.J.F. Martin, D.W. Pohl, Journal Of Chemical Physics, **112** (18), 7761 (2000)

[2.23] D.V. Labeke, D. Barchiesi, F. Baida, J. Opt. Soc. Am. A, **12**, 695 (1995)

[2.24] A Roberts, J. Appl. Phys., **70** (8), 4045 (1991)

[2.25] K. Karrai, R.D. Grober, Applied Physics Letters, **66** (14), 1842 (1995)

[2.26] E. Betzig, P.L. Finn, J.S. Weiner, Applied Physics Letters, **60**, 2484 (1992)

[2.27] R. Toledo-Crow, P.C Yang, Y. Chen, M. Vaez-Iravani, Applied Physics Letters, **60**, 2957 (1992)

[2.28] S. Davy, M. Spajer, D. Courjon, Applied Physics Letters, **73** (18), 2594 (1998)

[2.29] F.F. Froehlich, T.D. Milster, Applied Physics Letters, **70** (12), 1500 (1997)

[2.30] D. Sarid, *Scanning Force Microscopy*, Oxford University Press, New York (1991)

[2.31] R. Kashyap, *Fiber Bragg Gratings*, Academic Press, London, 142-145 (1999)

[2.32] E. Kreyszig, *Advanced Engineering Mathematics*, 5th Edition, Wiley, New York, 345 (1992)

[2.33] T. Erdogan, Journal of Lightwave Technology, **15** (8), 1277 (1997)

[2.34] I. Bennion, J.A.R. Williams, L. Zhang, K. Sugden, N.J. Doran, Optical and Quantum Electronics, **28**, 93 (1996)

[2.35] D.L. Williams, S.T. Davey, R. Kashyap, J.R. Armitage, B.J. Ainslie, SPIE, **1513**, 158 (1991)

[2.36] B. Poumellec, P. Niay, M. Douay, J.F. Bayon, J. Phys. D, Appl. Phys., **29**, 1842 (1996)

[2.37] A.J. Cohen, H.L. Smith, J. Phys. Chem., **7**, 301 (1958)

[2.38] R. Kashyap, *Fiber Bragg Gratings*, Academic Press, London, 16-29 (1999)

[2.39] F. Bhakti, J. Larrey, P. Sansonetti, B. Poumellec, *Bragg Gratings, Photosensitivity and Poling in Glass Fibers and Waveguides: Fundamentals and Applications*, OSA Technical Series, paper BSuD2, **17**, 55 (1997)

[2.40] R. Kashyap, *Fiber Bragg Gratings*, Academic Press, London, 29-35 (1999)

[2.41] P. Lemaire, R.M. Atkins, V. Mizrahi, W.A. Reed, Electron. Letts., **29** (13), 1191 (1993)

[2.42] G. Meltz, W.W. Morey, W.H. Glenn, Optics Letters, **14**, 823 (1989)

[2.43] M. Born, E. Wolf, *Principles of Optics*, New York: Pergamon, eq(8), sec 8.6.1 (1987)

[2.44] A.Yariv, *Coupled-Mode Theory for guided-wave optics*, IEEE J. Quantum Electron., **QE-9**, 919 (1973)

3. Construction Of The Scanning Near-field Optical Microscope (SNOM)

3.1 Chapter Introduction

The Scanning Near-field Optical Microscope (SNOM) used to obtain the data for this PhD thesis was designed and built as part of the overall project. Although the apparatus evolved over a period of several months and included many stages of improvement, this chapter describes only the final set-up of equipment. A characterization of the operational performance of the SNOM is ongoing throughout the chapter. The chapter begins with an overview of the operation of the complete SNOM system, followed by a description of its individual components. Finally, some corresponding experimental details are given, along with relevant data.

3.2 An Outline Of The SNOM's Operation And Its Components

The design of the SNOM, which was based on an idea by K. Karrai and R. D. Grober [3.1], consisted of a high Q-factor quartz tuning-fork that was used as a mount upon which a tapered optical fibre probe with a 50-100nm tip [3.2] was positioned and glued with a slight tip overhang, as seen in Figure 3.1. The tuning-fork/probe system was forced to oscillate at its resonant frequency by a nearby piezoelectric disc, with the result that the probe acquired a dithering motion [3.3]. With the overall dither assembly mounted such that its movement in three-dimensions could be controlled by a piezoelectric translation stage, the fibre probe could be made to approach a sample, whereupon its dither would be dampened by surface forces close to the sample [3.4, 3.5]. Since the amplitude of dither, and therefore the tuning-fork induced voltage, was dependent upon the distance between the tip and sample, it could be monitored by means of feed-back electronics, in order to control the probe's height [3.6, 3.7]. By fixing the height of the tip relative to the sample, computer controlled raster scanning over its surface enabled acquisition of data relating to sample topography. In addition, connection of a photomultiplier tube to the opposite end of the probe's fibre enabled simultaneous information to be acquired about the sample's surface optical field variation, with the tip acting as a local probe of optical field intensity [3.8]. By switching off the feed-back electronics and

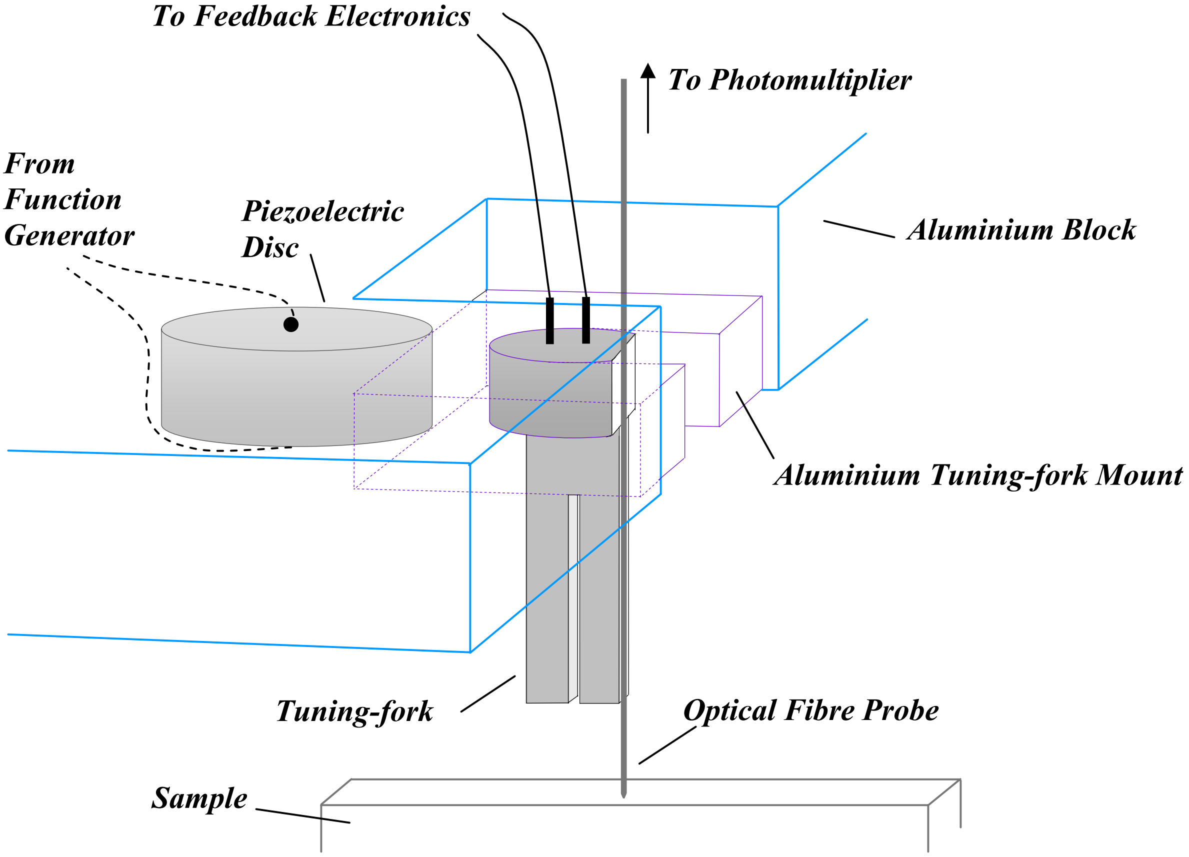

Figure 3.1: The Dither Assembly and sample. The optical fibre tip was super-glued to the quartz tuning-fork, which itself was super-glued to the aluminium tuning-fork mount. Likewise, the tuning-fork mount was attached with super-glue to the piezoelectric disc, whilst being allowed to oscillate freely within the cut away section of the aluminium block. The piezoelectric disc was fixed within the block from below. The aluminium block was bolted to an invar cantilever, which was mounted upon an xyz piezoelectric stage. See Figure 3.2 and subsequent text for more details.

moving the tip away from the sample, optical field intensity in regions of 'free-space' could be recorded at various heights above the sample [3.9, 3.10], corresponding to positions out of the range of the sample's surface forces.

Figure 3.2 shows a schematic of the complete set-up of equipment that combine to make the SNOM. All the items shown are explained in the text immediately following the figure.

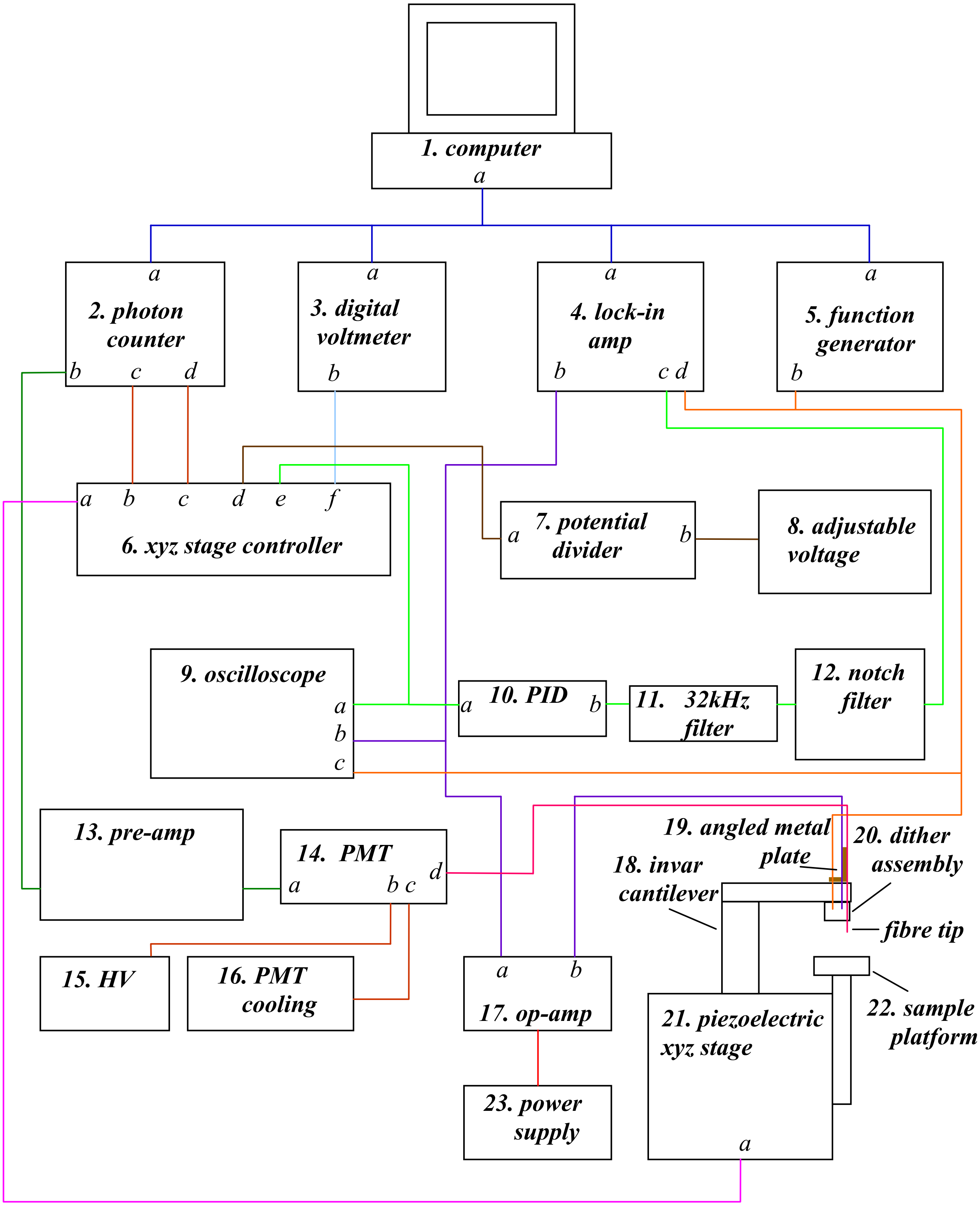

Figure 3.2: Layout and connection of the equipment that combine to make up the SNOM. Inputs and outputs represented by letters, are explained in the following text.

Description of the equipment shown in Figure 3.2.

1. Computer; Dell P60. Belkin F1D090E data switch to additional monitor, keyboard and mouse situated in adjoining office. Various computer programs to operate adjoining equipment were written in 'C' and 'C++'. Output ***a***: GPIB port.
2. Photon Counter; Stanford Research Systems SR400. Input ***a***: IEEE interface. Input ***b***: photon count from PMT, (dark count 20-30 c/s). Output ***c***: port 1, ±10V to stage controller y input (sum). Output ***d***: port 2, ±10V to stage controller x input (sum).
3. Digital Voltmeter; Keithley 196 System, serial no. 371567. Input ***a***: IEEE interface. Input ***b***: 0-10V signal from stage controller, equating to ~(0-19.7)μm z-direction movement. This instrument monitored height of the SNOM tip.
4. Lock-in Amp; Stanford Research Systems SR530, serial no. 06776. Input ***a***: IEEE interface. Input ***b***: signal from tuning-fork (A input). Output ***c***: Y component of tuning-fork signal relative to reference signal (±10V). Input ***d***: reference signal from function generator.
5. Function Generator; Stanford Research Systems DS335, 3.1MHz, serial no. 26921. Input ***a***: IEEE interface. Output ***b***: signal equating to resonant frequency of tuning-fork/tip system, 1V p-p sine wave.
6. XYZ stage controller; Melles Griot piezoelectric controller with feed-back, serial no. 500265. Terminal ***a***: xyz drive outputs 0-75V and xyz strain-gauge feed-back return. Input ***b***: y sum (+). Input ***c***: x sum (+). Input ***d***: z sum (+). Input ***e***, z diff (-). Output ***f***: z height information.
7. Potential Divider; output ***a*** potential equates to 9.1% of input ***b*** potential.
8. Adjustable Voltage; Thurlby Thandar Instruments, TSX 3510P. Manually operated z height fine positioning of tip.
9. Oscilloscope; Hitachi V-525, 50MHz. Input ***a***: channel 2. Input ***b***: channel 1. Input ***c***: external trigger.
10. PID unit; built at Southampton university physics dept, circuit diagram shown in *Appendix C*. Input = ***b***, output = ***a***. The 'D' element was not used during the project.
11. 32 kHz filter; used to reject noise from lock-in amp.
12. Notch filter; used to reject 50Hz noise.
13. Pre-amp; Stanford Research Systems SR445. PMT signal multiplication 5x.

14. Photomultiplier; Burle Industries Inc. C31034A, serial no. V23133. GaAs photocathode. Peltier cooled to -30 degrees Celsius. Quantum efficiency 20-30%. Anode = ***a***, cathode = ***b***, input ***c***: cooling power-supply, input ***d***: optical fibre from SNOM tip.
15. High Voltage; Brandenburg photomultiplier power supply. Fixed at 1500V.
16. PMT cooling power supply; Products For Research Inc. TE-104RF, serial no. 17363-90.
17. Op-amp; In order to achieve a measurable tuning-fork signal, a simple integrated circuit amplifier was mounted close to the 'dither assembly'. Input = ***b***, output = ***a***. Additional details and a circuit diagram are shown in *Appendix B*.
18. Invar cantilever; consisting of two lengths, horizontal and vertical. Designed and built during project. Technical drawing shown in *Appendix D.1*.
19. Angled metal plate; used to support the optical fibre, by means of two small magnets.
20. Dither assembly; shown in greater detail in Figure 3.1. Also shown attached to invar cantilever in drawing *Appendix D.4*. Assembly consists of an RS Components quartz tuning-fork with prongs 4mm in length and resonant frequency 32.768kHz, its cap removed and its head filed to produce a flat surface (see Figure 3.1); aluminium tuning-fork mount 6x6x2mm; piezoelectric disc 4mm diameter; aluminium block 25x15x6mm.
21. Piezoelectric xyz stage; Melles Griot, serial no. 500155. Output ***a***: communication link with controller. A drawing, and performance specification are shown in *Appendix D.3*.
22. Sample platform; Height adjustable, designed and built as part of this project. Adjustable upright support: aluminium. Horizontal platform: invar. Diagram shown in *Appendix D.2*.
23. Power supply; Instek PC-3030. 15V supply for op-amp.

3.3 Optical Fibre Probe Preparation And Attachment

The optical fibre used to create all of the SNOM probes used during the course of this project has its details shown in *Table 3.1*. The process to create a tip was fairly uniform throughout the whole project. Firstly, a ~2m length of fibre was removed from its drum whereupon it had a ~1cm length of its plastic coating stripped with either acetone or dichloromethane, towards one of its ends. After cleaning the stripped area with methanol and lens tissue, the fibre was clamped into a Sutter Instrument Company Micropipette Puller, Model No. P-2000, which was

Serial Number	YD148-01
Coating Diameter	210 μm
Cladding Diameter	125μm
Single-mode cut-off	665nm

Table 3.1: Details of the optical fibre used to create all of the SNOM probes used during this project.

factory configured for drawing optical fibres. The Puller's 10W CO_2 laser being incident on the fibre, heated the stripped section allowing it to be drawn and separated into two tips. Comprehensive details of the Sutter Puller's operation can be found in its manual [3.11]. However, there are five user-adjustable parameters that will be summarized here.

(i) HEAT (Range 0-999). This specifies the output power of the laser, and consequently the amount of energy supplied to the glass.

(ii) FILAMENT (Range 0-15). This specifies the rate at which the laser is scanned from side to side, and the length of scan. This function was not used during the project, and therefore the incident laser beam's position remained fixed.

(iii) VELOCITY (Range 0-255). With the fibre initially clamped under tension, the heat from the laser causes the clamping carriage to move as the glass melts. The 'velocity' parameter determines the speed at which the carriage should be moving when a 'hard-pull' is executed to separate the fibre. The velocity is dependent on viscosity, which in turn is dependent on the temperature of the glass.

(iv) DELAY (Range 0-255). This parameter controls the timing of the start of the 'hard-pull' mentioned above, relative to the deactivation of the laser. If DELAY < 128, then the 'hard-pull' is activated and HEAT turns off (128-DELAY)ms later. If DELAY >128, then the HEAT is turned off, and the 'hard-pull' is activated (DELAY-128)ms later.

(v) PULL (Range 0-255). This controls the force of the 'hard-pull'. A change of one unit represents a change of 4mA of current through the pull solenoid.

Although there was initially some investigation into how the shape of the SNOM tip can be changed by varying the above parameters, it was decided early on in the project to adopt the Sutter Company's recommended settings for pulling 125μm diameter fibres [3.11]. The details are shown in *Table 3.2*, along with Sutter's estimated dimensions of the resulting tip. All tips used to collect the data shown in *Chapters 3-7*, were created with these parameters.

HEAT	290
FILAMENT	0
VELOCITY	20
DELAY	126
PULL	150
Time to melt	0.15s
Tip diameter	50nm
Taper length	1.1mm

Table 3.2: Sutter Instrument Company recommended parameters for pulling 125μm diameter fibre tips, and the resulting tip dimensions. These were the parameters initialized to create all of the SNOM probes used to collect the data shown in Chapters 3-7.

The procedure described thus far for creating SNOM probes is complete for the tips used to derive the evanescent field optical data shown in *Chapters 5-7*. However, data displayed in *Chapter 4* represents 'free-space' measurements of propagating light. To maximize the resolution of these measurements (as discussed in *Chapter 2*), it was deemed necessary to coat the pulled probes in aluminium, to leave a small aperture at each tip [3.12]. An Edwards High Vacuum Coating Unit, Model 6E4 was utilized for this purpose. With the probe end of the fibre positioned vertically, and its tip pointing downwards, it was rotated within the vacuum chamber at approximately 120rpm for several seconds. Aluminium was simultaneously evaporated onto the fibre's surface from above at an angle of 45 degrees to its axis. The angled evaporation ensured that the lowest point, and therefore the end of the tip could not be coated. SEM pictures have shown aluminized tips produced in the way described here, to have a tip size of ~100nm.

The procedure to attach the prepared tip to the tuning-fork was the same for both coated and uncoated probes. Under the illumination of a Flexilux 150HL Universal Light Source and viewed through a traveling microscope, the fibre was positioned on the metal plate above the cantilever and held with a magnet, such that it was almost in contact with the tuning-fork below, yet with its tip ~2mm lower than the fork's tines. A piece of fine wire was dipped into super-glue and subsequently 'stroked' along the fibre at the position of the fork. A Prior 62345 micro-manipulator was utilized to gently push the fibre against the tuning-fork until the glue had dried. A second magnet was then placed on the fibre towards the bottom of the metal plate at a distance of ~30mm from the glued region. This had the effect of stiffening the system to increase its Q-factor to a workable level.

3.4 Shear-Force Control And Topographical Data Acquisition

The details pertaining to the acquisition of topographical data will be examined here.

3.4.1 Probe Resonance And Quality-Factor

The glue holding the tip to the tuning-fork (as described above) was left to harden for about 2 hours to allow the fork/tip system's resonant frequency and Q-factor to settle. Indeed, both qualities continued to vary marginally over the following ~24hrs, but not enough to adversely affect the SNOM's performance in the mean time. In general, the day after a tip had been glued, an increase of about 0.1% in resonant frequency and about 5.0% in the Q-factor would be recorded compared to a measurement taken 2 hours after fixing. Figure 3.3 shows typical lock-in amplifier voltages collected by computer whilst driving a tuning-fork/uncoated-tip system through resonance. The program for retrieving this data was coded in 'C'. The *r*-component, which represents a value proportional to the amplitude of tip dither, has been deduced from the *x* and *y* values at each data point. As can be seen, the resonant frequency is some distance away from the tuning-fork's independent value of 32.768kHz. This was a typical occurrence, and in general the resonant condition would take a value between the frequencies (31.9-32.4)kHz. Similarly, the Q-factor (resonant frequency/FWHM), which in this example for the *y*-component takes the value 1034, could range anywhere between 1000-1600. The result in each case was mainly a function of the amount of glue used, length of fibre attached to the fork, length of tip overhang and position of the lower magnet on the angled metal plate. The outcomes were therefore moderately unpredictable, although a reasonable Q-factor could be obtained for all experiments.

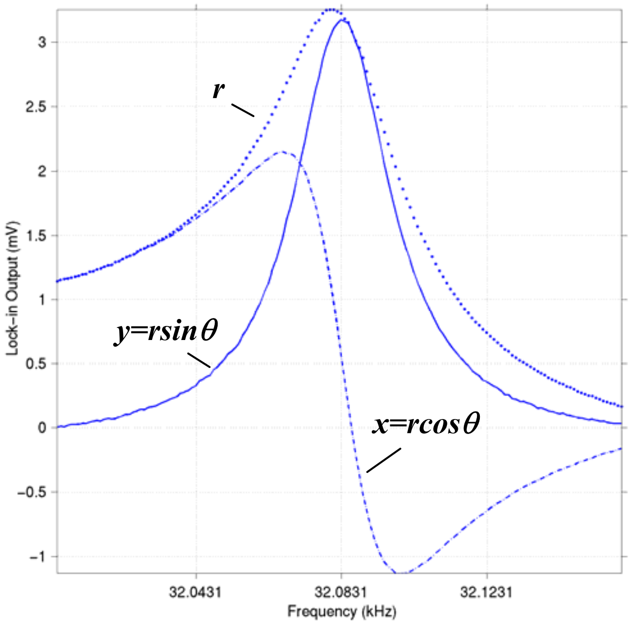

Figure 3.3: Resonance curve of a tuning-fork/uncoated-tip system, measured 2hrs after gluing. The lock-in voltage components x (dashes), y (line) and r (dots) are shown, where r represents a value proportional to the amplitude of tip dither, x=rcosθ, y=rsinθ and θ represents the phase angle between the oscillation of the tuning-fork and the reference signal. The Q-value (resonant frequency/FWHM) of the y-component shown here is 1034. The step size per data point is 1HZ.

3.4.2 Tip-Sample Approach

During all of the work in this thesis where the tip is locked to the surface of a sample, photons were counted at each data point for at least 1 second. However, for the data shown in Figure 3.3, the settling time to 1% of the tip system for the values of y-component Q-factor and resonant frequency, equates to [3.5]

$$5\tau = 5(2Q\sqrt{3}/\omega_0) \qquad (3.1)$$

$$= 89\text{ms}$$

It was therefore judged convenient to use the *y*-component voltage of the lock-in as a basis for the feed-back loop in order to position the tip relative to a sample. Figure 3.4 shows the result of holding a tip on resonance and recording the *y*-component voltage of the lock-in amplifier whilst moving the tip towards the flat, silica-clad surface of a D-fibre [3.13]. The reduction in the lock-in voltage as the tip approaches the sample is mainly caused by the reduction in tip amplitude due to its interaction with surface forces, and also to a lesser degree by a slight

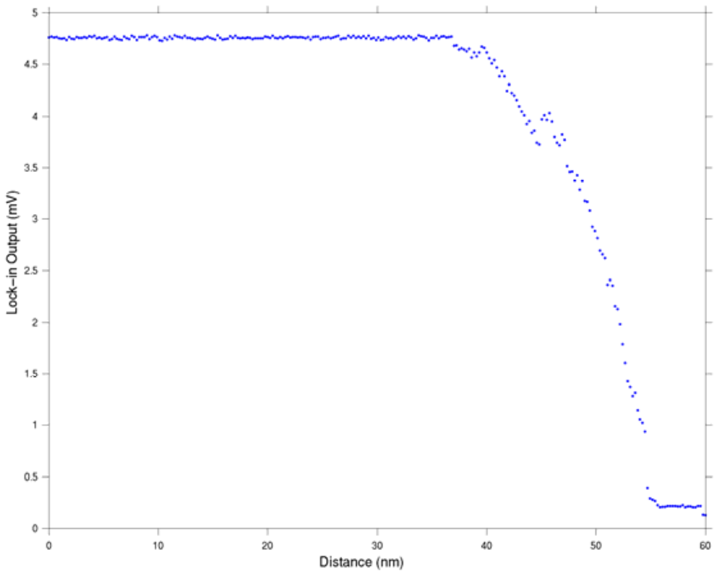

Figure 3.4: Surface 'force-curve' of an uncoated tip being lowered towards a silica sample. The y-component voltage of the lock-in amplifier is shown vs. distance of tip travel, as the tip is driven towards the sample's surface.

increase in the resonant frequency of the fork/probe system. The data was derived from a different uncoated tip from that shown in Figure 3.3. The shape of the graph however, is reasonably characteristic of all computer-controlled, thermally stable 'force-curve' measurements taken on these tips. However, no two 'force-curves' were the same. For example, it was found that an increase in the length of fibre glued to the fork, resulted in an increase in the measurable range of interaction between the tip and surface. Nevertheless, a common feature for all measured 'force-curves' was the fact that it was always difficult to determine exactly where the tip-sample contact point was as Figure 3.4 demonstrates. Over the course of this project interaction distances varied from ~20-40nm. Consequently, the positioning of the tip at about half this height resulted in scans being performed at heights varying between ~10-20nm. The forces that are believed to give rise to SNOM probe dampening, were discussed in *Chapter 2*, in addition to the theory relating to a fork/probe oscillating system.

3.4.3 Probe Positioning And Initiation Of Feed-back Electronics

In order to begin surface scanning, the feed-back loop had to be initiated. Basically, with the wiring loops as shown in Figure 3.2 in place, just four operations had to be carried out to achieve this:

(1) The tip was fine-positioned by using the Thurlby voltage source such that the lock-in *y*-component amplitude was reduced by half.
(2) The *y*-component amplitude was 'zeroed' by pushing the lock-in amp 'offset' button.
(3) The 'Proportional' element of the PID unit was initialized.
(4) The 'Integral' element of the PID unit was initialized.

A typical lock-in output variation of ~0.25mV/nm in response to tip movement relative to the position of the sample, can be compared to an input variation of ~0.51mV/nm for the *z*-height-positioning of the piezoelectric controller. However, the *y*-component BNC output used for the feed-back was amplified to a full scale of ±10V. Therefore the PID unit would typically receive an input of ~100mV/nm in response to tip movement relative to the sample surface. With the 'Proportional' dial set to zero ~(1:1 gain) and the 'Differential' disengaged, the 'Integral' function was found to have a gain of $1.931\mathrm{s}^{-1}$ with its dial also fixed on its minimum setting. The lowest setting on both the 'P' and 'I' sections of the unit was therefore found to be adequate to ensure that its response met the requirements of the speed of the system. However, in general, the 'P' control was optimized for each particular tip by trial and error, but as a rule did not exceed 1/10 of its full scale. The 'I' dial was always set to its minimum. The 'D' function was not utilized during this project. In order to smooth the output channel of the lock-in amp, a time constant of 300ms was engaged.

3.4.4 Calibration Of The Piezoelectric Stage

A regular occurrence during this project was a full calibration of the xyz piezoelectric stage, with reference to the voltages used to drive the stage and record its movement. This was done by scanning a tip along a Dasaw Pty Ltd. precision diffraction grating by holding it at 45 degrees to the horizontal, and measuring its topographical period. Both x and y directions were individually checked whilst monitoring the z-displacement. An engineered glass block with its upper face inclined at the required angle was used to position the grating under the SNOM tip. The period of the grating and the angle of incline of the glass block, were checked to a high level of accuracy (±0.1%) by HeNe (632.8nm) laser diffraction and reflection respectively.

3.4.5 Stability, Repeatability And Resolution Of Acquired Topographical Data

In order to investigate the stability and repeatability of any acquired height data, a one-dimensional line-scan was performed upon a well-characterized phase diffraction grating (QPS Technology Inc. phase-mask). The computer program for achieving this was coded in ‘C’. The data can be observed in Figure 3.5(a). The grating had evenly spaced rectangular elevations 568nm apart, and therefore overall period 1136nm. The height of each elevation was calculated to be 244nm from *Equation (4.1)*. The actual scan is over a length 19.425µm with 1025 data points, in a direction perpendicular to the grating’s rulings. Figure 3.5(b) shows a repeat run, carried out on immediate completion of the data acquisition for Figure 3.5(a). Figure 3.5(c) shows the two data sets again to enable a comparison to be made. As can be seen, there is good repeatability between the two scans, although one is laterally offset relative to the other by up to 35nm, due to thermal drift. Recorded scan lengths that exceed expected values by about 0.1% confirm the drift.

Throughout this thesis, thermal drift does not generally exceed an overall range of 40nm for the duration of any given run except for a few examples, where thermal stability had not been maximized. Indeed, before the scans shown in Figure 3.5 were performed, the SNOM’s thermal isolation was developed such that its piezoelectric stage and immediate attachments were enclosed within a polystyrene box having walls ~110mm thick, in order to smooth thermal fluctuations. Additionally, the SNOM laboratory was isolated for some time before data

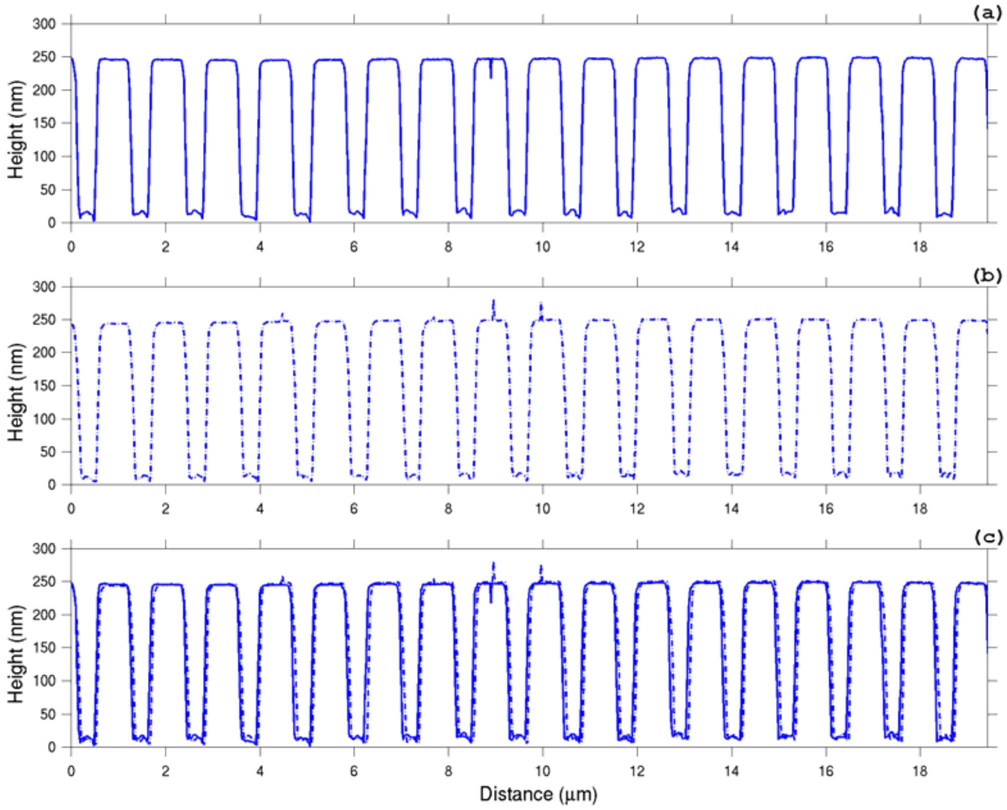

Figure 3.5: (a) A line scan across the rulings of a 'phase-mask' using an aluminized tip. The length of the scan is 19.425µm and has 1025 data points. The rest time at each position is 1 second, and the period of the mask is 1136nm. (b) Repeat of the scan shown in (a). (c) Comparison of the scans shown in (a) and (b).

acquisition commenced, with its operation controlled from an external computer to assure that the acquired stability was maintained. Nevertheless, these measures did not preclude the consequence of building vibration on obtained data, as Figures 3.5(a) & (b) clearly demonstrate, at around the 9µm position. However, vibration was never really a serious problem and therefore no additional steps were taken to eradicate its effect. Further inspection of the data shown in Figure 3.5 shows the rectangular profile of the phase-mask to be far from what is expected. This is due to the way that the tapered SNOM probe negotiates 90-degree corners and vertical drops. It is unclear whether or not the tip's shape has also affected its interpretation of the regions at the bottom of the grating's elevations, which appear not to be level. It may be possible that in these areas, trapped surface contaminants exist [3.14].

In order to acquire more detailed information about the resolution capability of the SNOM in its measurement of topography, a polished silica sample was scanned with the result shown in Figure 3.7. A 7.4µm length of the sample was mapped twice, with 58nm steps in between data points. The figure shows there to be thermal drift in the +ve *z*-direction between the first (blue) and second (red) data sets. Of course drift in this direction has less significance than in the *x* & *y* directions because the tip will always hold its position relative to the surface. Surface features that are about 1nm in height have been reproduced in both sets of data.

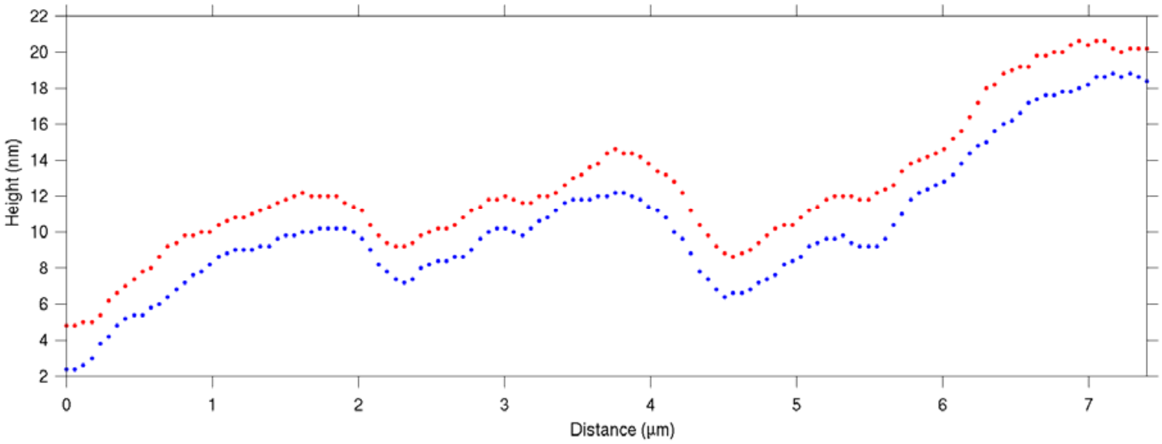

Figure 3.7: Repeat topographical measurement of a silica sample. The blue data was acquired prior to the red data. The steps between points are 58nm, and the total length of the scan is 7.4µm. The y-axis has been set to an arbitrary position and therefore shows relative height.

3.4.6 Probe Position Error Signal

During the acquisition of the height data shown in Figure 3.5(a), the corresponding error signal in the tip's position relative to the sample surface was also measured. By recording the value of the *y*-component lock-in output at each position lastly in the data-taking sequence, a measurement of the fluctuation in the system was gained well after its settling time. The result can be observed in Figure 3.6, where the vertical axis has been scaled such that it corresponds to ±0.5nm tip movement. As can be seen, with a tip-sample distance of ~10nm, the stability of the *z*-positioning of the probe is within ±3%.

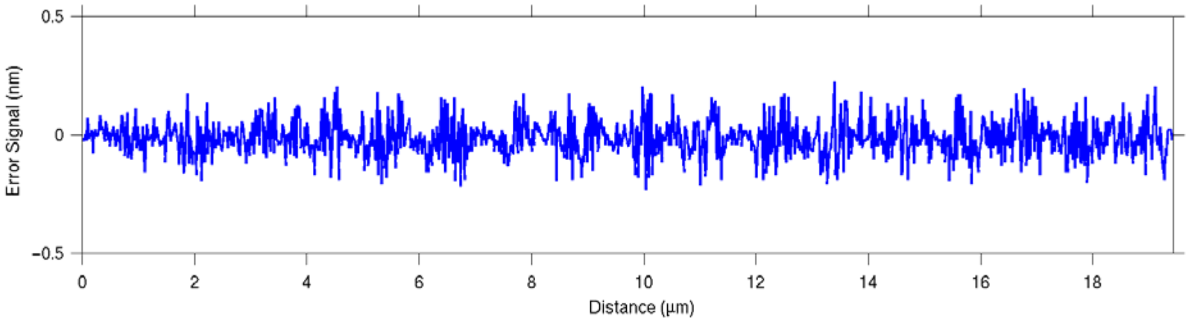

Figure 3.6: The error in the tip position relative to the sample surface. This data was derived simultaneously to the scan shown in Figure 3.5(a). The scan length is 19.425µm and there are 1025 data points. The rest time at each position was 1 second and the error signal was acquired last in the data acquisition sequence.

3.5 Optical Data Acquisition

The aspects relating to the collection of SNOM optical data will be presented in this section. However, theoretical details relating to the tip's measurement of incident light were covered during *Chapter 2*, and will not be described again here.

3.5.1 Repeatability Of Acquired Optical Data

The repeat topographical measurements shown in Figure 3.5 of a transmission phase grating were taken simultaneously to sets of optical data, which are shown in Figure 3.8. With a laser incident on the grating from below, the light collected by the aluminized tip as it followed the

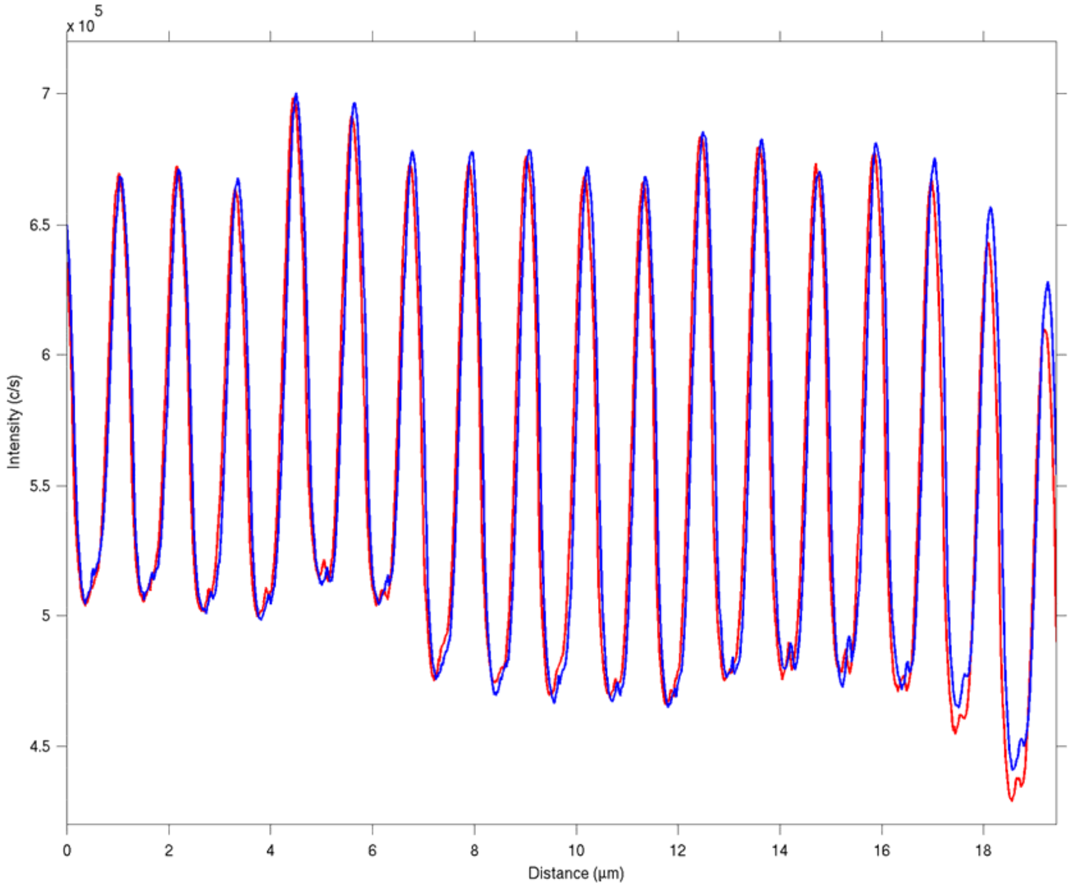

Figure 3.8: Repeat optical data acquired simultaneously to the topographical data of the phase-mask shown in Figure 3.5. The red data set relates to Figure 3.5(a) whilst the blue data set corresponds to that shown in Figure 3.5(b). The length of the scan is 19.425µm, with 1025 data points. The tip was aluminized for these measurements.

contours above the grating was detected by the photo-multiplier, and recorded by the computer via the photon counter. The measurements are interesting because they are a convolution of both evanescent and propagating light. As in the case of their related topographical data sets, they also function well as repeatability tests. As before, the thermal drift between scans can be clearly seen although in general, the data sets are very similar. However, a close inspection reveals the data to reproduce itself within statistical uncertainty (i.e. within the uncertainty given by the Poisson probability distribution, $\pm[c/s]^{1/2}$), only up to about the 3µm position. A comparison of the latter part of the scans shows them to increasingly differ, with the 'blue data' acquiring a higher count than the ‘red data’. It seems unlikely that the repeatability of this data would vary along its length, and therefore the effect is probably due to either the laser power increasing over time (each scan took about 20 minutes to complete), or increased aperture size due to loss of part of the tip’s aluminium coating.

Another example of repeated data is given in *Chapter 5*, Figure 5.9, where a similar length of optical data is entirely reproducible within statistical uncertainty. Interestingly, there seems to be a disturbance in the optical data of Figure 3.8 at the regions of lowest intensity. These positions correspond to the lowest part of the grating’s elevations where the associated topographical data was also uneven. The phenomenon adds weight to the suggestion that there may be contaminants trapped within these gaps.

3.5.2 Effect Of Thermal Drift On Long-Duration, Two-dimensional Scans

A section of the optical fibre described in Table 3.1 was cleaved at both ends during an earlier stage of this project and a HeNe laser (λ=632.8) was launched into one end, via a 10x objective. Both the objective and the fibre were supported upon a Martock translation stage. The opposite end of the fibre was positioned vertically upon a metal block, directly below an aluminized SNOM tip, and held in place with a magnet. A two-dimensional image was then collected with the SNOM probe locked to the fibre’s cleaved surface, and this is shown in Figure 3.9(a). The computer data-acquisition program for this type of scan was coded in ‘C++’. The result shows substantial thermal drift, which is elucidated by its associated contour map shown in Figure 3.9(b). However, the measured profile does indicate single-mode propagation of the light, although the wavelength is slightly below the single-mode cut-off of the fibre, which is 665nm. The image was collected with less substantial SNOM polystyrene casing than that described above in *Section 3.4*, and without laboratory isolation. It is shown here in order to demonstrate significant improvement to the system, by its comparison to a similar image that utilizes a length of identical optical fibre, and that can be seen in Figure 3.9(c). The latter image was derived with the final polystyrene casing described above in place, and with laboratory isolation for the duration of the data collection. The laser wavelength used here was 780nm and therefore this time, was definitely single-mode. Although the image only represents about 27% of the area actually scanned in this case, it is clear that there is enhanced stability,

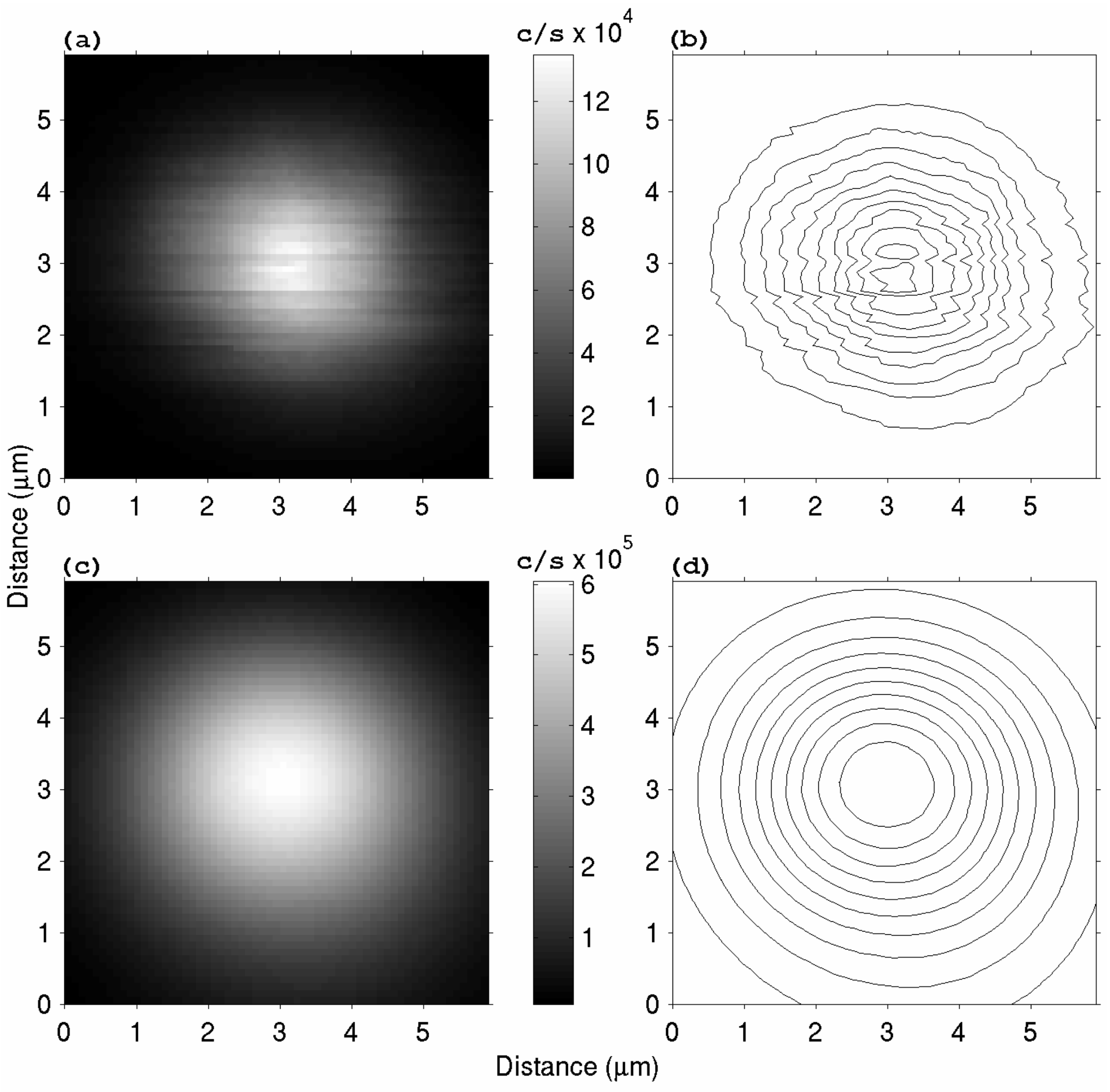

Figure 3.9: Two-dimensional, 1s per point, images of laser light exiting an identical optical fibre. (a) 6x6μm, 71x71 pixels, λ=632.8nm. (b) A contour map corresponding to the data shown in (a). (c) 6x6μm, 62x62 pixels, λ=780nm. (d) A contour map relating to the data shown in (c). Only ~27% of the area of the complete scan presented in (c) is shown. The images were acquired at different stages of the SNOM's construction. They are presented here in order to demonstrate significant improvement to the thermal stability of the system during the ongoing development of the apparatus.

compared to the data shown in Figure 3.9(a). However, the associated contour map of the data given in Figure 3.9(d) shows a distortion of the modal shape, representing an overall shift of several hundred nanometres. This is caused again by thermal drift. The image was one of the first acquired with the final set-up of equipment described in this chapter. It was therefore recorded before any of the data presented in subsequent chapters was taken, and in fact before the data shown in Figures 3.4-3.8. Although the laboratory was isolated during the scan as in the case of most other data shown in this thesis, the image was nevertheless produced without the lab having been left for a period of time beforehand. As more measurements were made throughout this project, it was found that the laboratory sometimes required up to 24 hours of isolation in order to achieve maximum thermal stability.

3.5.3 Mathematical Fit Of A Measured Single Mode Profile

It is unlikely that the thermal drift observed in Figure 3.9(c) had a significant affect on each individual line of data that made up the overall image. A close inspection of the figure shows the drift to be mostly in the y-direction, occurring over ~4.5 hours. The SNOM probe however, scanned in lines across the x-direction, each taking only 2 minutes to complete. A final test of the overall stability of the SNOM system and indeed the photomultiplier linearity, could therefore be performed with a mathematical fit of the single-mode profile shown in Figure 3.9(c), by using the line of data passing through the mode profile’s centre, having a total length of 11.75μm.

In the case of a true step-index optical fibre, the near-field mode profile should take the form of Bessel functions [3.15]. However, it was found that the chosen profile could be fitted more accurately to a Gaussian function. This has also been established by D.J. Butler et al during experiments under similar conditions, where it was speculated that the apparent inconsistency could be ascribed to a non-ideal fibre refractive index profile [3.16]. The Gaussian fit of the chosen mode profile can be observed in Figure 3.10(a), with the residual values (actual data – fitted data) plotted in Figure 3.10(b). As can be seen in Figure 3.10(a), there is a good correlation between experimental data and theory, which serves to confirm the accuracy and stability of the SNOM system. However, an inspection of the residual values plotted in Figure

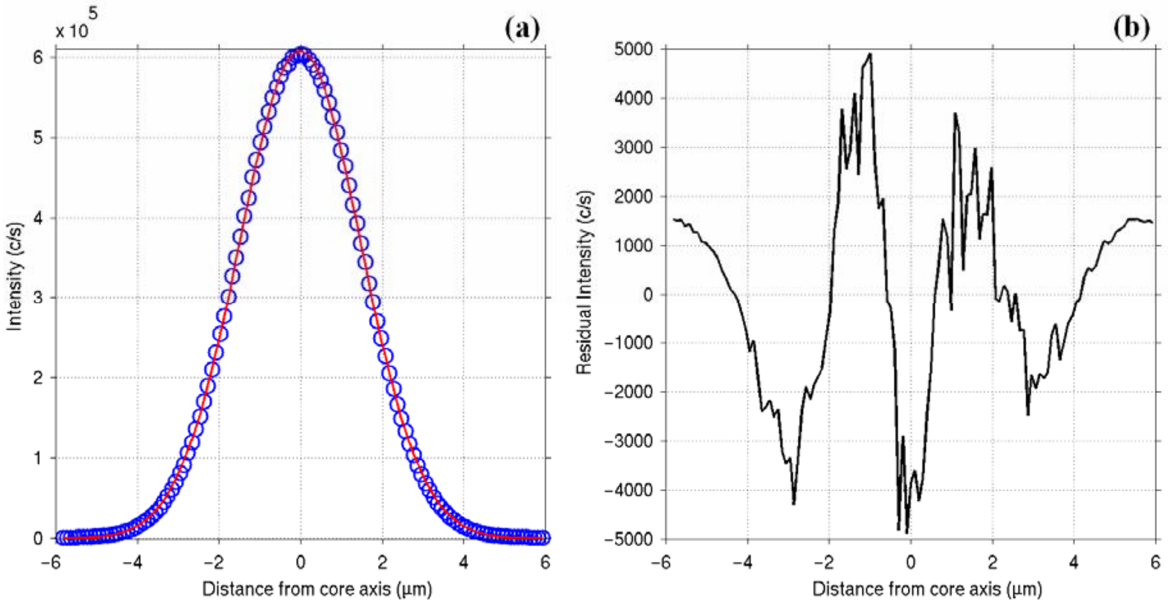

Figure 3.10: (a) A Gaussian mathematical fit of a line of data taken from across the centre of the mode profile shown in Figure 3.9(c), incorporating the data point of greatest intensity. The length of this full line of data is 11.75µm with 120 data points. (b) A plot of the residual values of the data shown in (a), calculated by subtracting the fitted data from the actual data.

3.10(b), indicates that there are some anomalies in the relationship between the measured data and the Gaussian function. The anomalies are interesting because of their symmetry, which is centred upon the axis of the fibre. Across the core region itself which has radius ~2.1µm, the curve resembles a typical refractive index profile of a Ge doped fibre. The index profile may therefore be the direct cause of these particular anomalies. The parameters of the fit are summarized below:

$$y0 = -997.11266 \pm 333.27868$$
$$xc = -0.06395 \pm 0.00141$$
$$w = 2.97164 \pm 0.00364$$
$$A = 2268094.34307 \pm 3224.74256$$

where $$y = y0 + \frac{A}{w\sqrt{\frac{\pi}{2}}} \exp\left[-2\left(\frac{x - xc}{w}\right)^2\right] \tag{3.2}$$

3.6 Chapter Summary

A Scanning Near-field Optical Microscope (SNOM) has been designed, constructed and tested in order to enable the acquisition of the data presented in this PhD thesis, *Chapters 4-7*. Its operation is based upon a tuning-fork/fibre-tip oscillating system [3.1], with an incorporated negative feed-back loop, to allow distance regulation. The set-up is such that both optical and topographical information beyond the diffraction limit [3.8], can be simultaneously acquired during the imaging of samples.

Initial tests on the system have shown that the SNOM tip can be locked to a sample's surface and held in position with a stability of ±3% of the tip's height, relative to the sample. However, it was found that fluctuations in this positioning can be induced by building vibration. Nevertheless, these effects were never deemed serious enough to require special vibration-isolation measures to be taken. Indeed, during the development of the SNOM it became apparent that the greatest noise affecting the system was in fact thermally induced. Steps were therefore taken to overcome this problem by recognizing the need for both thermal isolation of the SNOM from its laboratory, and also the isolation of the laboratory itself. Subsequent chapters will confirm the best achievable thermal stability for the system to be ±20nm over the duration of any scan. Repeatability tests were performed on both topographical and optical data during this chapter to confirm that measurements were reproducible. The output from a single-mode optical fibre was also measured and its result fitted to a mathematical function in order to further confirm the SNOM's overall accuracy and stability.

The discussion of the SNOM's performance continues throughout this thesis, as further data is obtained and analyzed.

3.7 References

[3.1] K. Karrai, R.D. Grober, Applied Physics Letters, **66** (14), 1842 (1995)
[3.2] G.A. Valaskovic, M. Holton, G.H. Morrison, Applied Optics, **34** (7), 1215 (1995)
[3.3] F.F. Froehlich, T.D. Milster, Applied Physics Letters, **70** (12), 1500 (1997)
[3.4] C. Durkan, I.V. Shvets, J. Appl. Phys, **79** (3), 1219 (1996)
[3.5] W.A. Atia, C.C. Davis, Applied Physics Letters, **70** (4), 405 (1997)

[3.6] R.D Grober, J. Schuck, D. Hessman, P.J. Kindlemann, J. Hespanha, A.S. Morse, Review of Scientific Instruments, **71** (7), 2776 (2000)

[3.7] K.B. Shelimov, D.N. Davydov, M. Moskovits, Review of Scientific Instruments, **71** (2), 437 (2000)

[3.8] D. Courjon, C.Bainier, Rep. Prog. Phys. **57**, 989 (1994)

[3.9] R. Toledo-Crow, J.K. Rogers, F. Seiferth, M. Vaez-Iravani, Ultramicroscopy, **57**, 293 (1995)

[3.10] B. Hecht, H. Bielefeldt, Y.Inouye, D.W.Pohl, L.Novotny, J. Appl. Phys, **81** (6), 2492 (1997)

[3.11] Sutter Instrument Company Operational Manual, P-2000 Micropipette Puller, rev. 1.0/060297

[3.12] C.W. Hollars, R.C. Dunn, Review of Scientific Instruments, **69** (4), 1747 (1998)

[3.13] S.T. Huntington, K.A. Nugent, A. Roberts, J. Appl. Phys., **82** (2), 510 (1997)

[3.14] S. Davy, M. Spajar, D. Courjon, Applied Physics Letters, **73** (18), 2594 (1998)

[3.15] A. Rogers, *Essentials of Optoelectronics: With Applications,* Chapman & Hall, 273-277, (1997)

[3.16] D.J. Butler, K.A. Nugent, A. Roberts, J. Appl. Phys., **75** (6), 2753 (1994)

4. Imaging Of Phase-Mask Diffraction Patterns Used To Manufacture Fibre Bragg Gratings

4.1 Chapter Introduction

A fibre Bragg grating is formed by exposing an optical fibre having either a Ge doped, or a Ge/B co-doped photosensitive core, to periodic interference fringes of UV light [4.1]. This induces a modulation of period Λ into the refractive index along a length of its core, which then performs as a wavelength selective mirror. In early experiments the periodic pattern of UV light was created by two-beam interference [4.2], but in recent years the use of a transmission phase diffraction grating, known as a phase-mask, has become a more widely used technique [4.3]. The phase-mask is designed such that for a particular wavelength, the depth d of the mask shown in Figure 4.1 causes a π phase lag to occur for light passing between the rectangular elevations relative to light passing through the elevations. Under this condition, d is given by [4.4]

$$d = \lambda_{UV}/[2(n_{PM}-1)] \tag{4.1}$$

where λ_{UV} is the wavelength of the incident UV light and n_{PM} is the refractive index of the phase-mask. The collective effect across the mask is an induced nulling of the zeroth diffraction order, which in turn creates a more effective writing pattern above the mask [4.5].

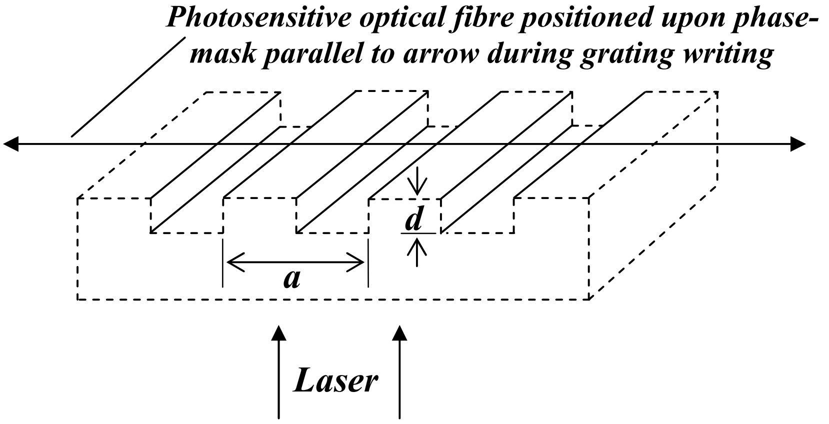

Figure 4.1: A section of a phase-mask and its position relative to an optical fibre and incident laser during the writing of a fibre Bragg grating.

The period of the modulating refractive index written into the fibre equates to the geometry of the phase-mask such that $2\Lambda = a$**,** the period of the mask.

4.2 Introduction To The Talbot Length

In 1836, H. Talbot recorded his observations of the pattern produced close to a phase diffraction grating [4.18]. The pattern is interesting because under certain conditions, it replicates the shape of the diffraction grating, at periodic distances from its surface. Lord Rayleigh first quantified the repeat length of the pattern, known as the Talbot length, in 1881 [4.19].

This section will show how Rayleigh's expression for the Talbot length can be derived. It will then explain how Rayleigh's expression becomes an approximation in situations where there are a small number of diffraction orders, as in the case of the creation of fibre Bragg gratings by phase-mask. Finally, a modified expression, developed during the course of this work will be presented. The new expression gives a more accurate result than the Rayleigh approximation (as will be confirmed in the experimental sections of this chapter), when calculating Talbot lengths, where few diffraction orders are present.

A phase-mask is a one-dimensional grating and thus the theory describing the Talbot length associated with a phase-mask can be treated one-dimensionally. The scalar field above an infinite grating with period a, positioned in the horizontal plane $z = 0$ can be described by the Fourier series [4.6]

$$E(x,z) = \sum_m C_m \exp(2\pi imx/a)\exp(ik_m z) \quad \text{where} \quad k_m = 2\pi(1/\lambda^2 - m^2/a^2)^{1/2} \tag{4.2}$$

Here, λ is the wavelength of the incident light and m is an integer. In the case of $\lambda << a$, as in Rayleigh's experiments, k_m can be binomially expanded to give

$$k_m z \approx 2\pi z/\lambda - 2\pi m^2(\lambda z/2a^2) \tag{4.3}$$

Since m^2 is also an integer, there is a particular distance

$$Z_T = 2a^2/\lambda \tag{4.4}$$

where all of the Fourier components have the same phase with respect to one another as they do at $z = 0$. Equation (4.4) is therefore Rayleigh's expression for the Talbot length. Under this particular condition, where a large number of diffraction orders are present, an image of the original grating can be replicated at Z_T, and indeed at integer multiples of Z_T [4.7]. However, under the conditions of the experiments in this chapter, the Talbot pattern does not reproduce the pattern of the original grating since $\lambda \sim a$ and therefore the number of diffraction orders is small. Here, and similarly in the production of fibre Bragg gratings, each diffraction order becomes important and has associated with it a characteristic repeating pattern relating to its interaction with each and every other diffraction order.

To illustrate this, Equation (4.2) can usefully be rewritten in analogy with x-ray diffraction theory [4.8] by substituting $k=2\pi/\lambda$ and $G=2\pi/a$ to give

$$E(x,z) = \sum_m C_m \exp(imGx)\exp(ik_m z), \quad \text{where} \quad k_m = (k^2 - m^2G^2)^{1/2} \tag{4.5}$$

Here, k is the wave-vector of the incident light and G is the unit 'reciprocal lattice vector' of the diffraction grating. The Ewald construction shown in Figure 4.2 portrays a condition whereby only two diffraction orders (Fourier components) are present. It demonstrates how a particular Talbot length pertaining to the interaction between two chosen diffraction orders is derived from the difference in magnitude of their wave-vector components in the direction perpendicular to the phase-mask.

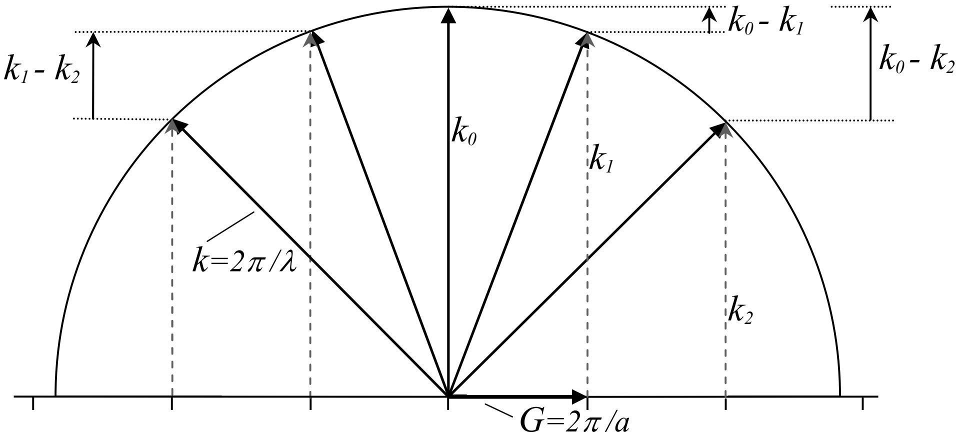

Figure 4.2: The Ewald Construction relating to the diffracting orders of a phase-mask. The modified expression for the Talbot length given as Equation 4.6 and resulting from the beating between pairs of wave-vectors, is deduced from the difference in the associated wave-vector components as indicated here.

An expression describing the Talbot length associated with the beating of two individual orders should therefore replace Rayleigh's approximation expression for the Talbot length, Equation (4.4). The new expression is given by

$$Z_T = \frac{2\pi}{(k^2 - m^2G^2)^{1/2} - (k^2 - n^2G^2)^{1/2}}$$

$$= 2\pi / (k_m - k_n) \tag{4.6}$$

where m and n are integers representing diffraction orders and Z_T is the Talbot length of a repeating pattern resulting from the interaction between two chosen orders. The greatest repeat length is for $m = 0$ and $n = 1$. Typically, during the manufacture of fibre Bragg gratings at telecom wavelengths there can be up to four diffracting orders present, which may cause complex and detailed patterns to develop above the phase-mask. These complex patterns may undergo regions of change as distance from the phase-mask increases, because the spreading diffracted beams have finite width and therefore limited interaction in the z-direction.

4.3 Diffraction Pattern Simulations

The free-space diffraction patterns measured and presented later in this chapter are compared to simulations during the course of their analysis. Two very different simulations are used for this purpose, which enable different variable parameters to be explored. The simulations will be referred to as 'Simulations no.1 and 2', and their parameters are outlined here as a reference. As will be demonstrated in Figures 4.4(b) and 4.9(a), the two methods are able to give very similar results.

4.3.1 Simulation no. 1

This is a numerical simulation, based upon Fresnel-Kirchoff diffraction theory and coded in C++. The experimental parameters that can be input before summing over grating elements are as follows:

(i) The period a, length and width of the grating

(ii) The single wavelength of the incident light

(iii) The phase variation of light across the grating elements given by the depth of its rectangular, uniformly distributed elevations, with width $a/2$

(iv) The FWHM of the normally incident, Gaussian beam

From the above parameters, it can be seen that the amplitude of the incident beam varies across the grating. However, the phase across the incident beam is simulated to be uniform before its interaction with the grating, in order to reproduce focusing of the beam onto the grating's surface.

4.3.2 Simulation no. 2

This simulation is based on theoretical work carried out by P.E. Dyer et al [4.5]. It is an analytical simulation incorporating the superposition of diffracted, infinite plane waves, excluding evanescent components. It was coded in Matlab, and includes the following variable parameters:

(i) The facility to emulate focusing of the incident beam
(ii) A finite line width of the incident beam as opposed to a single frequency
(iii) A power distribution across the diffracted orders
(iv) The number of orders up to three, plus the zeroth
(v) The grating period

This simulation was designed for the application of the analysis of fibre Bragg grating creation by excimer laser [4.5]. It is therefore able to account for the non-correctable divergence of this type of laser, by facilitating variable focusing.

4.4 Introduction To The Experimental Work

In the production of fibre Bragg gratings, the field variation of interest is in a plane perpendicular to both the phase-mask surface and its etched rulings. This is the plane within which an optical fibre is positioned parallel to the mask surface (as shown in Figure 4.1), in order to bring about the periodic refractive index modulation along its core. It is also the plane within which the probe in these experiments was positioned and scanned to acquire the presented data. The scans are in a two-dimensional form, and represent a cross-section of a uniform pattern (limited by the width of the incident laser beam) that continues along the phase-mask rulings and therefore across the core of a potential fibre Bragg grating.

A QPS Technology Inc. phase-mask having evenly spaced rectangular elevations 500nm wide and overall period $a = 1\mu m$, was used in all of the experiments in this chapter. In every example it was positioned horizontally to allow laser light to pass through from below and emerge at the phase-mask rulings above. The particular mask was designed to cause a π phase shift, and therefore a nulled zeroth diffraction order, for incident light at 365nm. At this wavelength, the proportion of incident power diffracted at zeroth and first order was specified by the manufacturer as 2.5% and 37.5% (per beam) respectively. The mask was manufactured with an E-beam system that incorporated a translation stage, which continuously moved as opposed to a 'step and write' system [4.9]. This prevented stitching errors from occurring in the ensuing photo-resist pattern. With a dry etching technique the pattern was transferred into a metal layer, which in turn was used to etch the fused silica substrate. Some of these details in addition to other properties of the phase-mask are summarized in *Table 4.1*.

Phase-mask period, *a*	1 micron
Diffraction order incident power distribution	At 365nm: zeroth order 2.5% first order 37.5%
Substrate Material	Fused silica
Optical Properties	Transmission at 365nm: 92% Refractive index at 365nm: 1.4745 Refractive index at 780nm 1.4537
Thermal coefficient of expansion	$5\text{x}10^{-7}$/C
Young's Modulus	7450kg/mm^2

Table 4.1: Properties of the QPS Technology Inc. phase-mask used in all of the experiments in this chapter.

An aluminized probe with a small (50-100nm) aperture at its tip was used during these experiments. Its method of preparation is described in *Chapter 3*. Since the tip was not locked to the sample surface, scans ran at typically quicker than normal speeds, ranging from 0.125 - 0.25 seconds per point, without fear of damage to the probe. Although the experiments involved scanning free-space fields, it was still necessary however to utilise the tuning-fork assembly [4.10] (also described in *Chapter 3*) to which the probe was fixed. This allowed shear forces to be detected close to the phase-mask, to enable the probe's height to be regularly checked by reference to a specific point. In all cases in this chapter, a given height above the phase-mask refers to the distance above a high elevation on the phase-mask. The photo-multiplier connected to the opposite end of the probe's 1.5 metre fibre meant that it was possible to collect detailed information in all three dimensions about the free-space optical field variation, with the aluminized tip acting as a local probe of optical field intensity [4.11]. The thermal insulation of the experimental apparatus provided stability of the tip's free-space position to within ±20nm on all three axes for the duration of all scans presented in this chapter.

4.5 Experiment And Results

The experiments and results that follow have been divided into two sections. *Section* 4.5.1 shows free-space interference patterns associated with a phase shift imposed by the phase-mask on the incident laser beam of 1.41 radians. For this phase shift, there is a significant contribution to the patterns from the zeroth diffraction order. *Section* 4.5.2 presents the particular case of a π radian phase shift, which causes the zeroth diffraction order to be suppressed. This is the normal condition used for fibre Bragg grating writing, and produces very different diffraction patterns compared to the general case.

4.5.1 Including Zeroth Order – 1.41 Radian Phase Shift

The output of a New Focus Inc. 6100 single frequency External Cavity Tunable Diode Laser with tunable range 772.2-788.7nm and maximum power 5mW, was allowed to pass through a 1.5cm diameter hole cut into the thermal housing surrounding the SNOM, whereupon it was aligned with mirrors and focused onto the phase-mask rulings using a long (10cm) focal length lens, mounted upon a Martock Design Ltd. translation stage. An Anritsu Corporation Optical Spectrum Analyzer MS9001A with a resolution of 0.1nm was utilized to select a laser

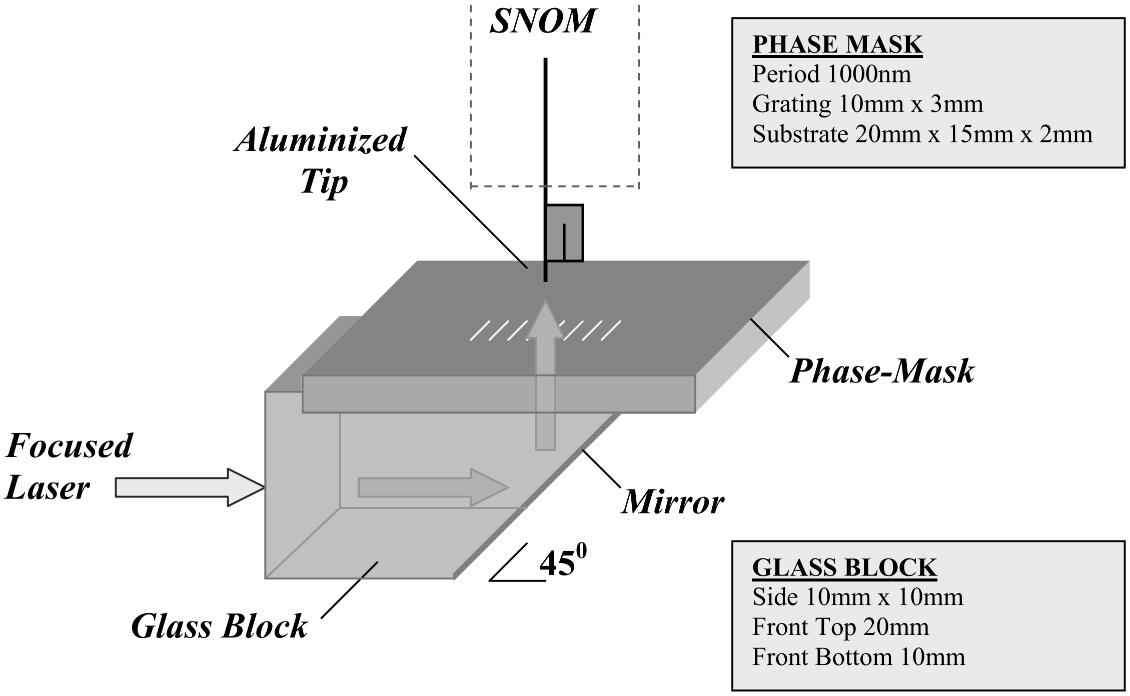

Figure 4.3: Free-space data collection. After alignment and focusing, the laser was reflected at 90 degrees within the glass block before passing through the phase-mask to emerge at its rulings. The aluminized tip scanned a vertical plane above the phase-mask, which in turn rested unfixed upon the glass block.

wavelength of 780.0nm. After passing through the glass block shown in Figure 4.3, and being reflected internally from its mirrored surface, the beam passed through the phase-mask to become normally incident upon the mask rulings with a polarization direction perpendicular to the rulings. The beam size, measured beforehand with the SNOM probe at the position of the phase-mask rulings with the mask removed, had a width of 106μm FWHM. With a mask period of 1μm, the setup generated only the zeroth and first orders of diffraction, constituting 61% and 15% (per beam) respectively, of the incident power.

A typical two-dimensional scan of the phase-mask interference pattern taken directly above the centre of the laser beam is shown in Figure 4.4(a). With a pixel size of 100nm, the scan height above the phase-mask ran from 5-10μm with a lateral width of 5μm. In this general case, a nonsuppression of the zeroth diffraction order has resulted in significant modulation between the first and strong zeroth orders in the direction normal to the phase-mask. A horizontal cross-section through any row of maxima would result in a period of intensity modulation matching the period of the phase-mask, *a*. This is pictorial evidence of what is understood to be the cause of Type II damage gratings where a critical level of absorbed energy induces damage tracks

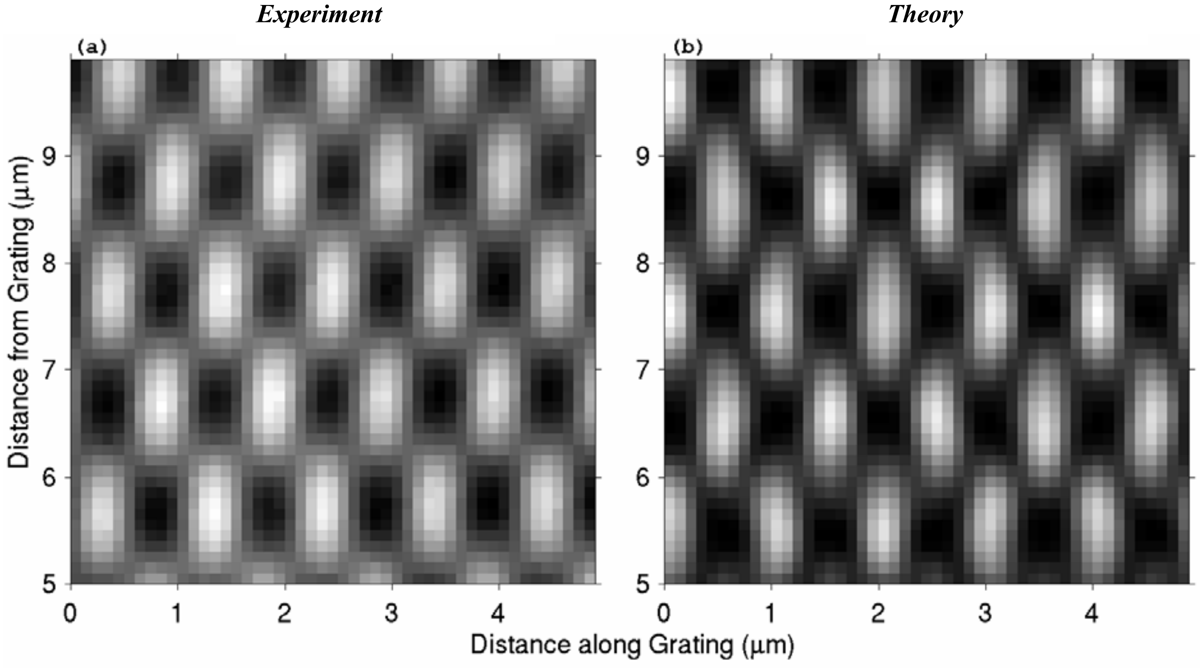

Figure 4.4: The Talbot diffraction pattern from a 1µm period phase-mask with a phase shift of 1.41 radians. The images are generated by a strong zeroth diffraction order and first order. Both diagrams show a 5µm x 5µm area in space, starting at a height of 5µm above the mask. The phase-mask is along the bottom of the picture in each case, and the propagation direction of the light is up the page. (a) shows the experimentally-measured data. The centres of the high elevations on the phase-mask are positioned directly below the centres of the lowest full row of maxima. (b) shows a numerical calculation of the expected field distribution using scalar Fresnel-Kirchoff diffraction theory (Simulation no.1). In both diagrams, the pattern repeat distance is 2.08µm, which matches the calculated value using the new expression, Equation (4.6).

with period *a* on one side only of the photosensitive core [4.12, 4.5]. The size, polarization and focusing of the laser beam onto the phase-mask replicate the conditions used in writing fibre Bragg gratings with frequency doubled argon ion lasers, with reduced zeroth order [4.13]. In Figure 4.4(a), the characteristic repetition of the Talbot pattern as a function of distance from the grating has an experimentally measured Talbot length of 2.08±0.03μm. A calculation of the Talbot length for our experimental parameters using the new expression, Equation (4.6) with m=0 and n=1 gives Z_T=2.08μm, in good agreement. This is significantly different from the value of 2.56μm calculated from Rayleigh's approximate expression, Equation (4.4), confirming the importance of the original theoretical expression in Equation (4.6), developed during the course of this work.

The observed Talbot diffraction pattern shown in Figure 4.4(a) can be predicted theoretically with either analytical or numerical simulations. Figure 4.4(b) shows the results of a numerical simulation of the pattern expected for the particular wavelength, FWHM of the beam and phase-mask period shown in Figure 4.4(a), using Simulation no.1. There is clearly a very close resemblance between the patterns displayed in these two figures, confirming the accuracy of the theoretical model. Comparable data can be generated using the analytical theories of several groups [4.5, 4.14]. A similar, yet larger image can be seen in *Appendix* E.4.1, where the reduced intensity either side of the centre of the Gaussian incident beam is evident in the free-space pattern.

Figure 4.5 shows cross-sections of Figures 4.4(a) and 4.4(b) taken across sets of Talbot maxima, normal to the phase-mask. The experimental data is within 3% of the mathematical model.

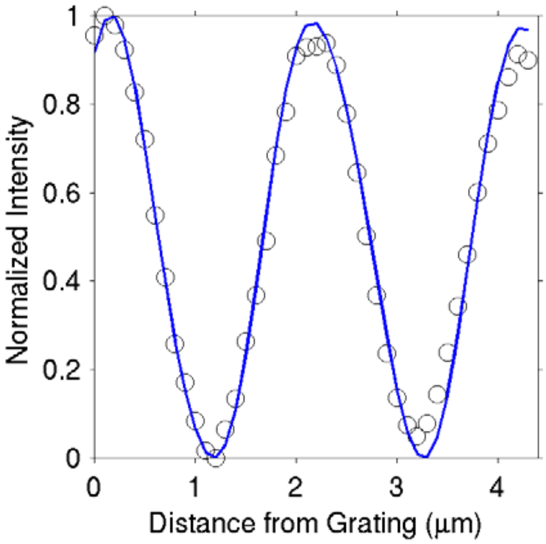

Figure 4.5: Cross sections of Figures 4.4(a) and 4.4(b) normal to the phase-mask, through sets of Talbot maxima, showing a more detailed comparison of the observed data (circles) with the numerical model (solid line).

4.5.1.1 The Effect Of A Varying Amplitude Across The Incident Beam

The agreement of Figure 4.4(a) with simple theory requires that the illumination over the phase-mask is approximately constant, and that the wave-front of the light incident on the mask is approximately flat. These conditions are satisfied if we work at the centre of a focused Gaussian beam with width much larger than our scan area. *Simulation no.1*, has shown that as real conditions vary from the ideal, for example towards the edge of the beam, the Talbot diffraction pattern becomes distorted due to the varying amplitude across the beam's wave-front. Figure 4.6 shows one such numerical simulation. Here, a repeat has been made of the parameters used in the simulation shown in Figure 4.4(b) with the lateral position this time chosen to be between 90µm and 95µm from the centre of the 106µm FWHM beam. It is clear that significant asymmetry has developed, causing the dots to merge into diagonal stripes. This is significant because it implies that well-focused beams do not necessarily produce distortion-free patterns.

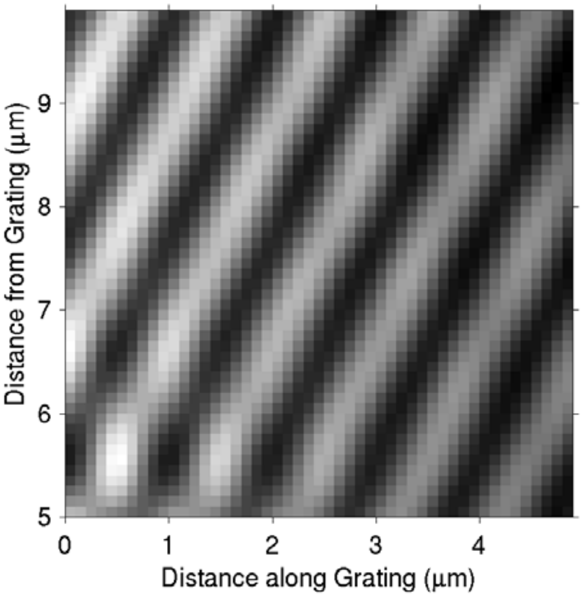

Figure 4.6: Simulation of the phase-mask diffraction pattern between 90µm and 95µm from the centre of the 106µm FWHM beam. The pattern distortions have occurred due to the rate of change in amplitude across the wave-front, at this region of the beam.

Experimental data has shown this prediction to be correct. Patterns obtained at relative distances of 0, 50, and 120µm towards the edge of the Gaussian beam are shown in Figure 4.7. The experimental parameters are identical to those of Figure 4.4(a), except for the lateral scanning position. It is possible that there is a small rate of changing phase across the wave-front in the case of the experimental data of Figure 4.7 in addition to the varying amplitude, since it is difficult to guarantee that the phase-mask rulings are precisely at the centre of the beam waist. However, the highest level of care was taken to ensure that the positioning of the mask maximized the flatness of the phase across the incident beam. Clearly, any degree of changing phase out at the edge of the beam would increase distortion effects further. The result of any such distortion on the pattern written into the core of a fibre Bragg grating would vary according to the concentration of doping and whether the incident laser was pulsed or CW, since these are factors which determine how the growth of the index change depends upon energy density [4.15]. For example, the lower intensity in the region of the incident beam

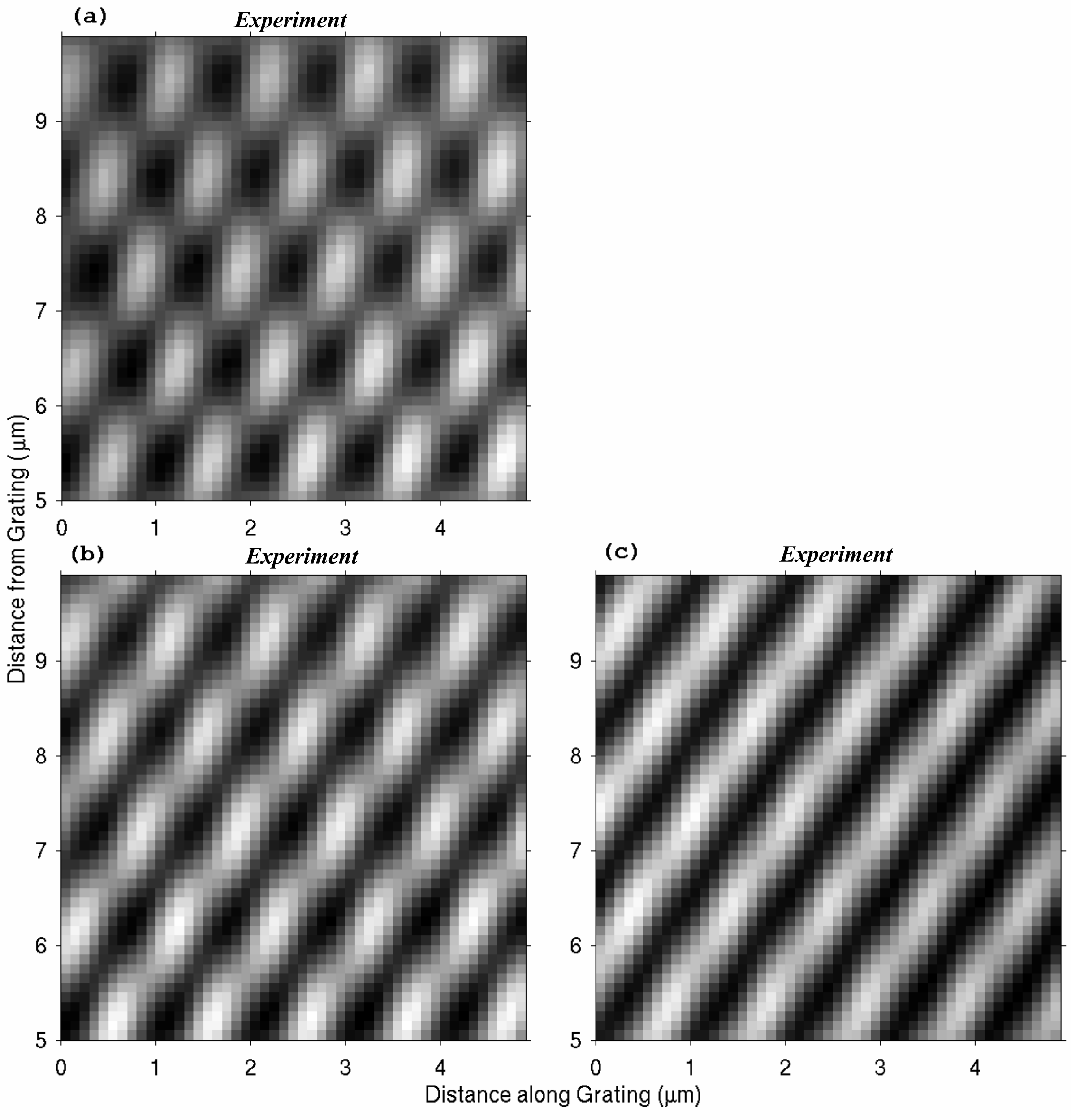

Figure 4.7: Experimentally measured Talbot diffraction patterns across the Gaussian beam shape. The three figures shown are recorded at relative positions (a) 0, (b) 50µm, and (c) 120µm towards the edge of the beam and include a strong zeroth diffraction order and first order. With the same experimental parameters as in Figure 4.4(a), the pattern distortions occur because of changes in the wave-front across the light incident on the phase-mask.

where these distortion effects are greatest should have little impact on a Bragg grating written with a pulsed laser into a standard telecommunications fibre, which has a typically low germania content. In this case, the growth rate of the UV induced refractive index change is proportional to the square of energy density. A similar, but larger image displaying the asymmetry of a distorted free-space pattern can be seen in *Appendix* E.4.2.

4.5.1.2 The Effect Of A Badly Focused Incident Beam

The effect of a de-focused incident laser on the diffraction pattern at the centre of its beam, can be seen in Figure 4.8. Again, with identical experimental parameters as in Figure 4.4(a), the focal point of the beam has been intentionally moved away from the phase-mask rulings by an arbitrary amount to observe the resulting effect. Under this new condition, the beam amplitude continues to be approximately flat at its centre and therefore the observed effect is almost entirely due to the curved phase-front.

Experiment

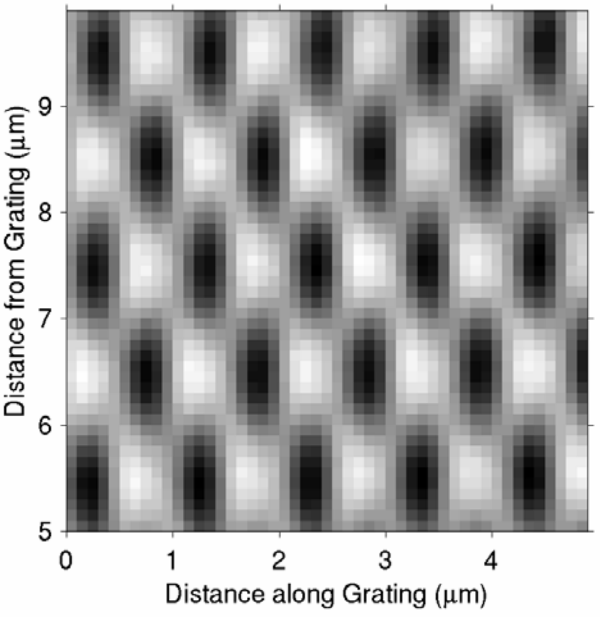

Figure 4.8: Experimentally measured pattern at the centre of a badly focused beam. The scan ran from a height of 5μm above the phase mask and has dimensions 5μm x 5μm. An initial comparison of this data to Figure 4.4(a) suggests that a change in focal point relative to the mask has caused an inverse-contrast effect.

An initial comparison of Figure 4.8 to 4.4(a) suggests that the change in focal point relative to the mask has caused inverse-contrast to occur. Further analysis using *Simulation no.2*, which has the facility to include the modeling of laser divergence angle, has enabled a more accurate interpretation of this data.

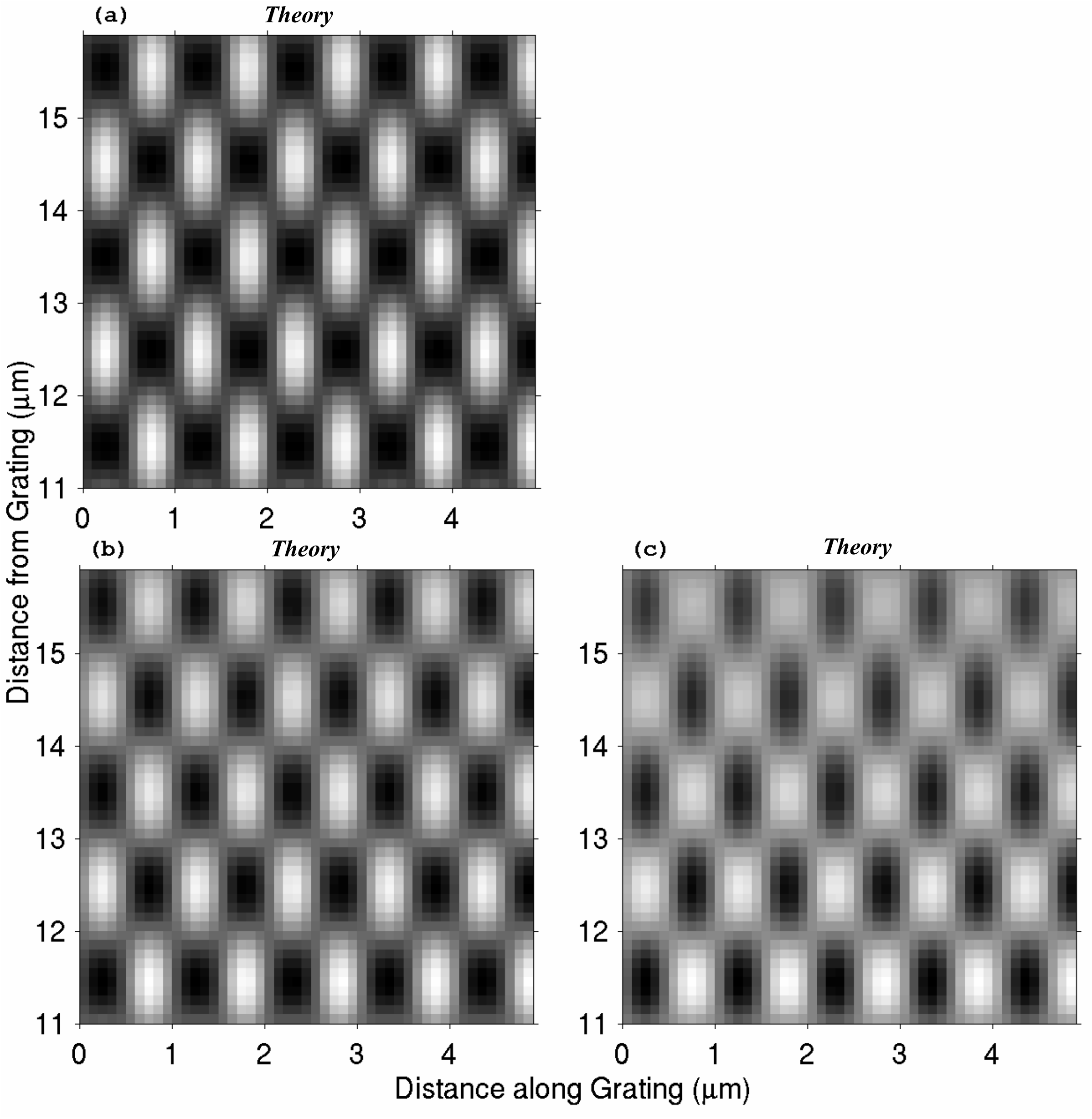

Figure 4.9: Simulations showing the effects of a varying focal point of the incident laser relative to the phase-mask. The full-beam angles are (a) 10 x10^{-3} radians (b) 20x10^{-3} radians and (c) 30 x 10^{-3} radians.

Figure 4.9 shows three such simulations, with varying incident laser divergence angles. Figure 4.9(c) has very similar characteristics to that of the experimental data of Figure 4.8. The full-beam angles in each case are 4.9(a) 10 x 10^{-3} radians, 4.9(b) 20 x 10^{-3} radians and 4.9(c) 30 x 10^{-3} radians. The effect on the interference pattern as a result of the increasing beam angle is a spreading of the intensity distribution leading to a less well-defined pattern. The de-tuning of the focal point may be a useful tool in the writing of structures other than fibre Bragg gratings. For example, the creation of two-dimensional photonic band-gap devices written into photo-polymer may be feasible, since the defocusing effect allows the more intense regions of the pattern to merge, making for greater rigidity in any subsequent structure.

The simulations and data shown in this section have provided evidence that the careful focusing of a laser incident onto a phase-mask is of considerable importance. The focusing procedure is therefore significant to the creation of good fibre gratings.

4.5.2 Excluding Zeroth Order - π Radian Phase Shift

When fibre Bragg gratings are created, phase-masks which induce a π phase shift across the incident beam are generally used because a nulling of the zeroth diffraction order significantly reduces the vertical modulation apparent in the general case of Figure 4.4. Ideally, the first order of diffraction alone would be required to produce two symmetrically crossing components within the Fresnel region, generating uniform vertical interference fringes at twice the frequency of the mask corrugations [4.5]. The fringes would display no Talbot beating in the vertical direction and would therefore create a uniform index change across the fibre grating's core, since the two-dimensional fringes become planes when viewed in three-dimensions. However in practice, π phase shift masks will always produce a small zeroth order of typically 1-3%, in addition to any higher orders, whose number are dependent on the phase-mask-period. There will therefore always exist a degree of non-uniformity in the refractive index profile written into the core of a fibre grating, in the direction perpendicular to its axis. This is certainly the case where phase-masks are used to write fibre Bragg gratings with UV lasers, at telecommunication wavelengths.

In order to measure these complex UV patterns, a Spectra Physics series 2000 Argon ion laser with UV mirrors (front: G3873-007; rear: G3802-016) installed had its 364nm line identified with the aid of a high index prism and subsequently isolated. The isolated beam passed through a 1.5cm hole cut into the thermally insulating casing of the SNOM, and was subsequently aligned with mirrors and focused onto the phase-mask rulings as per the experimental arrangement described in *Section 4.4.1*, using a long (10cm) focal length lens. The beam's direction of polarization was set orthogonal to the mask rulings as it would be during actual fibre grating production, where the alignment along the fibre core's axis would minimize subsequent birefringence effects [4.16]. At this wavelength the induced phase change was approximately π radians and consequently the zeroth order was minimized to 7.4% of the incident beam power. The 1μm phase-mask period allowed the first (28.8% per beam) and second (9.1% per beam) orders to be generated. A typical scan of the π radian interference pattern is shown in Figure 4.10(a). The scan height above the phase-mask ran from 3.63μm to

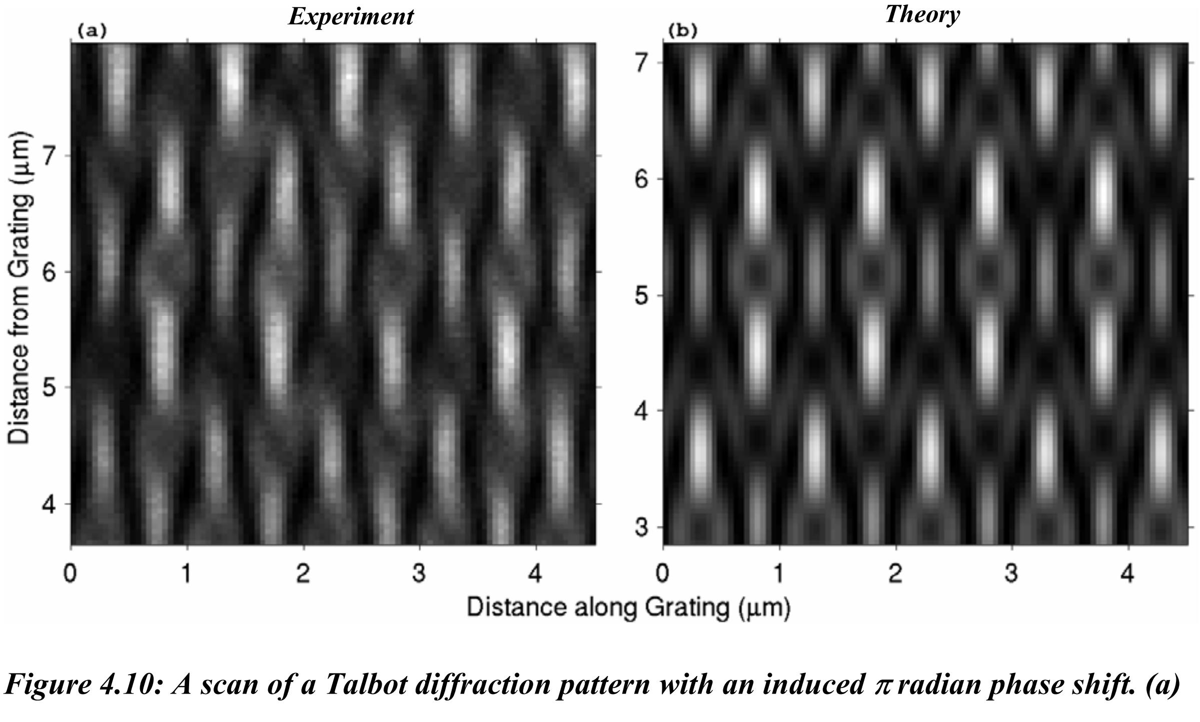

Figure 4.10: A scan of a Talbot diffraction pattern with an induced π radian phase shift. (a) shows the experimentally acquired data with the scan height above the phase-mask running from 3.63μm to 7.96μm and with a lateral width of 4.56μm. (b) shows the result of a simulation of (a) using Simulation no.2. The images include a suppressed zeroth diffraction order in addition to the first and second orders.

7.96µm, with a lateral width of 4.56µm, over a grid of 98x98 data points. The area shown was again directly above the centre of the laser beam, which had a Gaussian profile of 50µm FWHM, measured by free-space SNOM scanning at the position of the phase-mask rulings, with the mask removed. The pattern repeats itself as a function of distance from the grating with an experimentally measured Talbot length of 1.55±0.09µm. This compares well to the Talbot length of 1.48µm calculated with the new Equation (4.6), and identifies this structure to be a result of the interaction between the first and second diffracted orders.

Figure 4.10(b) shows the result of a simulation of Figure 4.10(a) (*Simulation no.2*). As in Figure 4.4(a), the experimental data in Figure 4.10(a) closely resembles its simulation. To best match the data it was necessary to shift the vertical position of the simulation by $Z_T/2$. This allowed the regions of ‘angled lines’, probably caused by the multiple-interaction of all the diffracting orders to correspond. The pattern in Figure 4.10(a) is leaning slightly to the right and this is usually indicative of a tiny misalignment of the incident beam. Talbot diffraction patterns are very sensitive to any such misalignments and this may have been the cause of the apparent variation in position.

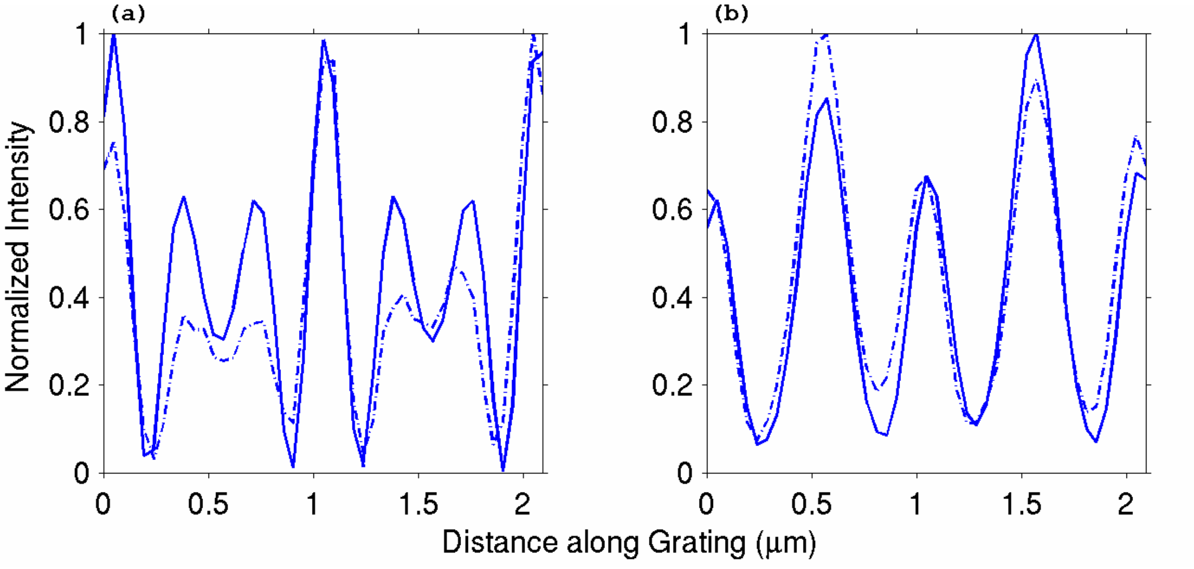

Figure 4.11: (a) Cross-sections of Figure 4.10 showing a more detailed comparison of the observed data (dashes) with the theoretical model (solid line) at a constant height across two of the 'circular' objects. (b) A comparison of the normalized sum of all the rows of data from Figures 4.10(a) and 4.10(b) within the range of one Talbot length. The observed data (dashes) and theoretical model (solid line) were summed from $Z_T/2$ below the line of data shown in Figure 4.11(a) to $Z_T/2$ above.

Figure 4.11(a) shows a closer comparison of the data in Figures 4.10(a) and 4.10(b) by taking constant height cross-sections through two 'circular' objects. Figure 4.11(b) compares the normalized sum of similar rows of data over the range of one Talbot length, starting from $Z_T/2$ below the row of data given in Figure 4.11(a) and ending at $Z_T/2$ above it. Figures 4.11(a) and 4.11(b) indicate that the possible misalignment of the incident beam used to generate the pattern in Figure 4.10(a) is clearly small enough in this case to have no harmful effect on the writing pattern. Although Figure 4.10 demonstrates that the pattern that is actually written into a fibre grating may be fairly complex, Figure 4.11(b) indicates that the average index profile across each Talbot length can be close to the pattern normally expected, although with an apparent double periodicity. Interestingly, the measurement of UV fluorescence directly from fibre Bragg gratings written by phase-mask, has given similar dual periodicity results [4.17].

4.5.2.1 The Effect Of Excluding Higher Diffracting Orders

The data in Figure 4.10 clearly shows the interaction between the first and second diffraction orders. Any interaction between the zeroth and second orders cannot be so clearly defined due to the relative low intensity of the zeroth order. However, it is possible to observe the beating between the weak zeroth and first diffraction orders by careful positioning of the probe. Prior to the production of fibre Bragg gratings it is normal procedure to remove the outer plastic coating from a length of the fibre in the writing region but to retain the cladding. Therefore, even with the fibre in contact with the phase-mask during the writing procedure, the core would still be positioned at least ~50-60μm from the mask surface.

Figure 4.12 demonstrates the effect of moving into this region by lifting the SNOM probe away from the phase-mask and out of the range of the second order rays. With the probe again directly above the centre of the incident beam, Figure 4.12(a) shows a scan which ran from 5.65μm to 12.46μm from the mask surface with lateral width 7.13μm. This image includes the second diffraction order and has a grid of 98x98 data points. Figure 4.12(b) has identical dimensions and is in the same lateral position as Figure 4.12(a) but here the probe has been raised to allow the scan to run from 53.40μm to 60.21μm above the phase-mask. With negligible second order interaction, the beating between the first order and the weak zeroth order becomes apparent as a vertical modulation with length 5.40±0.35μm. This compares well to the value given by the new Equation (4.6) of 5.31μm. This result is of great significance to fibre grating manufacture, where it is clear that the careful positioning of a fibre in relation to the phase-mask before exposure, would lead to a more effective index profile being written into its core. However, care must be taken not to position the core too high since the reduction of the first order beam intensity at its edge would mean a proportionally greater contribution to vertical modulation from the weak zeroth order, resulting in the extreme case to a pattern resembling Figure 4.4(a).

A simulation of Figure 4.12(b) (*Simulation no.2*) can be seen in Figure 4.12(c) where a small shift in vertical position of ~2% was necessary to best fit the data. This can be accounted for by the uncertainty in the coarse positioning of the piezoelectric stage upon which the probe was mounted.

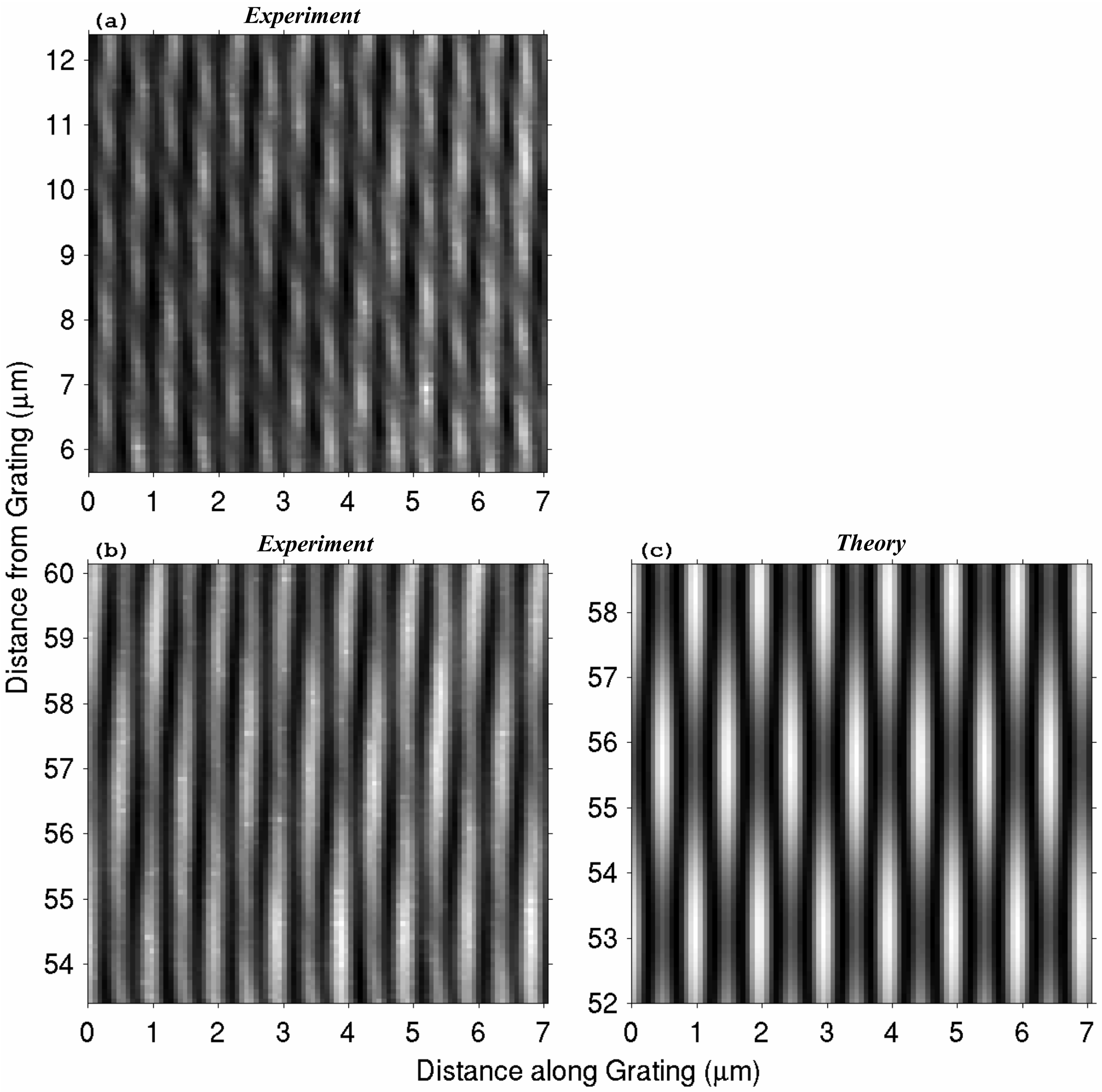

Figure 4.12: A demonstration of the effect of moving away from the phase-mask surface and out of the range of the second diffracted order. (a) ran from 5.65µm to 12.46µm from the mask surface and includes a suppressed zeroth order in addition to the first and second orders. (b) is in the same lateral position as (a) but here the probe has been raised to allow the scan to run from 53.4µm to 60.21µm above the mask. With no second order present the beating between the first order and the weak zeroth order becomes apparent. (c) shows a theoretical simulation of (b) using Simulation no.2.

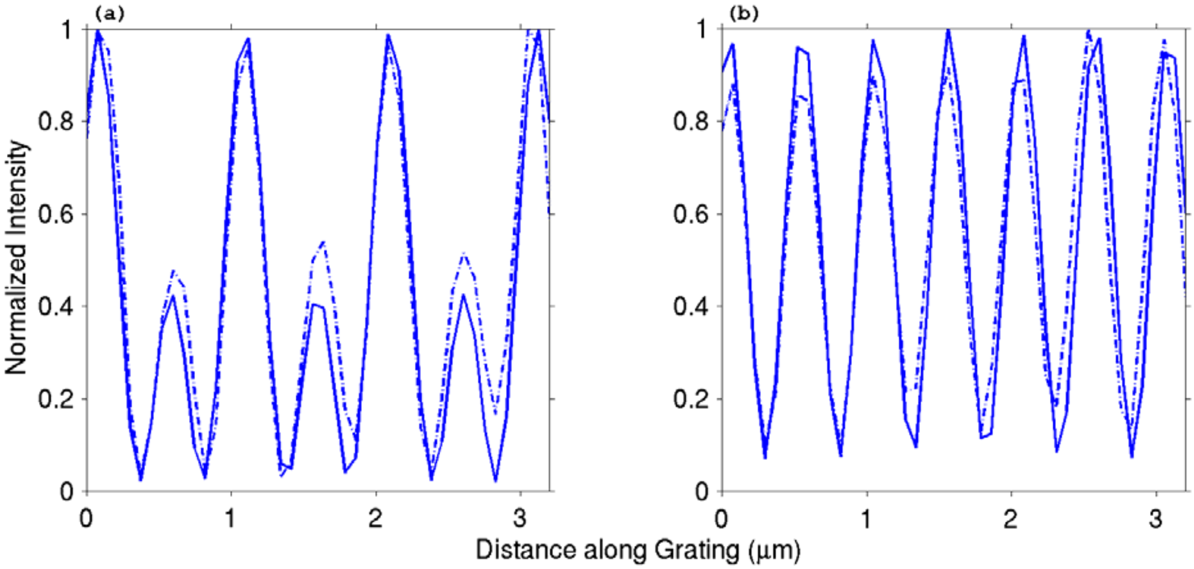

Figure 4.13: (a) Cross-sections of Figures 4.12(b) and 4.12(c) showing a more detailed comparison of the observed data (dashes) with the theoretical model (solid line) across a row of several vertical fringes at constant height. (b) The sum of rows of data from Figures 4.12(b) and 4.12(c) averaged across one Talbot length. Again, the solid line represents the theoretical simulation whilst the dashes represent the observed data.

Figure 4.13(a) examines these results more closely by showing normalized cross-sections of Figures 4.12(b) and 4.12(c) across a region of constant height through several vertical fringes. Figure 4.13(b) again compares Figures 4.12(b) and 4.12(c) this time by showing the normalized sums of rows of data across one Talbot length. Figure 4.13(b) clearly shows an excellent writing pattern for fibre Bragg gratings.

The close fit of the data in Figure 4.13 is a consequence of taking extreme care to position the phase-mask corrugations near to the centre of the incident beam-waist, where the phase-front is flat, and can be approximated by a plane-wave. Simulations have shown that with increased height, the free-space patterns acquire an increased sensitivity to de-focusing at the mask corrugations [4.5]. During these experiments, an increased level of difficulty in creating the expected patterns at greater distances from the mask confirms this observation.

4.5.2.2 The Effect Of An Inaccurate Beam Alignment

During the manufacture of fibre Bragg gratings the illuminating laser can usually be aligned by comparing the position of the incoming beam to its reflection from the rear face of the phase-mask at a point typically up to one metre away from the mask. Indeed, this was the method used in these experiments to ensure the beam's orthogonality relative to the phase-mask. Achieving a normally incident beam is important to the status of the wave-front on reaching the phase-mask corrugations. Figure 4.14 shows the effect on the free-space interference pattern above the phase-mask of a beam purposely misaligned from normal incidence by +0.01 degrees in Figure 4.14(a) and -0.01 degrees in Figure 4.14(b). Both images include the suppressed zeroth, first and second diffraction orders, and each has dimensions of height 4.33μm and width 4.56μm. Considerable distortion has resulted from the misalignment, which has caused the

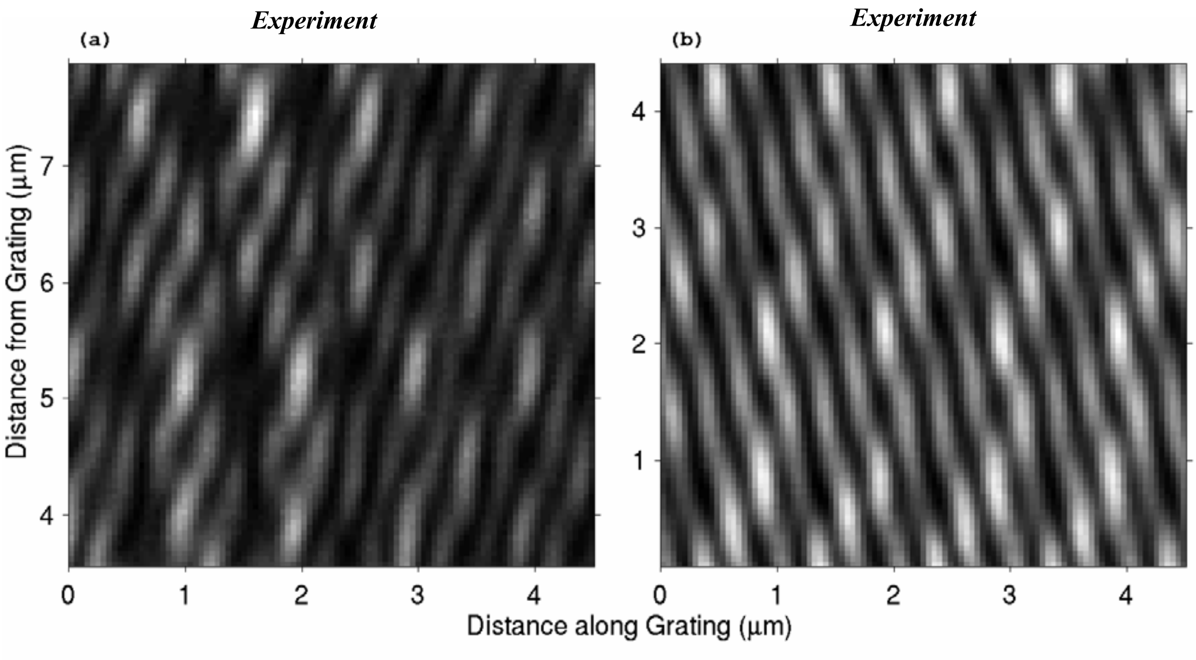

Figure 4.14: The effect on the free-space interference pattern of misaligning the incident beam from normal incidence to the phase-mask by +0.01 degrees (a) and -0.01 degrees (b). Both scans are experimentally acquired data, and include the suppressed zeroth, first and second diffracted orders.

patterns to lean to the side. These images contrast heavily to Figure 4.10(a) where a suspected misalignment of the incident beam led to an acceptable writing pattern. Figure 4.14(b) demonstrates how the pattern continues to be generated close to the mask itself, in this case with the probe beginning its scan just 90nm above a high corrugation on the phase-mask's surface. Optical data from line scans where the SNOM probe is actually locked onto the surface of a phase-mask, was seen in *Chapter 3*.

Figure 4.15(a) compares a cross-section of Figure 4.14(b) to a cross-section of Figure 4.10(a) taken in each case at a constant height of 4μm across 1.2 phase-mask periods. With identical experimental parameters, Figure 4.14(b) compares to the more accurately aligned Figure 4.10(a) by having 3 fringes per mask period instead of the expected 2 fringes. Figure 4.15(b) compares a normalized sum of rows of data taken from Figures 4.10(a) and 4.14(b) through one Talbot length. A comparison of the modulation depths thus averaged across one Talbot length shows them to differ by up to 40%. Although in practice it is reasonably straightforward to achieve an adequate alignment of the writing beam for Bragg grating production, a reasonable level of care is nevertheless required, since small deviations from normal incidence clearly have a significant effect on the writing pattern.

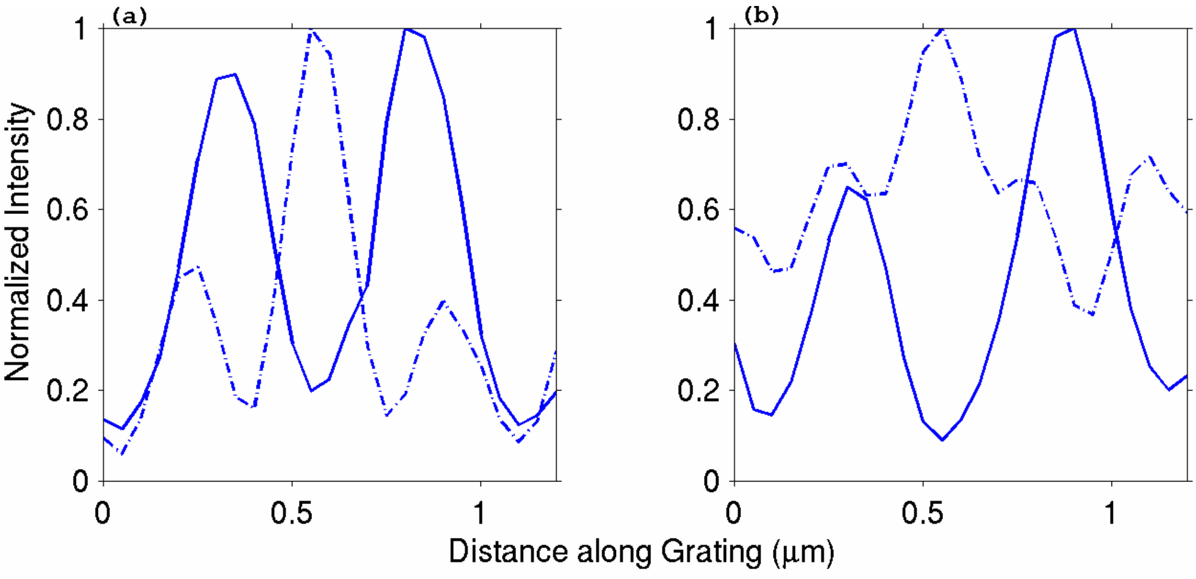

Figure 4.15: (a) Cross-sections of the experimental data shown in Figures 4.10(a) and 4.14(b) taken in each case at a height of 4μm. The line of data from Figure 4.10(a) (solid line) gives 2 periods of modulation per 1μm phase-mask period and the misaligned beam of Figure 4.14(b) (dashes) has generated 3 periods. (b) This figure shows that the modulation depths of a normalized sum of the data from Figures 4.10(a) (solid line) and 4.14(b) (dashes) averaged over one Talbot length, can vary by up to 40%.

4.6 Chapter Summary

In developing a technique to directly image free-space diffraction patterns near to a phase-mask, previous theoretical models have been confirmed, and some useful results relating to fibre Bragg grating manufacture have been established. In particular, some of the technical problems that might occur during the writing of fibre gratings have been exposed. It is clear from Figure 4.10 that free-space patterns used to produce fibre Bragg gratings with phase-masks are not as uniform as one would hope. Indeed, the actual pattern used to write gratings with UV light at 248nm for telecommunication wavelengths might have further complexity. This is due to a reduced writing wavelength compared to Figure 4.10, therefore resulting in increased beating from higher diffraction orders. Nevertheless, Figure 4.11(b) shows that the average writing intensity for each Talbot length would be more or less what is hoped for.

Figure 4.12 demonstrates how the writing pattern can be improved by carefully choosing the position of the fibre core relative to the phase-mask. A comparison of Figure 4.12(b) to Figure 4.12(a) shows that the selection of a writing position out of the range of a higher diffraction order can reduce the effect of the Talbot beating leading in this case, to Figure 4.13(b) which shows the improved writing pattern of Figure 4.12(b) (along with its simulation) averaged over one Talbot length. Nevertheless, under this condition care in focusing must be paramount since free-space patterns at increasing height, display an increased sensitivity to curved phase-fronts at the phase-mask corrugations.

Figure 4.8 compared to Figure 4.4(a), gives an indication of how the Talbot pattern can vary above the centre of a badly focused incident beam, which has the effect of smoothing out of the intensity distribution, to give a pattern resembling inverse contrast. The effects of wave-front curvature can be equally significant in the region above the edge of the incident Gaussian beam as shown in Figure 4.7. This part of the beam generates distortions that are difficult to avoid since an amplitude gradient alone will cause this harmful effect. However, a cause of asymmetry in the diffraction pattern that can be more easily avoided is bad alignment of the incident beam. The consequence of failing to position the beam normal to the mask can be significant, as Figure 4.14 demonstrates.

To underpin the analysis of the data collected for this chapter, an expression for the Talbot length shown as Equation (4.6) was developed by analogy with x-ray diffraction theory, during the course of this work. This should replace Rayleigh's approximate term Equation (4.4), which is often used as a general guide. Rayleigh's expression assumes that $\lambda << a$ where λ is the wavelength of the incident light and a is the period of the phase-mask. Since $\lambda \sim a$ during fibre Bragg grating production, each diffraction order becomes significant and has a measurable Talbot length associated with its interaction with each and every other diffraction order present. The experimental results confirm the new expression in all of the presented data.

4.7 References

[4.1] G. Meltz, W.W. Morey, W.H. Glenn, Optics Letters, **14**, 823 (1989)

[4.2] J.-L. Archambault, L. Reekie, P.St.J. Russell, Electronics Letters, **29** (1), 28 (1993)

[4.3] K.O. Hill, B.Malo, F. Bilodeau, D.C. Johnson, J. Albert, Applied Physics Letters **62**, 1035 (1993)

[4.4] Z.S. Hegedus, Applied Optics, **36** (1), 247 (1997)

[4.5] P.E. Dyer, R.J. Farley, R. Giedl, Optics Communications **115**, 327 (1995)

[4.6] I.I. Smolyaninov, C.C. Davis, Optics Letters, **23** (17), 1346 (1998)

[4.7] Lord Rayleigh, Phil. Mag. **11**, 196 (1881)

[4.8] C. Kittel, "Introduction to Solid State Physics", 6th edition, Wiley, New York (1986)

[4.9] S.K. Juma, P.Kung, C. Clark, "Phase Mask Technology Overview", QPS Technology Inc., Quebec (2000)

[4.10] K. Karrai, R.D.Grober, Applied Physics Letters, **66**, 1842 (1995)

[4.11] D. Courjon, C.Bainier, Rep. Prog. Phys. **57**, 989 (1994)

[4.12] J.-L. Archambault, L. Reekie, P.St.J. Russell, Electronics Letters, **29** (5), 453 (1993)

[4.13] M.J.Cole, W.H.Loh, R.I.Laming, M.N.Zervas, S.Barcelos, Electronics Letters **31** (17), 1483 (1995)

[4.14] J.D. Prohaska, E. Snitzer, J. Winthrop, Applied Optics, **33** (18), 3896 (1994)

[4.15] R. Kashyap, "Fiber Bragg Gratings", pp22-23, Academic Press, San Diego (1999)

[4.16] F. Ouellette, D. Gagnon, M. Poirier, Applied Physics Letters, **58** (17), 1813 (1991)

[4.17] M.N. Zervas, S. Sales, M.K. Durkin, R. Feced, Proceedings of *BGPP*, 75 (1999)

[4.18] H. Talbot, Phil. Mag. **9**, 401 (1836)

[4.19] Lord Rayleigh, Phil. Mag. **11**, 196 (1881)

5. Evanescent Field Imaging Of A Phase-Mask Irradiated Fibre Bragg Grating: *The Development Of A Scanning Procedure*

5.1 Chapter Introduction

This chapter represents the data collected as a result of probing the evanescent field associated with a single uniform fibre Bragg grating with the Scanning Near-field Optical Microscope (SNOM). The study was carried out in order to develop a technique to enable the characterization of fibre Bragg gratings via the evanescent field. It is the intention that the methods developed here should either be used as a research and development tool, or be straightforward enough to enable the routine comparison of gratings made with identical parameters from a batch. However, the evanescent field of a fibre Bragg grating is inaccessible to a SNOM probe without certain modifications being applied to the sample. This means that the scanning technique is invasive, and therefore destructive. The methods developed in this chapter will also be utilized in the following two chapters in order to characterize other grating samples. A general discussion continues throughout *Chapters 5*, *6* and *7*, with comparisons being made between results across chapter boundaries, in order to achieve a more complete analysis.

The fibre Bragg grating [5.1, 5.2] is one of the most significant new devices in the telecommunications area since the discovery of the erbium-doped fibre amplifier [5.3]. Gratings are already in use for dispersion compensation [5.4], add/drop multiplexers [5.5], DFB laser mirrors [5.6] and many other applications. The fibre grating is formed by using a periodic pattern of UV light to produce a periodic change in the refractive index along the

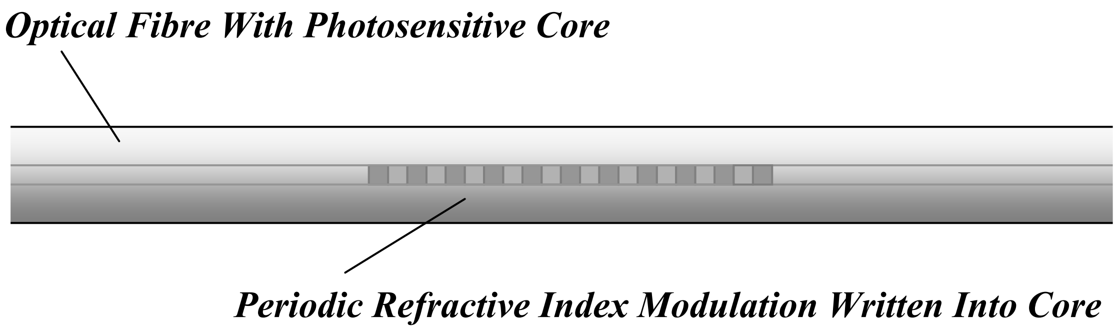

Figure 5.1: An Optical Fibre Bragg Grating. There are typically many thousands of periods along the grating length.

core of the fibre as shown in Figure 5.1, via UV-induced creation of defects within the core glass [5.7, 5.8, 5.9]. Like a multi-layer stack, the grating region within the core acts as a wavelength selective mirror to back-reflect light propagating down the fibre at the Bragg wavelength

$$\lambda_B = 2n_e\Lambda \tag{5.1}$$

where Λ is the period of the grating and n_e is the grating's modal effective refractive index. Some of the current procedures for examining the properties of fibre gratings include an analysis of the reflected and non-reflected components of light from the grating, and the mathematical modeling of the internal electric field using for example, coupled mode [5.10] or transfer matrix [5.11] methods.

5.2 Evanescent Field Of A Polished Fibre Bragg Grating

This section discusses what can be interpreted from a SNOM measurement of the evanescent field associated with a fibre Bragg grating. It describes the many parameters involved and explains how data may be collected and analyzed to greatest effect.

5.2.1 SNOM Measurement Of The Evanescent Field

The use of SNOM to image the evanescent field associated with an optical wave-guide is not a new technique [5.12]. Often referred to as Photon Scanning Tunneling Microscopy (PSTM), the method has already been used to map channel wave-guides [5.13], Y-branch wave-guides [5.14], and to observe the Tien effect in wave-guides [5.15]. In all of these cases, the evanescent field was directly accessible. However, in order to detect the evanescent field of a fibre Bragg grating, it is necessary to reduce the depth of the cladding surrounding the core, so that a measurable intensity of the exponentially decaying field can be reached. A straightforward method for achieving this is to polish the fibre’s cladding to within a small distance from its core so that the fibre grating resembles a D-fibre [5.16]. This also simplifies the subsequent SNOM scanning by allowing it to be performed upon a flat surface as can be seen in Figure 5.2.

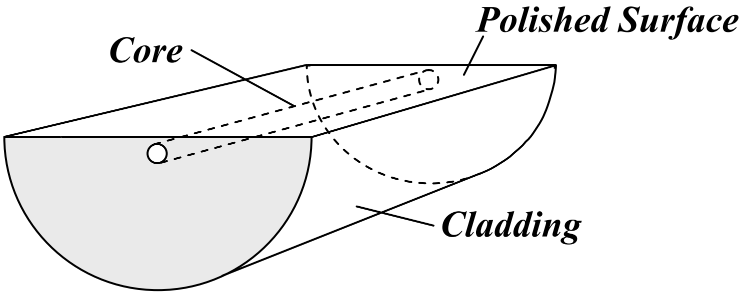

Figure 5.2: Part of the cladding surrounding the core of the fibre grating has been removed by polishing, to allow the evanescent field to be accessed.

When a SNOM tip is brought within the exponentially decaying evanescent field associated with a planar wave-guide, the detected intensity at a given point is expressed by [5.17]

$$I = I_0 \exp(-2\alpha z) + I_S \tag{5.2}$$

where I_0 is the intensity at the surface, z is the height above the surface, I_S is the stray scattered light intensity and the component of the evanescent field wave-vector in the z-direction is given by

$$\alpha = k(n_e^2 - n_0^2)^{1/2} \tag{5.3}$$

where $k = 2\pi/\lambda$, n_e is the effective refractive index of the wave-guide and n_0 is the refractive index of the scanning medium. In the case of a polished optical D-fibre Bragg grating, account must also be taken of the field decay within the cladding in order to understand how a given SNOM measurement relates to the electric field and physical structure at the core/cladding interface. To illustrate this, Figure 5.3 shows wave-vector relationships in two dimensions of a slab waveguide, introduced here to approximate a polished optical fibre with a single core refractive index, n_1. The model is based upon that described in ref. [5.20]. The mode propagation constant or axial component of the wave-vector, which is given by [5.18]

$$\beta = n_1 k \sin\theta = n_e k \tag{5.4}$$

is also the wave-vector component of the evanescent field both in the cladding and air, along the direction parallel to the core's axis. This is because the progression of the wave is uniform across its cross-section although it is interesting to note that where a greater proportion of the energy is transported in the evanescent wave, for example close to cut-off or higher modes, the effective refractive index can be closer to n_2 than n_1 [5.19]. It is therefore expected that the effective refractive index of a polished optical fibre is lowered as a result of part of the energy progressing through the air.

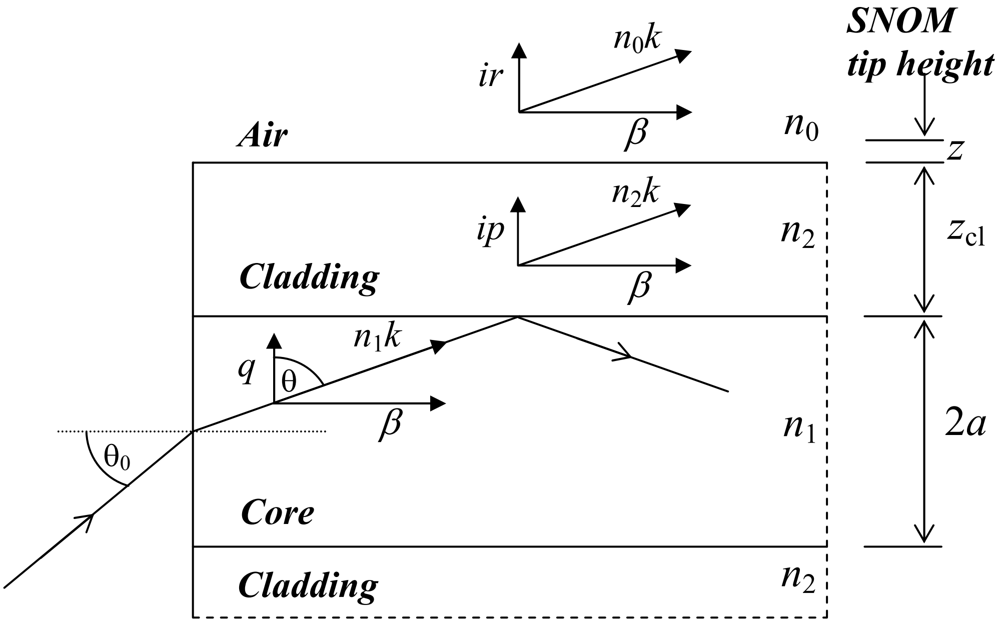

Figure 5.3: Wave-vector components and geometry of a slab waveguide, introduced here to approximate a polished optical fibre with a single core refractive index, n_1.

Figure 5.3 also shows the components of the wave-vector in the direction orthogonal to the core's axis, which are imaginary in the cladding and air regions [5.20]. This leads to exponential decay of the field in this direction, outside of the core. Taking air and cladding wave-vector components shown in Figure 5.3, i.e.

$$n_0{}^2k^2 = \beta^2 - r^2 \tag{5.5}$$

and

$$n_2{}^2k^2 = \beta^2 - p^2 \tag{5.6}$$

and substituting in Equation (5.4) leads to the relationships

$$r = k(n_e{}^2 - n_0{}^2)^{1/2} \tag{5.7}$$

and

$$p = k(n_e{}^2 - n_2{}^2)^{1/2} \tag{5.8}$$

Equations (5.2), (5.7) and (5.8) lead finally to the equation for the intensity measured by the SNOM tip

$$I = I_0 \exp(-2rz) + I_S \tag{5.9}$$

where r is given by Equation (5.7), z is the distance between the air/cladding interface and the SNOM tip (shown in Figure 5.3) and I_0, the intensity at the air/cladding interface is given by

$$I_0 = I_{cl} \exp(-2pz_{cl}) \tag{5.10}$$

where I_{cl} is the intensity at the core/cladding interface, z_{cl} is the depth of the cladding and p is given by Equation (5.8).

In the case of optical fibre Bragg gratings, it is clear that a modulating n_1 along the core will induce changes in the local values of n_e, r, p and therefore I. It is also clear that any change in I_{cl} along the length of the grating, will also manifest itself as a change in the detected intensity I, at the SNOM tip. Additionally, variations in the cladding depth z_{cl} will influence the measured intensity. For example, data from a line scan in a direction perpendicular to the axis of the D-fibre, will be affected by a varying depth of cladding between the flat surface and deeper regions of the cylindrical core.

5.2.2 Interpretation Of The Evanescent Field Measurement

When light is launched into a fibre grating at the Bragg wavelength λ_B, a standing wave within the grating region ensues. This manifests itself as a periodically varying intensity along the length of the grating, which can be detected by the SNOM. However, the apparent measurement of I_{cl} will have suffered a decay dependent upon the local difference in refractive index between the core and cladding. As such, the measurement is a function of both the standing wave intensity and the core refractive index at that boundary point. If the light passing through the grating is tuned off resonance (i.e. well away from the Bragg wavelength into a spectral region where there is no reflection), the field intensity along the grating will become approximately flat [5.21], allowing the refractive index variation along the grating to dominate the detected intensity, I.

This has been illustrated in Figure 5.4 where the slab waveguide Equations (5.9) and (5.10) have been employed to model the approximate evanescent field decay of two fibre grating examples. In each case, the exponential decay has been calculated at positions of both maximum and minimum effective refractive index, along the respective gratings. The

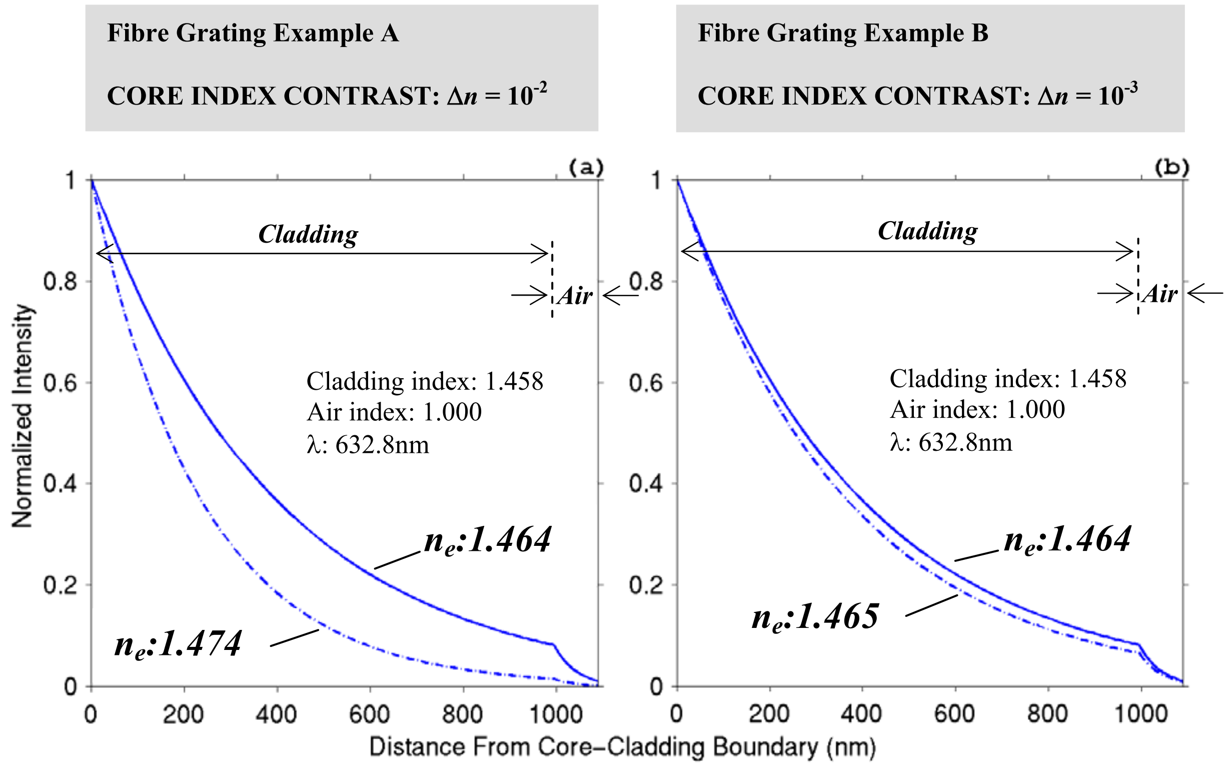

Figure 5.4: Modeling of the approximate evanescent field decay associated with two different fibre gratings by utilizing the slab waveguide formulation given by Equations (5.9) and (5.10). The calculation begins at the core/cladding boundary, and continues through 995nm of cladding and 95nm of air, in a direction perpendicular to the axis of each grating. In each case, the wavelength is assumed to be 'off resonance', and the normalized starting intensity is assumed to be equivalent for every value of n_e. The illuminating light for each grating has a wavelength of 632.8nm. 5.4(a) compares the decaying intensities at two separate positions along Fibre Grating Example A, where the effective index has varied by 10^{-2}. 5.4(b) compares the decaying intensities at two separate positions along Fibre Grating Example B, where the index has varied by 10^{-3}.

simulation starts at the core/cladding interface and continues through 995nm of silica cladding (n_2=1.458 at 632.8nm), and 95nm of air (n_0 = 1.000). The lower core index in each case of 1.464 is based upon standard fibre index with low (~3 mol%) germania doping. The illuminating laser is assumed to be 'off resonance' as described above, and the starting intensity I_{cl}, which is assumed to be equivalent for each value of n_e, has been normalized to 1. Figure 5.4(a) compares the decaying intensities at two separate positions along Fibre Grating Example A, where the effective index has varied by 10^{-2}, and Figure 5.4(b) compares the decaying intensities at two separate positions along Fibre Grating Example B, where the index has varied by 10^{-3}. For the pairs of data in each grating example, the ratio of normalized intensities at the air/cladding interface is 0.015:0.082 for the refractive index contrast of 10^{-2} and 0.066:0.082 for the index contrast of 10^{-3}. At a typical probe scanning distance of 10nm away from this interface into the air region, the ratios are 0.012:0.066 for the index contrast of 10^{-2} and 0.053:0.066 for the index contrast of 10^{-3}. It is reasonable to assume that the direct imaging of the index modulation along a fibre Bragg grating is therefore feasible. However, it must be emphasized that although the above modeling suggests that a greater value of z_{cl} will be associated with greater contrast, in practice it will be linked to a decrease in the visibility of variations in n_{e}. This is due to a proportionally greater contribution to the field at the SNOM tip from adjacent parts of the grating, coupled with a reduction in detectable intensity. Indeed, to achieve optimum fringe visibility in the imaging of the refractive index structure, the cladding thickness should be small compared to Λ, the grating period. However, this will produce data, in particular off resonance, with little or no measurable contrast.

A method of increasing contrast when cladding depth is shallow is to use a shorter wavelength of light. The downside of this is that shorter wavelengths produce faster decaying fields and therefore lower detectable intensities. Nevertheless, fringe visibility can be optimized with minimum cladding depth by measuring the evanescent field intensity as a function of z, by slowly pulling the SNOM tip away from the surface. This will yield the index value from the local decay constant. Of course, the process must be repeated at many positions to construct a full image, which may be time consuming. However, with sufficient thermal stability, it would be possible to carry out a two-dimensional free-space scan perpendicular to the grating surface, in order to image the decay constants over a length of the grating. Indeed, this type of scan was performed during the course of this project with an example given in *Chapter 7*. Unfortunately, thermal drift of the sample relative to the tip caused this measurement, and other similar measurements, to be incompatible with the acquisition of accurate refractive index data. However, one-dimensional vertical line scans, taking just a few seconds each to complete, have given excellent results.

5.2.3 Normalization Of Data Artifacts

5.2.3.1 Normalization With Respect To The Variation In Topography

During most of the scanning of the fibre Bragg gratings described in this and subsequent chapters, the SNOM probe is locked at a constant distance from the polished surface. Due to polishing defects left on the surface, this means that there will be topographically induced artifacts in the optical data. High points of topography will cause a lower signal since the light has decayed through a greater depth of cladding. In some cases, it has been possible to normalize the optical data with respect to the simultaneously collected topographical data. This is straightforward provided the operation is carried out on line scans parallel to the axis of the core, where the underlying cladding thickness is constant. Normalization of two-dimensional scans and line scans that are perpendicular to the axis of the grating would involve having a more detailed knowledge of core position relative to the surface. A program designed to normalize optical line scans with respect to topography was coded in Matlab, with results of its operation shown in *Chapter 7*.

5.2.3.2 Normalization With Respect To The Variation In Decay Constant

When the required data is an 'on-resonance' intensity profile at the core-cladding interface, a further operation can be performed. The process involves reducing the effects of the varying decay constant on the standing wave, along the length of the grating. In practice, even for the most carefully polished gratings, there will always be some cladding present which will perturb the measurement, since polishing must cease before the core has been reached [5.16]. Additionally, since the polishing technique used for all of the samples investigated for this thesis (described below in *Section* 5.3) required the grating to be slightly curved, interesting regions of the fibre grating may have been buried deeper within the cladding than other parts of the grating. In these cases, the acquired SNOM data taken on resonance can be divided point by point by data acquired from a repeat scan when the launched light is off resonance. The result of this operation is a reasonable approximation of the standing wave at the core-cladding interface. In order to express the approximation quantitatively the following assumptions first have to be made:

(i) *Only line scans that follow the axis of the grating will be treated*. This is basically for two reasons. Firstly, thermal drift over the time it takes to carry out a two dimensional scan would mean that identical data points taken in the same place during the two scans may be in different regions of the data matrix. Secondly, the greater the cladding depth, the less accurate the approximation as described below in *Table 5.1*. The curvature of the fibre in the direction perpendicular to its axis causes an unacceptably sharp increase in cladding depth.

(ii) *For the duration of a line scan along the axis of the grating the cladding depth remains constant*. This is approximately the case for micron-scale scans with both data sets having been topographically-normalized. Also, the effect of the above mentioned axial curvature of the samples examined in this thesis is negligible. For example, a 20μm scan (which is the maximum possible for the present SNOM set-up) would equate to a change in cladding depth of <1nm.

(iii) *The height of the tip above the sample surface,* z *is constant*. As explained in *Chapter 3*, characterization of the present SNOM system's feed-back mechanism has revealed stability in the *z*-axis positioning of the tip relative to the sample, of ± 3% for a typical tip-sample gap of 10nm.

(iv) *The intensity distribution off resonance, along the length of the grating is constant*. When away from resonance, light propagates through a fibre grating as if it were in a medium of uniform refractive index [5.21].

(v) *Any contribution from stray scattered light can be ignored*. There may be a small contribution to the intensity measured by the SNOM probe from light scattered by the probe itself and reflected from the sample surface. As can be seen in reference [5.22], this becomes significant at several hundred nanometres from the sample surface but is probably negligible at a height of 10nm, where the intensity of the evanescent field itself, is relatively high. The measured contribution of light scattered by the grating is difficult to determine since the concern is only with propagating light, and not evanescent components created by total internal reflection at either the core/cladding, or cladding/air interfaces.

(vi) *The local effective refractive index and absolute indices of core and cladding are the same for both 'on' and 'off' resonance wavelengths*. All of the data normalized by this technique in this thesis has 'on' and 'off' resonance wavelengths that are <10nm apart. Each wavelength therefore 'sees' a local refractive index in both the core and cladding that varies from the other wavelength by <0.1%. It is likely therefore that the variation in the local effective refractive index between wavelengths is similarly negligible.

Given these assumptions, the intensities measured by the SNOM during 'on' and 'off' resonance repeat line scans can be treated (point by point) in the following way, in order to approximate the standing wave intensity profile at the core/cladding interface:

From Equation (5.9), the result of dividing a data point from the 'on resonance' scan I_{SW}, by a data point from the 'off resonance' scan I_{RI} (at the same position), is given by

$$I_{SW} / I_{RI} = [I_{0_{SW}} \exp(-2r_{SW}\, z)] / [I_{0_{RI}} \exp(-2r_{RI} z)] \tag{5.11}$$

where $I_{0_{SW}}$ and $I_{0_{RI}}$ are the intensities at the cladding/air interface during the 'on' and 'off' resonance scans respectively, and r_{SW} and r_{RI} from Equation (5.7), are given by

$$r_{SW} = (2\pi/\lambda_{SW})(n_e^2 - n_0^2)^{1/2} \tag{5.12}$$

and

$$r_{RI} = (2\pi/\lambda_{RI})(n_e^2 - n_0^2)^{1/2} \tag{5.13}$$

where λ_{SW} and λ_{RI} are the respective illuminating wavelengths, 'on' and 'off' resonance. The individual wavelengths have different decay rates and so affect the 'on' and 'off' resonant intensities at the surface by differing amounts. These are given from Equation (5.10) by

$$I_{0_{SW}} = I_{cl_{SW}} \exp(-2p_{SW}\, z_{cl}) \tag{5.14}$$

and

$$I_{0_{RI}} = I_{cl_{RI}} \exp(-2p_{RI}\, z_{cl}) \tag{5.15}$$

where $I_{cl_{SW}}$ and $I_{cl_{RI}}$ are the intensities at the core/cladding interface during the 'on' and 'off' resonance scans respectively, and p_{SW} and p_{RI} are given from Equation (5.8) by

$$p_{SW} = (2\pi/\lambda_{SW})(n_e^2 - n_2^2)^{1/2} \tag{5.16}$$

$$p_{RI} = (2\pi/\lambda_{RI})(n_e^2 - n_2^2)^{1/2} \tag{5.17}$$

By substituting Equations (5.12) through to (5.17) into Equation (5.11), rearranging, and using assumption (iv) above, to replace $I_{cl_{RI}}$ with the constant 1/C, this leads finally to the expression

$$I_{SW} / I_{RI} = \mathrm{C} I_{cl_{SW}} \exp(-\sigma) \tag{5.18}$$

where σ is given by

$$\sigma = 4\pi[\ (\lambda_{SW}^{-1} - \lambda_{RI}^{-1})\ [z_{cl}(n_e^2 - n_2^2)^{1/2} + z(n_e^2 - n_0^2)^{1/2}\ ]\ ] \tag{5.19}$$

Equation (5.18) demonstrates that if the uncertainty in exp(-σ) can be shown to be small, then dividing 'on resonance' data, point by point by 'off resonance' data, the result is essentially the 'on resonance' intensity at the core/cladding interface, multiplied by a constant. This result is interesting because there must always be some cladding between the core and the SNOM probe in order to guide the light efficiently along the fibre [5.16]. It is therefore data that probably cannot be acquired by direct measurement.

Table 5.1 below gives calculated values of exp(-σ) from the above equations, and its range of uncertainty for particular magnitudes of Δn, the difference between the minimum and maximum level of the grating's modulating index. These values have been expressed for various depths of cladding. In each case, the value of σ in Equation (5.19) has been calculated using n_e= 'average effective refractive index' and therefore has a given uncertainty relating to $\pm \Delta n/2$. The 'on' and 'off' resonance wavelengths are 775nm and 784nm respectively, z = 10nm, $n_0 = 1.000$, $n_e = 1.470$ and $n_2 = 1.454$.

Depth of cladding (μm)	Δn_e	**exp(-σ)**	***Uncertainty in* exp(-σ)**	***Percentage uncertainty***
0.5	10^{-2}	0.9797	0.0058	0.59 %
1.0	10^{-2}	0.9617	0.0114	1.18 %
2.0	10^{-2}	0.9268	0.0219	2.36 %
0.5	10^{-3}	0.9797	0.0007	0.07%
1.0	10^{-3}	0.9617	0.0013	0.13%
2.0	10^{-3}	0.9268	0.0025	0.27%

Table 5.1: In order to demonstrate the feasibility of generating an image of the standing wave intensity at the core/cladding interface as a result of normalizing resonant data wrt non-resonant data, calculations of exp(-σ) from Equation (5.18) and associated uncertainties for given values of depth of cladding and index modulation are shown here. The small value of each uncertainty in exp(-σ), which is caused by the respective modulating refractive indices, indeed confirms the usefulness of this data-normalizing technique.

Certainly, all of the data in this project was collected above regions where the cladding depth and value of Δn was no greater than that shown in *Table 5.1*. Therefore it is clear that the result of performing the operation $I_{\mathrm{SW}} / I_{\mathrm{RI}}$ in Equation (5.18), is essentially $I_{\mathrm{cl}_{\mathrm{SW}}}$ times a constant and $\exp(-\sigma)$, with the latter modulating by <3%, depending on the particular grating index at each data point. Since the constant C in Equation (5.18) cannot be accurately known, any derived data sets of $I_{\mathrm{cl}_{\mathrm{SW}}}$ show only a picture of intensity contrast and not absolute magnitude.

Uncertainties generated in the actual SNOM measurements are small as described in *Chapter 3*, and therefore have little effect on these normalization procedures. As will be demonstrated in *Chapter 7* of this thesis, both the topography-normalization and the 'on resonance' decay-constant-normalization routines become useful analytical tools.

5.3 Sample Preparation

A single, uniform fibre Bragg grating, originally designed to be utilized as part of a Grating Assisted Coupler system [5.23] had its evanescent field probed to acquire the data presented in this chapter. The preparation of the sample was therefore partially complete before this PhD project began. A similar process of preparation is described in detail in *Chapter 7*,

Sample identification:	Fibre Grating Sample No.1
NA of non-grating part of fibre:	0.125
Single mode cut-off of non-grating part of fibre:	1250 nm
Fibre cladding diameter:	125 μm
Cladding material:	Silica
Fibre core radius, a:	3.83 μm
Core material:	Silica/Germania/Boron
Preparation of fibre:	Hydrogen loaded at room temperature
Method of grating writing:	Multiple shot Type I grating. KrF excimer laser irradiated phase-mask. Pitch of mask: a = 1048nm.
Index modulation, Δn:	~5 x 10^{-3}
Grating length, L:	8 mm

Table 5.2: Details of the fibre Bragg grating used to collect the data presented in this chapter.

where several polished fibre gratings were manufactured specifically for this project. However, a brief account highlighting some of the differences in the preparation of this sample compared to those in *Chapter 7*, and some of the modifications that were made to the sample are given in this section. *Table 5.2* outlines the sample parameters.

Once the grating had been written into the fibre with a Lambda Physik EMG-150 KrF excimer laser, it was then prepared by gluing its fibre with an Auriga Ltd. EpoTek 353ND epoxy resin along a groove of radius 1m, cut into the surface of a pyrex glass block, which had engineered dimensions 44mm x 25mm x 10mm. This enabled it to be held securely whilst being polished down as part of the block very close to its core. The 8mm grating, which had its centre positioned at the highest point of the groove, was subsequently at the location of shallowest cladding. The final depth of the cladding at its shallowest point after polishing, was estimated to be ~1µm, by measuring the throughput of a laser with an appropriate index matching oil covering the polished region [5.16]. The end-points of the grating were an additional ~8 microns deeper into the cladding than its central point, due to its curvature. Now in the form of a D-fibre, the grating's evanescent field could be accessed [5.24]. However, the position of scanning did not deviate from the centre of the grating further than 1mm in either direction, to ensure that the additional depth of cladding in the scanning region did not exceed 500nm.

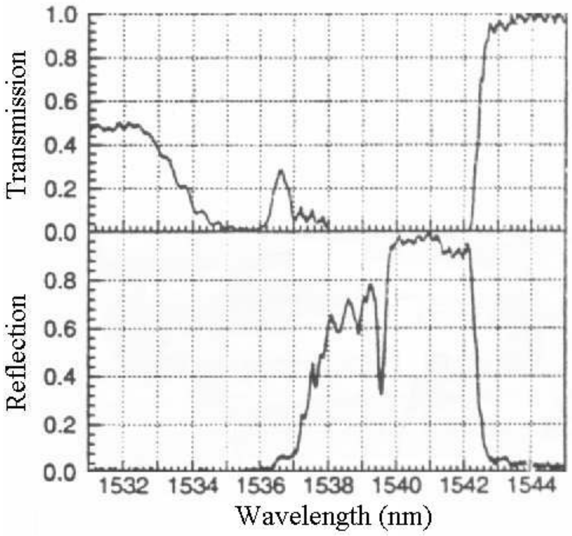

Figure 5.5: Transmission and reflection spectra of Fibre Grating Sample No.1 [5.23].

The reflection spectrum of the sample, which can be seen in Figure 5.5, shows the first order Bragg wavelength λ_B, to be at ~1540nm. To maximize detection efficiency, it was decided to work at second order resonance λ_2, at about half this wavelength, where the bandwidth of reflection ranged from ~774-778nm for the LP_{01} mode. The second order wavelength does not correspond to exactly half the Bragg wavelength due to the variation of refractive index of the fibre (and its grating), as a function of wavelength. However, with a single mode cut-off of 1250nm, second order wavelengths would inevitably cause many modes to propagate along the fibre. In order to avoid the scrambling of the modes, it was necessary to minimize the fibre's length. This was achieved by trimming the pigtails of the fibre to the length of the 44mm glass block and further polishing its end faces to ensure that light could be coupled easily into the grating, and the mode pattern examined at its output. The end-face polishing consisted of firstly lapping with a de-ionized water solution of 9µm Al_2O_3 powder, followed by polishing for ~20 minutes with syton. The condition of the surface was monitored periodically with a microscope.

5.4 Experimental Procedure

During all evanescent field SNOM scanning of fibre Bragg gratings contained within this chapter and subsequently within *Chapters 6-7*, an uncoated tip was used to collect the data. Details of the preparation of the probe are contained within *Chapter 3* along with a description of the scanning procedure. Any additional details not covered in *Chapter 3* will be explained in this section. Evanescent field scans of Fibre Grating Sample No.1 were also carried out with an aluminized tip incorporating a tiny aperture during the early stages of this project, with no apparent increase in resolution. Details of this type of tip production are again included in *Chapter 3* with an example of an image collected by this method displayed in *Appendix* E.5.3.

Prior to evanescent field scanning, the position of the grating was checked under a microscope by noting where its exposed cladding either side of the grating became buried into the glue due to the fibre's curvature within the block. After the glass block was cleaned with lens tissue and acetone, it was placed upon the sample platform in order to perform a test scan upon its surface, to check that the platform was level. One end of the block was then raised by positioning it upon metal washers so that the base of the block formed an angle of 2.2 degrees with the platform. This ensured that a laser could be launched parallel to the input axis of the slightly curved fibre.

Once this had been achieved, a Martock Design Ltd. translation stage supporting a horizontally positioned x10 objective was aligned to point along the fibre's axis. As can be seen in Figure (5.6), two mirrors were also used in order to ensure the laser, which was launched from outside the thermal housing, would propagate along the same axis. Any light that was reflected from the grating back along this path was separated by means of a 50:50 beam splitter to become incident upon a further x10 objective via two aligning mirrors, which focused the reflected light into a 50μm core multi-mode fibre. This fibre in turn delivered the reflected light to an Anritsu Corporation Optical Spectrum Analyzer MS9001A that had a resolution of 0.1nm. Within the thermal housing, a Newport 818UV photo-diode was connected externally to a Newport 840 Optical Power Meter to monitor the intensity of light passing through the grating.

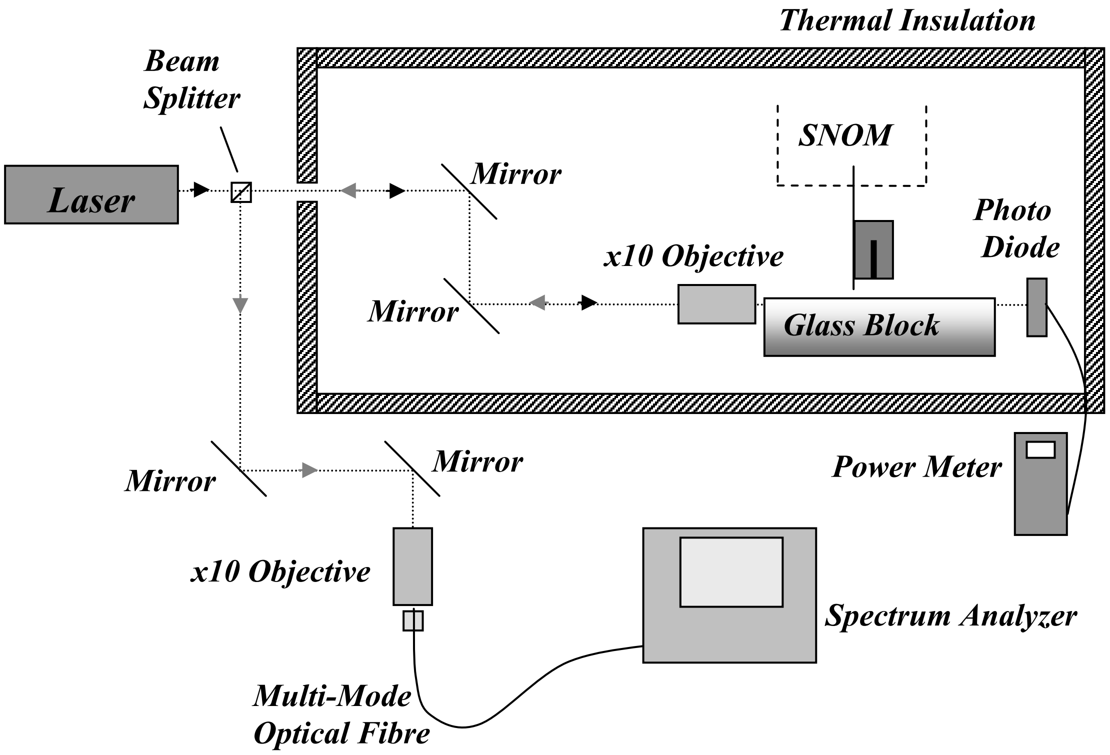

Figure 5.6: The experimental set-up during the evanescent field SNOM scanning of Fibre Grating Sample No. 1.

A piece of white card was periodically positioned either between the block and the photo diode or between the beam splitter and the spectrum analyzer to inspect both the forward and backward propagating mode patterns exiting the fibre. For all of the data presented in this chapter, a single-mode pattern was clearly evident on the card, both before and after each scan. Scans taken where doubt existed about the modal pattern are not presented here. However, examples of two-dimensional scans where thermal instability associated with the laser launch angle caused higher modes to be randomly introduced, are shown in *Appendix* E.6.1. Although neither the forward nor backward modal patterns were monitored during a scan due to thermal isolation of the SNOM laboratory, the developing image viewed on a computer screen external to the laboratory gave a clear indication of any modal variation. The total energy transported via the evanescent field [5.19] varied during such periods, causing obvious jumps in measured intensity.

Two types of laser were utilized during the experiment, a Spectra-Physics 0.95mW HeNe laser at 632.8nm and a New Focus, Inc. 6100 single frequency External Cavity Tunable Diode Laser with a range 772.2-788.7nm and maximum power 5mW. The height of the SNOM probe in all of the scans presented in this chapter was ~10-20nm above the sample surface. In order to ensure maximum resolution and to guarantee against unwanted artifacts due to tip damage, the SNOM probe was regularly replaced.

5.5 Results and Discussion

The data presented in this section was collected as a result of scanning the evanescent field of Fibre Grating Sample No.1 described in *Table 5.2*. A general discussion throughout the section continues in view of the ongoing characterization of the scanning procedure.

5.5.1 Constant Gap Evanescent Field Imaging Of A Fibre Grating

5.5.1.1 On-Resonance vs Off-Resonance

The New Focus diode laser was launched into the grating on second order resonance at a wavelength of 774.8nm. Figure 5.7(a) shows the result under this condition of a 3.79μm x 3.79μm scan with 63nm pixel size. The axis of the grating is down the centre of the image and the position of the image is in the region central to the grating. The standing wave pattern with fringes of average period $\Lambda/2$=262nm can be observed, which have produced

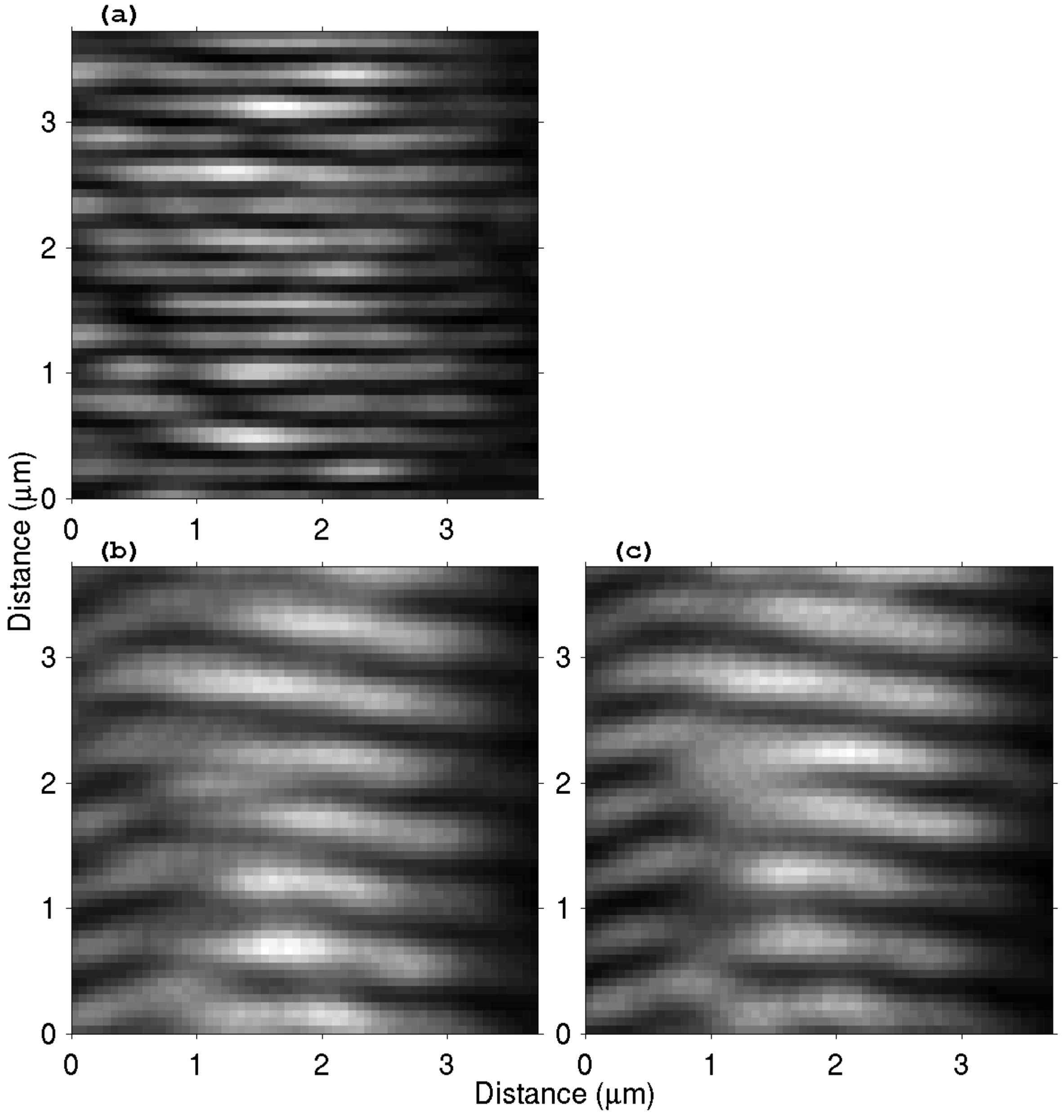

Figure 5.7: Evanescent field images of Fibre Grating Sample No.1. Photons were counted for one second per data point. (a) On second order resonance (774.8nm) with fringes of 262nm period. The area shown has dimensions 3.79 x 3.79 μm with 60x60 pixels. (b) Off-resonance scan over the same area as that shown in (a) with laser tuned to wavelength 784.0nm. (c) Repeat scan of (b), taken immediately afterwards. The axis of the grating is down the centre of the image in each case. Similar 'on' and 'off' resonance scans taken in a different region of this grating are illustrated in Appendix E.5.1.

strong changes in I_{cl} along the grating. Close examination reveals that there is a degree of non-uniformity in the intensity distribution across and along the grating due to the effect of the local decay constants, but also to phase errors resulting from non-uniformity in Λ itself. This becomes clear by comparing Figure 5.7(a) to Figure 5.7(b), which shows a non-resonant scan in the same position, with $\lambda = 784.0$ nm. In this figure, the electric field intensity I_{cl} along the grating is approximately flat, allowing local variations in n_{e} to dominate the detected signal. As can be seen, the refractive index contrast along the grating is clearly not uniform, although the average period Λ is (505±20)nm, which can be compared to the expected value of half the phase-mask period, $a/2 = 524$nm. Inspection of Figures 5.7(a) and (b) illustrate that the standing wave is indeed superposed above the refractive index data (having been subject to its range of decay constants through 1 μm of cladding), although this fact alone cannot account for all of its non-uniformity.

Figure 5.7(c) shows the result of a repeat scan carried out on immediate completion of the scan shown in Figure 5.7(b), with identical parameters. Although these two images are very similar, there are some variations which are probably caused by thermal drift due to the length of the scans each being ~75 minutes long. Drifts of this nature were shown to occur during the characterization of the SNOM apparatus in *Chapter 3*, and in general have been found not to exceed a range of ±20nm in both the x and y directions, over scans lasting several hours. However, this is subject to the laboratory having reached a state of thermal equilibrium, which as a rule, has taken anything up to 24 hours to achieve, after all of the necessary electrical equipment has been switched on. During the collection of data for Figure 5.7, it is likely that thermal equilibrium was not fully optimized since the drift is >20nm. Figure 5.7(c) also appears to have reduced resolution compared to Figure 5.7(b). This may be a result of sustaining damage to the tip during earlier scans.

The non-uniformity of the refractive index fringes shown in the off-resonance scans of Figures 5.7(b) and 5.7(c) may be caused by the following reasons. When the grating was excited on second order resonance at 774.8nm, the reflected power was ~60% of the input power. Gratings that display this degree of second order reflectivity have generally been irradiated for a longer period of time during writing than conventional Type I gratings, since this order of reflection takes a longer period of time to grow than the first order. The growth of the second order has been correlated to the saturation of the first order reflection, as a function of laser exposure time [5.25]. In the case of Fibre Grating Sample No.1, the probable extended exposure may have caused small temporal drifts to occur in the position of the fringe pattern relative to the fibre, which in turn may have led to perturbations in the index profile [5.25]. Additionally, the low spatial coherence and wave-front phase distortions of the excimer-writing laser itself may have also contributed to the non-uniformity of the fringes. The measurements shown in *Chapter 4* of free-space patterns above a phase-mask indicate that distortions can be considerable for incident lasers with non-uniform wave-fronts.

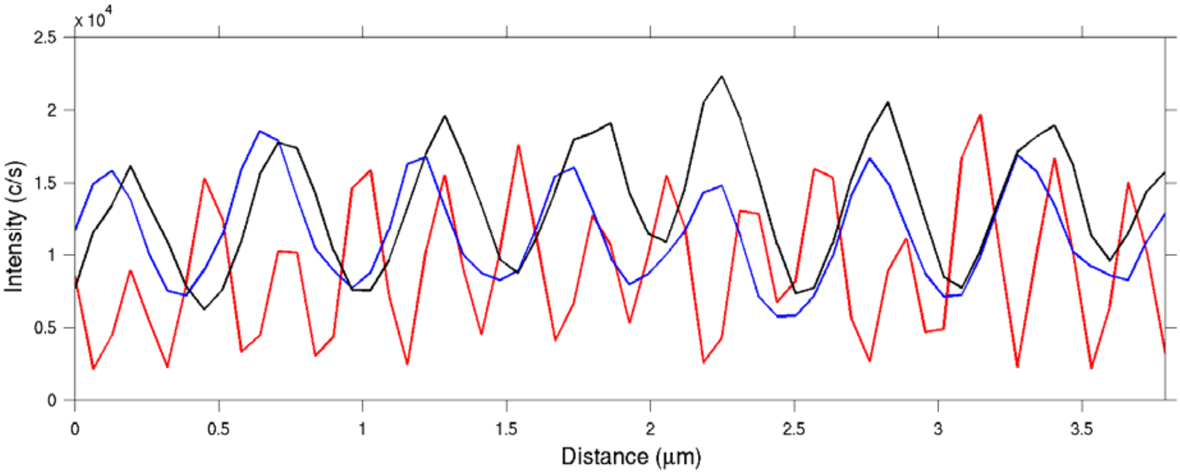

Figure 5.8: Cross-sections of the images displayed in Figure 5.7, In each case, the line of data has been taken from the central column of the image matrix, believed to be directly above the axis of the grating. The red line represents a cross-section of Figure 5.7(a), the blue line represents a cross-section of Figure 5.7(b) and the black line is the cross-section of Figure 5.7(c).

Figure 5.8 offers completeness to Figure 5.7 by comparing cross-sections of all three images. In each case, the line of data has been taken from the central column of the image matrix, believed to be directly above the axis of the grating. The standing wave of Figure 5.7(a) is represented by the *red* line, whilst the 'off resonance' figures of 5.7(b) and 5.7(c) are represented by the *blue* and *black* lines respectively. As can be seen from these cross-sections, the 'off resonance' lines have double the period of the 'on resonance' data, but with reduced contrast. Comparison of the 'off resonance' lines alone, confirms that thermal drift occurred during these scans, as predicted from their two-dimensional images, shown in Figures 5.7(b) and 5.7(c).

5.5.1.2 An Estimation Of Δn From The Off-Resonance Ratio Of Intensities

The ratio of intensities between bright and dark regions in both of the 'off resonance' cross-sections shown in Figure 5.8 indicate that the variation in the index Δn along this section of the grating is of the order 4-6 x 10^{-3} which agrees remarkably well with the Δn of the grating given in *Table 5.2*, which was calculated from the reflectivity and dimensions of the grating. This indicates that the contrast mapping of the 'off resonance' profile is a method that can be employed to estimate the Δn along gratings in general. This technique would be particularly useful for apodised gratings, which do not have a uniform Δn along their length. Evident also in Figure 5.8 are the phase and amplitude errors in Δn.

5.5.1.3 One-Dimensional Resonant Line Scans

In order to examine the standing wave further, a more detailed line scan along the axis of the fibre grating was carried out and can be seen in Figure 5.9(a). With 1024 data points at one second per point, the 19.61μm scan took ~17 minutes to complete. The oscillations are clearly irregular, and this is caused by phase errors in the standing wave. The data is therefore further evidence that a significant non-uniformity exists in the periodicity of this grating. Figure 5.9(b) shows a repeat of the scan shown in Figure 5.9(a) started immediately afterwards. A 10μm section from both scans between positions 5-10μm is shown in Figure 5.9(c), where a small (29nm) shift due to thermal drift (easier to determine in the one-dimensional case) is present. The data is reproducible within statistical uncertainty (i.e. within the uncertainty given by the Poisson probability distribution, $\pm[c/s]^{1/2}$). The simultaneously acquired topographical data of these two evanescent field scans are plotted in Figure 5.9(d). Some of the measured features on the surface of the polished cladding which are <1nm in height have shown up in both scans. However, a few unwanted glitches have appeared in parts of the data probably caused by building vibration.

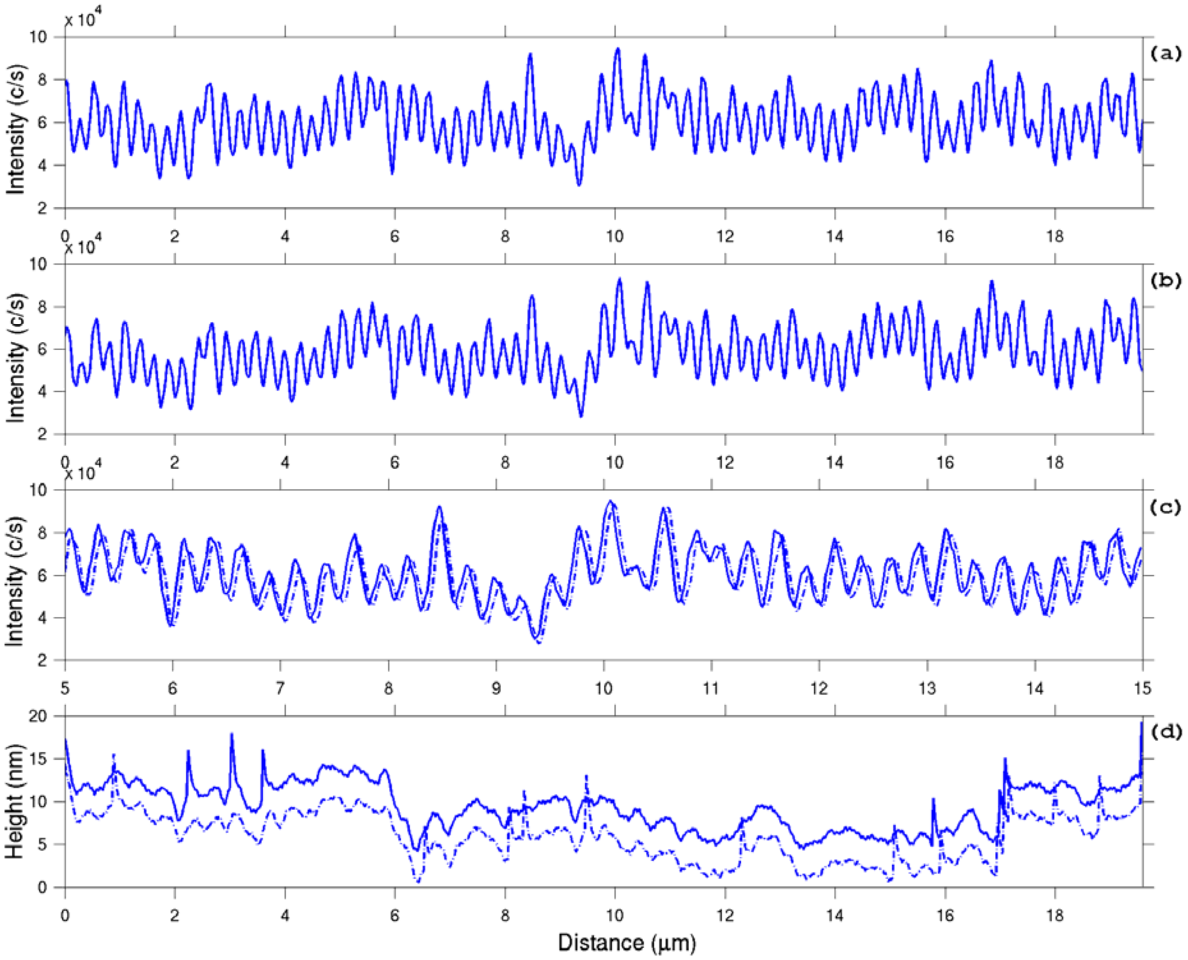

Figure 5.9: (a) A 'second order resonance' (774.8nm), 19.61μm scan along the axis of the fibre grating close to its central region, with 1024 data points. (b) A repeat of the scan shown in (a) taken immediately afterwards. (c) A 10μm section of the repeat scans shown in (a)(line) and (b)(dashes) in the range 5-15μm. (d) The topographical data associated with (a)(line) and (b)(dashes). This data has been rotated to account for the slope of the sample. The two topographical scans have also been shifted relative to each other by a small amount for clarity.

The irregularity of the envelope of the standing wave was investigated further by taking data along a greater length of the grating's axis. Although the piezoelectric stage upon which the SNOM probe was mounted had a maximum range of 20μm, by careful handling of the coarse adjustment (13.3μm per quarter turn) a longer region of data could be acquired. By allowing time for the apparatus to become thermally stable in between scans, three data sets were obtained and joined by identifying similar features in the intensity profile. The result can be observed in Figure 5.10 where the fringe irregularity is still evident. Rather unexpectedly, even scans covering several hundred microns along the axis of this grating reveal no uniform structure.

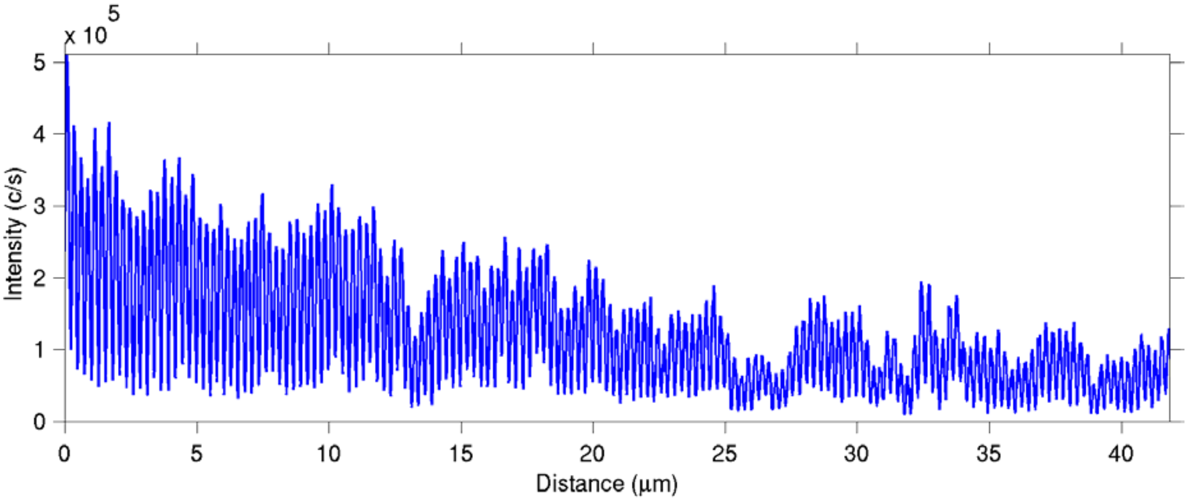

Figure 5.10: A 41.85 μm scan along the axis of the grating on second order resonance, (774.8nm). The period of the fringes is 262nm and there are 2182 data points.

The second order standing waves of Figures 5.9(a) and 5.10 each had a Fast Fourier Transform (FFT) performed on them, with the results displayed in Figures 5.11 and 5.12 respectively. There is an obvious main peak in each case, which corresponds to the standing wave fringes of 262nm period. In both figures there are also peaks at half this frequency, which represent the secondary modulation due to the periodically varying decay constant of the grating. There also appears to be high frequency periodicity hidden in the data, which can be clearly seen in both FFT's with a period of about 3-8 data points. This is characteristic of a sample that has surface contaminants that cause the SNOM probe to stick. During the early stages of this project, the 'sticking' effect appeared as noise in both the optical and topographical data, as it was not always convenient to surface-clean samples

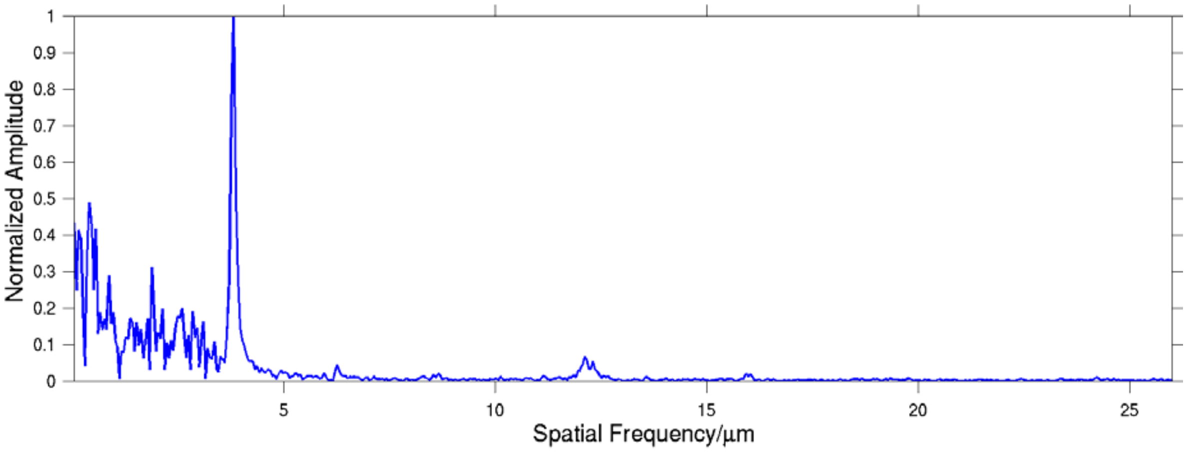

Figure 5.11: FFT of the standing wave data displayed in Figure 5.9(a) which covered a length of 19.61 µm. The dc component of the FFT has been excluded for clarity. The main peak corresponds to a frequency of 3.82µm^{-1}, (period of 0.262µm). There is also a clear peak at half this spatial frequency 1.91µm^{-1}, (period of 0.524µm), which illustrates that the standing wave is modulated by the variation in decay constant, caused by the refractive index profile of the fibre grating.

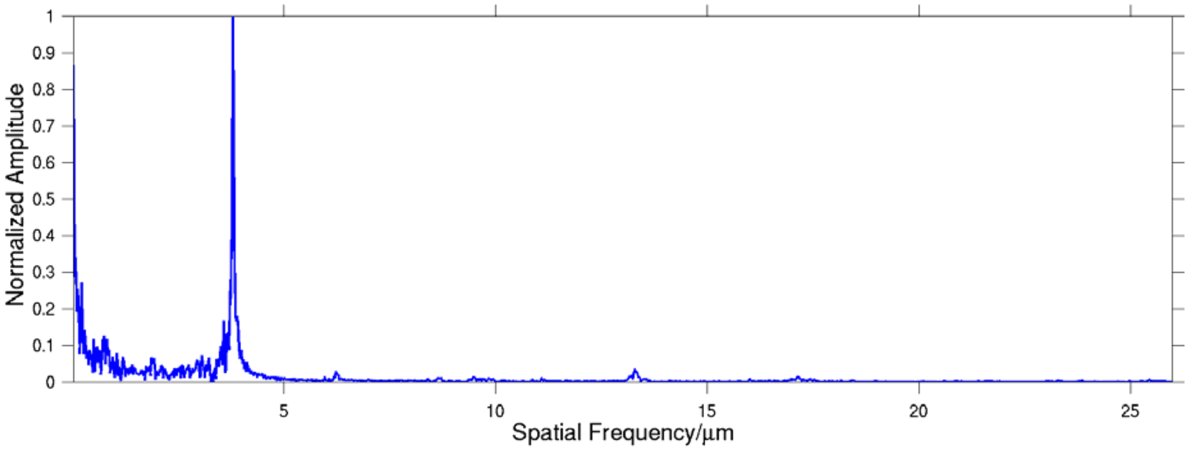

Figure 5.12: FFT of the standing wave data displayed in Figure 5.10, which spanned a length of 41.85 µm of the grating. The dc component has again been excluded for clarity. The very sharp main peak corresponds to the standing wave fringe frequency. A small bump exists at half the frequency showing the component of modulation caused by the refractive index profile. In both Figures 5.11 and 5.12, the higher frequency periodicity is probably caused by the SNOM probe sticking, due to surface contaminants.

during a series of experiments. The SNOM computer control program was subsequently modified to enable each data point 'step' to be broken down into many 'sub-steps'. This action virtually eradicated the problem.

5.5.1.4 The Effect Of Moving Far From Resonance

The evanescent field images displayed in Figures 5.7(b) and (c) which reveal the refractive index contrast have an 'off resonance' incident laser wavelength close to (~6nm) the edge of the second order reflection bandwidth. In order to confirm that the ensuing periodic contrast measured in the evanescent field was indeed related to the refractive index and not

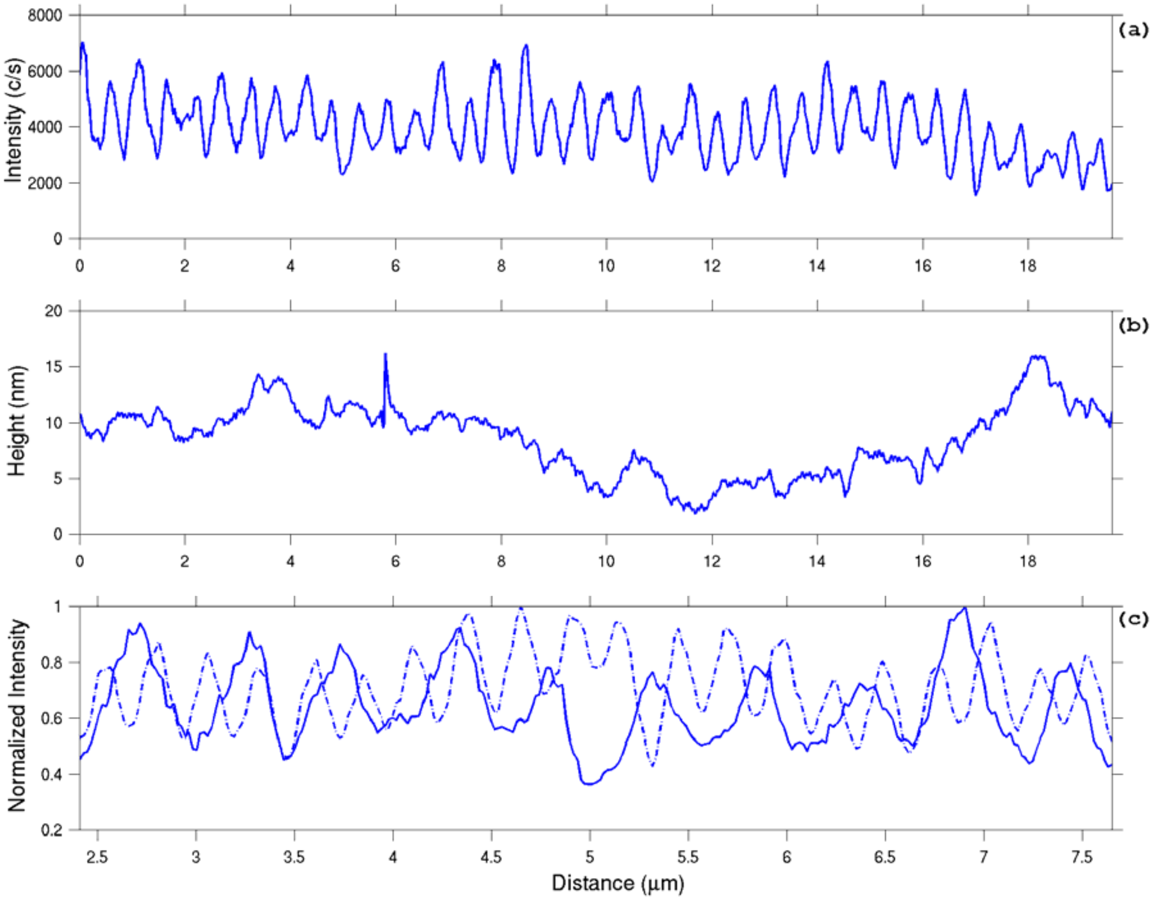

Figure 5.13: (a) A 19.61µm 'off resonance' line of data with 1024 points, along the fibre grating's axis. The illuminating laser was a HeNe at 632.8nm. (b) The topographical data collected simultaneously with the optical data shown in (a). (c) A section of the optical data shown in (a)(line) along the length 2.41-7.67µm compared to an identical length of standing wave data (dashes) from Figure 5.9(a).

to the laser frequency itself, a HeNe laser with wavelength λ = 632.8nm was launched into the grating. The result of a 19.61μm line scan along the grating's axis under this condition is shown in Figure 5.13(a). The measured period of (524±3)nm agrees extremely well with the expected period Λ=524nm, which is derived from the dimensions of the phase-mask itself. This confirms that the measurement is in fact due to the rate of decay of the evanescent field, determined by the refractive index of the core. The longer off-resonance scan shows that the modulation in refractive index Δn along the grating length is uneven due to both phase and amplitude errors. This has clearly contributed to the noise in the standing wave identified earlier.

The associated topographical data of Figure 5.13(a) is shown in Figure 5.13(b), having been rotated to account for the slope of the sample. As in the topographical data of Figure 5.9(d), surface features that are less than 1nm in height have been detected. There also appears to be one 'glitch' in the data at about the 6μm point, probably due again to building vibration.

A comparison of a section of the optical data in Figure 5.13(a) taken from points 2.41μm to 7.67μm, to an identical length of standing wave data from Figure 5.9(a), is shown in Figure 5.13(c). The 'off resonance' data (line) exactly overlays the 'on resonance' data (dashes) by a period ratio of 2:1 as expected.

5.5.1.5 Visual Identification Of Topographically Induced Artifacts

When inspecting one-dimensional line scans such as those displayed in Figures 5.9 and 5.13, it is not immediately obvious how the variation in topography may have affected the optical data. However, unequivocal evidence of the effect can occasionally be found in two-dimensional images that include isolated 'bumps' of sufficient height. An example of this can be seen in Figure 5.14, where topographical features circled in Figure 5.14(b) are clearly evident in the associated optical data of Figure 5.14(a). These isolated 'bumps' are about 20nm in height and 200nm wide.

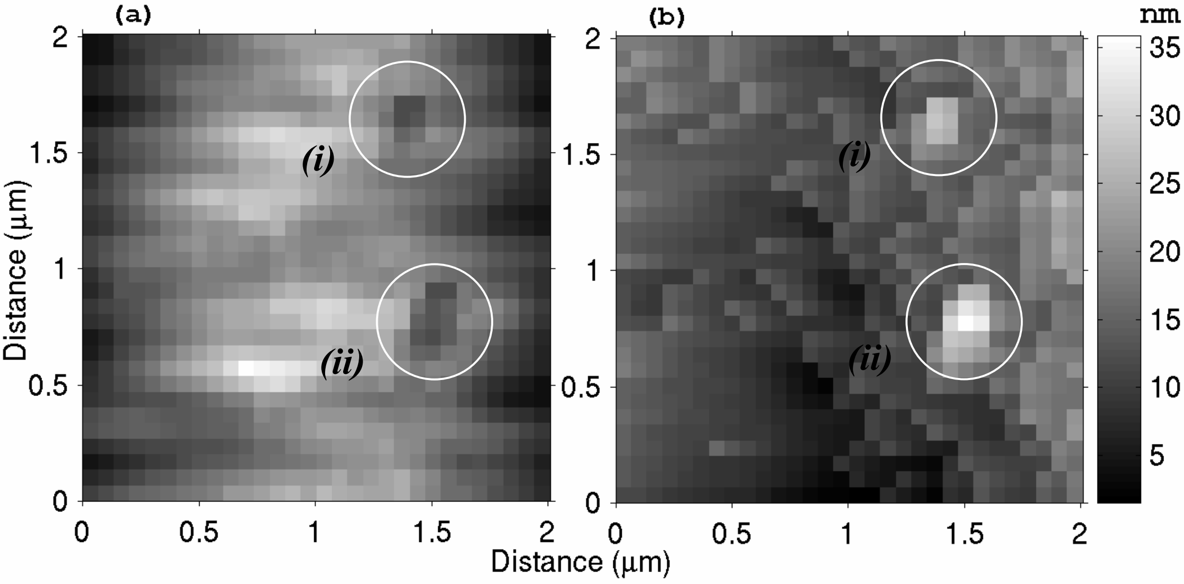

Figure 5.14: The effect of topographical artifacts on the optical data. (a) shows part of an evanescent field scan with (b) displaying the simultaneously acquired plane-removed topography. The image has dimensions 2.077µm x 2.077µm with 31x31 pixels. The wavelength of the illuminating light is tuned to resonance.

Cross-sections of both figures through their marker circles can be seen in Figure 5.15. The artifacts contained within the marker circles (i) have their optical and topographical cross-sections displayed in Figures 5.15 (a) and (b) respectively, and the artifacts contained within marker circle (ii) have their cross-sections shown in Figures 5.15 (c) and (d). Given the experimental parameters, a reduction of about 9% in the optical data would be expected for an increase in cladding depth of 20nm. The cross-sections shown in Figure 5.15 indicate that this calculation may be an underestimation because the optical data reduces in intensity in the artifact regions by about 20%. It may be that there was an over-estimation of the final cladding thickness during the polishing process, which would account for some of the variation. However, it is expected that the actual cladding depth does not vary by more than 5% from the estimated depth of ~1µm. This is due to the estimated value being used to accurately determine the Δn of the grating from the intensity contrast, earlier in this section. It is however possible, that the decay constants are slightly different in the region of the artifacts. This is because the smaller the surface detail, the higher the decay constant, and consequently the stronger the field confinement over the surface [5.27]. Since the occurrence of such small artifacts with comparable changes in height are very rare on the samples imaged during this project, it is not expected that either general evanescent field imaging, or the topography-normalization routine described in *Section 5.2.3*, will be greatly affected by any such irregularity.

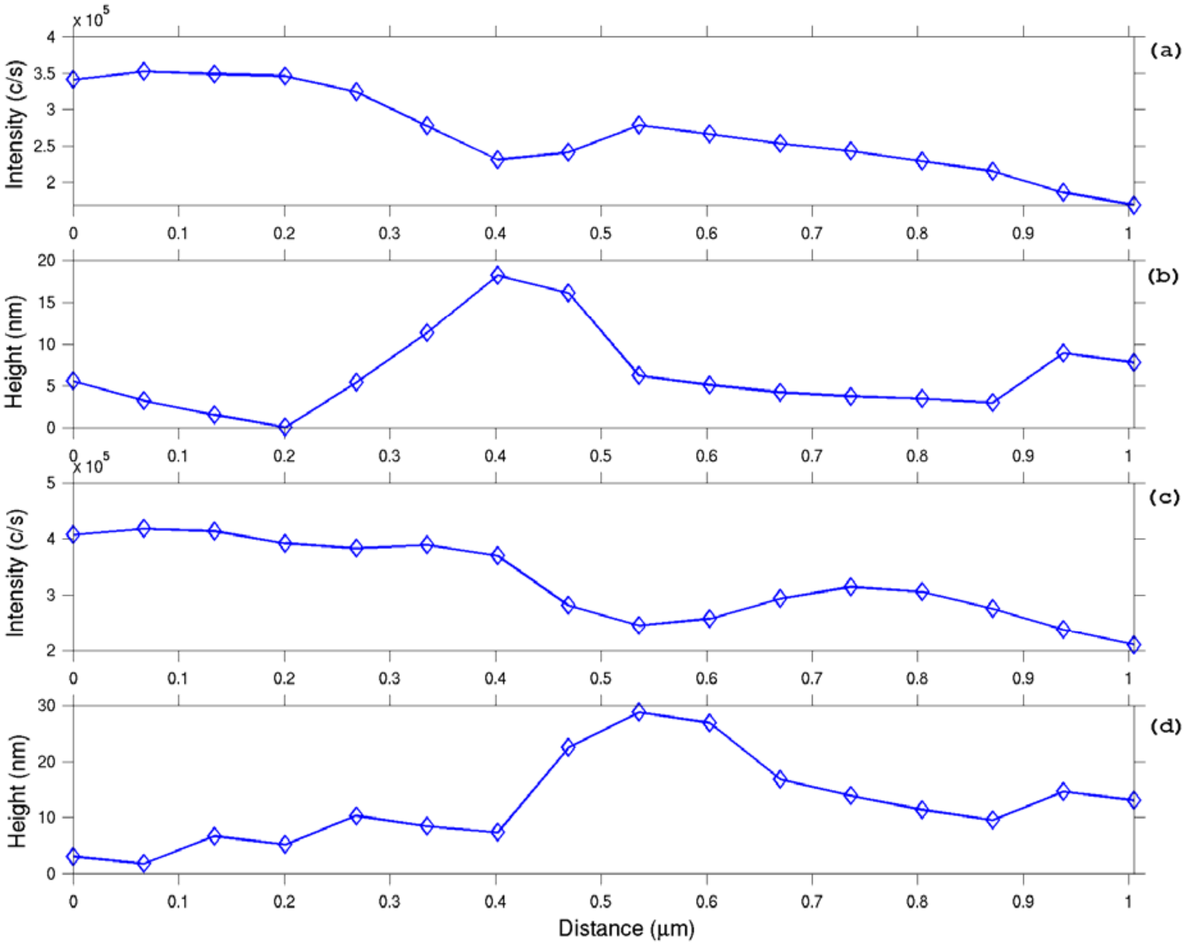

Figure 5.15: Cross-sections of the optical and topographical images shown in Figure 5.14. (a) A cross-section through the region of the marker circles no. (i) in the optical data, and (b) its corresponding topographical cross-section. (c) A cross-section through the region of the marker circle (ii) in the optical data, and (d) its corresponding topographical cross-section. Each cross-section has a length of 1.005μm.

5.5.1.6 Large Scale Two-Dimensional Images

Figure 5.16(a) shows a larger scan on second order resonance at λ = 774.8nm with dimensions 10.19μm x 10.19μm and with 128x128 pixels. The image presents several other interesting details for discussion. As in previous 'on resonance' scans, the standing-wave fringes are 262nm apart. However, the greater dimensions of this image compared for example to Figure 5.7, offer a clearer picture of phase errors in the standing wave. There appears to be a secondary modulation in the form of undulations, which occur diagonally to the axis of the grating.

The simultaneously acquired topographical data is displayed in Figure 5.16(c). This shows that the darker region towards the top of the optical image is caused by the SNOM probe increasing its height by ~200nm. This was not surface-feature induced, as the data was not repeatable. The most likely explanation is that the probe attracted dust, which in turn dampened its oscillation and caused it to be temporarily raised by the feedback electronics. A feature that is real, is marked by the circle in Figure 5.16(c). Here, the raised topography again has an effect on the corresponding optical data, although it is not so pronounced as in the cases of Figure 5.15. Finally, in a large region of the topographical image surrounding its centre, there are many ridges probably caused by the polishing process. Fortunately, as in the artifacts of Figure 5.15, this was a rare occurrence and indeed was only ever recorded once. However, it has caused substantial periodic defects to arise in the optical image perpendicular to the grating's axis.

A large 'off resonance' image is shown in Figure 5.16(b). The dimensions of the scan are 10.48μm x 10.48μm with 128 x 128 pixels. A HeNe laser (λ = 632.8nm) was used to illuminate the grating. The index profile has an average period $\Lambda = (522 \pm 44)$nm, again demonstrating the independence of the non-resonant image to the wavelength of laser used. Towards the centre of this image a faint standing wave can be seen with fringes corresponding to $(632.8/2n)$nm, probably formed by reflection off the back face of the glass block. Scattered light can be observed within the cladding region on either side of the image. The obvious curving of the fringes may be due again to the excimer writing laser. *Chapter 4* showed free-space, phase-mask induced diffraction patterns where either misalignment, or a non-uniform wave-front of an incident beam, caused various angled planes to occur. If this type of irregularity were the case here, not only would it explain the

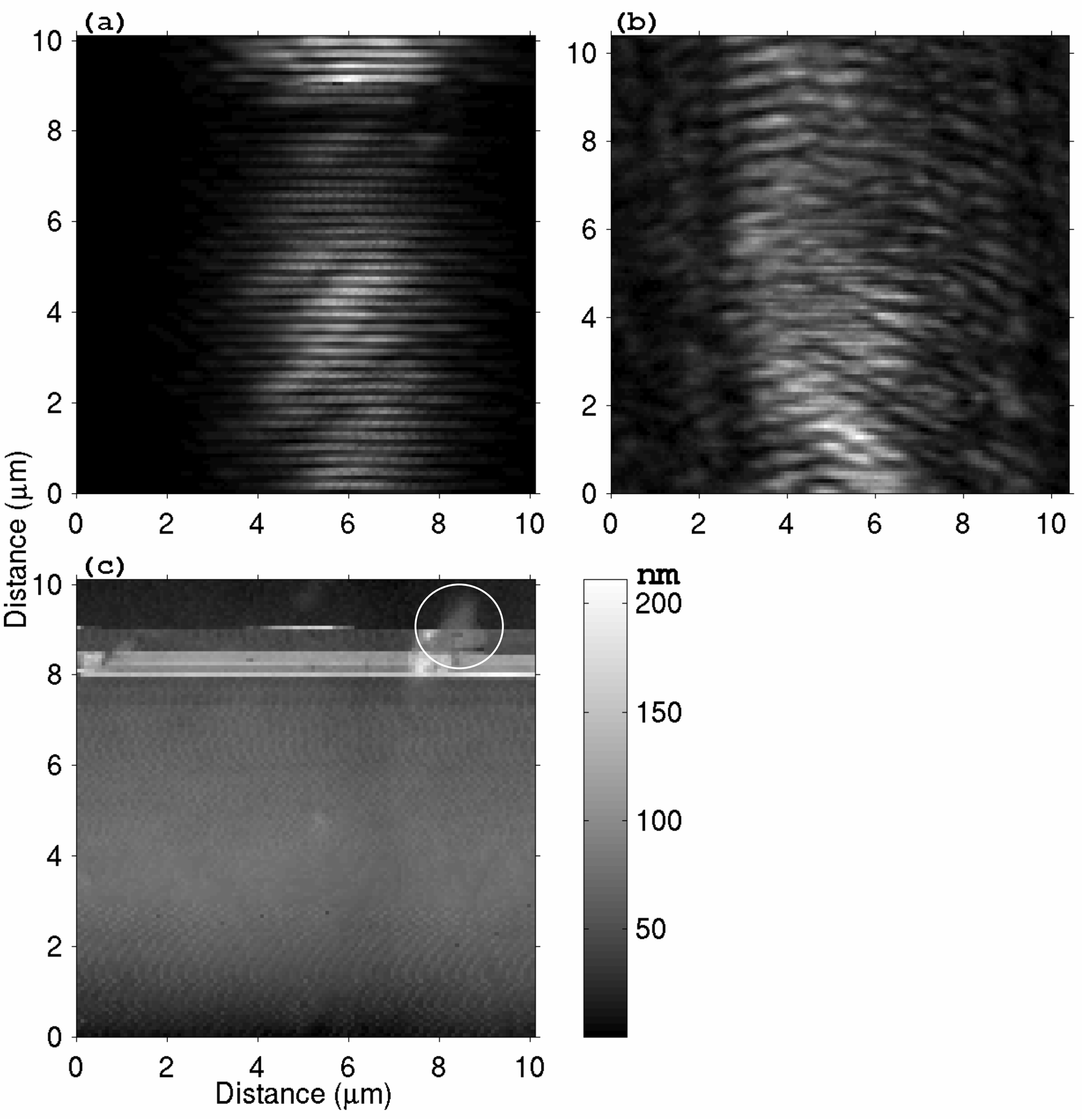

Figure 5.16: (a) A 10.19µm x10.19µm image with the illuminating laser tuned to second order resonance at wavelength λ=774.8nm. The standing wave fringes are 262nm apart and the pixel matrix is 128 x128. (b) A 10.48µm x 10.48µm 'off resonance' scan with the HeNe laser (λ=632.8nm) launched into the grating. Again, there are 128 x 128 pixels. (c) Topographical data acquired during the 'on resonance' image shown in (a).

apparent orientation of the fringes relative to the cylindrical core, but their inherent tilt would also indicate a possible cause of some of the radiated loss, discussed earlier in this chapter [5.28]. The scattering loss is exemplified by the transmission spectrum of the grating shown in Figure 5.5, where wavelengths shorter than the Bragg wavelength have been tapped out of the fibre.

The overall appearance of the data in Figure 5.16(b) has very similar characteristics to one derived by the imaging of a fibre Bragg grating with diffraction limited Differential Interference Contrast [5.29]. By this method, the refractive index of the grating was constructed by recording the phase shift of a light field passing through a grating.

5.5.2 Decay Constant Measurements

A measurement of the exponentially decaying evanescent field of the fibre Bragg grating in a direction normal to its surface enables the local effective refractive index of the grating to be estimated from its decay constant, which in turn can be approximated by utilizing the planar waveguide theory described earlier in this chapter. Such measurements were carried out on Fibre Grating Sample No.1 but before doing so, the overall grating effective refractive index was calculated. This was achieved by measuring the standing wave fringes at a known wavelength with a carefully calibrated piezoelectric stage. The average modal effective refractive index of the grating at $\lambda = 774.8$nm was subsequently calculated to be 1.476 ± 0.005. It is expected that the index at $\lambda = 784.0$nm would differ by <0.1% from this figure.

From the planar Equation (5.9), the following expression can be derived

$$\ln(-\mathrm{d}I/\mathrm{d}z) = \ln(2rI_0) - 2rz \tag{5.20}$$

where a gradient of its plot will yield the decay constant - $2r$, which in turn will give the value of n_e from Equation (5.7). With the incident laser wavelength off grating resonance at $\lambda = 784.0$nm, a test line scan at the centre of the grating, similar to that shown in Figure 5.13(a) with the tip locked into the surface, was performed. Having done so, the probe was then moved to an identified position of high intensity in the evanescent field, directly above the axis of the grating. With the SNOM tip then taken out of lock, it was placed at a convenient z-scan starting height. Four consecutive scans were taken, each one 262nm ($\Lambda/2$) away from the previous, in order to identify points of maximum and minimum refractive index. The details are shown in Figure 5.17 with a summary of the results displayed in *Table 5.3*. In each scan, the start height of the tip was very close to 0nm with subsequent 10nm steps in the *z* direction. In Figures 5.17 (a) and (e), the probe is actually in contact with the surface, producing a lower than expected intensity in the first data point, probably caused by the tip bending. To ensure the best measurement of the decay constants, the first data point in all scans was therefore excluded from the subsequent analysis. The refractive index of air n_0, was assumed to be 1.000.

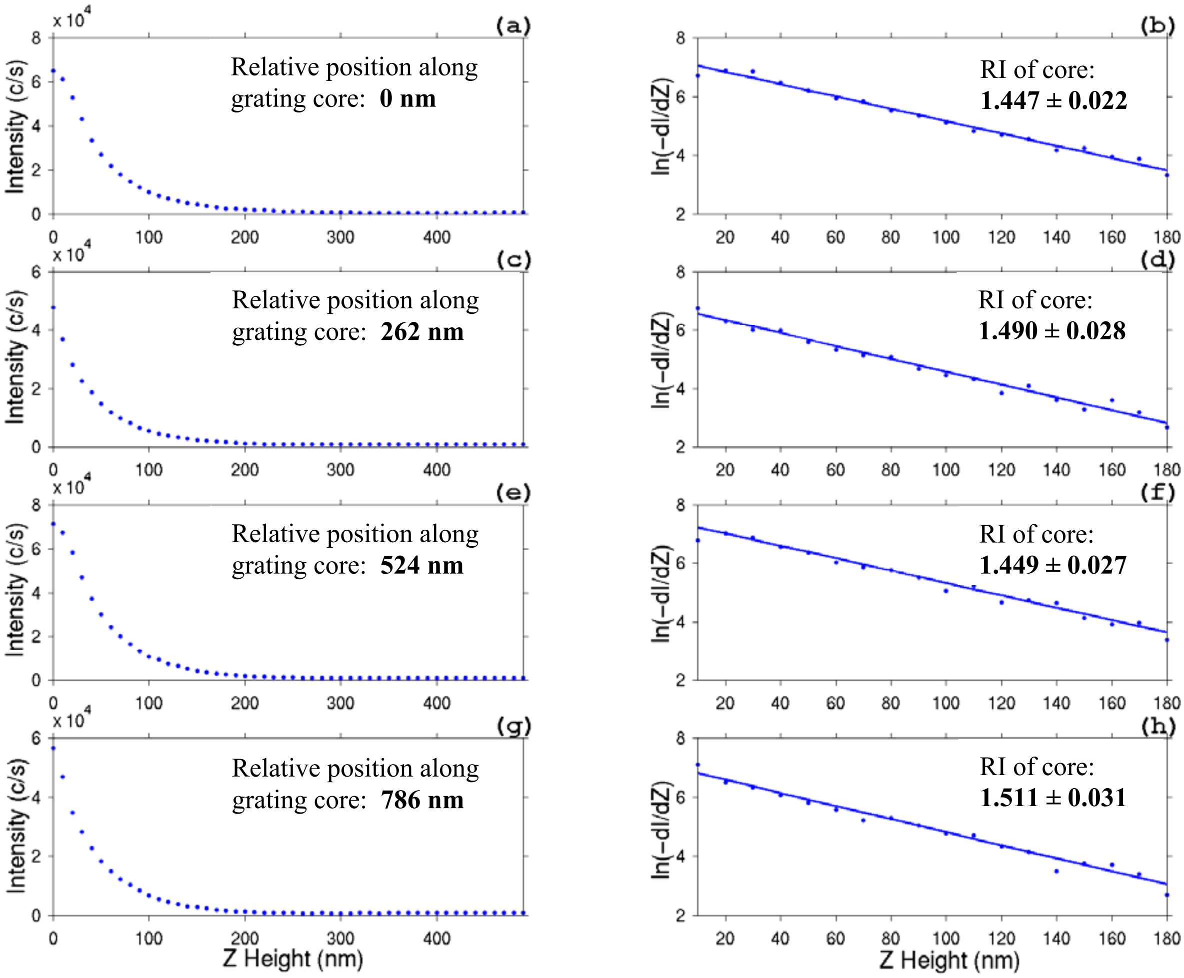

Figure 5.17: An estimation of the effective refractive indices derived from vertical z line scans of the evanescent field above Fibre Grating Sample No.1. Each exponentially decaying data set on the left is accompanied on the right by its associated plot of ln(-dI/dz) vs. z.

Relative Position along grating (nm)	*0*	*262*	*524*	*786*
Measured Intensity at Surface I_0 *(c/s)*	*65313*	*47844*	*71363*	*56715*
Decay Constant $-2r$ *(nm*$^{-1}$*)*	0.0207 ± 0.0006	0.0219 ± 0.0007	0.0208 ± 0.0007	0.0224 ± 0.0008
Decay length δ *(nm)*	48.3 ± 1.4	45.7 ± 1.4	48.1 ± 1.4	44.6 ± 1.5
Refractive index n_e	1.447 ± 0.022	1.490 ± 0.028	1.449 ± 0.027	1.511 ± 0.031

Table 5.3: Summary of the details associated with the refractive index measurements of Fibre Grating Sample No.1. The data is approximated from vertical z direction line scans in the air above the polished surface of the grating.

From the data in *Table 5.3*, a number of observations can be made. Firstly, the intensity I_0 at the surface is greatest at positions 0nm and 524nm and much lower in positions 262nm and 786nm. This is due to the decay within the cladding being slower at the former two positions than the latter two. This can be seen in the calculated decay lengths in air, which are closely related to the decay in the cladding. At positions 0nm and 524nm the decay lengths are ~48nm compared to ~46nm at the other two positions. The final row in the table presents the approximated effective refractive indices, which do in fact average out at 1.474 compared to the 1.476 ± 0.005 calculated beforehand. However, the value of Δn between subsequent scans is an order of magnitude larger than that expected as shown in *Table 5.2*, due to the approximation in the utilized theory.

5.6 Chapter Summary

This chapter has shown that it is possible to gain much information about a fibre Bragg grating from its evanescent field by applying SNOM in the scanning mode widely known as Photon Scanning Tunneling Microscopy (PSTM). The collection of data to a sub-wavelength resolution relating to the refractive index structure, grating period and electric field distribution of fibre gratings has been shown to be feasible. In particular, the position of the ‘on resonance’ standing wave field distribution has been imaged relative to the refractive index profile for the first time.

The intensity distribution in the evanescent field surrounding a fibre Bragg grating is dependent upon both the effective refractive index of the grating and the intensity of the field in the grating. PSTM has enabled a local measurement of the evanescent field to extract this information about the grating. By tuning the laser incident upon the grating on or off resonance, either the field distribution or the refractive index profile respectively, can be forced to dominate subsequent measurements. An example of this could be seen in Figures 5.7(a) and (b), where images of identical regions of the evanescent field associated with a UV irradiated, phase-mask written fibre Bragg grating (known as Sample No.1) were displayed. The 'on resonance' image in 5.7(a) demonstrated how the greatly varying field of a standing wave will dominate the image compared to 5.7(b), where the 'off resonance' image with an approximately flat electric field along the grating, allowed the refractive index profile to dominate, via its modulating decay constant. The scans have revealed non-uniformity in the index profile of the sample, which in turn has caused phase errors to occur which affect the resonant standing wave distribution. There is also evidence to suggest that the nature of the measured non-uniformity of the index fringes is responsible for the radiated loss of the grating. The irregularities are most likely to have been caused by the generally low spatial coherence of the excimer writing laser itself. There is also the possibility that the non-uniform, free-space Talbot pattern created by the 'writing' phase-mask, exacerbated the level of fringe non-uniformity. Measured examples of Talbot patterns were shown in *Chapter 4*.

The chapter has shown that the contrast of fringes in the 'off-resonance' measurements of Sample No.1 have enabled its Δn to be estimated, agreeing with the calculated value from the grating's dimensions. This technique would prove useful for apodised gratings where the Δn varies along the grating's length. In order to estimate absolute values of the effective refractive index of Sample No.1, vertical line scans were performed in a direction normal to the axis of the grating. The acquired data enabled the approximation of local decay constants by utilizing planar waveguide theory.

The average effective refractive index of the grating examined in this chapter was calculated by measuring the standing wave fringe period created by a known wavelength of light. The procedure could prove a useful alternative to the method of estimating this value from the reflection spectrum [5.30].

5.7 References

[5.1] K.O. Hill, Y. Fujii, D.C. Johnson, B.S. Kawasaki, Applied Physics Letters, **32** (10), 647 (1978)

[5.2] P.E. Dyer, R.J. Farley, R. Giedl, K.C. Byron, D.Reid, Electronics Letters, **30** (11), 860 (1994)

[5.3] R.J. Mears, L. Reekie, I.M. Jauncey, D.N. Payne, Electronics Letters, **23** (19), 1026 (1987)

[5.4] W.H. Loh, R.I. Laming, X. Gu, M.N. Zervas, M.J. Cole, T. Widdowson, A.D. Ellis, Electronics Letters, **31** (25), 2203 (1995)

[5.5] F. Bakhti, P. Sansonetti, C. Sinet, L. Gasca, L. Martineau, S. Lacroix, X. Daxhelet, F. Gonthier, Electronics Letters, **33** (9), 803 (1997)

[5.6] A. Asseh, H. Storoy, J.T. Kringlebotn, W. Margulis, B. Sahlgren, S. Sandgren, R. Stubbe, G. Edwall, Electronics Letters, **31** (12), 969 (1995)

[5.7] G. Meltz, W.W. Morey, W.H. Glenn, Optics Letters, **14**, 823 (1989)

[5.8] A.D. Heaney, T. Erdogan, N. Borrelli, Journal of Applied Physics, **85** (11), 7573 (1999)

[5.9] G. Brambilla, V. Pruneri, L. Reekie, Applied Physics Letters, **76** (7), 807 (2000)

[5.10] T. Erdogan, Journal of Lightwave Technology, **15** (8), 1277 (1997)

[5.11] M.A. Muriel, A. Carballar, J. Azana, IEEE Journal of Quantum Electronics, **35** (4), 548 (1999)

[5.12] H.E. Jackson, J.T. Boyd, Optical and Quantum Electronics, **23**, S901 (1991)

[5.13] A.G. Choo, M.H. Chudgar, H.E. Jackson, G.N. De Brabander, M. Kumar, J.T. Boyd, Ultramicroscopy **57**, 124 (1995)

[5.14] Y. Toda, M. Ohtsu, Photonics Technology Letters, **7**, 84 (1995)

[5.15] S. Bourzeix, J.M. Moison, F. Mignard, F. Barthe, A.C. Boccara, C. Licoppe, B. Mersali, M. Allovon, A. Bruno, Applied Physics Letters, **73**, 1035 (1998)

[5.16] M.J.F. Digonnet, J.R. Feth, L.F.Stokes, H.J.Shaw, Optics Letters, **10**, no.9, 463 (1985)

[5.17] D.P. Tsai, H.E. Jackson, R.C. Reddick, S.H. Sharp, R.J. Warmack, Applied Physics Letters, **56**, 1515 (1990)

[5.18] T. Erdogan, Journal of Lightwave Technology, **15** (8), 1277 (1997)

[5.19] J. Wilson, J.F.B. Hawkes, *Optoelectronics: An Introduction,* 2nd ed., Prentice Hall International (UK) Ltd., 310-334 (1989)

[5.20] A. Rogers, *Essentials of Optoelectronics: With Applications,* Chapman & Hall, 264-272, (1997)

[5.21] J.-L. Archambault, P.St.J. Russell, S. Barcelos, P. Hua, L. Reekie, Optics Letters, **19** (3), 180 (1994)

[5.22] D. P. Tsai, J. Kovacs, M. Moskovits, Ultramicroscopy, **57**, 130 (1995)

[5.23] L. Dong, P. Hua, T.A. Birks, L. Reekie, P.St.J. Russell, IEEE Photonics Technology Letters, **8** (12), 1656 (1996)

[5.24] S. T. Huntington, K. A. Nugent, A. Roberts, J. Appl. Phys. **82** (2), 510 (1997)

[5.25] W.X. Xie, M. Douay, P. Bernage, P. Niay, Optics Communications, **101**, 85 (1993)

[5.26] B. Malo, D.C. Johnson, F. Bilodeau, J. Albert, K.O. Hill, Optics Letters, **18** (15), 1277 (1993)

[5.27] D. Courjon, C. Bainier, Rep. Prog. Phys., **57**, 989 (1994)

[5.28] R. Kashyap, *Fiber Bragg Gratings*, Academic Press, 69 (1999)

[5.29] A. Roberts, School of Physics, University of Melbourne, Australia, Private Communication (2000)

[5.30] J.-L. Archambault, P.St.J. Russell, S. Barcelos, P. Hua, L. Reekie, Optics Letters, **19** (3), 180 (1994)

6. Comparative Study Of The Evanescent Fields Of Two Holographically Side-Written Multi-Mode Fibre Bragg Gratings

6.1 Chapter Introduction

The methods developed in *Chapter 5* for scanning the evanescent fields associated with polished fibre Bragg gratings will be applied to two separate samples in this present chapter. The grating samples were created with an identical technique and mounted into glass blocks some time before the commencement of this PhD project. They were originally designed to be utilized in combination, as a Grating-Frustrated Coupler [6.1]. Comparisons are made between the two samples and further contrasted with the results obtained in *Chapter 5* from Fibre Grating Sample No.1, which was made by a very different process.

6.2 Preparation Of The Samples

The two grating samples were produced from the same optical fibre and have identical parameters (summarized in *Table 6.1*), except for their Bragg wavelengths, which have

Sample identification:	Fibre Grating Sample No.2, $\lambda_B = 1550$nm
Sample identification:	Fibre Grating Sample No.3, $\lambda_B = 1535$nm
Single mode cut-off of non-grating part of fibre:	1250 nm
Fibre cladding diameter:	125 μm
Cladding material:	Silica
Core material:	Silica/Germania/Boron
Method of grating Writing:	Side exposure for ~10mins to two interfering KrF excimer UV beams
Index modulation, Δn:	$\sim 1 \times 10^{-3}$
Grating length, L:	15mm

Table 6.1: Some details of the fibre Bragg gratings used to collect the data presented in this chapter.

individual values $\lambda_B = 1550$nm (Sample No.2) and 1535nm (Sample No.3). The gratings were holographically side-written with a line-narrowed Lambda Physik EMG-150 KrF excimer laser using an interferometer arrangement similar to that in [6.2]. The uniformly periodic gratings were then mounted into pyrex glass blocks and polished down to a cladding depth estimated to be ~1μm from each core, using the methods described in *Chapter 5*. As in the case of Fibre Grating Sample No.1, the centres of the gratings were at the position of least cladding, and all SNOM scanning took place no further than 1mm in either direction from this point.

To maximize detection efficiency, it was decided to excite the gratings on second order resonance (λ_2) at wavelengths shorter than the single-mode cut-off of each fibre. Under normal circumstances, this would have caused many modes to propagate along the fibres but as in the case of Sample No.1, steps were taken to minimize this effect. By reducing the lengths of the pigtails of the gratings to ~100mm, careful alignment of the incident laser along the axis of each input fibre allowed a single-mode condition to be achieved.

6.3 Experimental Procedure

Most of the procedure carried out to acquire the SNOM evanescent field images of Fibre Grating Samples No.2 and No.3 is identical to that already detailed in *Chapter 5* for Sample No.1. The experimental set-up shown in Figure 5.6 has also been repeated here. However, there are a small number of changes, which will be described below.

As explained in *Chapter 5*, Fibre Grating Sample No.1 had its pigtails completely removed, which meant that in order to launch a laser along its axis, the glass block had to be tilted slightly to allow for the curvature of the fibre. With Samples No.2 and No.3 retaining their pigtails, this was not necessary and therefore it was convenient to allow their glass blocks to remain horizontal. The Martock translation stage supporting the x10 objective, had an additional platform attached to it, upon which a fibre mount was fixed. The cleaved ends of each input pigtail of the gratings were positioned upon the mount in turn (depending upon which sample was being scanned), and fixed with a magnet. The position of the laser, mirrors and objective were subsequently adjusted to ensure that the accurate alignment of the laser along the fibre's axis was maximized.

Thermal shifting of the fibre mount's platform relative to the objective's translating platform introduced an enhanced level of unpredictability into the system, which resulted in a number of files of data being non-usable, due to the laser switching between fibre modes. The 100mm length of input pigtail compared to the short and rigid fibre of Sample No.1 probably compounded matters. However, the occurrence was easily identifiable by a marked change in intensity of the recorded data, as described in *Chapter 5*. Examples of two-dimensional scans where thermal instability associated with the laser launch angle caused higher modes to be randomly introduced are shown in *Appendix* E.6.1. As in *Chapter 5*, for all of the data presented here, a single-mode output pattern was evident from each grating both before, and after each scan. Scans taken where doubt existed about the guided mode are not presented here.

A single laser was used during all of the experiments in this chapter: the New Focus, Inc. External Cavity Tunable Diode Laser with wavelength range, 772.2-788.7nm.

6.4 Results And Discussion

The data presented in this section was collected as a result of scanning the evanescent fields of Fibre Grating Samples No.2 and No.3, described in *Table 6.1*. Similar data sets were acquired for both samples to allow comparisons to be made. There also exist a small number of data sets exclusive to either one sample or the other.

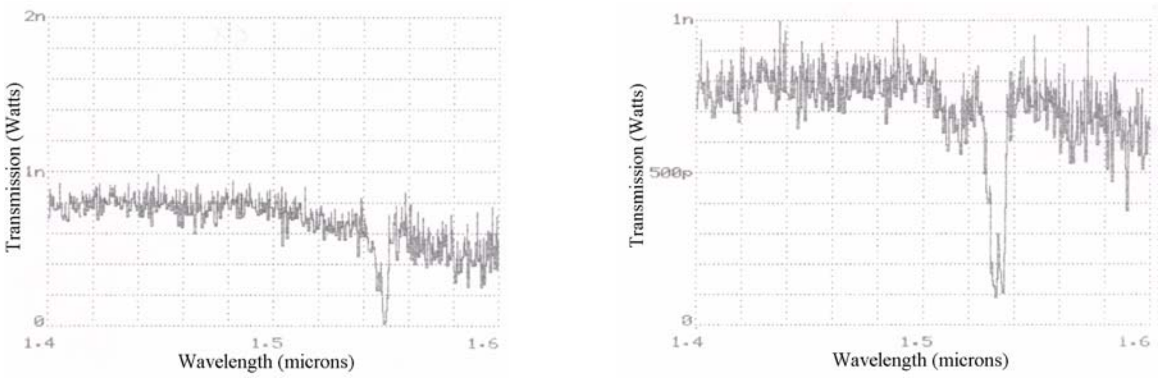

Sample No. 2 ***Sample No. 3***

Figure 6.1: The white-light transmission spectra of Fibre Grating Samples No.2 and No.3.

Initial tests were performed on Samples No.2 and No.3 to confirm their Bragg wavelengths and to determine if a measurable second order resonance could be achieved. The white-light transmission spectra of Figure 6.1 clearly confirm the Bragg wavelengths of Samples No.2 and No.3 to be 1550nm and 1535nm respectively. Similar white-light transmission spectra at about half this wavelength showed no distinguishable dips in intensity at $\sim\lambda_B/2$. Although there does not necessarily have to be a discernible second order reflection from a fibre Bragg grating [6.3], further tests using the New Focus Tunable Diode Laser showed that second order reflections were indeed possible. With greater signal per unit wavelength and therefore less noise, the laser was able to effect a detectable second order reflection from both gratings, accompanied by a reduction of ~10% in their throughput power.

The small reflection at second order may be indicative of an enhanced uniformity within the modulation of the index along the length of each grating [6.3], compared to the highly reflecting (~60% at second order), and non-uniform Sample No.1 of *Chapter 5.* Although a purely sinusoidal grating profile would cause a small second order reflection to occur, deviations from this will increase the second order reflection. This is because the profile $\Delta n(y)$, where y represents the direction along the axis of the grating, can be expanded as a Fourier series where the first order diffraction efficiency, which comes from the second sinusoidal term, will enhance the second order of the first term [6.4]. The refractive index fringe uniformity of these samples is investigated and further discussed, later in this chapter. The second order resonant wavelengths for Samples No.2 and No.3 were established to be

	Fibre Grating Sample No.2	*Fibre Grating Sample No.3*
Second order resonant wavelength, λ_2	779.0nm	773.0nm
Average effective refractive index at the second order resonant wavelength, n_e	1.475 ± 0.005	1.475 ± 0.005

Table 6.2: Details of the second order resonant wavelengths and the effective refractive indices of Samples No.2 and No.3.

779.0nm and 773.0nm respectively as displayed in *Table 6.2*. The range of wavelengths over which the gratings could be excited on resonance was estimated to be approximately 2-4nm due to the many possible excitable modes.

6.4.1 Constant Gap Evanescent Field Imaging

6.4.1.1 Determination Of The Average Effective Refractive Index

Evanescent field measurements with the SNOM probe locked to the surface of Samples No.2 and No.3 were initially carried out in order to determine the average effective refractive index of each grating at their second order resonant wavelengths. A measurement of the standing wave fringes along the axis of each grating after a careful calibration of the SNOM piezoelectric stage, yielded an index measurement of 1.475 ± 0.005 for each grating as displayed in *Table 6.2*. The agreement between the values further confirms the similarity between these two gratings. The corresponding second order standing wave fringe periods for Samples No.2 and No.3 were measured to be 264nm and 262nm respectively.

6.4.1.2 One-Dimensional Resonant Line Scans

'On resonance' line scans taken with the SNOM probe locked directly above the axis of each grating can be seen in Figure 6.2. An initial inspection of both figures shows the data to have an overall modulation depth of about 45%. This is comparable to the 'on resonance' axial line scans of Sample No.1, displayed in Figures 5.9(a) and 5.9(b). However, Figures 6.2(a) and 6.2(b) appear to contain larger period structure unlike the standing wave of Sample No.1. In particular, Sample No.3 in Figure 6.2(b) shows an interesting beating effect within the first 9μm of the scan. The data was repeatable and was not topographically induced. The variation in maximum intensity between Figures 6.2(a) and 6.2(b) is not significant and is due to a variation in laser output.

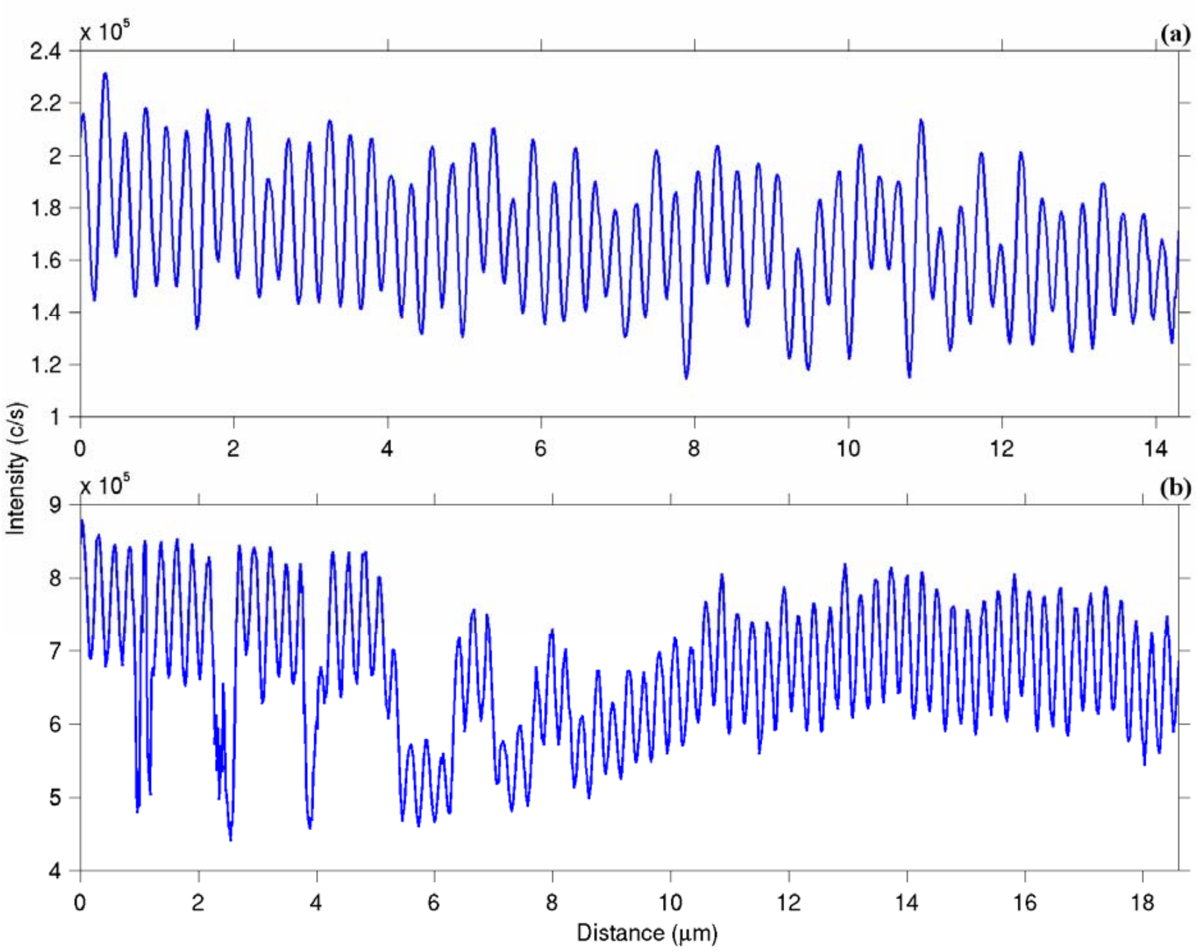

Figure 6.2: (a) A 14.297μm axial, evanescent field line scan of Fibre Grating Sample No.2 with 788 data points. The grating is excited on second order resonance at λ=779.0nm. The standing wave fringes have a period of 264nm. (b) An 18.602μm axial, evanescent field line scan of Fibre Grating Sample No.3 with 1025 data points. The grating is excited on second order resonance at λ=773.0nm. The standing wave fringes have a period of 262nm.

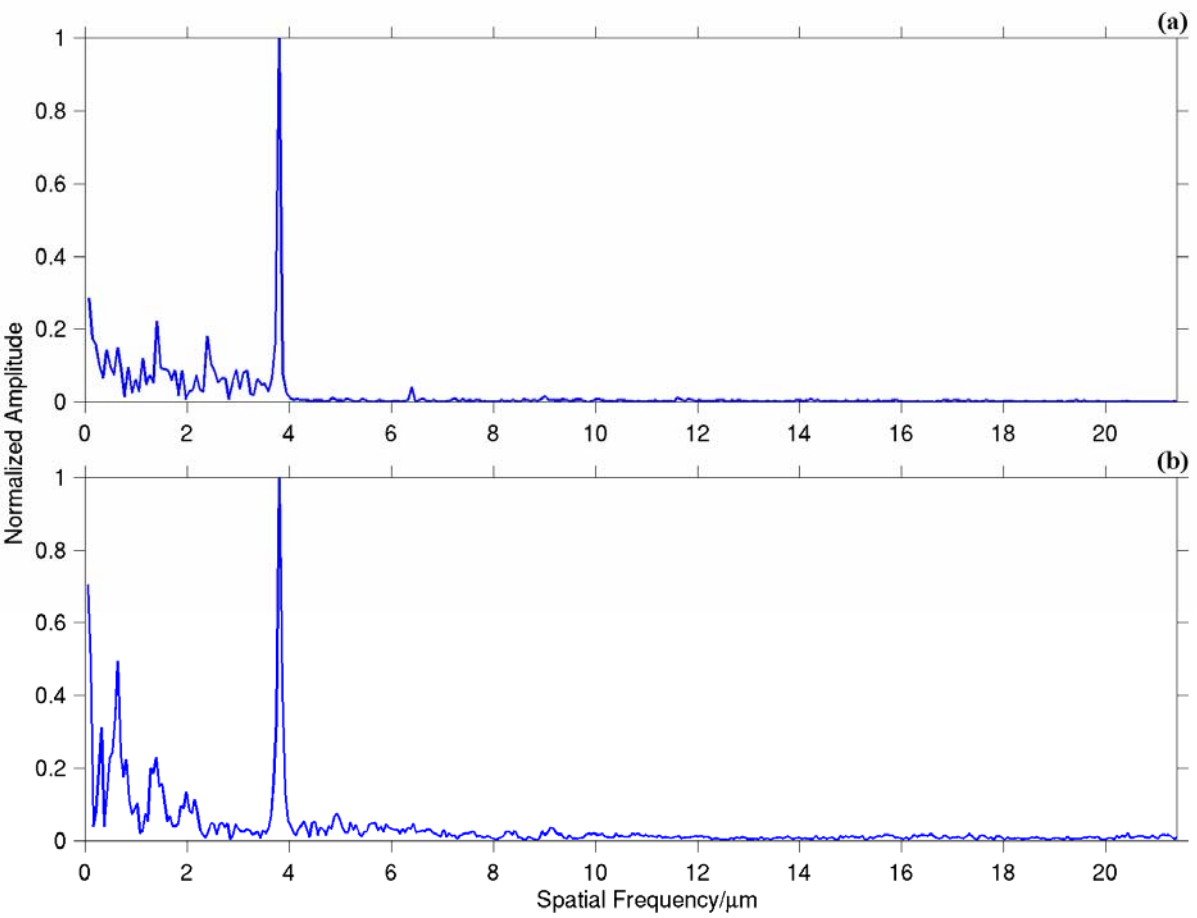

Figure 6.3: (a) An FFT of the standing wave data displayed in Figure 6.2(a), taken from Fibre Grating Sample No.2. The main peak, at frequency 3.78µm^{-1} relates to the period of the fringes at 264nm. (b) An FFT of the standing wave fringes shown in Figure 6.2(b), taken from Sample No.3. The main peak, at frequency 3.81µm^{-1} equates to its fringe period of 262nm. In each case, the dc component has been excluded for clarity.

A Fast Fourier Transform (FFT) was performed on the standing wave data of Figures 6.2(a) and 6.2(b), with the results displayed in Figures 6.3(a) and 6.3(b) respectively. In both cases, there are definite peaks at lower frequencies than the main standing wave peak, corresponding to the larger period structure identified previously. In Figure 6.3(a), the three spikes in the data including the main peak, represent spatial frequencies of 1.44, 2.41 and 3.78 µm^{-1}. There is also a small 'bump' at 6.33μm^{-1}. The frequencies (except for the one representing the standing wave fringes) do not appear to be harmonically related to the wavelength of the incident light or indeed to each other. However, the FFT in Figure 6.3(b) does contain harmonically related frequencies. The three peaks centred at spatial frequencies 0.67, 1.34 and 2.01μm^{-1} are integer multiples of each other, although again, there is no obvious relationship to the standing wave spatial frequency at 3.81μm^{-1}.

The lower frequency activity seen in Samples No.2 and No.3 was often observed in various line scans on these two samples (and indeed was observed in some of the scans of the holographically written samples of *Chapter 7*). This can be contrasted with the phase-mask written Sample No.1, which never displayed such phenomena. It may well be that the mechanism causing the phase errors in the standing wave of the phase-mask created sample is different to that of the holographically written samples. For example, the degree of non-uniformity in the refractive index fringe period Λ and/or the refractive index modulation Δn along the gratings may vary considerably. However, this remark is far from conclusive since the project has limited its study to just one phase-mask written sample. It is possible that the considerable non-uniformity seen in the refractive index period Λ of Sample No.1, was simply due to drift of its fibre during grating writing as was suggested in *Chapter 5*. It is certainly the case, that in the direction perpendicular to the axis of the grating, the two-beam interference technique would produce greater uniformity in its UV writing fringes than was seen in the measured phase-mask patterns of *Chapter 4*. However, the transmission spectra of Samples No.2 and No.3 shown in Figure 6.1, do illustrate a small reduction in throughput for wavelengths immediately below λ_B. This can be indicative of a Bragg grating with refractive index fringes that do not extend uniformly across its core [6.5]. Nevertheless, the effect is extremely small compared to that shown in the transmission spectrum of Sample No.1, displayed in Figure 5.5.

6.4.1.3 Two-Dimensional Resonant Scans

In order to acquire more information about the level of uniformity of the refractive index fringes in samples No.2 and No.3, two-dimensional standing wave images were produced, to allow inspection of the field intensity over a wider area. Figure 6.4(a) shows a 3.536 x

3.536μm, 60x60 pixel scan of Sample No.2 on second order resonance. The data was collected near to the region of the line scan in Figure 6.2(a), and at the position of shallowest cladding. In this image, there appear to be none of the phase errors that were evident in the two-dimensional standing wave patterns of Sample No.1, shown in *Chapter 5*. This offers support to the postulate of a higher level of uniformity in the refractive index fringes across the axis of Sample No.2, compared to Sample No.1. The cross-section of Figure 6.4(a) shown in Figure 6.4(b), offers completeness to Figure 6.4(a) by showing its intensity profile.

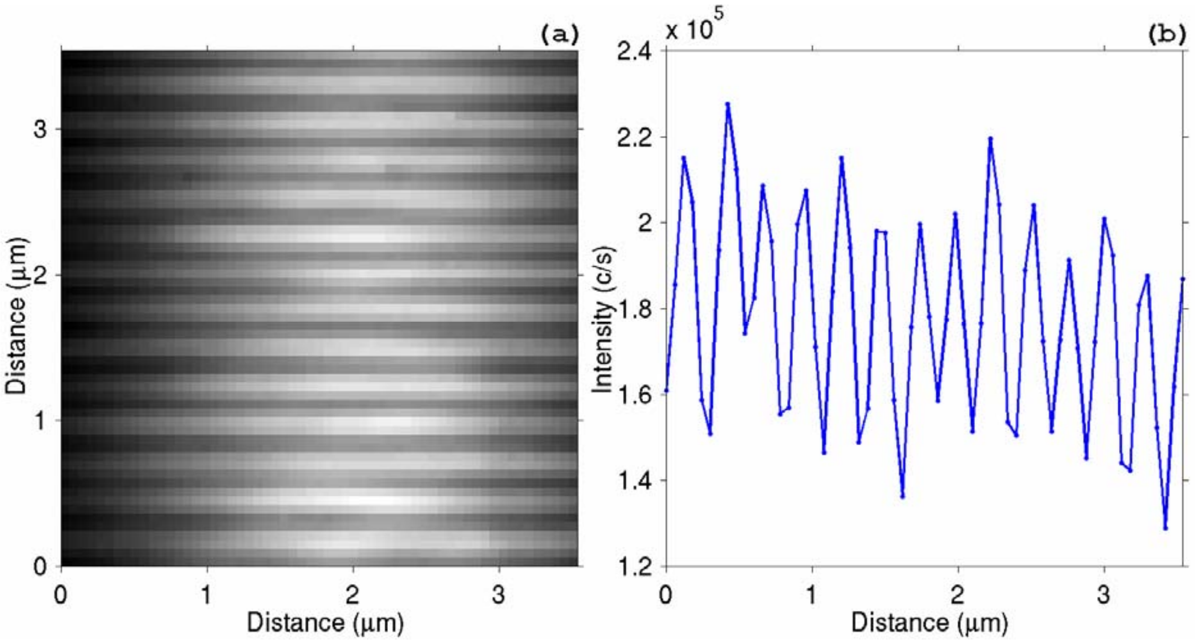

Figure 6.4: (a) A 3.536 x 3.536μm second order resonant scan of Fibre Grating Sample No.2 with 60x60 pixels. (b) Cross-section of (a) up through its centre, column 30. The period of the standing wave fringes is 264nm. The illuminating laser wavelength is 779.0nm.

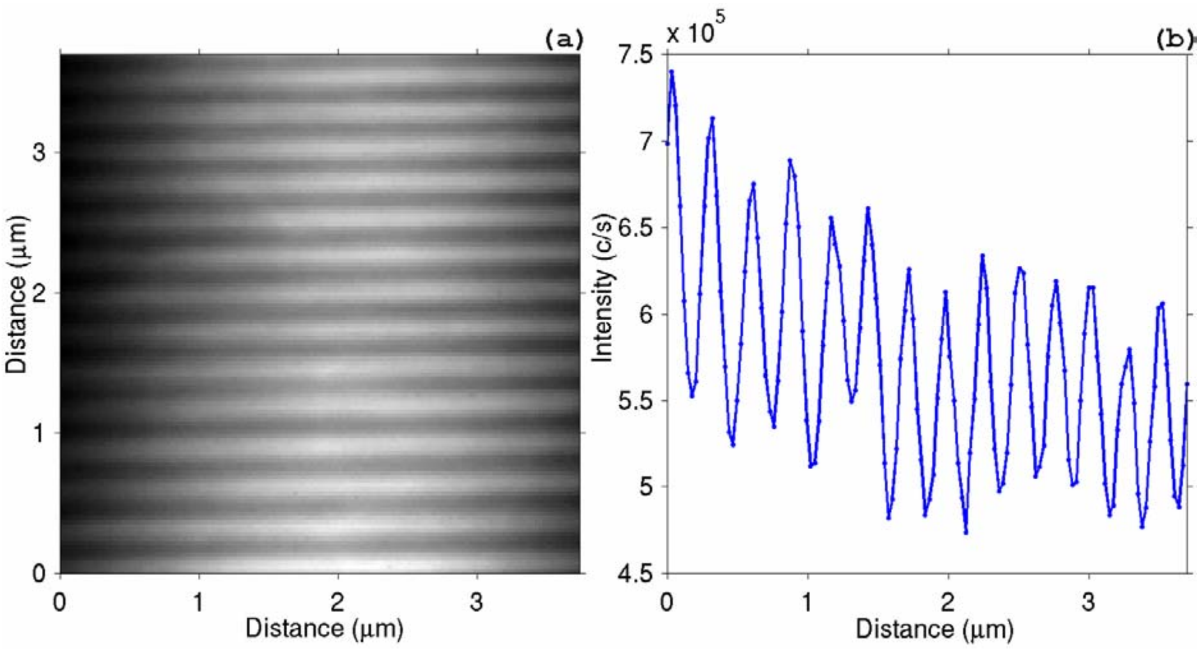

Figure 6.5: (a) Two–dimensional second order resonant evanescent field scan of Sample No.3, with 128x128 pixels. The dimensions of the image are x=3.741μm, y=3.696μm. (b) Cross-section of (a) up through its centre, column 64. The period of the fringes is 262nm and the illuminating wavelength is 773.0 nm.

Sample No.3 had a more detailed scan performed upon it to obtain higher resolution information about the quality of standing wave able to be supported by the holographically written gratings. The result can be seen in Figure 6.5(a) where a 128x128 pixel image, taken in the region of shallowest cladding is shown, with dimensions x = 3.741μm and y = 3.696μm. As in the standing wave image of Sample No.2 displayed in Figure 6.4(a), this image is also apparently free of phase errors. In fact, the standing wave fringes are remarkably uniform both along, and across the grating. The pixel size of the image at ~30nm, is probably just beyond the resolution of the SNOM probe. Therefore, there may be a small amount of averaging occurring between data points, although this is unlikely to affect the overall impression. The data was collected in a region slightly removed from the position of this grating's line scan, shown in

Figure 6.2(b). Again, for completeness, Figure 6.5(b) shows a cross-section of the intensity profile of Figure 6.5(a).

In order to examine a larger area of the standing wave of Sample No.3, a greater scan was performed, again at the position of minimum cladding. Figure 6.6(a) shows an ‘on resonance’, two-dimensional image with dimensions x = 7.482μm and y = 7.392μm, over a matrix of 100x100 data points. The illuminating laser had wavelength 773.0nm. With a much larger pixel size (~74nm) than in Figure 6.5, the standing wave fringes are more fragmented. Nevertheless, the high level of uniformity both along, and across the grating is still evident.

A cross-section of the image in a direction perpendicular to the axis of the grating can be seen in Figure 6.6(b). The shape of the curve is dependent upon the uniformity of the electric field intensity around part of the circumference of the core, and upon the decay of the field through the cladding, which for each data point is different. This lateral cross-section offers support to the claim that the scans were performed under a single-mode condition. A further cross-section is displayed in Figure 6.6(c), which was taken from Figure 6.6(a) in the direction along the grating’s axis. The topographical data associated with this axial cross-section is displayed in Figure 6.6(d). As can be seen, by comparing Figures 6.6(c) and 6.6(d), the overall drop in the intensity of the optical data over the 7.392μm length, is mainly due to the ~25nm overall rise in the topographical profile.

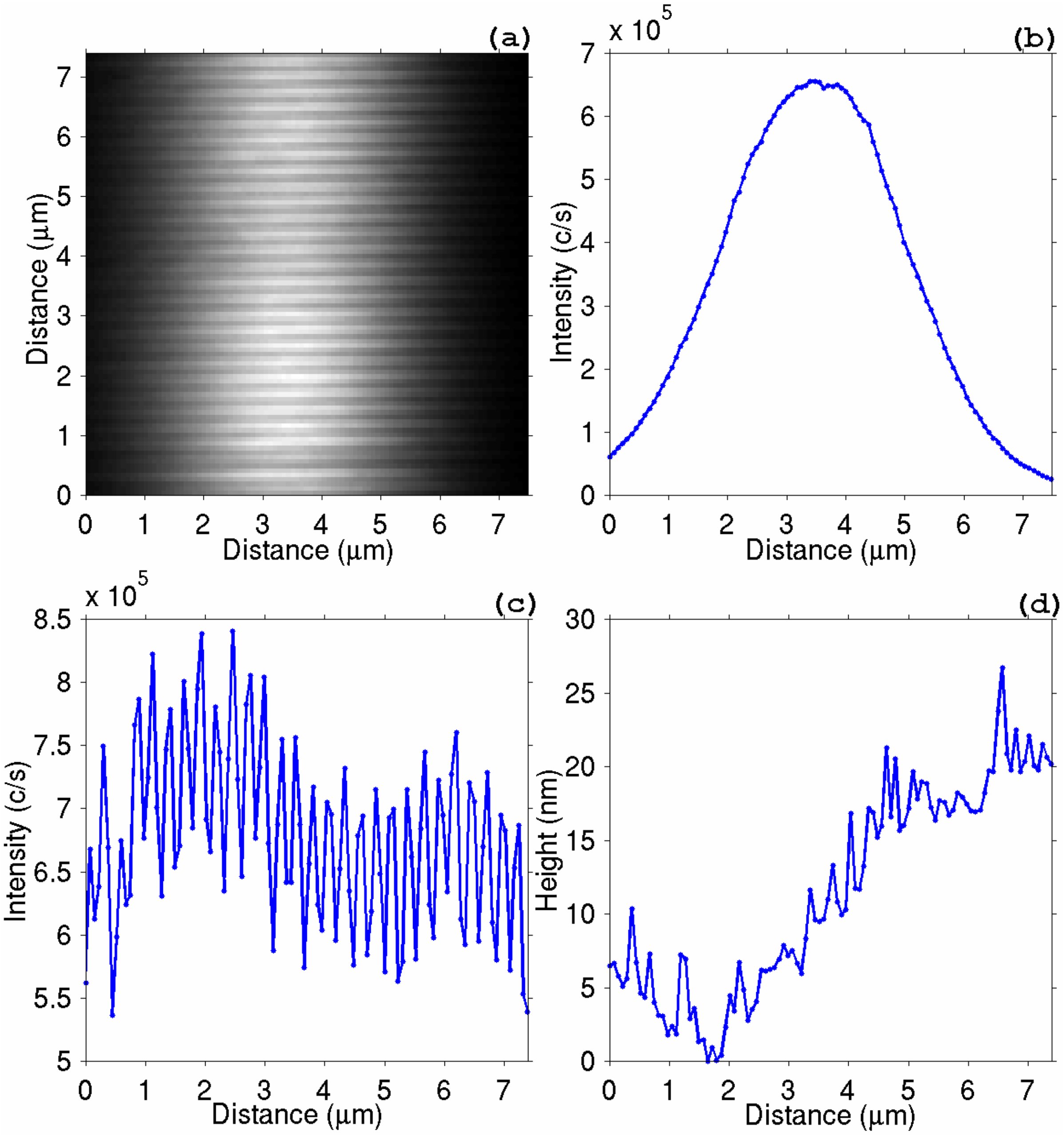

Figure 6.6: (a) Two dimensional, 'on resonance' evanescent field image of Sample No.3. The dimensions of the scan are x = 7.482µm and y = 7.392µm, with 100x100 data points. The illuminating laser had a wavelength of 773.0nm and the period of the fringes is 262nm. (b) A cross-section of (a) in a directional perpendicular to the axis of the grating (x-direction). (c) A cross section of (a) in the direction along the axis of the grating (y-direction). (d) The topographical data relating to the optical data of (c).

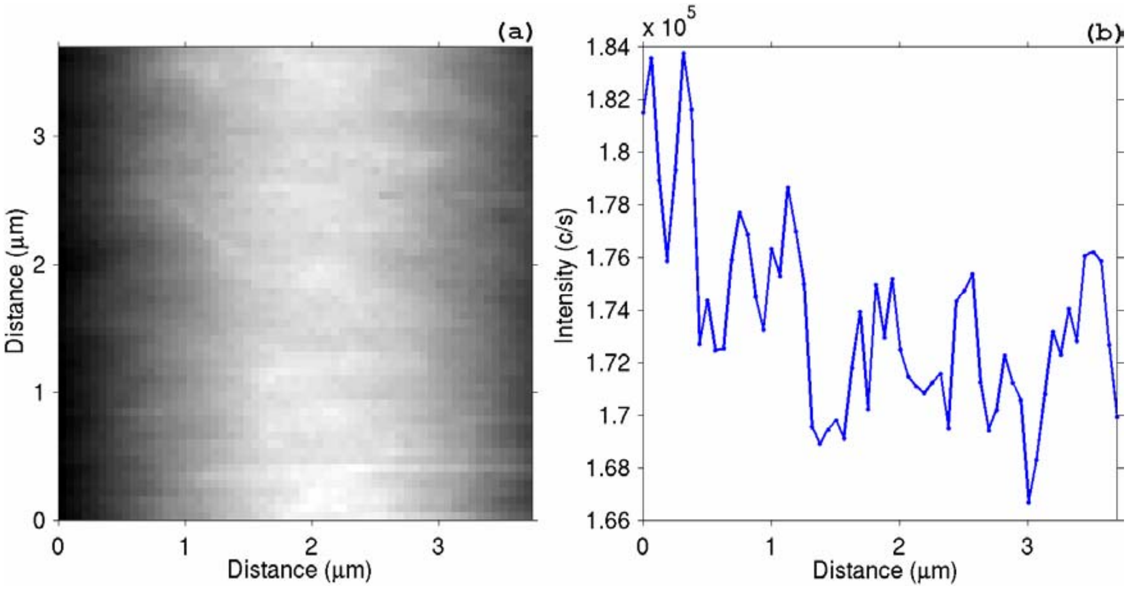

Figure 6.7: (a) Evanescent field scan of Sample No.3, off resonance with an incident laser wavelength of 784.0nm. The image is in an identical position to the image shown in Figure 6.5, and has dimensions x = 3.741µm, y = 3.696µm, and a grid of 60x60 pixels. (b) Cross-section of (a) up through column 30.

6.4.1.4 Off-Resonance Scans

The two-dimensional, resonant evanescent field images shown in Figures 6.4, 6.5 and 6.6 are not noticeably affected by the modulating decay constant present along the length of each grating. In order to understand what impact the decay constants are actually having on these data sets, a scan was performed upon Sample No.3 with the laser tuned off resonance, at λ=784.0nm. The result, which has a matrix of 60x60 pixels, is displayed in Figure 6.7(a). The image represents a scan taken immediately after, and in the same position, as the one shown in Figure 6.5. It also has the same x and y dimensions, and is produced from an identical laser output power. The intensity profile appears to be very flat although fringes with a period Λ= 524nm (262nm x 2) were expected. A cross-section, taken from column 30 of the data, is shown in Figure 6.7(b). Given that the measured value of the average effective refractive index of this sample was 1.475, and assuming the index values of the silica cladding at λ=784.0nm and air to be 1.454 and 1.000 respectively, the varying index $\Delta n \sim 1 \times 10^{-3}$ would be expected to cause a modulation depth in the measured 'off resonance' profile of about 15% of the maximum intensity. The cross-section of Figure 6.7(a) shown in Figure 6.7(b) has a depth of about 9% of the maximum intensity and does not show up the expected periodicity.

It is possible that an over-estimation of the final cladding depth has occurred during the polishing of these samples, which would account for the fairly flat, non-periodic profile. Of course, the flatness would also account for the apparent zero effect on the standing wave profiles of the decay constants. However, it would not account for the scarcity of phase errors. Similar 'off resonance' scans performed on Sample No.2 have also shown non-periodic, relatively flat profiles.

To establish if it was at all possible to directly image the refractive index profiles of Samples No.2 and No.3, the SNOM probe was positioned an arbitrary distance (not greater than 1mm) from the centre of each grating, and axial, 'non resonant' line scans were performed. The results of these scans are shown in Figure 6.8, where the greater depth of cladding and increased number of data points has both strengthened the contrast, and defined some of the

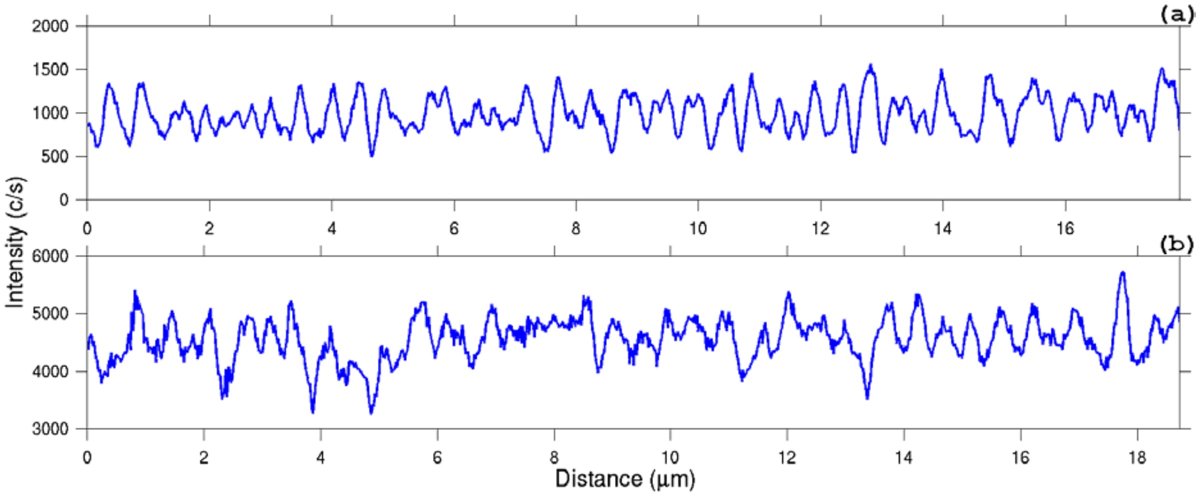

Figure 6.8: (a) An 'off resonance' axial line scan along Sample No.2, with 1002 data points, at wavelength 787.0nm. The length of the scan is 17.868µm. (b) An 'off resonance' line scan of Sample No.3 with 1025 data points. The illuminating wavelength was 784.0nm and the length of scan 18.720µm.

refractive index fringes more clearly. However, in both scans there is a significant amount of irregular activity, which is not related to the refractive index periodicity.

Both sets of data have been regenerated to appear in Figure 6.9 where they have been over-laid with cos^2, periodic profiles in order to identify the regular refractive index fringes. Figures 6.8(a) and 6.9(a) show the axial scan along Sample No.2 which had 1002 data points over a length of 17.868µm, at an illuminating laser wavelength of 787.0nm. The data best fits a period of 525nm which is not equivalent to twice the standing wave fringe period of 528nm (2x264nm) given earlier in this chapter for this sample. The discrepancy between the two values is acceptable due to the range of excitable modes at this wavelength. Figure 6.9(a) also displays arrows which indicate regions where the two plots seem to be in phase. In between the arrows, the plots appear out of phase. The de-phasing is a complex function of both the grating

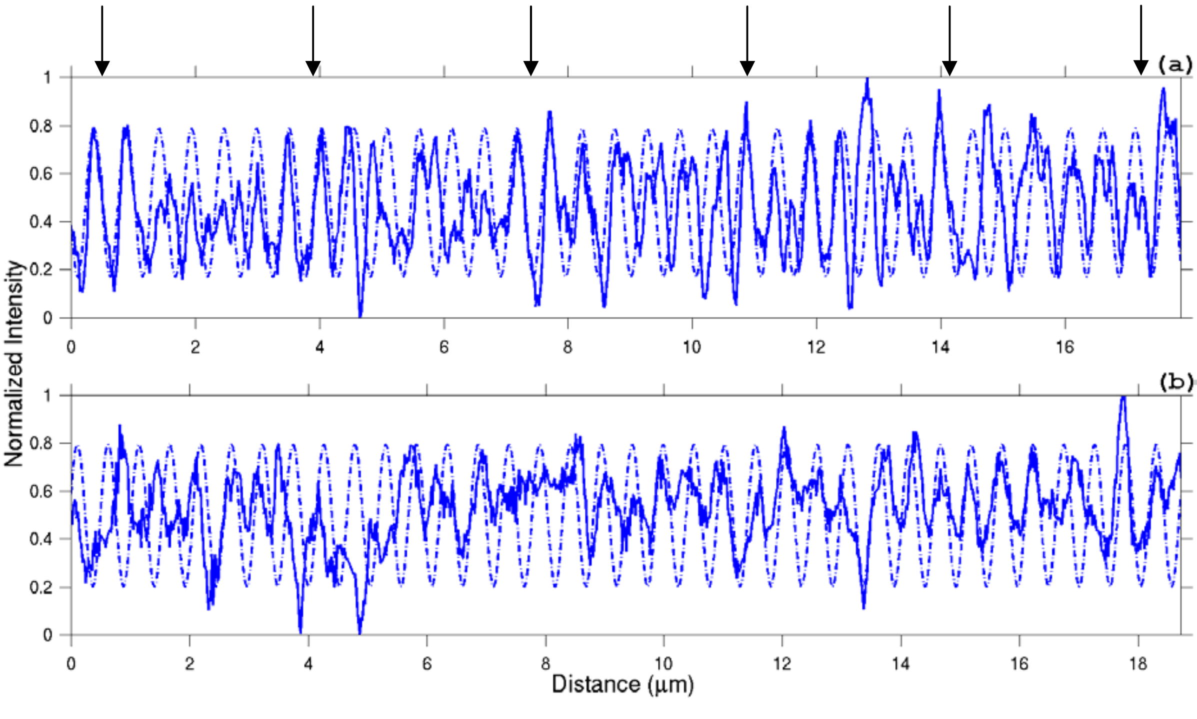

Figure 6.9: (a) Normalized data of Sample No.2 already shown in Figure 6.8(a), over-laid with cos^2 fringes with a 525nm period. The arrows represent regions where the cos^2 fringes are in phase with the refractive index profile. (b) Normalized data of Sample No.3, previously shown in Figure 6.8(b) and matched to periodic cos^2 fringes of 521nm.

characteristics and the interrogating wavelength. In places along the scan, there is a superimposed periodicity within the intensity data, which is approximately half that of the index fringes. This may be due to reflected light from the end of the fibre, which has interfered with the forward propagating light. The effect was also observed in 'off resonance' data relating to Sample No.1 of *Chapter 5*. In *Chapter 7*, where the fibre samples are illuminated at wavelengths above their single-mode cut-off, it was not necessary to monitor the modal outputs, and therefore results will be presented that represent gratings with exit pigtails terminated in index oil, thus reducing the effect.

Figures 6.8(b) and 6.9(b) show the result of scanning Sample No.3 where the incident laser was set to the 'off resonance' wavelength of 784.0nm. The scan ran for 18.720μm with 1025 data points. Here, the closest fitting period is 521nm. Again, this is not equivalent to twice the standing wave fringe period of 524nm (2x262nm). As mentioned before, the discrepancy is acceptable due to the range of excitable modes at the given wavelength. In this case, the fringes are not so well defined and have merged in places. The loss of resolution here, may have been caused by a proportionally greater contribution to the field at the SNOM tip from adjacent parts of the grating, due to the increase in depth of the cladding away from its centre.

There is a degree of noise apparent in the scans of both gratings, which may be caused by the generally low signal. In each case, the average measured intensity was only ~1% of the average intensity measured in all previous data shown in this chapter. The equivalent 'off resonance' line scan of Sample No.1 was given in Figure 5.13(a). This figure shows its refractive index fringes much more clearly, although there are still many similarities to the 'off resonance' line scans of Samples No.2 and No.3. However, the estimated value of Δn for Samples No.2 and No.3 is only 20% of that estimated for Sample No.1, and so there is bound to be greater difficulty in achieving the successful imaging of their fringes. The line scan in Figure 5.13(a) also had the advantage of being generated by an incident laser with shorter wavelength (HeNe at 632.8nm), which brings about an improvement in contrast over longer wavelength illumination. However, it would not have been practical to use the HeNe laser utilized in *Chapter 5* to examine Samples No.2 and No.3 because of the laser's lower maximum output and faster decay through the cladding, compared to the laser used in this chapter.

It might well be that the present SNOM system in constant-gap imaging mode, has a limit of resolution with respect to measuring the refractive index of these samples, that is comparable to the Δn of Samples No.2 and No.3. If this is the case, then an improvement in resolution using the constant gap method could only be achieved by introducing a higher-powered laser of reduced wavelength. Ultimately, the limit of resolution in this type of Δn SNOM imaging may only be decided (as described in *Section 5.2.2* and further discussed in *Section 7.4.2*), by two-dimensional vertical evanescent field scans of the gratings, where a row of decay constants could be calculated over a region of minimum cladding. Under the condition that the height of each scan is small compared to the grating period Λ, the resolution would then be determined mainly by the dimensions of the SNOM probe itself.

6.4.2 Decay Constant Measurements

In *Section 5.5.2* of *Chapter 5*, it was explained how it can be possible to estimate the effective refractive index at any point along a polished fibre Bragg grating by measuring the decay of the evanescent field in the direction perpendicular to its surface. Such measurements were made on Fibre Grating Sample No.2 at the region of least cladding depth. With the SNOM tip starting at a height very close to 0nm, it was then held for one second per point at 10nm intervals up to a height above the grating's polished surface of z = 200nm. The measurement was repeated along the axis of the fibre grating at 100nm intervals, up to a length, y = 1.8μm. With the use of the planar waveguide Equations (5.7) and (5.20), the set of decay constants were then approximated from the 19 data sets and the effective refractive index at each point estimated. The results are displayed graphically in Figure 6.10(a) and numerically in *Table 6.3*. Figure 6.10(b) shows the result of a line scan taken over the same region, immediately after the data displayed in Figure 6.10(a) was collected. Here, the SNOM tip was re-locked to the surface of the grating. The topographical data relating to this line of intensity data was essentially flat, having a range of <5nm for the complete scan. During the collection of data for both Figures 6.10(a) and (b), the laser was tuned to its 'off resonance' wavelength of λ = 787.0nm.

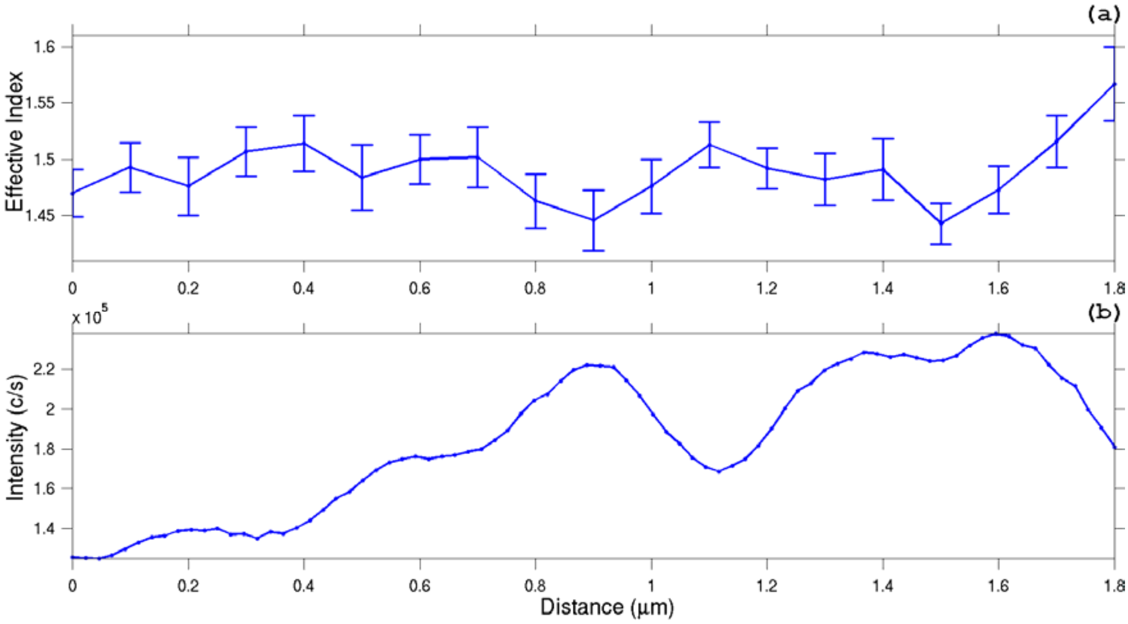

Figure 6.10: (a) The refractive index profile at 100nm steps along the grating axis of Sample No.2, derived by approximating each individual decay constant from the evanescent field measurement. (b) The measured ('off resonance') intensity along the same region of the grating as (a), taken immediately afterwards, with the SNOM tip re-locked to the surface. The topographical data relating to (b) is essentially flat, having a range of <5nm for the complete scan. There are 102 data points in (b). In both (a) and (b), the range is over 1.8μm.

Relative position along grating axis (nm)	*Effective refractive index, n_e*	*Relative position along grating axis (nm)*	*Effective refractive index, n_e*
0	1.470 ± 0.021	1000	1.476 ± 0.024
100	1.493 ± 0.022	1100	1.513 ± 0.020
200	1.476 ± 0.026	1200	1.492 ± 0.018
300	1.507 ± 0.022	1300	1.482 ± 0.023
400	1.514 ± 0.025	1400	1.491 ± 0.027
500	1.483 ± 0.029	1500	1.443 ± 0.018
600	1.500 ± 0.022	1600	1.473 ± 0.021
700	1.502 ± 0.027	1700	1.516 ± 0.023
800	1.463 ± 0.024	1800	1.567 ± 0.033
900	1.446 ± 0.027		

Table 6.3: The numerical values of the data shown graphically in Figure 6.10(a).

The experimental procedure carried out in order to obtain the results displayed in Figure 6.10(a) was such that the SNOM and sample were not completely thermally isolated from the laboratory. Since it was important to periodically check the modal output from the grating, it was deemed least harmful to the stability of the results, to remove the thermally insulating front cover for the duration of the 19 short scans. This was not the case for the decay constant measurements carried out in *Chapter 5*, where it was judged not to be necessary to monitor the mode pattern during the collection of data as in this case, only 4 data sets were taken over a much reduced period of time. The consequence to the results shown in Figure 6.10(a) and *Table 6.3* is that there may have been a degree of uncertainty in the z-direction step size of the tip, relative to the surface of the sample. This will have enhanced the level of uncertainty in the optical data leading to the results shown in Figure 6.10(a). Of course, the drift of the probe relative to the sample is not normally an issue when the tip is locked to the surface, because the feedback electronics ensure a constant gap.

However, comparison of the overall shapes of the graphs in Figures 6.10(a) and (b) suggest that there may be a connection between the two sets of data. Each set should be proportionally inverse to the other, and there is visual evidence to suggest that this is approximately the case. In the next chapter, a study is carried out on single-mode fibre gratings where the refractive indices are calculated with much improved stability and reliability, due to the mode pattern not having to be monitored. There will also be clearer evidence of inverse proportionality in the optical and refractive index data sets.

6.5 Chapter Summary

The methods developed during *Chapter 5* for imaging the evanescent field of a fibre Bragg grating with a Scanning Near-field Optical Microscope (SNOM) have been successfully applied to two samples in the present chapter. A comparative study of the two gratings (Samples No.2 and No.3), via their respective evanescent fields, was therefore possible. The gratings were originally made from the same holographic side-writing technique, and various data sets have confirmed their similarity. Both gratings were further compared to data taken from Sample No.1, shown in *Chapter 5*, which was made from the very different phase-mask writing technique.

It was possible to achieve a small (~10%) second-order reflection from both Samples No.2 and No.3, which enabled their second-order resonant wavelengths to be identified. With each grating in turn tuned to their resonant wavelength, evanescent field scans were performed. The standing wave images thus produced, were apparently free of phase errors unlike similar images produced from Sample No.1. This offered evidence of a greater level of uniformity in the written refractive index fringes both along and across each grating's core, compared to that of Sample No.1. An experiment that should be included as part of any future development to this work, is the direct imaging of the phase evolution of light traveling along fibre Bragg gratings. This could be achieved using a method such as that described in ref [6.6], and would enable the acquisition of definitive phase information.

With the holographically-written samples tuned off resonance, their refractive index fringes could only be imaged by positioning the SNOM tip at a region of deeper cladding than that necessary for Sample No.1. Although this improved imaging contrast, the inevitable reduction in resolution was coupled with increased noise. It was speculated that with the present SNOM system in constant gap mode, the limit of resolution in imaging the refractive index variations of fibre gratings may be of the order of the Δn present in Samples No.2 and No.3, that is to say $\sim 1 \times 10^{-3}$.

An attempt was made to deduce the numerical values of the refractive indices along a section of Sample No.2 by measuring decay constants from the exponentially decaying evanescent field. Unfortunately, a higher than expected uncertainty in the results ensued, probably caused by thermal drift of the SNOM probe relative to the sample surface during the measuring process. The uncertainty may have been compounded by the approximation of the theory utilized to calculate the decay constants. However, there was visual evidence to suggest that a relationship between this refractive index data, and corresponding off-resonance optical line data existed.

It is possible that the difficulties experienced in imaging the refractive index variation along the gratings examined in this chapter, may be overcome by polishing the samples right into their cores and performing 'Reflection-SNOM' [6.7] directly on their grating structure. This is discussed in the 'Future Work' section of *Chapter 8*.

6.6 References

[6.1] J.-L. Archambault, P.St.J. Russell, S. Barcelos, P. Hua, L. Reekie, Optics Letters, **19** (3), 180 (1994)

[6.2] G. Meltz, W.W. Morey, W.H. Glenn, Optics Letters, **14** (15), 823 (1989)

[6.3] W.X. Xie, M. Douay, P. Bernage, P. Niay, Optics Communications, **101**, 85 (1993)

[6.4] W.X. Xie, P. Niay, P. Bernage, M. Douay, J.F. Bayon, T. Georges, M. Monerie, P. Poumellec, Optics Communications, **104**, 185 (1993)

[6.5] B. Malo, D.C. Johnson, F. Bilodeau, J. Albert, K.O. Hill, Optics Letters, **18** (15), 1277 (1993)

[6.6] M.L.M. Balistreri, J.P. Korteric, L. Kuipers, N.F. van Hulst, Physical Review Letters, **85** (2), 294 (2000)

[6.7] M. Svalgaard, S. Madsen, J.M. Hvam, M. Kristensen, IEEE Photonics Technology Letters, **10** (6), 848 (1998)

7. Comparative Study Of The Evanescent Fields Of Three Holographically Side-Written Single-Mode Fibre Bragg Gratings

7.1 Chapter Introduction

In this final data chapter, a comparative study of the evanescent fields of three single-mode fibre Bragg gratings will be presented, by once again utilizing the SNOM scanning methods developed in *Chapter 5*. For identification purposes the fibre gratings, which were written with identical parameters into lengths of a single optical fibre, are named Fibre Grating Samples No. 4, 5, & 6. The three particular gratings were written and side-polished actually during the course of this project, unlike the gratings described earlier in this thesis. However, they were created under similar conditions to that used to write the Bragg gratings examined in *Chapter 6*, and in fact were written with the same laser as the gratings in both *Chapters 5* and *6*. In addition, the mounting and polishing of the single-mode gratings was identical to the methods used to prepare the samples described in the previous chapters for their use as grating couplers. This chapter will therefore continue the trend developed so far in this thesis, of comparing results across chapter boundaries, in order to enhance the characterization of all of the fibre Bragg gratings investigated during this project.

7.2 Preparation Of The Single-Mode Samples

In the previous two chapters, Fibre Grating Samples No.1, 2 & 3 had their evanescent fields scanned whilst being illuminated with a laser that was operating at a wavelength below the single-mode cut-off of each grating. Nevertheless, with considerable care taken to align the laser and fibre, a single-mode condition could be achieved. The modal status was monitored in each experiment by checking the output from the gratings' fibres, and by watching for 'jumps' in the overall intensity measured by the SNOM probe. The single-mode condition was necessary to allow a straightforward interpretation of results. This non-ideal situation prompted the fabrication of Bragg gratings within an optical fibre with a cut-off far enough below the illuminating laser wavelength, to guarantee an unequivocal single-mode condition, even within the grating region itself.

A 20m length of Fibercore Ltd. PS750 optical fibre, with a dual doped Germania/Boron photosensitive core and single-mode cut-off of 730nm, was hydrogen-loaded at room temperature for several days to enhance its photosensitivity [7.1]. On removing the fibre from the hydrogen cell, it was divided into ten lengths, measuring 2m each. Approximately half way along each cut section, a 40mm length of the plastic coating was removed. The fibre samples were then in turn irradiated along a 15mm region at the centre of each stripped section, with a line-narrowed Lambda Physik EMG-150 KrF excimer laser, using a two-beam interferometer arrangement similar to that in [7.2]. The reason for writing more gratings than was required for the study, was to allow for failure during the mounting and polishing processes later. The resulting ten fibre Bragg gratings, written with identical experimental parameters each had a first order Bragg reflection (determined during exposure) ranging from ~774nm to ~778nm. This corresponded to a modulating

Identification of samples	Fibre Grating Samples No. 4, 5 & 6, written with identical parameters from the same optical fibre.
Fibre type	Fibercore Ltd. PS750
Single mode cut-off of non-grating part of fibre:	730 nm
Cladding outer diameter:	125 μm
Core diameter:	4.65 μm
Cladding material:	Silica
Core material:	Silica/Germania/Boron
NA of non-grating part of fibre	0.12
Coating material	Single coat acrylate
Coating outer diameter	245 μm
Preparation of fibre before grating writing	Hydrogen loaded at room temperature
Method of grating writing:	Side exposure to two interfering KrF excimer UV beams
Bragg wavelength λ_B	~(774-778)nm
Index modulation, Δn:	~2 x 10^{-3}
Grating length, L:	15mm

Table 7.1: Parameters of the base optical fibre, writing conditions and subsequent fibre Bragg gratings created for the comparative study shown in this chapter.

refractive index, Δn along the length of each grating of ~2 x 10^{-3}. The single-mode cut-off within the grating region was subsequently estimated to be about 760nm. A summary of the grating parameters can be seen in *Table 7.1*.

The procedure to prepare the single-mode fibre gratings for SNOM scanning was carried out upon one grating at a time, until three samples in total were successfully completed. Indeed, the process was attempted on six gratings in total, with three becoming cracked sometime during the operation. However, it was difficult to identify exactly when the cracking occurred, because it only became apparent well into the polishing stage.

The first step of the preparation involved cutting a 1m radius groove along the surface of a pyrex glass block, which had engineered dimensions 44mm x 25mm x 10mm. The apparatus for completing this task can be seen in Figure 7.1. It was found to be generally useful to cut the groove to a depth of at least 200μm at its shallowest point, to ensure that

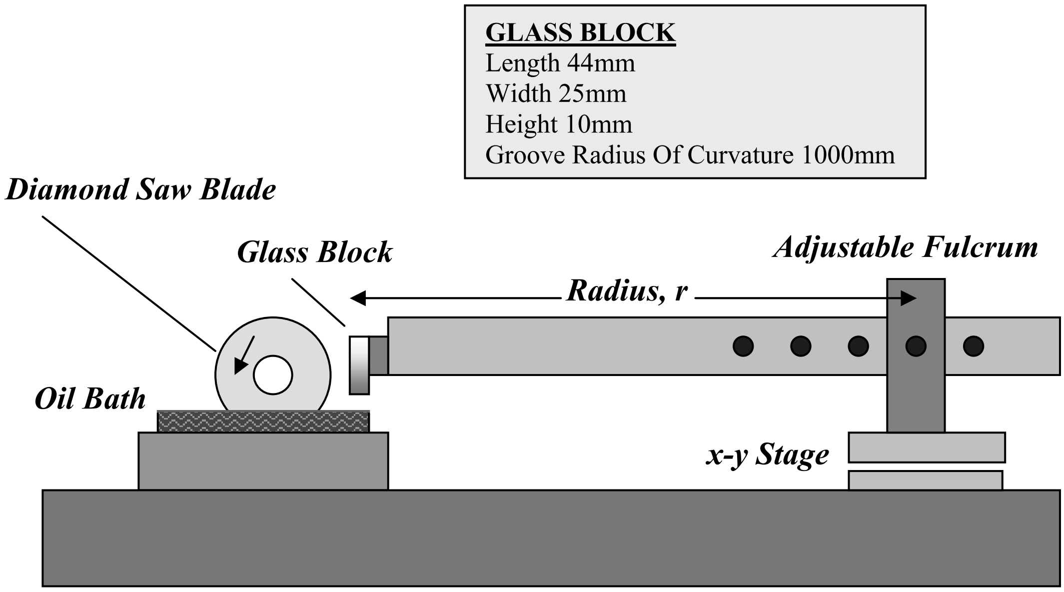

Figure 7.1: Glass Block Cutting Apparatus. The glass block was secured and moved gradually towards the saw blade with the action of the x-y stage. It was simultaneously moved slowly up and down by the action of the fixing arm, which rotated about the fulcrum. Consequently, a curved groove with a radius, r was cut along the length of the glass block. The shallowest point of the groove was central to the block.

the stripped optical fibre that was to be located along the groove, would not rise above the block's surface. An additional deeper notch was cut into each end of the groove to allow the fibre at these points, to be angled away from the surface, in order to hold the grating more securely.

After the pyrex block was prepared, it was then clamped into the gluing jig shown in Figure 7.2. A fibre grating was placed along the groove ensuring that it was central to the block. Since the stripped section of the fibre was 4mm shorter than the block itself, a 2mm length of coated fibre existed at the ends of the grooves, which served to strengthen the pigtails at the point of exit. One pigtail was clamped into position whilst the other had a weight attached in order to apply tension. An Auriga Ltd. EpoTek 353ND epoxy resin was carefully applied to fix the grating into position, and subsequently inspected under a microscope so that any air bubbles could be removed (a probable cause of the aforementioned cracking of the gratings). The gluing jig along with the sample was subsequently placed in an oven for one hour, so that the resin could be cured at 120 degrees

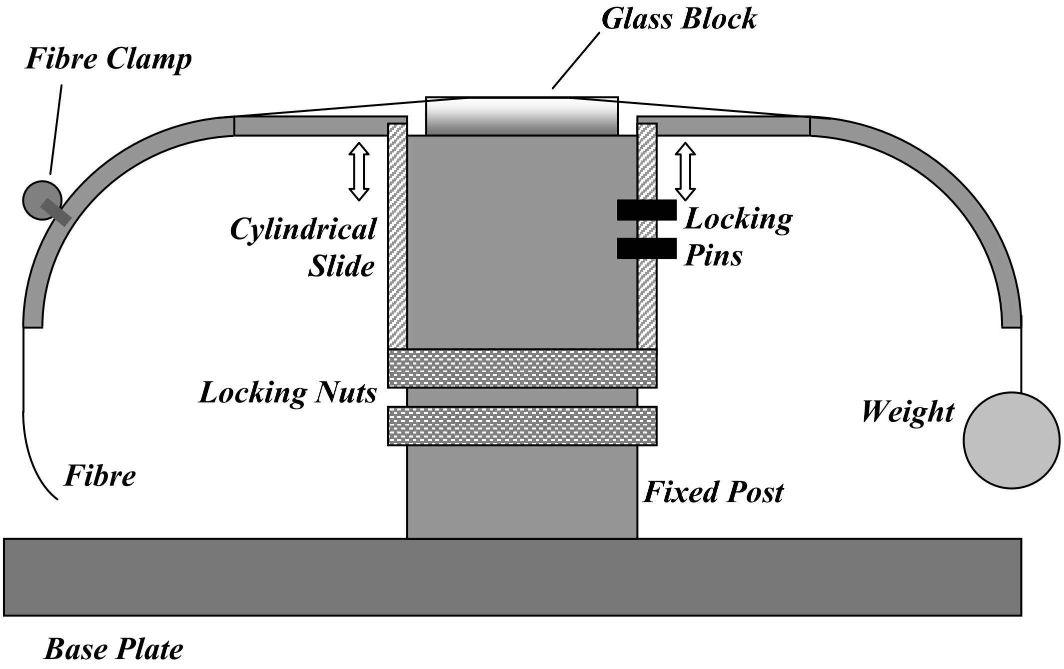

Figure 7.2: Gluing Jig. The glass block was secured with clamps upon the jig. The optical fibre was then positioned along the groove with the centre of its grating at the highest point of the groove (centre of the glass block). The fibre was subsequently glued into place. The jig was mostly constructed of brass.

Celsius to achieve maximum hardness. With a fibre Bragg grating now firmly fixed into the glass block, polishing of the face of the block commenced by lapping with a de-ionized water solution of 3μm Al_2O_3. Regular inspection under a microscope revealed when the cladding had eventually been reached. As polishing progressed, the exposed cladding developed an elliptical shape due to the fibre's curvature. By accurately measuring both the length of the ellipse and the depth of polish from the moment that the cladding was touched, an estimation of the cladding depth could be made. At about 5μm from the core, the Al_2O_3 mixture was exchanged for a de-ionized water solution of 3μm Cerium Oxide in order to slow the process, and to procure a finer polish. However, the core of many commercially available fibres is not perfectly concentric with the fibre's outer surface [7.3], and therefore a further method had to be introduced to monitor the accuracy of these measurements. The throughput attenuation of a HeNe laser (λ = 632.8nm), was recorded with an appropriate

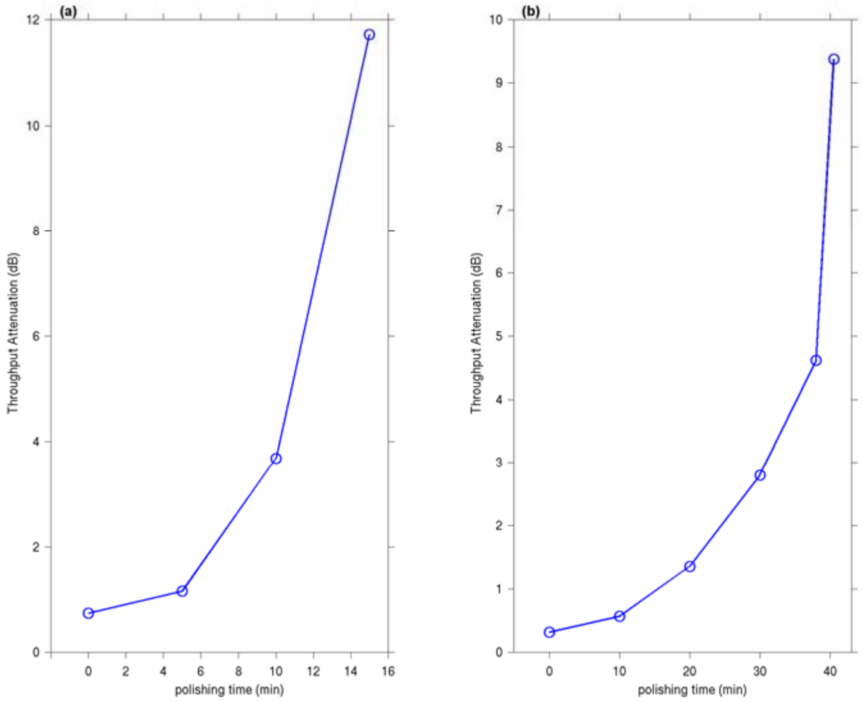

Figure 7.3: The final minutes of polishing, with the associated throughput attenuation of (a) Fibre Grating Sample No.5 and (b) Fibre Grating Sample No.6. The illuminating laser in each case was a HeNe operating at the wavelength λ = 632.8nm.

index matching oil covering the polished region, in order to identify the final approach to the core [7.3]. Graphs of the concluding minutes of polishing vs. the associated throughput attenuation in the cases of Samples No.5 & 6, can be seen in Figure 7.3. By utilizing the methods discussed above, the depth of cladding at its shallowest point was estimated for the required single-mode gratings, and recorded below in *Table 7.2*.

	Estimated final depth of cladding
Fibre Grating Sample No.4	1.5 μm
Fibre Grating Sample No.5	0.9 μm
Fibre Grating Sample No.6	1.0 μm

Table 7.2: The estimated depth of cladding at the centre of each single-mode grating.

7.3 Experimental Procedure

The SNOM evanescent field scanning performed on Fibre Grating Samples No.4, 5 & 6 during the course of this chapter, followed an almost identical experimental procedure to that described previously in *Section 5.4*. A difference occurred in the fact that the launching of the illuminating laser into the single-mode fibre gratings was simplified, due to the presence of the 1m long pigtails. Launching of the light could therefore be carried out external to the SNOM thermal housing directly into a cleaved pigtail, via a 10x objective. A Martock Design Ltd. translation stage was utilized to support both the objective and pigtail. Also, when required the opposite pigtail could be terminated in index matching oil to minimize unwanted reflection from the exiting face of the fibre. Both the tunable diode laser and the HeNe laser used in *Chapter 5*, were re-employed to acquire data for this chapter.

7.4 Results And Discussion

The data presented in this section was collected as a result of scanning the evanescent fields of Fibre Grating Samples No.4, 5 & 6, described in *Table 7.1*. In general, similar data sets have been acquired for all three samples to allow comparisons to be made. However, there exist a small number of supplementary results, which involve either one, or two gratings only.

During *Chapters 5* and *6*, part of the discussion on the characteristics of the evanescent fields of grating samples, took into consideration their transmission spectra. This is because transmission spectra indicate the extent of scattered light from a grating, which in turn gives valuable clues as to the level of uniformity of the grating's refractive index profile [7.4]. White light transmission spectra of Grating Samples No.4, 5 & 6 were therefore measured before SNOM scanning began. The spectra can be seen in Figure 7.4 and will be discussed in the following text. However, one immediate comment is that the individual figures obviously have very similar characteristics. Measurements were also made on non-polished gratings from the same batch, with comparable results.

Sample No. 4 ***Sample No. 5***

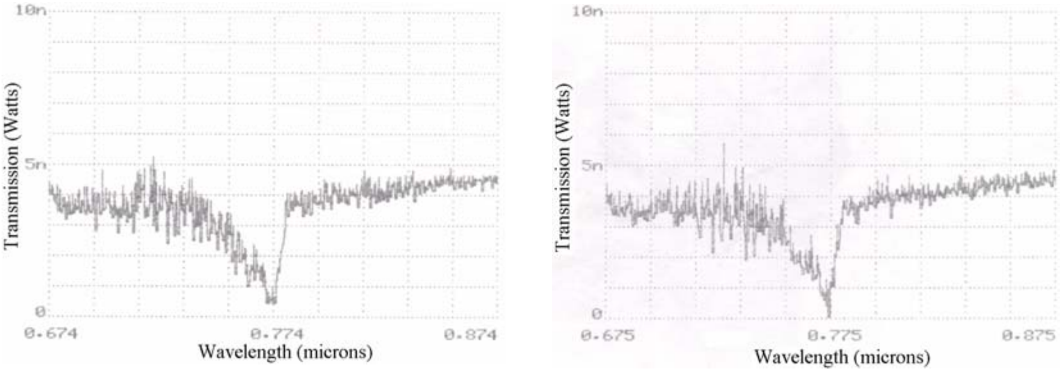

Sample No. 6

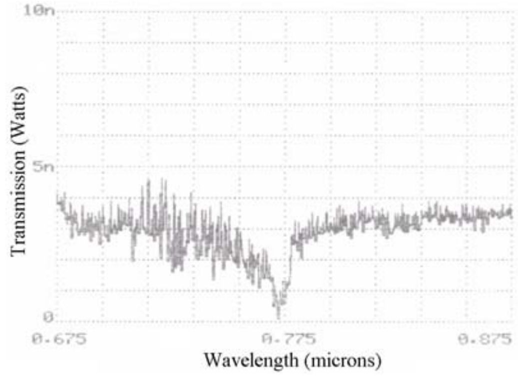

Figure 7.4: The white-light transmission spectra of Fibre Grating Samples No.4, 5 & 6 at their Bragg wavelengths.

7.4.1 Constant Gap Evanescent Field Imaging

The results that follow have been divided into sections for clarity. Each fibre grating is examined individually, before continuing with the next. In all three cases, one-dimensional data is presented before two-dimensional images. As the sections progress, a discussion develops in order to compare and contrast the data collected from the individual gratings.

7.4.1.1 Fibre Grating Sample No.4: One-Dimensional Scans

Sample No.4 was illuminated on first order resonance, $\lambda_B = 775.0$nm with an uncoated SNOM probe locked to its polished surface at a height of 10nm, directly above the axis of its grating. The probe, which was positioned at the centre of the grating and therefore at its region of shallowest cladding, was set to scan over a length of 19.080µm along the grating's axis. The result is shown in Figure 7.5(a), where a standing wave with average fringe period 265nm can be observed. From this data, the average effective refractive index along the grating region was calculated to be 1.462 ± 0.005. The associated topographical data is displayed in Figure 7.5(b), where the lowest data point has been set to 0nm.

Since much of the one-dimensional data in this chapter will be subject to the normalization procedures described in *Section 5.2.3*, a demonstration of the effect of the 'topography-normalization' routine is shown in Figure 7.5(c). Here, the black line represents a repeat of the optical data given in Figure 7.5(a) from points 4-12µm, and the red line represents the same data normalized with respect to its simultaneously acquired topographical data. The method involved a 'reversal' of the evanescent field decay through the varying depths of cladding, over and above the relative position of 0nm, shown in Figure 7.5(b). Its function was to model a SNOM measurement of the grating, given that its polished surface is absolutely flat, and therefore topography-artifact free. The average effective index calculated from Figure 7.5(a) was used to determine the decay constants for the computation. As can be seen in Figure 7.5(c), the variation between real data and normalized data is more pronounced where topography is higher, as expected. The topography-normalization operation is a prerequisite to the 'on-resonance' intensity-normalization procedure used in this chapter, as described in *Section 5.2.3*.

The standing wave displayed in Figure 7.5(a) has some unusual properties that are not caused by the uneven surface alone. This is elucidated by Figure 7.5(c), which shows a relatively small variation in the normalized data, compared to the actual data. In order to identify the particular features of the standing wave that may have been caused by the underlying decay constants along the length of the grating, an ‘off-resonance’ scan was performed on immediate completion of the scan shown in Figure 7.5(a), along the same region. The result is displayed in Figure 7.6(a) where the wavelength of the illuminating laser was set to 784.0nm. As detailed previously in *Chapters 5 & 6*, away from resonance, the intensity distribution along the length of a grating is constant [7.5]. Therefore aside from

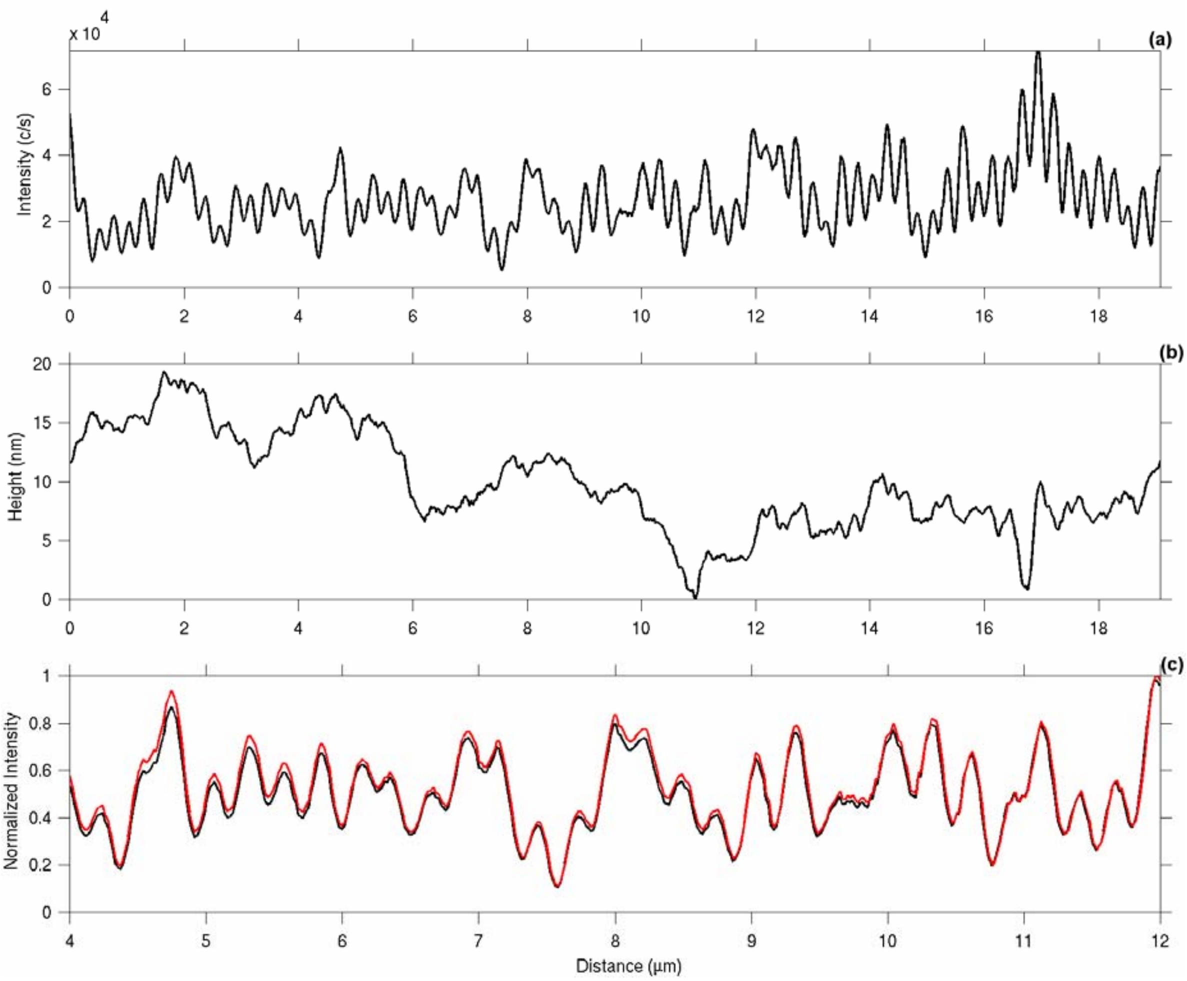

Figure 7.5: Fibre Grating Sample No.4. (a) A resonant evanescent field line-scan over a length of 19.080μm, with 1025 data points. The average period of the standing wave fringes is 265nm. The illuminating laser wavelength was 775.0nm. (b) Topographical data acquired simultaneously to the optical data shown in (a). (c) (Black data): A repeat of the optical data shown in (a), from positions 4-12μm. (Red data): Optical data from (a), normalized with respect to the topographical data shown in (b).

the minor influence of uneven topography, the variation in the measured intensity in Figure 7.6(a), is mainly due to the variation in the local effective refractive index, n_e given by Equations (5.7–5.10). A comparison of Figure 7.5(a) to 7.6(a) illustrates that there are indeed similarities between the overall shapes of each scan. In particular, the rise and subsequent fall in intensity between the points 15-19μm is a feature of both figures. The

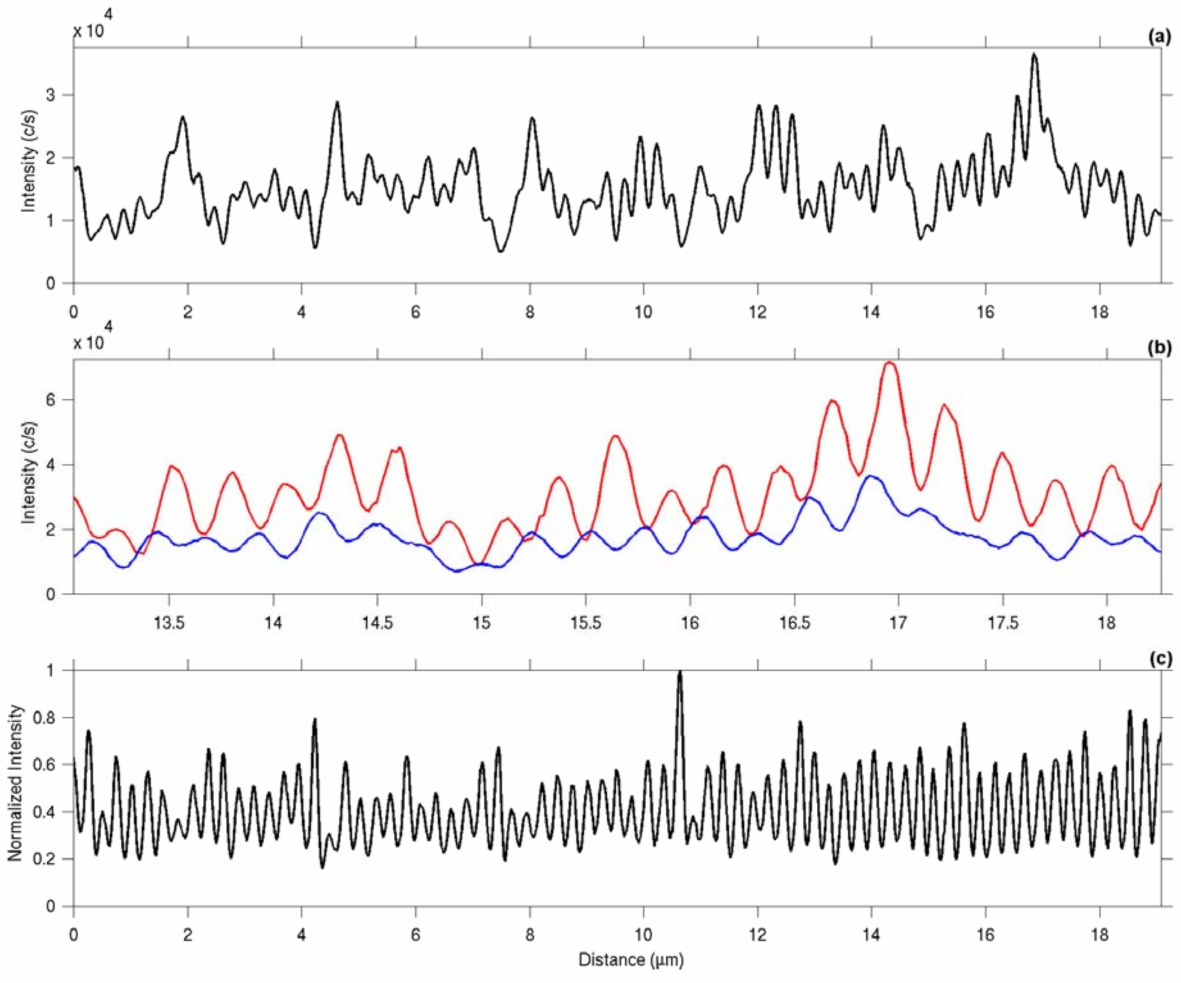

Figure 7.6: Fibre Grating Sample No.4. (a) An 'off-resonance' line scan carried out immediately after the 'on-resonance' scan shown in Figure 7.5(a), over the same region. In this case, the incident laser has been tuned to λ=784.0nm, otherwise all other scanning parameters are identical. (b) (Red data): A section of resonant data from Figure 7.5(a) from points 13.042–18.260μm. (Blue data): A section of non-resonant data from Figure 7.6(a) along the same region. Both sets of data have 281 points. (c) The result of the 'on-resonance' intensity-normalization procedure described in Section 5.2.3 operated upon the 'on' and 'off' resonance data shown in Figures 7.5(a) and 7.6(a) respectively.

larger structure variation in decay constant has therefore had a significant effect on the overall profile of the standing wave in Figure 7.5(a). What is not so clear is the effect that the smaller ripples in the 'off-resonance' data have had. As expected, these ripples have an average period of 265nm, as in the case of the standing wave fringes. This is due to the fact that on first order resonance, the wavelength of the illuminating laser within the grating region equates to two periods of the grating itself, from Equation (5.1). Figure 7.6(b) compares the optical data from both Figures 7.5(a) and 7.6(a), along the region from 13.042-18.260μm, to demonstrate how one set of data varies with respect to the other. As can be seen, the undulations of the data sets appear to be out of phase by a factor of π. Since the lower intensity measurements in the 'off-resonance' data correspond to regions of higher refractive index, this means that a greater proportion of the energy in the 'on-resonant' standing wave is residing within regions of greater refractive index, agreeing with predictions of photonic crystal theory [7.6]. Other similar 'on' and 'off' resonance data sets were acquired for Sample No.1 in *Chapter 5*, but in that instance the position of each data set relative to the other was inconclusive, due to thermal drift.

The distorting effect of the decay constants along the resonant data in Figure 7.5(a) can be considerably reduced by initializing the 'on-resonance' intensity-normalization procedure, detailed in *Section 5.2.3*. By this method, the 'on' and 'off' resonant data sets discussed above were used to generate Figure 7.6(c), which to a good approximation, represents the standing wave intensity distribution at the core/cladding interface. This result is interesting because it is probably data that cannot normally be acquired by direct SNOM measurement, since there must always be some cladding present in order to efficiently guide light along a grating [7.7]. A comparison of the data shown in Figure 7.6(c) to its 'un-normalized' equivalent data given in Figure 7.5(a), makes clear the usefulness of the intensity normalization procedure. The normalized line scan appears to suffer none of the original distorting effects of the decay constants along the fibre grating, and displays a greater uniformity across its fringes. In addition, the position of every peak and trough is clear, unlike before normalization, where some ambiguity existed. However, there probably does exist some 'smoothing' along the normalized set, because of the averaging effect caused by the original measurements being made some distance from the core/cladding boundary. This effect was discussed in *Section 5.2.2*.

A Fast Fourier Transform (FFT) was performed upon each of the ‘on resonance’, ‘off resonance’ and ‘intensity-normalized’ data sets shown respectively in Figures 7.5(a), 7.6(a) and 7.6(c). The results are displayed in an equivalent order in Figures 7.7(a), 7.7(b) and 7.7(c). In all three FFT’s, the main peak represents a spatial frequency of 3.77μm^{-1}, which equates as expected, to the previously calculated period in each case, of 265nm. The ‘on resonance’ FFT illustrated in Figure 7.7(a) shows a high level of lower frequency activity which appears to have originated from the low frequency ‘noise’ present in the ‘off-resonance’ FFT displayed in Figure 7.7(b). The ‘noise’ is a consequence of the decay constant variation along the measured section of the grating. This is confirmed by the FFT of the ‘intensity-normalized’ data in Figure 7.7(c), where the lower frequency activity has

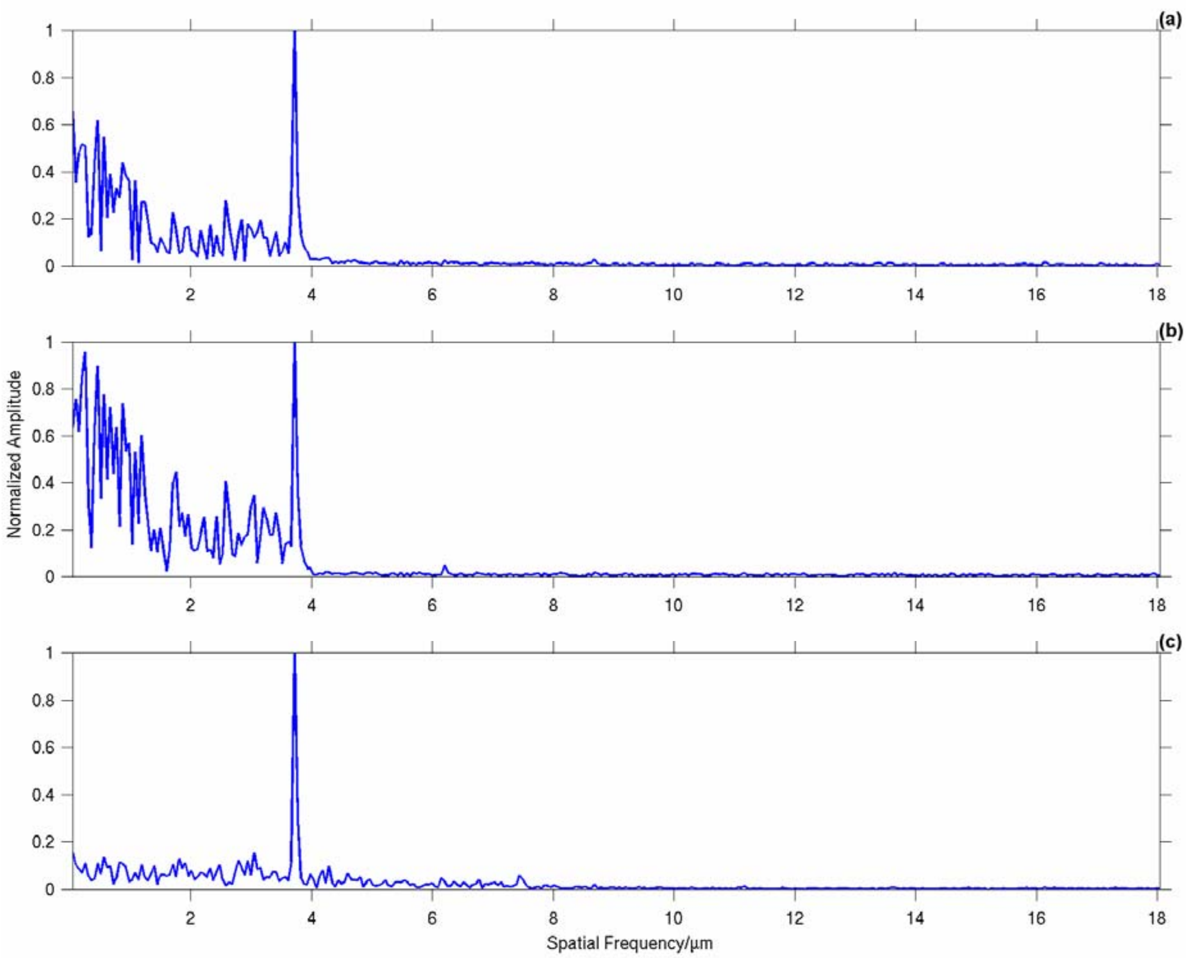

Figure 7.7: (a) An FFT of the ‘on resonance’ standing wave data shown in Figure 7.5(a). (b) An FFT of the ‘off resonance’ data displayed in Figure 7.6(a). (c) An FFT of the intensity-normalized data shown in Figure 7.6(c). In all three figures, the main peak corresponds to a spatial frequency of 3.77μm^{-1}, which equates to a period of 265nm.

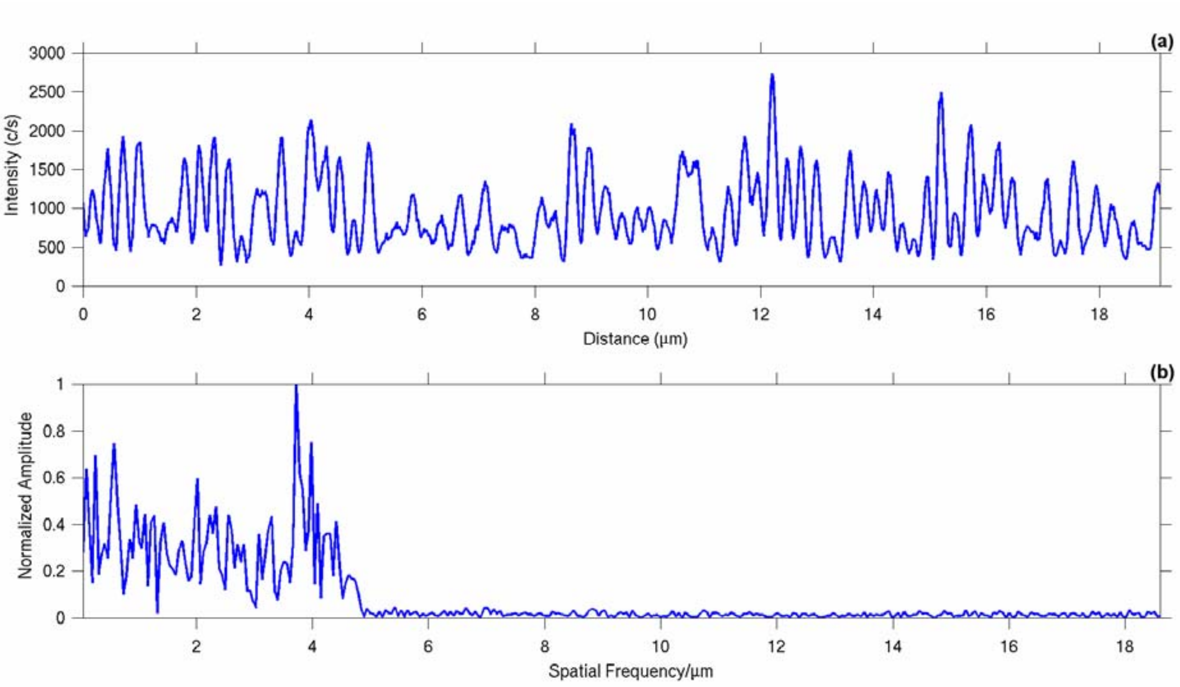

Figure 7.8: Fibre Grating Sample No.4. (a) A 19.080μm, 1025 data points, 'off-resonance' line-scan along the axis of the grating. The illuminating source was a HeNe laser (λ=632.8nm). The position of the scan was in the region central to the grating, although not in exactly the same place as previous data sets in this section. (b) FFT of Figure 7.8(a), with the main peak corresponding to a spatial frequency of $3.77\mu m^{-1}$, equating to a period of 265nm.

virtually disappeared on removal of the effect of the underlying decay constants.

The 'off-resonance' condition was investigated further by launching a HeNe laser (λ=632.8nm) into the fibre grating and performing a line-scan along its axis. The data can be observed in Figure 7.8(a). Although the scan was again carried out within the central region of the grating, it was not performed in exactly the same place as previous figures in this section. However, the fringes are equally as distinguishable as those shown in the 'off-resonance' data of Figure 7.6(a), where the illuminating laser was tuned to 784.0nm. The shorter wavelength however, has procured greater contrast as predicted in *Section 5.2.2*. A Fast Fourier Transform of the data shown in Figure 7.8(a) is presented in Figure 7.8(b), where the main peak corresponds again to $3.77\mu m^{-1}$. As before, there is a great deal of 'noise' in this 'off-resonance' FFT, although unlike before, frequencies greater than the expected period of the grating are also prevalent. The highest significant frequency peak which is at position ~4.6-4.7μm^{-1}, probably relates to reflected laser light interfering with the forward propagating light. The actual spatial frequency of standing wave fringes corresponding to the laser wavelength $\lambda=(632.8/2n)$nm, is estimated to be 4.63μm^{-1}. Indeed, this particular artifact has been much reduced compared to gratings examined in previous chapters, because in the present case, the exiting pigtail was terminated in index oil. However, other peaks in the FFT both above and below the expected index period cannot be accounted for by such imaging artifacts, and therefore must be assumed to be a consequence of a non-uniformly varying decay constant.

7.4.1.2 Fibre Grating Sample No.4: Two-Dimensional Scans

The irregularity of the refractive index contrast of Sample No.4 identified by the line-scans and Fourier Transforms so far in this section becomes more obvious on inspection of two-dimensional images of the grating. An example of an 'off-resonance' evanescent field image of the fibre grating is shown in Figure 7.9(a), where the illuminating laser

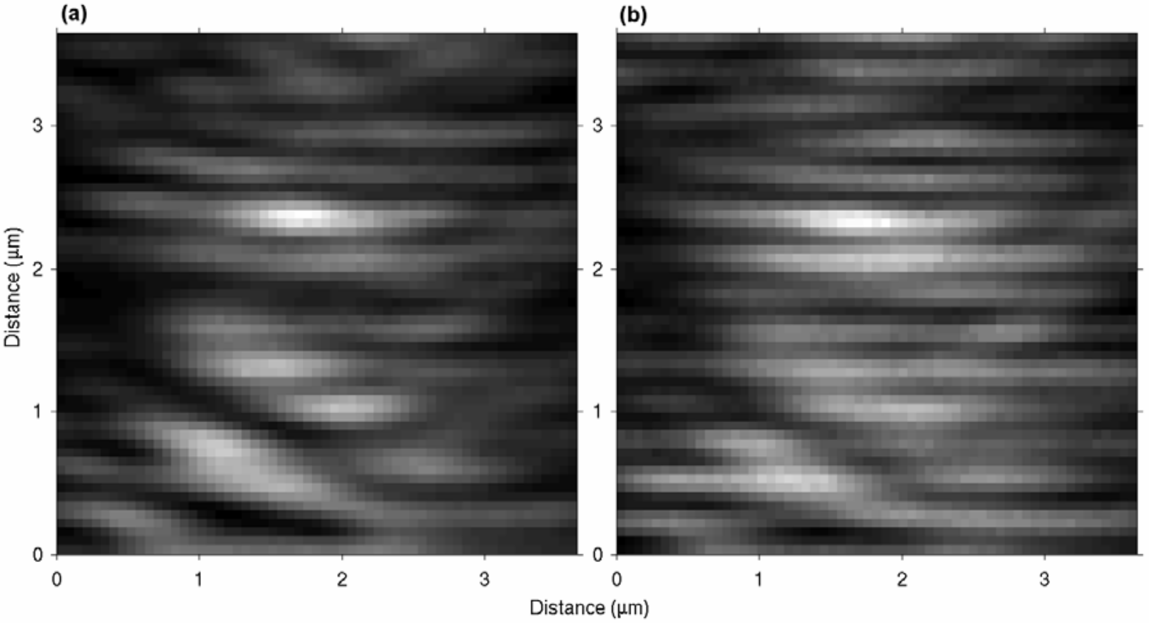

Figure 7.9: Fibre Grating Sample No.4. (a) An 'off-resonance' image. The illuminating laser wavelength was 784.0nm. (b) An 'on-resonance' image, taken on the immediate completion of the scan shown in (a), with an illuminating laser wavelength of 775.0nm. In both figures, the dimensions are 3.71x3.71μm with 60x60 pixels.

wavelength was tuned to 784.0nm. The axis of the fibre grating is positioned down the centre of the scan, which has dimensions 3.71x3.71μm and a 60x60 pixel matrix. The periodic refractive index fringes across the image can be seen to be generally straight, and perpendicular to the axis of the grating. This can be contrasted with the slightly curved index fringes of Sample No.1 shown in *Chapter 5*, which were created by a phase-mask. However, there does appear to be 'breaks' in the lines caused by areas of darkness (high effective index) and brightness (low effective index). These anomalous regions have superimposed themselves onto the image shown in Figure 7.9(b), which was taken with the grating tuned on resonance at the wavelength, λ=775.0nm. The data for the image in Figure 7.9(b) was collected on immediate completion of the scan displayed in Figure 7.9(a).

7.4.1.3 Fibre Grating Sample No.5: One-Dimensional Scans

From the data shown in the previous section, it is clear that there was little difficulty in making a measurement of the periodic evanescent field intensity variation of Sample No.4, caused by the variation in its grating's refractive index profile, when illuminated off resonance. In the case of Sample No.5 however, the periodic modulation of 265nm caused by the variation in its decay constant was not so easy to identify. This is demonstrated in Figure 7.10(b), which shows an 'off-resonant' line scan of Sample No.5, taken within the region central to the grating, along its axis. As can be seen, the modulating decay constant has a very strong periodic component of ~800nm, which equates to approximately three times the magnitude of the expected period. However, since all of the gratings examined during this chapter were created under identical conditions, it must be assumed that the properties of the gratings are also similar. Indeed, it is likely that the scans performed upon Samples No.4 & 5 were at different locations of each core, relative to the original position of the incident writing laser. It is known that in some types of gratings, particularly when the incident writing laser is a high energy single pulse, one side of the core suffers greater damage than the other [7.9]. Although the gratings examined in this chapter were not written by this single pulse technique, the SNOM measurements suggest that the incident laser energy density was high enough to create an imbalanced effect across the grating, probably to a level that is unidentifiable by previous methods [7.4, 7.9].

This postulate of non-uniformity is strongly supported by the nature of the transmission spectra of these gratings displayed in Figure 7.4. A potent scattering of light shorter in

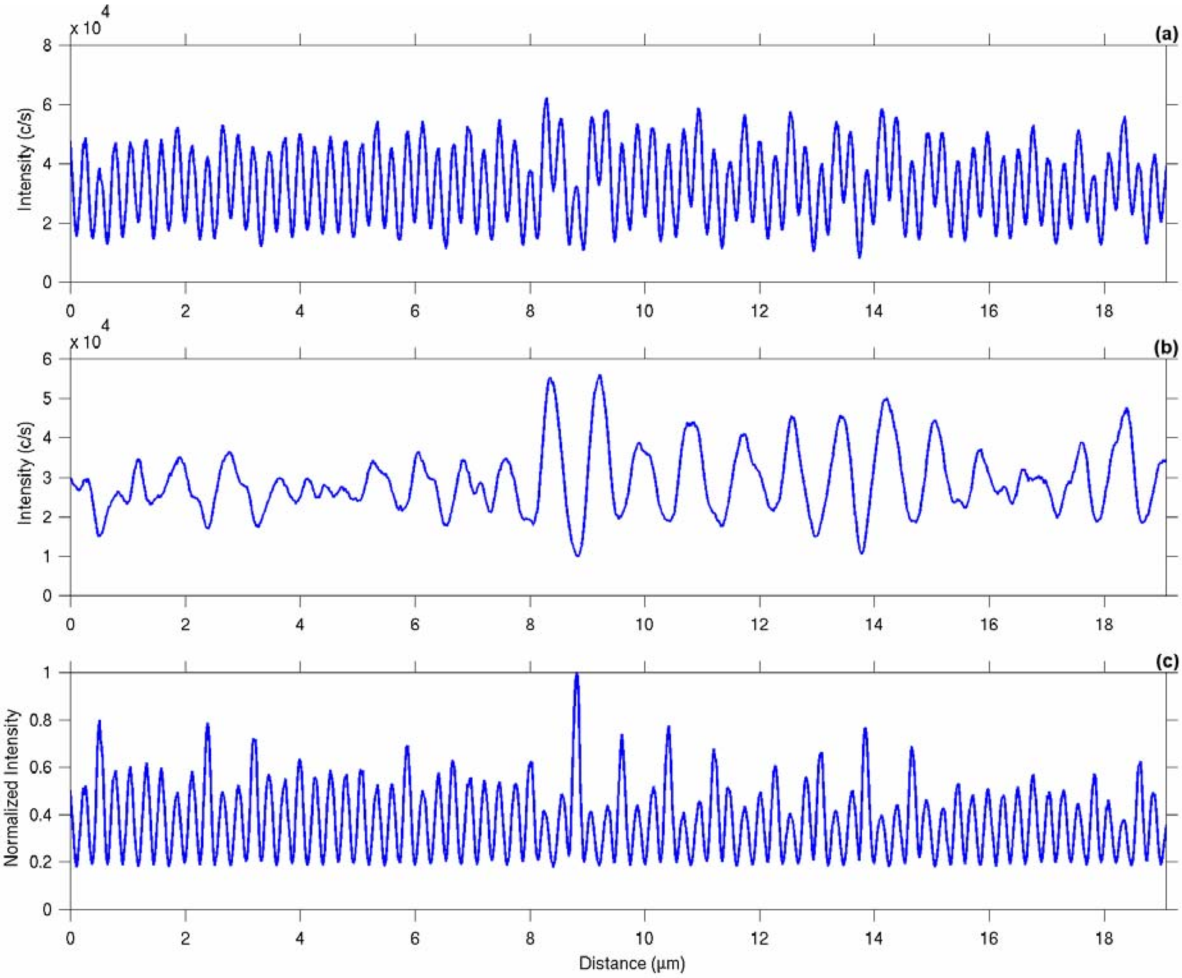

Figure 7.10: Fibre Grating Sample No.5. (a) On resonance with the incident laser tuned to 775.0nm. (b) Off resonance with the incident laser tuned to 784.0nm. This scan was performed immediately after the resonant scan shown in (a), along the same region. (c) The result of the 'on resonance' intensity-normalization procedure (described in Section 5.2.3) operated upon the data shown in (a) with respect to the data in (b). In the case of all three figures, the scan length is 19.08µm with 1025 data points.

wavelength to λ_B, is present in all three spectra. This is a typical feature of gratings that have a non-uniform refractive index profile in a direction perpendicular to their axes [7.8].

A line scan of Sample No.5 taken on resonance along the same region to that shown in Figure 7.10(b) can be observed in Figure 7.10(a). Here, there is no difficulty in identifying the 265nm standing wave period. Figure 7.10(c) shows the result of normalizing the resonant data of Figure 7.10(a), with respect to the non-resonant data shown in Figure

7.10(b), using the procedure described in *Section 5.2.3*. A consequence of this action, is that this approximated measurement of the standing wave at the core/cladding interface, has a more or less flat line of minimum intensity along the length of the normalized wave. This effect was not seen on any other grating examined in this thesis.

Fast Fourier Transforms of the data shown in Figures 7.10(a), 7.10(b) and 7.10(c) are shown in Figures 7.11(a), 7.11(b) and 7.11(c) respectively. Surprisingly, the ‘on-resonance’ FFT of Sample No.5 shown in Figure 7.11(a) displays none of the decay constant noise present in

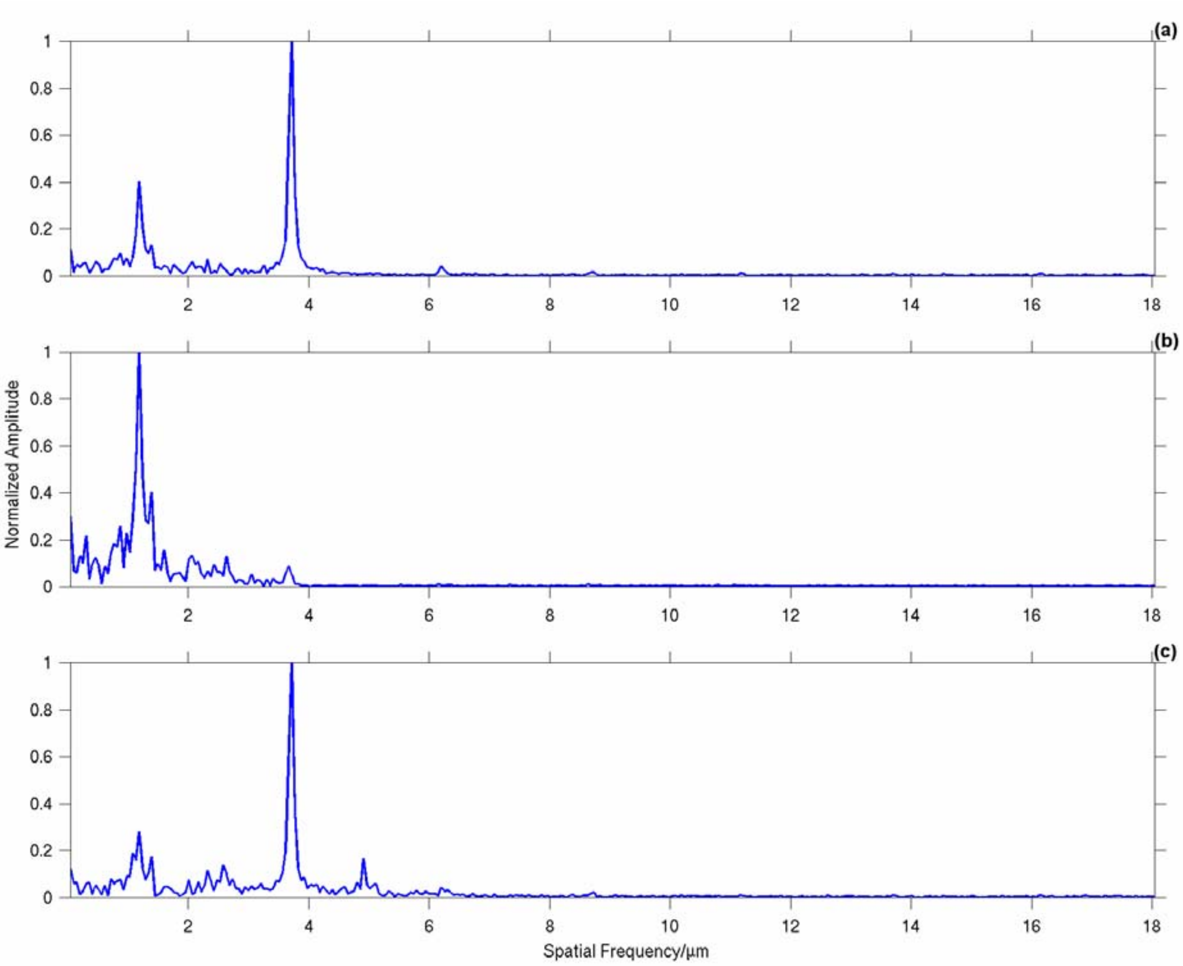

Figure 7.11: (a) An FFT of the ‘on resonance’ standing wave data shown in Figure 7.10(a). (b) An FFT of the ‘off resonance’ data displayed in Figure 7.10(b). (c) An FFT of the intensity-normalized data, shown in Figure 7.10(c). In (a) and (c), the main peak corresponds to a spatial frequency of $3.77\mu m^{-1}$, which equates to a period of 265nm. However, in (b), the main peak corresponds to a frequency of $1.25\mu m^{-1}$, which equates to a period of 800nm.

the ‘on-resonance’ FFT of Sample No.4 shown in Figure 7.7(a), except for the peak at 1.25μm^{-1}. This atypical peak, which corresponds to a period of 800nm as mentioned above, can be seen again in the equivalent ‘off-resonance’ FFT in Figure 7.11(b). There is a small ‘bump’ also seen on this FFT at 3.73μm^{-1} which unfortunately corresponds to a wavelength of $\lambda=(784/2n)$nm and therefore is a function of the illuminating laser, and not any refractive index variation. However, the final FFT of this group is more interesting. An inspection of Figure 7.11(c) shows four main peaks which have spatial frequencies corresponding to spatial periods that are all within 2% of the following: $3.0(\lambda/2n)$, $1.5(\lambda/2n)$, $1.0(\lambda/2n)$ and $0.75(\lambda/2n)$. It is clear from this FFT, that there is some harmonic activity present in the normalized standing wave of Figure 7.10(c).

Similar activity was also seen in the holographically written samples of *Chapter 6*, where it was suggested that the mechanisms causing the phase errors in the standing waves may have been different to those present in the phase-mask written Sample No.1. It is possible that the non-uniformity in Λ and Δn is far more pronounced in Sample No.1 compared to samples made by two-beam interference, leading to a more complicated intensity distribution. Indeed Sample No.1, had many more resonant SNOM scans performed upon it than any of the subsequent gratings, with no harmonic activity ever pinpointed. Nevertheless, it is clear from the discussions above that non-uniformity, albeit diminished compared to Sample No.1, is prevalent at least across the axis of the gratings presented in this chapter.

Figures 7.12 and 7.13 show further examples of intensity-normalized standing waves and their associated FFT’s acquired from varying positions along Sample No.5. In both of these supplementary examples, a careful examination of the standing wave itself reveals evidence of larger period structure caused by beating between the propagating waves. Indeed, the phase errors are again caused by variations in Λ and Δn. The visual evidence of structure is confirmed by the lower frequency activity in each grating’s FFT where in each case, the corresponding spatial period of the three most prominent frequencies are again within 2% of $3.0(\lambda/2n)$, $1.5(\lambda/2n)$ and $1.0(\lambda/2n)$.

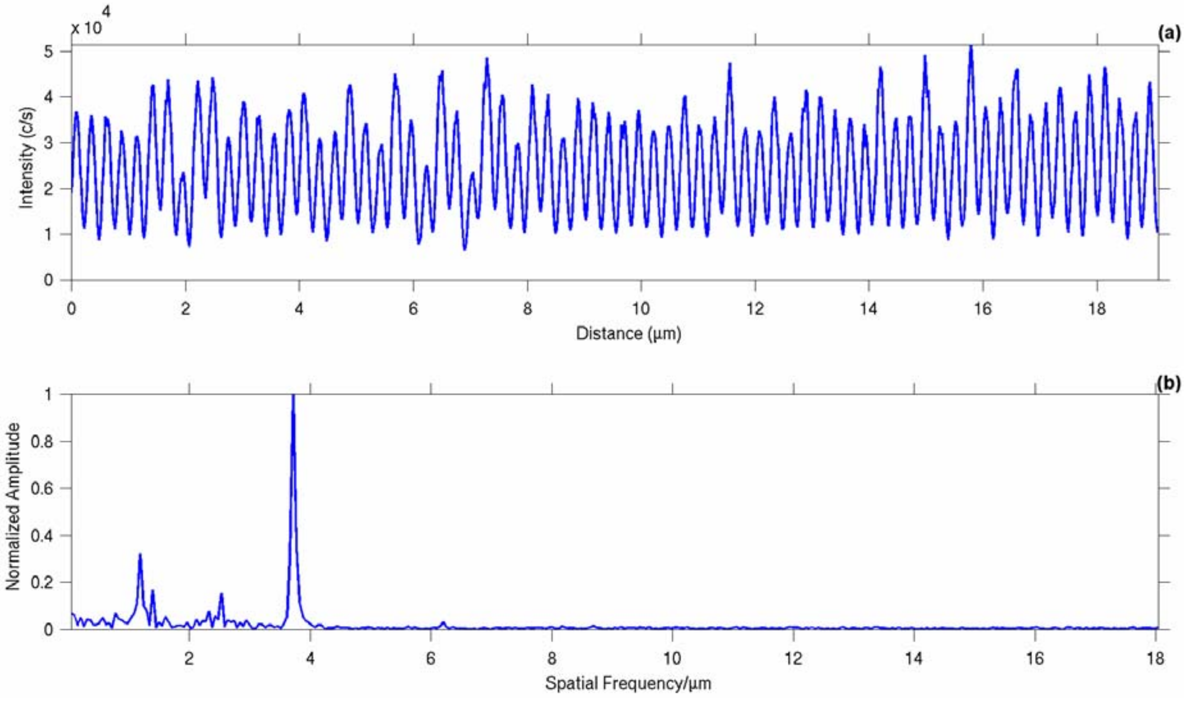

Figure 7.12: (a) An example of an 'intensity-normalized' standing wave taken from Sample No.5 at wavelength λ=775.0nm. (b) The associated FFT.

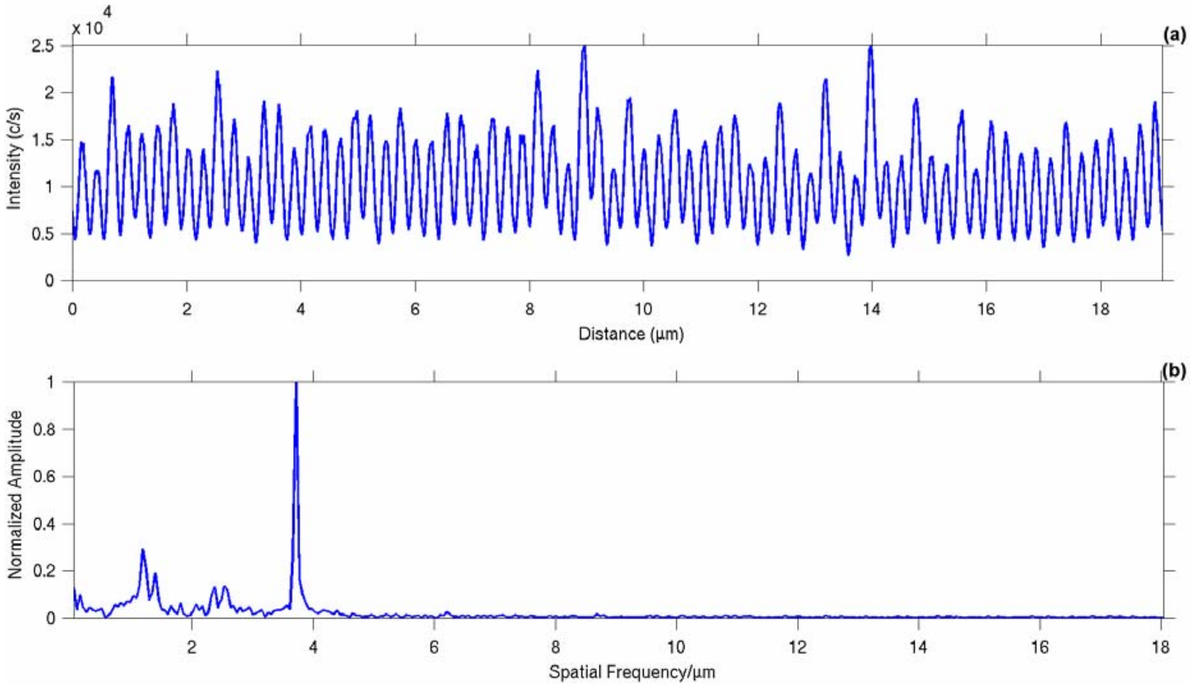

Figure 7.13: (a) A further example of an 'intensity-normalized' standing wave taken from Sample No.5. (λ=775.0nm). (b) The associated FFT. The resonant examples given in Figures 7.10, 7.12 and 7.13 are taken from different positions along Sample No.5.

7.4.1.4 Fibre Grating Sample No.5: Two-Dimensional Scans

Figure 7.14 introduces two-dimensional images of Fibre Grating Sample No.5. In each case, the grating's axis is positioned down the centre of the scan, and all scans have dimensions 7.552x7.552μm, with 100x100 pixels. Firstly, an 'off-resonance' data set is shown in Figure

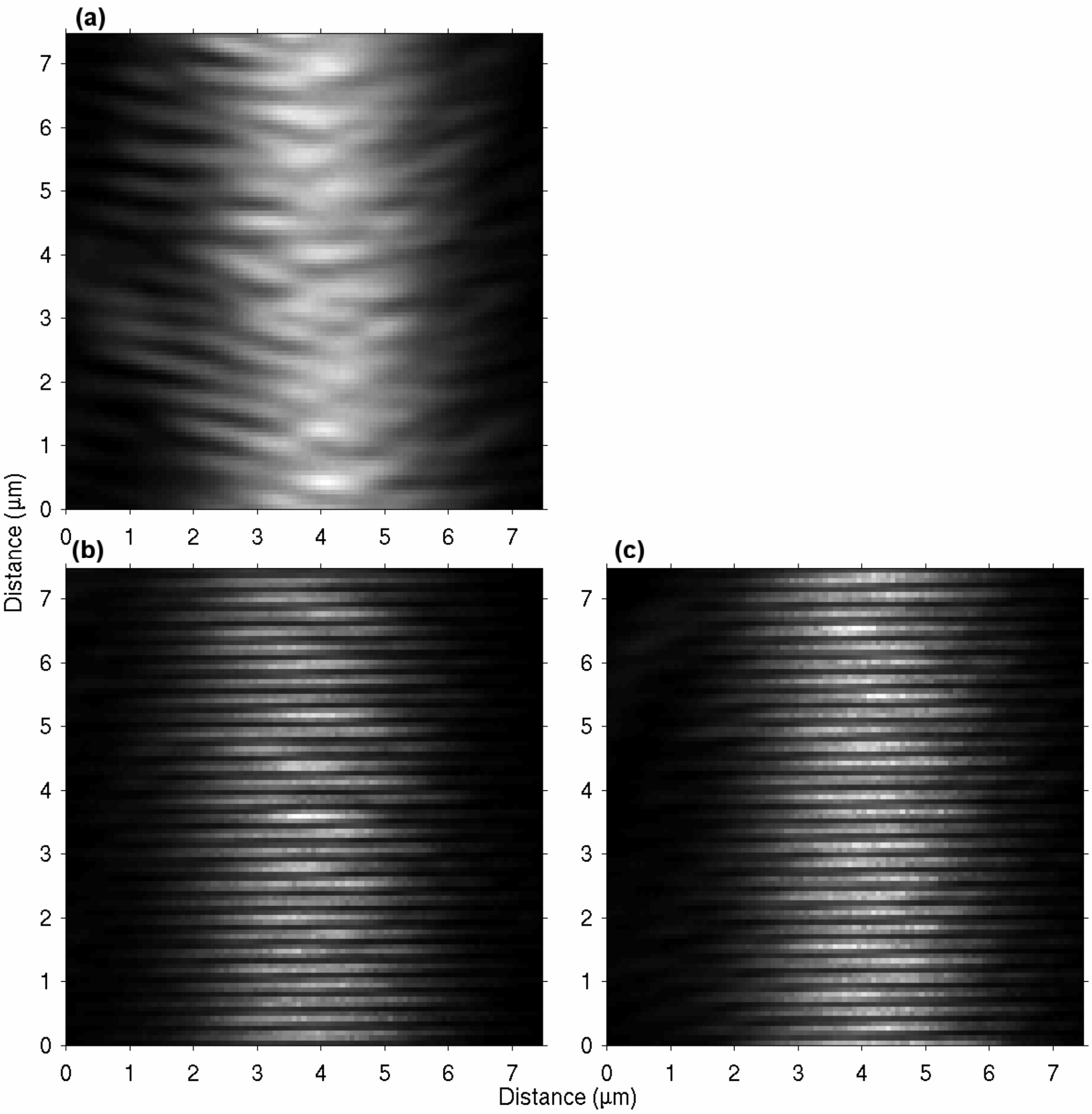

Figure 7.14: Fibre Grating Sample No.5. (a) Off resonance, with the incident laser tuned to wavelength, λ=784.0nm. (b) On resonance at a wavelength, λ=775.0nm. This image was collected on immediate completion of the scan shown in Figure 7.14(a). (c) Again on resonance at a wavelength, λ=775.0nm, although not in the same place as the scans shown in Figures 7.14(a) and 7.14(b). In all three figures, the dimensions were 7.552x7.552μm with 100x100 pixels.

7.14(a) where the illuminating laser has been tuned to 784.0nm. As in the example of the 'off-resonance' line scan and its associated FFT given in Figures 7.10(b) and 7.11(b) respectively, there is no recognizable variation here that equates to the expected 265nm index period. Nevertheless, towards the sides of the image, in particular on the left, there appears to be periodic structure. However, this almost certainly exists as a consequence of scattered light, because the diameter of the grating is much narrower than the image, at only 4.65μm.

Examination of the central region of the scan where the cladding is shallowest and directly above the Bragg grating, reveals a form of interwoven pattern, which may be a result of periodic index variation, complicated by areas of the anomalous 'darkness' and 'brightness' seen in the example of Figure 7.9(a). Figure 7.14(b) shows a repeat scan taken immediately after the image was collected for Figure 7.14(a) over the same region, only this time with the laser tuned on resonance at λ=775.0nm. As can be seen, a standing wave with period 265nm has been recorded. Unlike the resonant two-dimensional scan of Sample No.4 shown in Figure 7.9(b), this scan is not visibly affected by the underlying decay constants recorded in Figure 7.14(a), confirming the notion that many of the features in this figure were induced by scattered light. In Figure 7.14(b) however, there is some noise across many of the lines of data that was most likely caused by unsteadiness in tip height, due to the lock in system slipping from its optimum condition. This can sometimes be caused for example, by the sample becoming gradually contaminated with surface water, or even slight damage to the tip. Nevertheless, as in the case of the holographically written samples of *Chapter 6*, there appear to be no phase errors present in the standing wave of Figure 7.14(b). Again, this is in contrast to the phase-mask produced Sample No.1.

A repeat resonant scan taken over a different region of the same grating is shown in Figure 7.14(c). This image clearly has very similar characteristics to 7.14(b).

7.4.1.5 Fibre Grating Sample No.6: One-Dimensional Scans

So far in this chapter, the examination and subsequent comparison of Samples No.4 & 5 has shown up some differences between the two gratings, despite being made under identical conditions. Fibre Grating Sample No.6 is the third and final grating to be inspected from this batch of gratings, and as this section will show, some characteristics that have been observed in both of the previous two samples and indeed in the holographically written samples of *Chapter 6*, will be seen again here. There will also be some qualities shown that are peculiar to Sample No.6 alone.

Fibre Grating Sample No.6 was tuned on resonance at a wavelength, λ=775.0nm and a line-scan was performed along its axis, close to the central part of its grating. The result is shown in Figure 7.15(a), where a standing wave with period 265nm has been produced. The fringes of the standing wave appear to be regular, well defined and also show evidence of larger period activity, especially between the regions ~(1-5)μm along the scan. Its

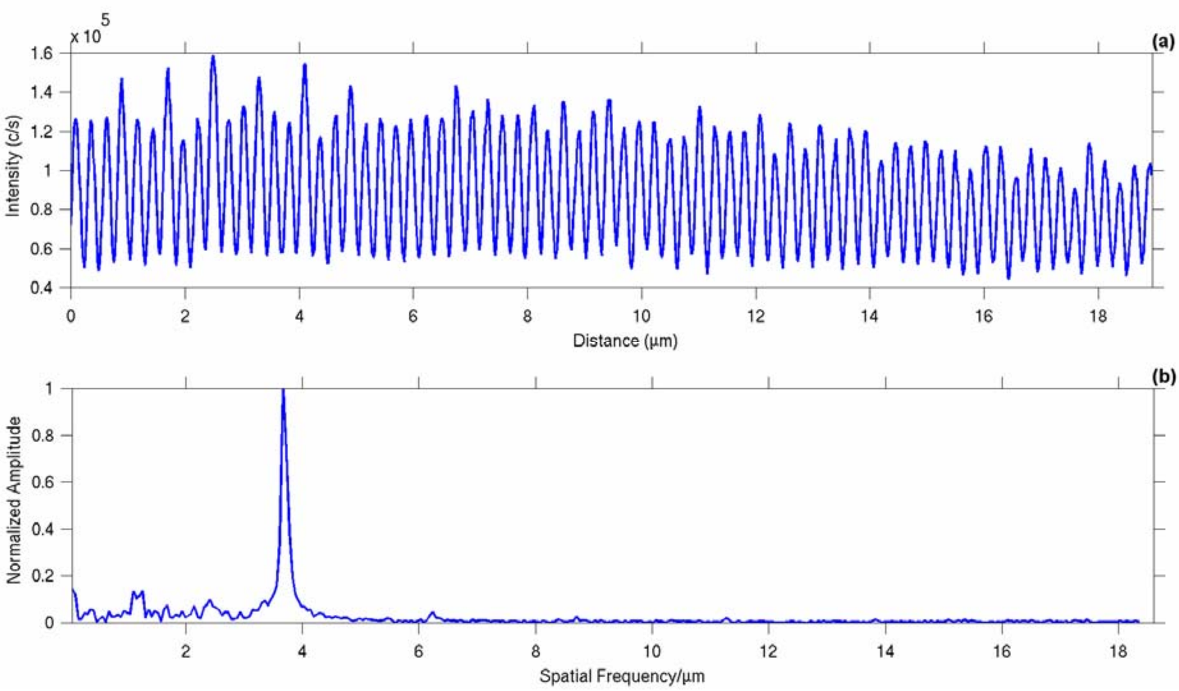

Figure 7.15: Fibre Grating Sample No.6. (a) On resonance, with the incident laser tuned to a wavelength of 775.0nm. The length of the line scan is 18.947μm and has 1025 data points.. (b) An FFT of the data shown in (a), with the main peak corresponding to a spatial frequency of 3.77μm^{-1}, which equates to a spatial period of 265nm.

associated Fast Fourier Transform, which is illustrated in Figure 7.15(b), confirms the observed harmonic behaviour with three of its frequency peaks having related spatial periods within 2% of 3.0($\lambda/2n$), 1.5($\lambda/2n$) and 1.0($\lambda/2n$). This result was seen also in the case of Sample No.5. An additional similarity between the data shown in Figure 7.15 and that of the 'on-resonance' Sample No.5, is that there is little significant lower frequency decay constant 'noise' present, in stark contrast to the resonant data derived from Sample

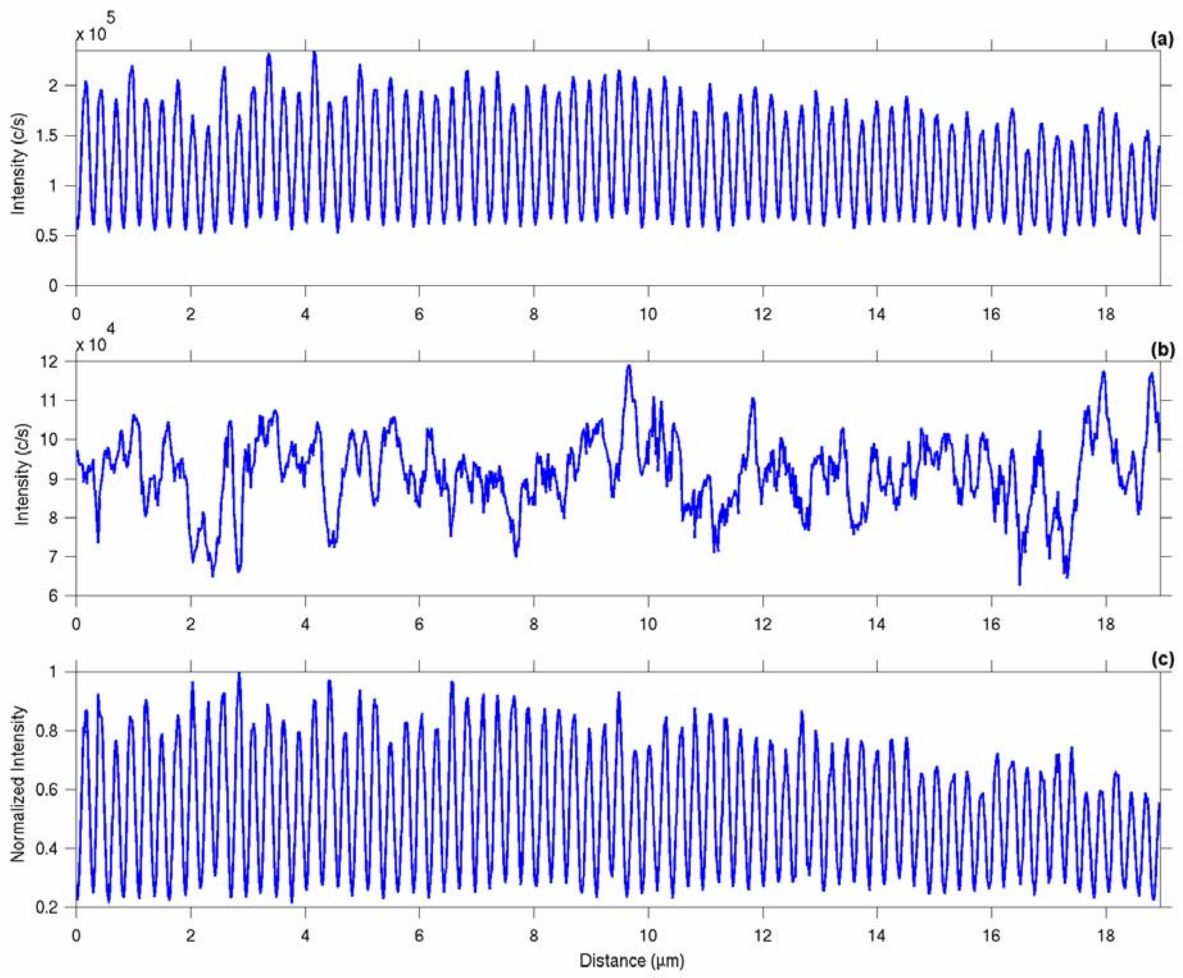

Figure 7.16: Fibre Grating Sample No.6. (a) On resonance at wavelength, λ=775.0nm. This line-scan is in a slightly different place to that in the previous figure. The length of the scan is 18.947μm and it has 1025 data points. (b) Off resonance at wavelength, λ=784.0nm. This data is taken from the same region as that shown in Figure 7.15. (c) The result of the 'on resonance' intensity-normalization procedure (described in Section 5.2.3) operated upon the data shown in (a) with respect to the data in (b).

No.4, whose FFT is shown in Figure 7.7(a). However, the data shown in Figure 7.16 indicates why this is the case. Figure 7.16(b) shows an ‘off-resonance’ scan of Sample No.6 that was taken in a slightly different region of the grating to that shown in Figure 7.15. The modulation depth is comparatively small compared to that seen in similar data acquired from Sample No.4, and therefore will not influence the shape of any resonant data to such a degree. The associated resonant data of Figure 7.16(b) can be seen in 7.16(a), which represents a scan over the same region immediately before its ‘off-resonant’ partner, at a wavelength of 775.0nm. Not unlike the resonant scan of this grating displayed in Figure 7.15(a), the data in 7.16(a) indeed shows little sign of being affected by the underlying decay constants. Confirmation of this minimal influence on the standing wave can be seen in Figure 7.16(c), where only slight variations have resulted from the ‘intensity-normalization’ procedure.

Interestingly, both the overall appearance and modulation depth of the ‘off-resonant’ line-scan given in Figure 7.16(b) is similar to the ‘off-resonance’ data set of Sample No.3, shown in Figure 6.8(b). Significantly, the same data does not compare to either of the ‘off-resonance’ scans of Samples No.4 & 5, shown in Figures 7.6(a) and 7.10(b) respectively. This clearly adds weight to the postulate of non-uniformity in the refractive index profile around the circumference of these single-mode gratings, as discussed in the previous section. If the non-uniformity is a typical function of holographic writing, then it might well be that if Samples No.2 & 3 were originally polished on an alternative region of their fibre circumference, then the images displayed in *Chapter 6* may have been very different.

Fast Fourier Transforms of the data displayed in Figures 7.16(a), (b) and (c) are shown in Figures 7.17(a), (b) and (c) respectively. Figures 7.17(a) and (c), once again show up the standing wave main peak at 3.77μm^{-1} and the smaller, lower frequency ‘bumps’, that were identified in the previous resonant FFT of this grating, given in Figure 7.15(b). Likewise, the ‘off-resonance’ FFT in Figure 7.17(b) shows a peak corresponding to the spatial frequency of 3.77μm^{-1}, representing the Δn period of 265nm. This was also seen in the ‘off-resonance’ FFT’s of Sample No.4, but not Sample No.5. Conversely, the standing wave harmonic activity described above for Sample No.6, was seen in Sample No.5, but not Sample No.4. Clearly, a picture is emerging of three uniformly created Bragg gratings that do not offer uniform information via their evanescent field about their internal structure.

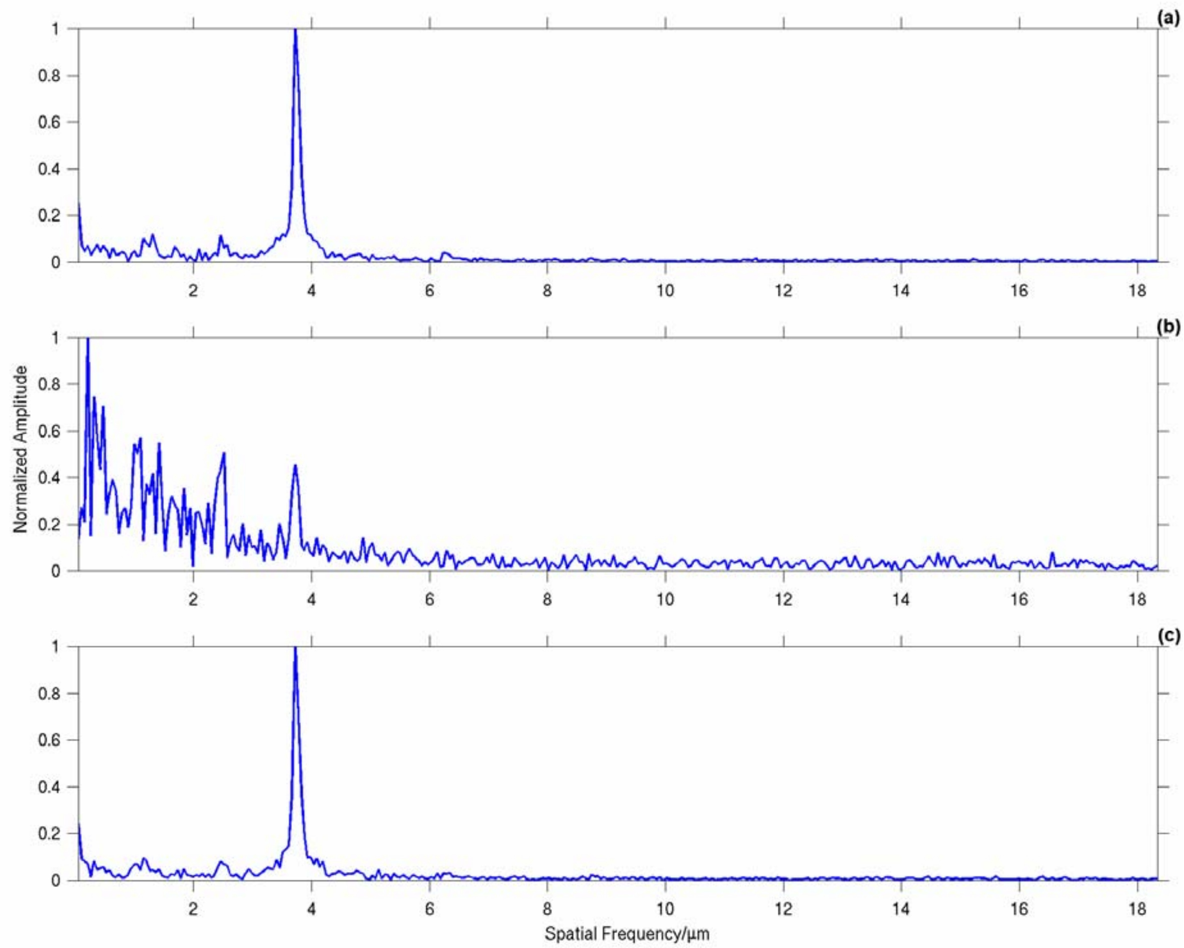

Figure 7.17: (a) An FFT of the 'on resonance' standing wave data shown in Figure 7.16(a). (b) An FFT of the 'off resonance' data displayed in Figure 7.16(b). (c) An FFT of the intensity-normalized data shown in Figure 7.16(c). In all three figures, the main peak corresponds to a spatial frequency of 3.77μm^{-1}, which equates to a period of 265nm.

7.4.1.6 Fibre Grating Sample No.6: Two-Dimensional Scans

During *Chapter 6*, extremely regular, two-dimensional standing wave images were presented of Sample No.3. The images displayed no visible decay constant 'noise', or indeed any phase errors. It should not be surprising therefore, that since similarities have already been identified between Sample No.3 and Sample No.6, that two-dimensional standing wave images of Sample No.6 are the most regular out of all of the single-mode gratings presented in this chapter.

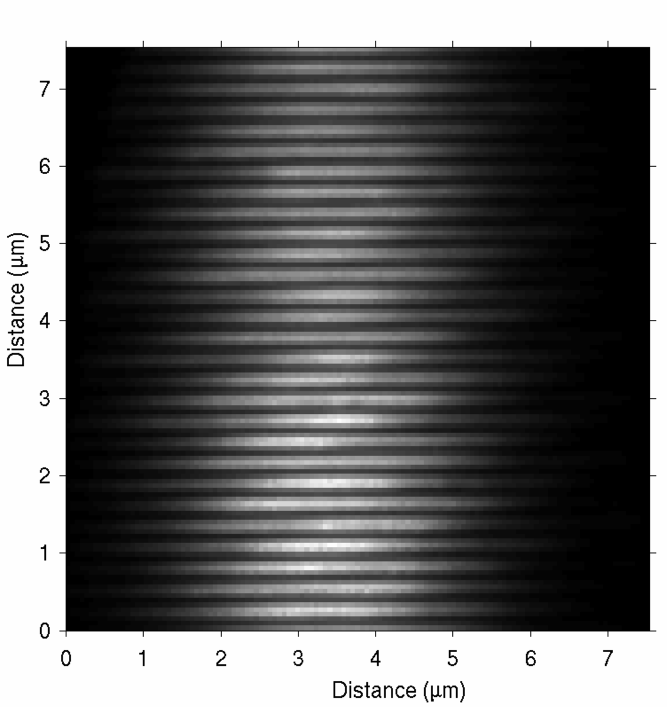

Figure 7.18: Fibre Grating Sample No.6, on resonance, at a wavelength of 775.0nm. The image has dimensions 7.54x7.54µm with 128x128 pixels. The period of the standing wave fringes is 265nm.

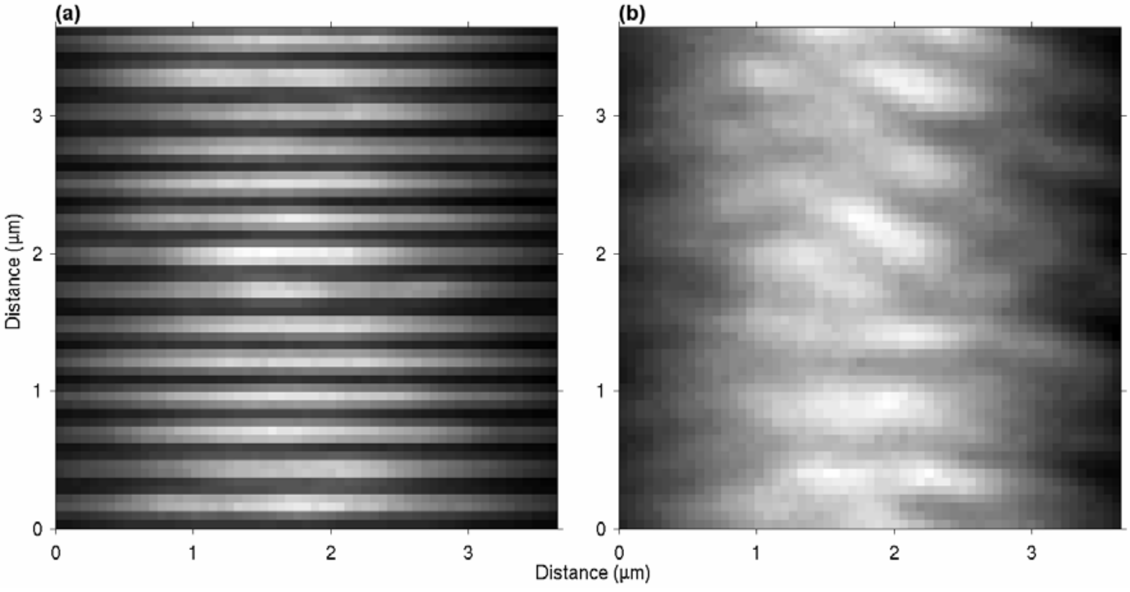

Figure 7.19: Fibre Grating Sample No.6. (a) On resonance at 775.0nm and (b) off resonance at 784.0nm. Both figures are in the same place, and have dimensions 3.71x3.71µm, with 60x60 pixels. These images are not in the same position of the grating as the scan shown in Figure 7.18.

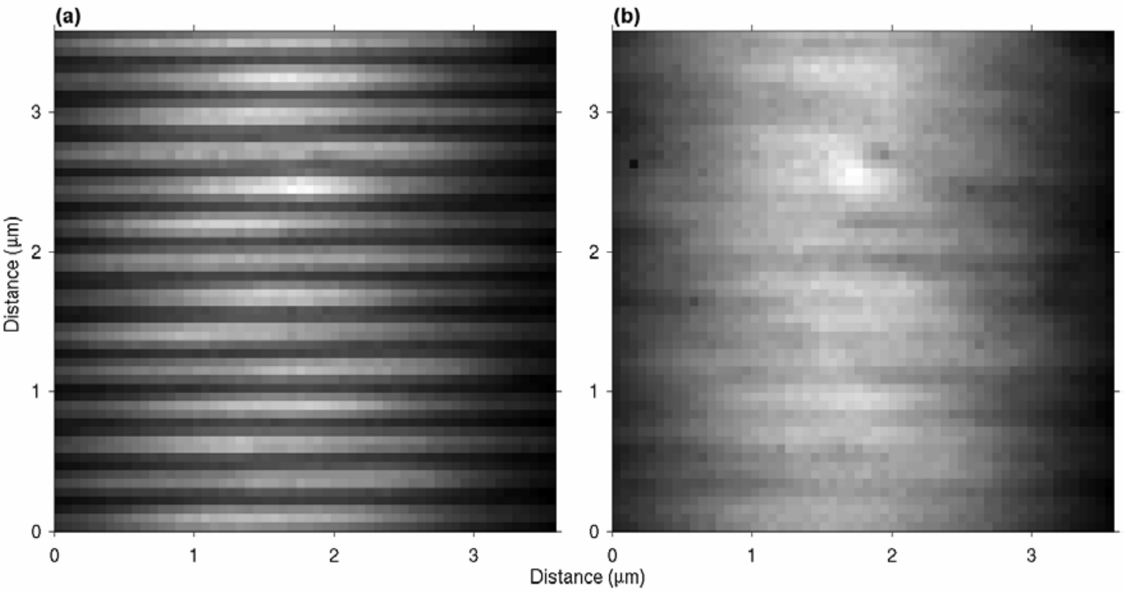

Figure 7.20: Fibre Grating Sample No.6. (a) On resonance at 775.0nm and (b) off resonance at 784.0nm. Both figures are in the same place, and have dimensions 3.65x3.65µm, with 59x59 pixels. These images are not in the same position as any of the scans shown in either Figures 7.18 or 7.19.

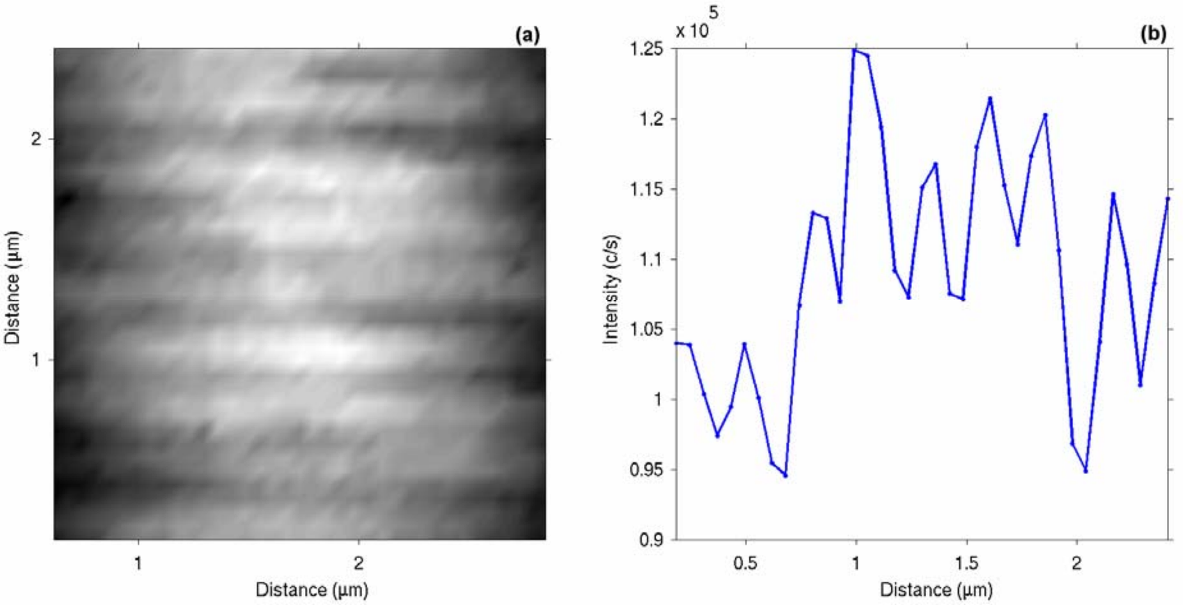

Figure 7.21: (a) Interpolated 'off-resonance' data from Figure 7.20(b), from pixels x=10-46 (0.62-2.84µm) and pixels y=3-39 (0.18-2.41µm), showing up the refractive index variation more clearly. (b) Cross-section of the data shown in (a), up through its centre. The interpolation has been 'undone' for the cross-sectional data.

Examples of two-dimensional, resonant images taken from different regions of Fibre Grating Sample No.6 can be seen in Figures 7.18, 7.19(a) and 7.20(a). All three figures display very uniform standing wave fringes and give the clearest indication yet that these single-mode gratings are not subject to the phase errors that were prevalent in the images of Sample No.1, shown in *Chapter 5*. Additionally, there are two ‘off-resonant’ scans in Figures 7.19(b) and 7.20(b), that were taken at the same positions as the resonant images shown in Figures 7.19(a) and 7.20(a) respectively. Firstly, the image shown in Figure 7.19(b) has periodic bright ‘spots’ down through its centre, that correspond to about twice the period of the known refractive index variation along this grating. Similar features were seen down the centre of the ‘off-resonant’ image of Sample No.5, shown in Figure 7.14(a).

However, the ‘off-resonance’ image in Figure 7.20(b), taken in the same place as the resonant scan shown in 7.20(a), does show the correct refractive index periodicity of 265nm, albeit faintly. Figure 7.21(a) repeats part of the ‘off-resonance’ data shown in this figure, by interpolating the region where the fringes are most prominent. This procedure has facilitated a clearer view of the modulation. A non-interpolated cross-section of the data used to generate Figure 7.21(a) can be seen in Figure 7.21(b), in order to show the modulation depth of the recorded fringes.

7.4.2 Fibre Grating Sample No.6: Free-Space Evanescent Field Imaging

During *Chapter 5* it was suggested that with sufficient thermal stability, it would be possible to carry out a two-dimensional free-space scan perpendicular to a grating’s surface, in order to derive the decay constants over its length, from the columns of data. Of course this would be useful because it offers an alternative method of directly imaging the refractive index variation along the grating. Unfortunately, the necessary thermal stability was not achievable with the current SNOM set-up. However, the trials enabled some rather interesting images to be acquired, of which one is shown in Figure 7.22. This particular scan began at a height of 10nm from the polished surface of Sample No.6, and continued up to a height of 500nm, with the SNOM probe feed-back loop switched off. The length of the scan in the direction parallel to the grating’s axis is 2.385μm, and the overall pixel matrix size is 50x50.

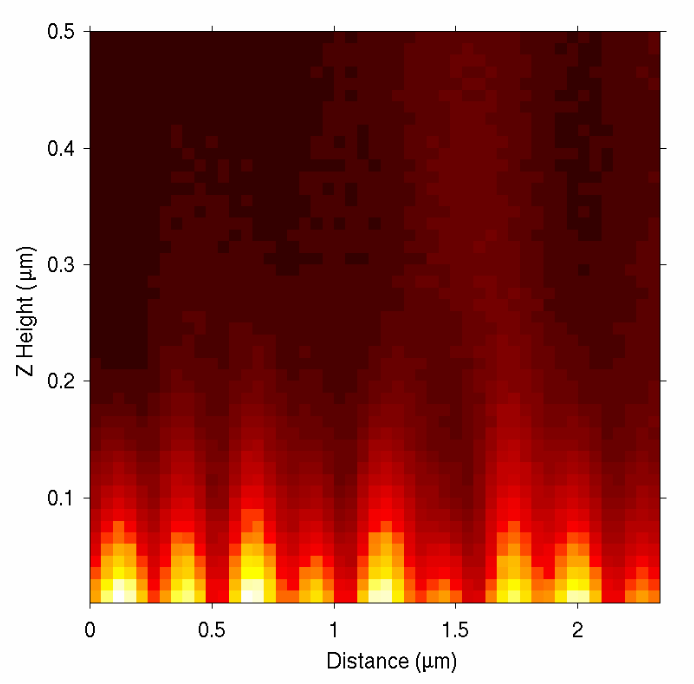

Figure 7.22: Fibre Grating Sample No.6. A 2.385x0.500µm vertical, free-space scan. The grating was tuned on resonance and there are 50x50 pixels. The scan started at a height of 10nm from the grating's polished surface, and the SNOM was set to count photons for 0.5 seconds per data point.

This type of 'free-space' SNOM scan was used extensively during *Chapter 4* to retrieve electric-field intensity data from the region above a phase-mask, but in that case the measurement was of propagating light, and therefore was diffraction limited. However, the data displayed in Figure 7.22 does not have such a restriction and indeed displays sub-wavelength, free-space intensity variations. Whilst the data was being collected for Figure 7.22, the laser was tuned to grating resonance and therefore the periodic, higher intensity region at the bottom of the image is in fact a cross-section of the evanescent component of the standing wave. As can be seen, the contrast in the field caused by the standing wave fringes can be identified over 200nm from the grating's surface.

7.4.3 Decay Constant Measurements

The collection of the data set shown in Figure 7.22 was achieved by scanning the SNOM tip parallel to the grating's axis before moving up a step, and then along the next row. This process was repeated until the row of data furthest from the surface was collected. However, in the time taken to achieve the measurement of a complete line of data, the location of the tip relative to the sample varied on return to its starting position. This was due to thermal drift on a nanometre scale. The cumulative effect of the drift consequently made decay constant calculations difficult. Scanning in columns rather than rows could have solved the problem, except that thermal drift in the z-direction over the time taken to acquire a two-dimensional scan may have endangered the tip. Indeed, this problem could have also been overcome by starting the scan some distance (at least 45-50nm) away from the sample, but the refractive index fringe visibility (as described in *Section 5.2.2*) would then have been compromised. An improvement to the SNOM's computer functionality by enabling it to monitor and react to surface forces, coupled with an improvement to thermal stability would solve these problems. Clearly, there is scope for future work here. Nevertheless, single column scans taking just seconds to complete, have produced reliable and repeatable measurements of the decay constants along these single-mode gratings.

Following the procedure already detailed in *Section 5.5.2*, the incident laser was tuned to 784.0nm and launched into Samples No.5 & 6 in turn. In both cases, the following identical sets of data was collected from above each grating's axis, close to each grating's central region. Firstly, lines of data were acquired in the z-direction at 11nm intervals starting at a height very close to 0nm, and continuing for 22 data points up to a height of ~231nm. The photon counting time per data point was 1 second. The measurement was repeated at regular intervals of 61.6nm along each grating, up to a total length of 985nm. With the use of the planer waveguide Equations (5.7) and (5.20), sets of decay constants were then approximated from the data and the effective refractive index at each point estimated.

The results for each grating are displayed both graphically and numerically. Figure 7.23(b) and *Table 7.3* show the results collected from Sample No.5, whereas the results from Sample No.6 can be observed in Figure 7.24(b) and *Table 7.4*. Immediately after the completion of the experimental part of the above operation for each grating, a line scan was taken over the same region with the tip re-locked to the surface. This was done in order that comparisons could be made between the measured decay constants and the shape of the 'off-resonance' field close to the surface. The associated optical and topographical surface measurements can be seen respectively in Figures 7.23(a) & (c) for Sample No.5, and Figures 7.24(a) & (c) for sample No.6.

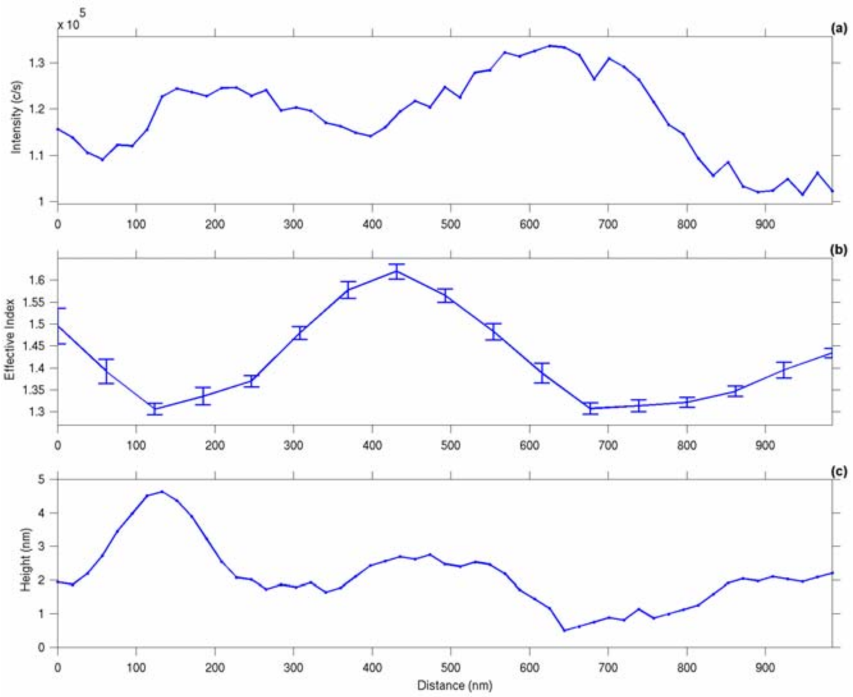

Figure 7.23: Fibre Grating Sample No.5. (a) A 985nm, 53 data point 'off resonance' scan with the SNOM probe locked to the surface. The laser was tuned to 784.0nm, (b) The calculated effective refractive index along the same region as that shown in (a). (c) The topographical data acquired simultaneously to the optical data shown in (a).

Relative position along grating axis (nm)	*Effective refractive index, n_e*	*Relative position along grating axis (nm)*	*Effective refractive index, n_e*
0	1.495 ± 0.040	554.1	1.482 ± 0.018
61.6	1.392 ± 0.027	615.6	1.388 ± 0.022
123.1	1.306 ± 0.013	677.2	1.307 ± 0.013
184.7	1.335 ± 0.019	738.8	1.313 ± 0.013
246.3	1.370 ± 0.012	800.3	1.321 ± 0.011
307.8	1.479 ± 0.014	861.9	1.347 ± 0.011
369.4	1.577 ± 0.019	923.4	1.395 ± 0.017
430.9	1.619 ± 0.016	985.0	1.434 ± 0.010
492.5	1.565 ± 0.015		

Table 7.3: The numerical values of the data shown graphically in Figure 7.23(b).

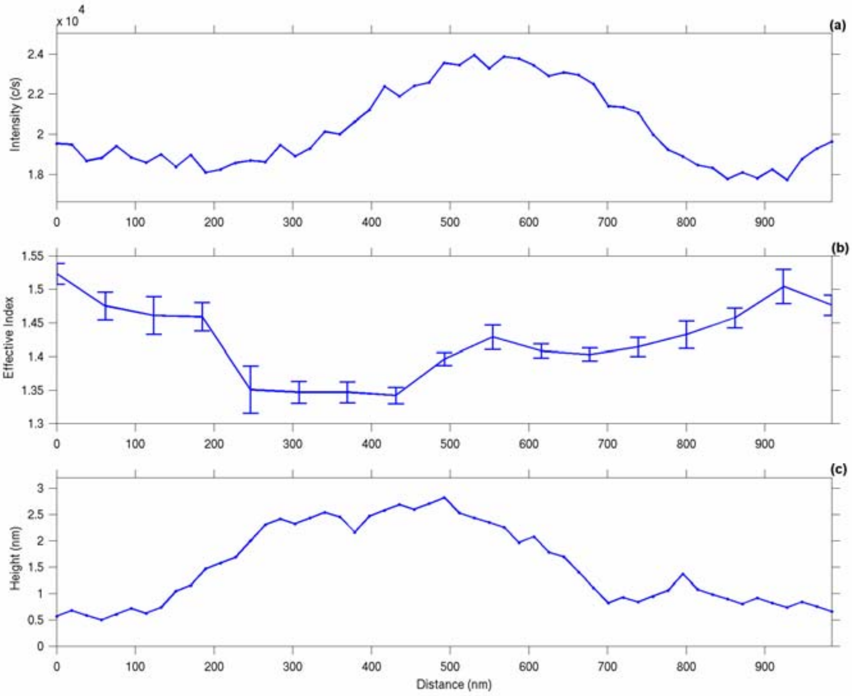

Figure 7.24: Fibre Grating Sample No.6. (a) A 985nm, 53 data point 'off resonance' scan with the SNOM probe locked to the surface. The laser was tuned to 784.0nm, (b) The calculated effective refractive index along the same region as that shown in (a). (c) The topographical data acquired simultaneously to the optical data shown in (a).

Relative position along grating axis (nm)	*Effective refractive index,* n_e	*Relative position along grating axis (nm)*	*Effective refractive index,* n_e
0	1.523 ± 0.015	554.1	1.428 ± 0.018
61.6	1.475 ± 0.020	615.6	1.408 ± 0.010
123.1	1.460 ± 0.028	677.2	1.403 ± 0.009
184.7	1.459 ± 0.021	738.8	1.414 ± 0.014
246.3	1.350 ± 0.035	800.3	1.432 ± 0.020
307.8	1.346 ± 0.016	861.9	1.457 ± 0.014
369.4	1.346 ± 0.015	923.4	1.504 ± 0.025
430.9	1.341 ± 0.012	985.0	1.475 ± 0.015
492.5	1.396 ± 0.009		

Table 7.4: The numerical values of the data shown graphically in Figure 7.24(b).

An inspection of the results presented in Figures 7.23 and 7.24 indicates that the topographic variation along each set of data is not large enough to cause any significant artifacts within the surface optical data. With an overall range of <5nm in each case, the corresponding optical variation will be <4%. The general shape of the surface optical scans will therefore be preserved. A visual comparison of the optical data and its associated refractive index data in both Figures 7.23 and 7.24, shows them to be approximately inversely proportional. The optical data in Figure 7.23(a) basically has two 'peaks' that are mirrored by two 'dips' in the refractive index data of Figure 7.23(b). Moreover, the surface optical data of Figure 7.24(a) has got one 'peak' that is basically mirrored by one 'dip' in the refractive index data of Figure 7.24(b). Indeed, the left hand 'peak' shown in Figure 7.23(a), would in fact be marginally enhanced by any normalization with respect to the associated topographical data shown in Figure 7.23(c), which rises sharply in this region. The 'inverse-proportionality' seen in these figures, was expected because more intense areas of the 'off-resonant' line-scans correspond to regions of lower core refractive index.

In both Figures 7.23(b) and 7.24(b), the effective index does not display the expected periodicity of 265nm, which is known to be present along these gratings. However, this chapter has seen many 'off-resonance' scans of Samples No. 5 & 6 that also do not display the required period. This will be discussed in the next section. One unexpected aspect of the refractive index graphs of both of these gratings is the range of results. It was anticipated that the effective indices of these gratings would be within ~1.45 and ~1.47. However, in both cases, the range is an order of magnitude larger. This is due to the planar waveguide equations used here being an approximation only. It may also be that the effective index has been considerably lowered in places, because part of the energy of the illuminating laser, has been forced to propagate through the air [7.10].

7.5 Chapter Summary

Throughout this chapter, a comparative study has been carried out upon three holographically written single-mode fibre Bragg gratings, by using the SNOM scanning techniques developed in *Chapter 5*. The fibre gratings are named 'Fibre Grating Samples No.4, 5 & 6' for identification purposes. The fibre gratings were created under identical conditions, but did not show identical characteristics during these measurements. It was postulated that the inconsistencies were a direct result of non-uniformity across the gratings' refractive index profiles, in a direction perpendicular to their axes. This postulate was supported by the nature of the grating's transmission spectra. The irregularities were revealed because SNOM scanning was almost certainly performed on different regions of the gratings' circumferences, relative to the direction of the incident writing laser.

It was possible to record standing waves at the Bragg wavelength on all three fibre gratings, from a measurement of their evanescent fields. The periodicity of the standing wave fringes in each case was 265nm, corresponding to an average effective refractive index of 1.462 ± 0.005. Some lower frequency harmonic activity was observed in the resonant images due to phase errors caused by variations in the index fringe period Λ, and modulation Δn. This can be compared to the holographically written fibre gratings examined in *Chapter 6*, which also displayed low frequency harmonic activity, unlike the phase-mask written Sample No.1, which did not.

The observation of the refractive index fringes of the single-mode gratings was not so straightforward. Indeed, Sample No.4 showed up the correct index periodicity, but Sample No.5 did not. Sample No.6 showed evidence of the 265nm periodicity in only one image out of many taken during the investigation. It is known that when a particular writing laser energy threshold is exceeded, that damage is created on one side of the core of the grating. The damage then scatters the writing laser light, which consequently does not then reach the other side of the core [7.9]. It is indeed possible from the evidence derived in this chapter, that a similar, but weaker effect has occurred here, which has created the imbalance in the index periodicity across the core. The abnormal index variation seen on Samples No.5 & 6, was confirmed by a series of decay constant measurements, taken from the exponential decay of the evanescent field along the axes of these gratings.

7.6 References

[7.1] R. Kashyap, *Fiber Bragg Gratings*, Academic Press, 32-34 (1999)
[7.2] G. Meltz, W.W. Morey, W.H. Glenn, Optics Letters, **14** (15), 823 (1989)
[7.3] M.J.F. Digonnet, J.R. Feth, L.F.Stokes, H.J.Shaw, Optics Letters, **10**, no.9, 463 (1985)
[7.4] B. Malo, D.C. Johnson, F. Bilodeau, J. Albert, K.O. Hill, Optics Letters, **18** (15), 1277 (1993)
[7.5] J.-L. Archambault, P.St.J. Russell, S. Barcelos, P. Hua, L. Reekie, Optics Letters, **19**

(3), 180 (1994)

[7.6] J.D. Joannopoulos, R.D. Meade, J.N. Winn, *Photonic Crystals*, Princeton University Press, 16 (1995)

[7.7] M.J.F. Digonnet, J.R. Feth, L.F.Stokes, H.J.Shaw, Optics Letters, **10** (9), 463 (1985)

[7.8] B. Malo, D.C. Johnson, F. Bilodeau, J. Albert, K.O. Hill, Optics Letters, **18** (15), 1277 (1993)

[7.9] J.-L. Archambault, L. Reekie, P.St.J. Russell, Electronics Letters, **29** (5), 453 (1993)

[7.10] J. Wilson, J.F.B. Hawkes, *Optoelectronics: An Introduction,* 2nd ed., Prentice Hall International (UK) Ltd., 310-334 (1989)

8. Conclusions

8.1 General Conclusions

During the course of this project, a Scanning Near-field Optical Microscope (SNOM) has been designed, constructed and characterized in order to facilitate the acquisition of the presented data. Its operation is based upon a tuning-fork/fibre-tip oscillating system [8.1], where positioning of the optical fibre probe close to samples is enabled by detection of surface forces. The set-up has allowed both optical and topographical information beyond the diffraction limit to be obtained. Results have shown highly repeatable data with the occurrence of only small uncertainties corresponding to thermal drift of the SNOM probe relative to the samples. Steps were taken to minimize the thermal drift, which was consequently stabilized to within ±20nm in all three dimensions over the duration of any scan.

The SNOM has been utilized to directly image free-space Talbot patterns close to a phase-mask (transmission diffraction grating). In carrying out these measurements, previous theoretical models have been confirmed, and some useful results relating to fibre Bragg grating manufacture have been established. In particular, some of the technical problems that might occur during the writing of fibre gratings by the phase-mask method [8.2] have been exposed, and therefore will be useful to engineers working in the field. For example, SNOM images shown in *Chapter 4* of this thesis demonstrate the importance of the accurate focusing of an incident laser on the rulings of a phase-mask during grating writing. Fibre grating engineers would normally expect a diffraction pattern consisting of periodic interference fringes of UV light at twice the frequency of the mask rulings and directed orthogonally to the mask surface [8.3]. However, interference fringes that lean towards the phase-mask surface have been shown to result from variations in phase and amplitude across the incident wave-front. Additionally, diffraction features resembling inverse contrast have also been identified from a badly focused incident beam. It is likely that in most cases these distortions cannot be totally eradicated since SNOM measurements have shown that an amplitude gradient alone will induce the harmful effect. Other SNOM measurements of free-space patterns have indicated a further cause of asymmetry in the diffraction pattern that can be more easily avoided – the bad alignment of the incident beam. Failure to align the beam in a direction normal to the phase-mask can have disastrous consequences. An incident angle of just 0.01 degrees results in both the ‘leaning’ effect of the interference fringes *and* a change in their frequency. SNOM measurements performed some distance away from the phase-mask have shown that a general improvement to the fibre grating writing pattern can be achieved by positioning the fibre core out of the range of higher diffracting orders. It would be possible therefore that with appropriate knowledge of an incident beam’s width and its angles of diffraction, the positioning of a fibre relative to a phase-mask during grating inscription could be optimized for minimum beating between orders, resulting in a more uniform writing pattern.

To underpin the analysis of the phase-mask free-space measurements performed during the course of *Chapter 4*, a modified expression for the Talbot length was developed during this project by analogy with x-ray diffraction theory, and is given as Equation (4.6). The equation should replace Rayleigh’s approximate term Equation (4.4), in situations where there are few diffracting orders present. Rayleigh’s expression assumes that $\lambda << a$ where λ is the wavelength of the incident light and a is the period of the phase-mask. Since $\lambda \sim a$ during fibre Bragg grating production, each diffracting order becomes significant and has a measurable Talbot length associated with its interaction with each and every other diffracting order present. The experimental results confirm the new expression in all of the free-space measurements presented in this thesis.

In addition to the free-space measurements of phase-mask diffraction patterns, an examination of the evanescent fields of six separate fibre Bragg gratings has been carried out, which constitutes the major part of the work presented in this thesis. Fibre Bragg gratings are currently used extensively throughout the telecommunications industry and the device can be manufactured with well controlled reflection and transmission characteristics. However, there are limitations in current characterization procedures in the respect that they are mainly macroscopic techniques, offering no localized sub-wavelength information about the electric field distribution and refractive index profile. The most general of these procedures is a measurement of the grating’s reflection and transmission spectra [8.4] but this gives little information about grating structure. Additionally the use of simulation [8.5] has obvious limitations. Nevertheless, photography [8.6] has been utilized in order to identify properties of the grating's structure but this is diffraction limited. Indeed, Transmission Electron Microscopy (TEM) [8.7] has been used to identify structural densification but this too has its limitations due to the fact that it does not give any information about the way that the light is propagating through the grating. Clearly, the electric field intensity and the physical structure of a fibre grating are intimately linked, and therefore high-resolution information on both is extremely useful.

Chapters 5-7 show that it is possible to gain much information about a fibre Bragg grating from its evanescent field by applying SNOM in the scanning mode widely known as Photon Scanning Tunneling Microscopy (PSTM) [8.8]. The collection of data to a sub-wavelength resolution relating to the refractive index structure, grating period and electric field distribution of fibre Bragg gratings has been shown to be feasible. In particular, the position of the 'on resonance' standing wave field distribution has been imaged relative to the refractive index profile for the first time. In the case of the grating discussed during the course of *Chapter 5* which was written by phase-mask, phase and amplitude errors were identified in its local refractive index profile, also for the first time. These errors induced noise in the grating's standing wave, which could be directly imaged by the SNOM probe. Moreover, the contrast of locally imaged refractive index fringes has enabled the Δn of this particular grating to be estimated. This technique would prove useful for apodised gratings where the Δn varies along the grating's length.

In order to estimate absolute values of the local effective refractive indices of all six fibre gratings, vertical line scans were performed in a direction normal to the axis of the gratings. The acquired data enabled the approximation of local decay constants by utilizing planar waveguide theory. Additionally, the average effective refractive index of all of the gratings was calculated by measuring the standing wave fringe period created by a known wavelength of light. The procedure could prove a useful alternative to the method of estimating this value from the reflection spectrum [8.9].

During *Chapter 6* a comparative study of two multi-mode, holographically side-written fibre Bragg gratings was performed, via their respective evanescent fields. SNOM imaging of these gratings showed their standing waves to be apparently free of the noise seen in the standing wave images of the phase-mask written grating studied in *Chapter 5*. This demonstrated that phase and amplitude errors written into the refractive index profile of these gratings was much reduced compared to the phase-mask written sample. However, the refractive index fringes of the holographically-written samples could not be imaged easily leading to the assumption that with the present SNOM system, the limit of refractive index fringe visibility of gratings may be of the order ~1×10^{-3}.

Throughout *Chapter 7*, a comparative study was carried out upon three single-mode holographically-written fibre Bragg gratings. Although these gratings were created under identical conditions, they did not show identical characteristics to each other during examination of their evanescent fields. It would not have been possible to identify this peculiarity with standard characterization methods. It was postulated that the inconsistencies were a direct result of non-uniformity across the gratings' refractive index profiles, in a direction perpendicular to their axes. The irregularities were revealed because SNOM scanning was almost certainly performed on different regions of the gratings' circumferences, relative to the direction of the incident writing laser.

It is hoped that the SNOM measurement procedures and results described in this thesis, will complement existing methods of manufacture and characterization of fibre Bragg gratings and in doing so assist the ongoing development of Bragg gratings, used throughout the telecommunications industry and elsewhere.

8.2 Future Work

There is much scope to further the work begun during the course of this project, in characterizing fibre Bragg gratings. However, if the scanning methods developed here are to be continued, then several limitations identified in sample production, and equipment operation should be advanced. Firstly, it would be useful to mount fibre gratings within their blocks so that they were flat rather than curved, at least along the length of their grating region, in order to allow examination of their entire length. It would also be useful to know in which direction the gratings were mounted relative to the incident writing laser, so that similar regions of different gratings from a batch could be compared. Additionally, it would be an advantage to devise a method to enable scanning to be performed all around a grating's axis. Etching rather than polishing might be a way of achieving this. An improvement to the SNOM itself would be the attachment of stepper-motors to the piezoelectric stage, to enable scans over much larger regions to be routinely performed. The larger period activity identified in grating standing waves, could then be more conclusively investigated, and compared to simulation. There is also considerable scope to improve the speed of the system by tracking phase rather than amplitude [8.10].

There are several experiments that could be implemented as a natural progression to the work begun here. For example, the phase errors that were identified could be examined further. The direct imaging of the phase evolution of light traveling along fibre Bragg gratings would enhance this investigation. This could be achieved using a method such as that described in reference [8.11]. The examination of the power distribution along the complete length of the grating would also be useful in order to confirm the 'coupled mode' formalism, described in *Chapter 2*. There is also much scope to develop thermally stable, unlocked evanescent field imaging in a vertical plane, in order to extract decay constants from columns of data. Indeed, if the interest is solely in the acquisition of sub-wavelength refractive index data, the most useful scheme would be to polish samples right through to their grating cores, and perform SNOM in reflection-mode [8.12]. However, this would preclude examination of the electric field, as light could no longer be guided through the grating. A final suggestion for a future experiment would be to image the free-space electric field intensity of the two-beam interference pattern used to create the holographically side-written gratings. This would complement the data acquired from the phase-mask free-space patterns.

8.3 References

[8.1] K. Karrai, R.D. Grober, Applied Physics Letters, **66** (14), 1842 (1995)

[8.2] K.O. Hill, B.Malo, F. Bilodeau, D.C. Johnson, J. Albert, Applied Physics Letters **62**, 1035 (1993)

[8.3] G. Meltz, W.W. Morey, W.H. Glenn, Optics Letters, **14**, 823 (1989)

[8.4] R. Kashyap, *Fiber Bragg Gratings*, Academic Press, London, 409 (1999)

[8.5] F. Ouellette, P.A. Krug, R. Pasman, Optical Fiber Technol., **2**, 281 (1996)

[8.6] B. Malo, D.C. Johnson, F. Bilodeau, J. Albert, K.O. Hill, Optics Letters, **18** (15), 1277 (1993)

[8.7] P.Cordier, S. Dupont, M. Douay, G. Martinelli, P. Bernage, P. Niay, J.F. Bayon, L. Dong, Appl. Phys. Lett., **70** (10), 1204 (1997)

[8.8] R.C. Reddick, R.J. Warmack, D.W. Chilcott, S.L. Sharp, T.L. Ferrell, Rev. Sci. Instrum., **61** (12), 3669 (1990)

[8.9] J.-L. Archambault, P.St.J. Russell, S. Barcelos, P. Hua, L. Reekie, Optics Letters, **19** (3), 180 (1994)

[8.10] W.A. Atia, C.C. Davis, Applied Physics Letters, **70** (4), 405 (1997)

[8.11] M.L.M. Balistreri, J.P. Korteric, L. Kuipers, N.F. van Hulst, Physical Review Letters, **85** (2), 294 (2000)

[8.12] M. Svalgaard, S. Madsen, J.M. Hvam, M. Kristensen, IEEE Photonics Technology Letters, **10** (6), 848 (1998)

Appendix A: Publications

APPENDIX A.1: Journals

[1] J.D. Mills, C.W.J. Hillman, W.S. Brocklesby, B.H. Blott, *'Evanescent Field Imaging Of An Optical Fiber Bragg Grating'*, Applied Physics Letters, **75** (26), 4058-4060 (1999)

[2] John D. Mills, Chris W. J. Hillman, Barry H. Blott, William S. Brocklesby, *'Imaging Of Free-space Interference Patterns Used To Manufacture Fiber Bragg Gratings'*, Applied Optics, **39** (33), 6128-6135 (2000)

APPENDIX A.2: Conferences

[1] J.D. Mills, W.S. Brocklesby, B.H. Blott, *'Scanning Near-field Optical Microscopy Of Optical Waveguides'*, Optoelectronics Research Centre Internal Colloquium, 26th March (1998)

[2] C.W.J. Hillman, J.D. Mills, W.S. Brocklesby, B.H. Blott, *'Free-space SNOM Of Illuminated Phase Masks And Applications To Fibre Grating Fabrication'*, Optoelectronics Research Centre Internal Colloquium, 19th January (1999)

[3] J.D. Mills, C.W.J. Hillman, L. Reekie, W.S. Brocklesby, B.H. Blott, *'Near-field Imaging Of Fiber Bragg Gratings'*, Materials Research Society Spring Meeting, San Francisco, 5th-9th April (1999)

APPENDIX A.3: Other

[1] An article was written by Dexter Johnson, Editor of 'Sensor Technology' about the results described in *Chapter 4* of this thesis, as a consequence of the Applied Optics publication described above:

'Technique Measures New Fiber Bragg Grating Shapes', Sensor Technology Alert, John Wiley & Sons, Inc., New York, 29th December (2000)

[2] The free-space image of the field above a phase-mask shown in Figure 4.4(a) of this thesis, was used by J. Frey, Dept. of Chemistry, University of Southampton, as part of a display of *'Art In Science'* images, funded by an EPSRC *'Public Understanding Of Science'* grant, (2000).

Appendix B: Operation Amplifier

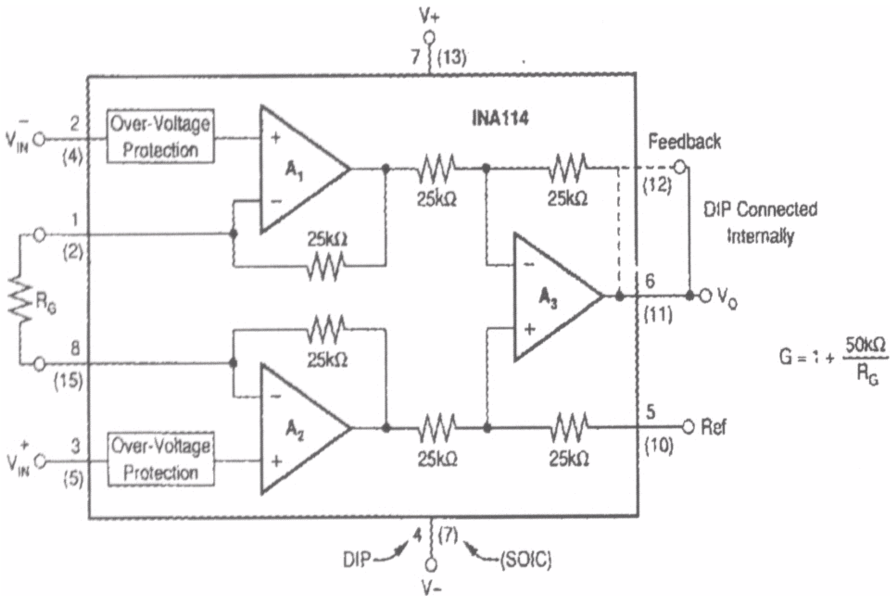

To increase the signal received from the quartz tuning-fork by the lock-in amp, a Burr-Brown precision instrumentation amplifier, INA114 was used to amplify its signal. The circuit of the device is shown above. A single external resistor can set the gain from 1 to 10000. It has input protection and can therefore withstand ±40V.

The Gain, G is set by connecting an external resistor, R_G where

$$G = 1 + (50kW/R_G) \qquad \text{(C.1)}$$

A gain of ~20 was used during this project.

Appendix C: PID Circuit Diagram